POLITECNICO DI MILANO

Dipartimento di Fisica

Dottorato di Ricerca in Fisica

XXV ciclo

MAGNETIC, ORBITAL AND CHARGE FLUCTUATIONS IN LAYERED CUPRATES STUDIED BY RESONANT SOFT X-RAY SCATTERING

Relatore e Tutor: Prof. Giacomo GHIRINGHELLI

Coordinatore: Prof. Franco CICCACCI

Tesi di Dottorato di:

Matteo MINOLA

Matr. 754140

Anno Accademico 2012–2013

Magnetic, orbital and charge fluctuations in layered cuprates studied by resonant soft x-ray scattering

Matteo Minola

January 28, 2013

to my Mother,
and to all those people
that will always be
in my heart
like Her

"[. . .] They expected me to be wonderful...
But I wasn't wonderful. And therfore I realised a new principle:
I'm not responsible for what other people think I'm able to do.
I don't have to be good because they think I'm going to be good.
And somehow or other, I could relax about this.
I thought to myself I haven't done anything important,
well, I'm never going to do anything important...
So I decided I'm only going to do things for the fun of it."

Richard P. Feynman, *The Pleasure Of Finding Things Out*

This thesis presents the results achieved on cuprates with resonant soft x-ray scattering (RXS) during my activity in the group of Prof. G. Ghiringhelli and Prof. L. Braicovich of the Physics Department of the Politecnico di Milano (Italy). The group has a well-established experience in synchrotron-based spectroscopies for the study of magnetic and electronic properties of transition-elements and rare earth compounds. In the last two decades, the activity of the group has been focused especially on soft x-ray emission spectroscopy and resonant inelastic x-ray scattering (RIXS). In particular they contributed substantially to the development of the latter, both from the point of view of science and instrumentation. They designed and built two high resolution spectrometers dedicated to RIXS measurements: AXES (Advanced X-ray Emission Spectrometer) and SAXES (Super-Advanced X-ray Emission Spectrometer). AXES is working since 1995 at the beamline ID08 of the European Synchrotron Radiation Facility (ESRF) in Grenoble, France. SAXES, which is the evolution of AXES, has been installed in 2006 at the RIXS end station of the ADRESS beamline at the Swiss Light Source (SLS) in Villigen, Switzerland. It is working since July 2007 and by now it holds the world record of resolution with a combined resolving power around 8000 at Cu L_3 edge (930 eV). On both the beamlines a continuous work of improvement has been carried out in these years in order to achieve better performances, allowing to obtain some ground-breaking scientific discoveries.

Here I will present some of the results obtained with these spectrometers in the last three years and regarding the study of insulating and superconducting layered cuprates by means of Cu L_3 edge RIXS.

RIXS is shown to be the optimal probe to study magnetic, orbital and charge fluctuations in the CuO_2 planes of these compounds, allowing energy- and momentum-resolved measurements in different regions of the reciprocal space. CuO_2 planes are the common feature of all layered cuprates and the set where high-T_c superconductivity emerges: these planes consist of Cu^{2+} ions alternated to O^{2-} ions and they are separated each other by "block-

ing layers". Although it has one electron (or hole) per Cu site, each CuO_2 plane is originally insulating, due to the large electron correlation typical of transition-element oxides. In particular this behaviour can be described, in first approximation, as that of a Mott insulator state, in which all the conduction electrons are tied to the atomic sites. More in detail, in the Mott-insulating state of a crystal the d electrons are almost entirely localized on the atomic sites and their spin and orbital degrees of freedom combine to produce different ordering patterns. The Cu^{2+} ions ($3d^9$ configuration, one-hole system) have one unpaired spin-1/2 per site and they are coupled via super-exchange interaction, i.e. the exchange mediated by oxygen, so to produce a bidimensional antiferromagnetic lattice. The hybridization with the neighboring oxygen ions is so strong that the super-exchange interactions are usually exceptionally high in cuprates (coupling costants > 100 meV), allowing the study of the associated magnetic excitations without the need of a few meV resolution. When the insulating parent compounds are doped, the additional degrees of freedom from dopant charges further complicate the electronic situation. In particular the substitution of one chemical element for another (e.g. Sr^{2+} for La^{3+} in $La_{2-x}Sr_xCuO_4$) or the addition of oxygen atoms in the reservoir layers, changes the net charge of the network formed by copper and oxygen ions, without relevant modifications of the basis crystal structure. A critical doping is required to destroy the various long range orders and substantially superconductivity emerges when holes coming from the blocking layers dope the CuO_2 sheets in a number that alters the situation and triggers the transition.

Despite more than 25 years of studies, the origin of the superconducting state in cuprates is still unclear and remains the subject of intense scrutiny. In particular one of the central unanswered questions concerns the nature of the normal-state spin fluctuations that may be responsible for the pairing. Because of technical limitations, the experimental investigation of doped cuprates has been until now largely focused on low-energy excitations in a small range of momentum space. In this thesis we used high resolution RIXS to show that a large family of high-T_c superconductors (HTS), including underdoped $YBa_2Cu_4O_8$, overdoped $YBa_2Cu_3O_7$ and intermediate cases, exhibits damped spin excitations (*paramagnons*), with dispersions and spectral weights closely similar to those of magnons in undoped cuprates. The comprehensive experimental description that comes out from our systematic data acquisition enables quantitative tests of magnetic Cooper pairing models and supports the paramagnons as strong candidates to cover the role of glue for the Cooper's pairs.

Subsequently we have exploited the capability of RIXS to work very well thin films, in order to study both insulating and superconducting cuprate-

based heterostructures. Recently the high pace technical progress in epitaxial growth has lead to the discovery of a panoply of exceptional magnetic and transport properties in artificial heterostructures of $3d$ transition metal oxides in general. Electronic, lattice and orbital reconstruction occurring at the interfaces can in fact influence the charge transfer between the different oxides (often inducing a doping of the interface layers), while the modified dimensionality can affect the magnetic properties of the oxides. Among these heterostructures cuprate-based superlattices (SLs) are particularly interesting since they can be considered as new, artificial materials belonging to the family of HTS, offering the opportunity of freely choosing the two building blocks i.e., the superconducting CuO_2 planes and the charge reservoir blocking layer that provides the extra charge needed to dope the planes and make them superconduct. Therefore we have carried out Cu L_3 RIXS measurements on both insulating and superconducting $(CaCuO_2)_m/(SrTiO_3)_n$ superlattices, and compared the results with those on a 14 nm thick $CaCuO_2$ film. This has been done in order to understand what happens to magnons when the CuO_2 planes are at the interfaces of a SL and if a (para)magnon-mediated superconductivity could still be possible. Moreover the orbital excitations, visible in RIXS spectra together with magnons and due to the ligand field felt by Cu^{2+} ions, have revealed a pyramidal coordination of copper atoms at the $CaCuO_2/SrTiO_3$ interfaces. In all insulating samples spin excitations are in the form of dispersing magnons. More in detail we show that in the SLs magnons have similar spectral intensity but reduced dynamics with respect to pure $CaCuO_2$. By fitting the dispersions within linear spin wave theory we have obtained the leading term of the in-plane superexchange parameters: $J = 127$ meV, 138 meV and 157 meV for $m = n = 2$, $m = n = 3$ SLs and $CaCuO_2$ respectively. These results demonstrate that the antiferromagnetic order is preserved in the insulating SLs down to very small cuprate layer thickness and despite the chemical and structural alterations at the interface. On the other hand the superconducting SLs exhibit dispersing paramagnons, similarly to the case of superconducting $YBa_2Cu_3O_{6+x}$. These findings open the way to the production of new, artificial HTS based on cuprate/noncuprate SLs where the charge reservoir layer is constituted by the interface itself.

Finally, since any successful theory for HTS requires a detailed understanding not only of the spin but also of the charge correlations in the normal state from which superconductivity emerges, we have devoted our attention to the study of charge fluctuations in CuO_2 planes by means of RXS. Despite intense efforts, to the present date only two clear ordering phenomena have been reported for correlations in the copper oxide sheets of cuprates: the above cited uniform antiferromagnetism that characterizes

undoped insulating cuprates and a uniaxially modulated antiferromagnetism combined with charge order in CuO_2 planes of the so-called "214" family [with chemical composition $La_{2-x-y}(Sr,Ba)_x(Nd,Eu)_yCuO_4$]. The latter is known as "stripe order", with a commensurate charge modulation of period $4a$ (where the lattice unit a is the distance between neighboring Cu atoms in the planes), which greatly reduces the superconducting transition temperature (T_c) of 214 materials at a doping level $p \sim 1/8$ per planar Cu atom. Incommensurate spin and charge fluctuations in 214 materials with $p \neq 1/8$ have been interpreted as evidence of fluctuating stripes. These findings have generated a long-standing debate around the questions of whether stripe order is a generic feature of the copper oxides and if stripe fluctuations are essential for superconductivity. We have used resonant soft x-ray scattering to assess this issue and identify two-dimensional charge fluctuations with an incommensurate periodicity of $\sim$3.2 lattice units in the CuO_2 planes of the superconductors $(Y,Nd)Ba_2Cu_3O_{6+x}$, with hole concentrations of 0.09 to 0.13 per planar Cu ion. The intensity and correlation length of the signal increase strongly upon cooling down to the superconducting transition temperature (T_c), while further cooling below T_c abruptly reverses the divergence of the charge correlations. In combination with earlier observations, these data indicate an incipient *charge density wave* (CDW) instability that competes with superconductivity and, for the first time, we have the evidence that the anomalously low T_c found in underdoped cuprates is due to CDW, and not other phenomena.

Contents

List of Tables

List of Figures

Introduction

This thesis is aimed to show the unique power of *resonant inelastic* soft *x-ray scattering* to probe magnetic, orbital and charge fluctuations in cuprates. Resonant inelastic x-ray scattering (RIXS hereafter) is a photon *in*-photon *out*, synchrotron-based spectroscopic technique, that is well known since more than 30 years [1] but has gone through a "Renaissance", as defined by Kotani and Shin [2], in the past decade. Indeed with the recent developments of dedicated RIXS instrumentation at third generation synchrotron radiation facilities, and the consequent improvement of photon flux and energy resolution, RIXS is today a fantastic tool to study elementary, low-energy excitations, that were in the past precluded by the modest energy resolution typically achieved. As a consequence many synchrotron facilities all over the world at present date are planning to have or they have already designed advanced high resolution RIXS endstations, scheduled to be fully operative in the months and years to come.
RIXS offers in fact the unique possibility of study energy- and momentum-resolved neutral elementary excitations, with bulk sensitivity. Moreover, being based on a resonance, RIXS is also chemical-selective. All these properties cannot be achieved simultaneously by any other technique.

In particular, when performed at the Cu $2p_{3/2}$ absorption threshold (L_3 edge), RIXS is very powerful to measure both ligand field (dd) excitations [3] and magnon dispersion in layered quasi-2D cuprates (both in single crystals and thin films), as recently demonstrated experimentally [4] and theoretically [5]. In Cu L_3 RIXS an incoming photon with energy $\hbar\omega_i \simeq 930$ eV and momentum $\mathbf{k} \simeq 0.81$ $\mathring{A}^{-1}$ promotes a core electron from a $2p$ state to an empty $3d$ state. One observes then the radiative decay of this highly excited intermediate state corresponding to the transition of a $3d$ electron back to the $2p$ core level. The energy $\hbar\omega_o$ of the emitted photons in a given direction is accurately measured, to obtain the energy transferred in the

scattering event from the x-ray photon to the sample: $E_{loss} = \hbar\omega_i - \hbar\omega_o$. The scattering geometry determines the momentum transfer $\mathbf{q} = \mathbf{k'} - \mathbf{k}$ and its projection onto the ab plane $\mathbf{q}_{\parallel}$, which is the meaningful quantity in the experiment, given the quasi-2D nature of layered cuprates. Cu L_3 RIXS has quickly challenged inelastic neutron scattering (INS) for the study of magnetic fluctuations in high temperature superconductors (HTS), thanks to the exceptional enhancement provided by the resonance and to the very strong Cu $2p$ spin-orbit interaction in the intermediate state, that opens the access to spin-flip excitations, and thus to magnons. In particular, despite some limitations due to finite energy resolution are still present, Cu L_3 RIXS sensitivity is many orders of magnitude higher than the one of INS, so that experiments can be made on sub millimeter crystals and thin films [4, 6, 7]. Therefore RIXS in its high resolution version can be considered a renewed technique, which can be applied to the study of old, unsolved problems in a different perspective, such as cuprates, as well as to the investigation of fresh, recently discovered materials. Since the Renaissance of RIXS much has been already understood about the technique itself, also from a theoretical point of view, mostly studying the prototypical case of cuprates. However there is still much to learn about both the technique and cuprates, and this thesis is also aimed to show and underline potential and capabilities of RIXS in this sense.

In Chapter 1, the technique is briefly presented in very general terms, emphasizing all characteristics that together make RIXS unique. Moreover excitations probed by the RIXS process are classified and briefly introduced. In the last Section of the Chapter, the theoretical background needed for the understanding of the RIXS cross-section is recalled.

Before the discussion of some of the most ground-breaking results obtained with Cu L_3 RIXS in the past few years, Chapter 2 introduces the reader to the experimental apparatus and the typical instrumentation needed for RIXS measurements. The two synchrotron beam lines mostly used for the experiments presented hereafter are described and compared. These are the ID08 beam line of the European Synchrotron Radiation Facility (ESRF) in Grenoble and the ADRESS beam line of the Swiss Light Source (SLS) at Paul Scherrer Institut (PSI) in Villigen (CH). Also the two spectrometers, AXES and SAXES, currently operating at the two beamlines, are presented in their general layout, with particular emphasis on the different performances offered by the two systems. A brief description of the prototype *polarimeter* currently mounted on AXES is also given. The device has been successfully tested and provides for the first time the possibility to detect the polarization of the scattered beam in energy resolved soft x-ray scattering experiments. Moreover we make a short comparison between a typical RIXS spectrome-

ter and a traditional diffractometer for conventional energy-integrated RXS measurements, that is preparatory to the understanding of the results on charge density waves in cuprates, obtained with a combination of RIXS and RXS experiments.

Chapter 3 gives a concise introduction to general aspects of insulating and superconducting layered cuprates and their properties of strongly correlated electron systems are discussed. Since the discovery in late 1986 by Bednorz and Müller [8] that in cuprates superconductivity can be achieved at critical temperatures (T_c) above the limits imposed by Bardeen, Cooper and Schrieffer (BCS) theory [9] a lot of efforts have been devoted to the study of these materials that, differently from conventional superconductors, allow the production of superconducting devices working at liquid N_2 temperatures. However, most part of the large variety of phenomena occuring in these systems has still to be understood and the mechanism behind high-T_c superconductivity remains substantially unknown. In this respect RIXS can provide crucial information on magnetic and charge fluctuations in CuO_2 planes, which constitute the set in which superconductivity emerges, thus giving a crucial help in gathering together the pieces of the high-T_c puzzle. Moreover Chapter 3 opens also to the experimental results, dealing with the systematic study of magnetic excitations, as a function of the transferred momentum, in doped layered cuprates, over a wide range of doping. After recalling briefly Cu L_3 RIXS results on magnons in undoped cuprates, the aim of the chapter is to show that a large family of superconductors exhibits damped spin excitations (called *paramagnons*) in the CuO_2 planes, with dispersions and spectral weights closely similar to those observed in undoped cuprates. The comprehensive experimental description of the low energy spectrum in these systems supports the hypothesis of a magnetic Cooper pairing model for high-T_c superconducting cuprates, allowing also some quantitative analysis.

In Chapter 4 we use RIXS to assess the effects on magnetic fluctuations when CuO_2 planes are close to the interfaces of an artificial cuprate-based heterostructure, such as $CaCuO_2/SrTiO_3$ superlattices (SLs). The proximity of interfaces in fact could in principle affect magnons in different ways, due to the unavoidable presence of chemical and structural alterations of the cuprate system when it is combined with an another compound. Incidentally the information provided by RIXS on *dd* excitations and associated ligand field, helps to get deeper insights into these alterations and on the local coordination of Cu ions close to the interfaces of these artificial systems. We show that these have a pyramidal coordination and, most importantly, that the antiferromagnetic order is preserved in these SLs down to very small cuprate layer thickness: magnetic excitations in the form of magnons and param-

agnons are in fact shown to be present in both insulating and superconducting superlattices, respectively, despite the alterations at the interfaces.

Finally, the last Chapter of this thesis deals with a different use of soft RIXS aimed at clarifying the issue of charge fluctuations and charge order in the CuO_2 planes of cuprates. So far, RIXS results have been restricted to the inelastic part of the spectrum. In this respect the elastic peak is basically considered as a nuisance in RIXS experiments, because it might hinder the very low energy loss spectral features. This situation is even more extreme at Cu L_3 edge for layered cuprates, where the inelastic component, given mainly by *dd* excitations, is greatly enhanced and is overwhelmingly dominant over the elastic signal, which represents 5% of the total valence emission. This circumstance is favorable for RIXS spectroscopy but tremendously complicates resonant elastic x-ray scattering (REXS) experiments, which are the common way to study possible charge orders in materials. Indeed in the absence of any energy filtering the signal to background ratio is very low. In this respect RIXS spectra, although more difficult to measure as they require a high resolution spectrometer, can be used to single out the true elastic component. This is what we have done for (Y,Nd)$Ba_2Cu_3O_{6+x}$ superconductors: we combined RIXS with ordinary REXS measurements and we obtained direct evidence of two-dimensional incommensurate charge fluctuations in the CuO_2 planes of these systems, indicating an incipient charge density wave (CDW) instability that competes with superconductivity. In particular the use of RIXS has been crucial at first to discover and detect the elastic scattering from CDW, thanks to the energy-resolved nature of RIXS spectra.
Cu L_3 RIXS is, thus, proven to be a unique tool for the study of magnetic, orbital and charge fluctuations in cuprates, in the sense that it is here shown to effectively probe the spin and charge orders in the CuO_2 planes of layered cuprates, providing a wealth of information helpful to put together the pieces of the HTS puzzle.

I note here that, for the sake of brevity and clarity, I have made the choice to present only some of the nice results that I have obtained with my group in these years and in which I was directly involved. It is clear that the huge amount of work that I will describe hereafter could not be done by just one single person. However I want to stress that I actually carried out all the measurements described in Chapters 3, 4, and 5. For the results of Chapter 4 I also performed in first person the data analysis, whereas for the extensive data sets presented in Chapters 3 and 5 I have given my contribution in various ways to the analysis carried out by my collaborators and coworkers. On the other hand it is also true that in the past three years I have participated also to many other experiments that I will not present in this Thesis and whose results are partially contained in my publications (see the list at

page 169).

Chapter 1

RIXS to probe the properties of cuprates

Resonant inelastic x-ray scattering is hereafter presented in very general terms, emphasizing all characteristics that together make this technique unique, such as "neutrality", bulk sensitivity, element selectivity, and **q**-resolution. The scattering process is described and the excitations probed by this process are classified and briefly introduced, showing the capabilities of RIXS useful for the study of magnetic and electronic properties in solids and in particular in cuprates. Finally, in the last Section of the Chapter, the theoretical background needed for the understanding of the double differential RIXS cross-section is briefly developed and discussed, by deriving and commenting the Kramers-Heisenberg expression in the electric dipole approximation.

Contents

1.1 Introduction

Resonant inelastic x-ray scattering (from now on, RIXS) is a "photon *in*-photon *out*" synchrotron-based spectroscopic technique, well known since a

few decades and suitable for the study of elementary excitations in solids. In general when a photon hits the sample, the result of light-matter interaction is a photon scattered out in an arbitrary direction, with a certain energy, momentum and/or polarization state, that is not necessarily the same of the initial photon. Moreover because of the interaction, also the system is usually left in a state different from the ground one, i.e. an excitation takes place. One can accurately measure the energy $\hbar\omega_o$ of the emitted photons in a given direction in order to obtain the energy transferred in the scattering event from the x-ray photon to the sample: $E_{loss} = \hbar\omega_i - \hbar\omega_o$ and to generate a spectrum of excitations with different energy losses. Moreover the scattering geometry determines the momentum transfer $\mathbf{q = k' - k}$, so that one can obtain different spectra for different geometries of the measurement.

By studying the inelastic features of these RIXS spectra, one can thus infer about the energy, momentum-dependence, symmetry and physical origin of the excitations that occurred in the sample. Besides these facts RIXS is a resonant technique, i.e., the energy of the incoming photon is tuned on purpose at an absorption edge of the studied compound: this ensures not only chemical selectivity, on which we will return later, but also a more favorable scattering cross-section with respect to the non-resonant case and to other techniques. In particular with the recent improvements in energy resolution RIXS performed at the $2p_{3/2}$ absorption threshold (L_3 edge) of copper has quickly challenged inelastic neutron scattering (INS) for the study of magnetic fluctuations in high temperature cuprate superconductors (HTS) as we will see. This is mostly due to the exceptional enhancement provided by the resonance that assures a sensitivity many orders of magnitude higher than that of INS, so that experiments can be made on sub millimeter crystals and thin films.

We note here that actually the energy resolution has been for a long time the limiting factor of RIXS (especially in the soft x-ray energy range) and that a huge work has been recently done on the instrumentation to overcome this issue. We will return on these considerations later in Chapter 2, that is entirely dedicated to the experimental apparatus needed for RIXS.

Hereafter in this Chapter a general introduction to RIXS is given, together with a brief theoretical description of its cross-section, mostly following Refs. [10] and [11], that are more exhaustive on the topic.

1.2 The scattering process

RIXS is based upon a two-step process, as shown in Fig. 1.1: an x-ray photon with energy $\hbar\omega_i$ hits the sample and, through its resonant absorption, a core

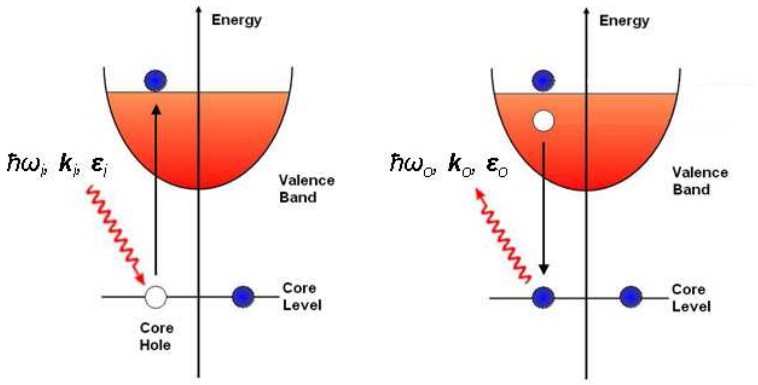

Fig. 1.1: Scheme of the RIXS scattering process: the absorption of the incoming photon $\hbar\omega_i$ promotes a core electron to an empty state above the Fermi level and creates a core hole (left panel). Afterward a valence electron fills the core hole and a photon $\hbar\omega_o$ is emitted (right panel).

electron is promoted to an empty state above the Fermi level and a deep core hole is created. The system, initially in its ground state, is thus promoted into a highly excited intermediate state. This is really unstable and within its lifetime ($\approx$ 1 fs) the system rapidly decays back into a final state by emitting an another x-ray photon of energy $\hbar\omega_o$ when a valence electron fills the core hole. In general, the final state may not coincide with the ground state: in such a case the system is left in an excited state of energy $\hbar\omega_i - \hbar\omega_o$ ($\hbar\omega_o < \hbar\omega_i$) above the ground state. On the other hand it can also happen that $\hbar\omega_o = \hbar\omega_i$, elastic scattering occurs and no excitations are left in the system, that goes simply back to its ground state. More in detail, if the process takes place at the L absorption edge of a transition element, such as copper, photons energies are in the soft X-ray range ($\hbar\omega_i \sim$1 keV), the core level involved is $2p$ and the valence states above the Fermi level have a $3d$ character.

As previously said, an excitation is the result of the scattering process. Generally speaking one has to consider the conservation laws for energy and momentum of the whole system, including both photon and scatterer, before and after the scattering process. Given that the system lies in the ground state before the interaction with x-rays, one can obtain the energy and the momentum of any excitation occurred in the sample by imposing that:

$$\hbar\omega_i = \hbar\omega_o + E^{exc} \tag{1.1}$$

$$\hbar\mathbf{k}_i = \hbar\mathbf{k}_o + \hbar\mathbf{q}^{exc}, \tag{1.2}$$

where $\hbar\omega_i$ ($\hbar\omega_o$) is the energy of the ingoing (outgoing) photon and $\hbar\mathbf{k}_i$ ($\hbar\mathbf{k}_o$) is the corresponding momentum. Moreover a third conservation law applies to the angular momentum of the whole system and regards the polarization state of the ingoing ($\boldsymbol{\varepsilon}_i$) and outgoing ($\boldsymbol{\varepsilon}_o$) photons. If one is able to retrieve all information needed to fully characterize ingoing and outgoing photons in terms of energy ($\hbar\omega_i$ and $\hbar\omega_o$), momentum ($\hbar\mathbf{k}_i$ and $\hbar\mathbf{k}_o$) and polarization ($\boldsymbol{\varepsilon}_i$ and $\boldsymbol{\varepsilon}_o$), then he has a complete knowledge of the excitation that has taken place in the system. Actually in real experiments the parameters describing the ingoing photons are usually well-known: $\hbar\omega_i$ and thus $|\mathbf{k}_i|$ are fixed by the resonance at which one is working (Cu $L_3 = 931$ eV for the measurements presented hereafter) while the use of synchrotron radiation generally guarantees a well defined polarization $\boldsymbol{\varepsilon}_i$. What takes an effort (and a spectrometer) to get are the parameters of the outgoing photons. In particular in the soft x-ray energy range the measurement of the polarization of the scattered photons ($\boldsymbol{\varepsilon}_o$) is highly complicated and demands smart technicalities [12, 13].

In first approximation one can think of the whole process as the *inelastic scattering* of a photon, so that RIXS could be defined as an "energy loss spectroscopy", not to be confused with other techniques like Electron Energy Loss Spectroscopy (EELS). A number of characteristic makes in fact RIXS an unequalled technique for the study of elementary excitations in condensed matter physics. We try to list the most important ones hereafter.

First of all, being RIXS a "photon *in*-photon *out*" technique, no charge is added to or removed from the studied sample as a consequence of the scattering process. Therefore, the overall *neutrality* of the system is preserved, unlike other spectroscopic techniques, such as direct or inverse photoemission for example, where the total charge of the system changes. This fact is fundamental in order to avoid possible unwanted charging problems, especially when insulating compound are measured, given also that several correlated systems are insulators.

Another feature of RIXS strictly related to the use of x-rays is the *bulk sensitivity*. As well known the penetration depth of photons varies considerably depending on their energy. However when one deals with x-rays this depth ranges from tens of nm in the soft x-ray regime to few μm towards the hard x-ray energy range, as shown in in Fig. 1.2, allowing the study of bulk excitations without artifacts due to surface effects or contaminations. This means also that there is no need of critical and fastidious procedures for the sample surface preparation. Nevertheless bulk sensitivity does not prevent to use RIXS to investigate in a safe way also surface states. Indeed, exploiting the resonance with a certain atomic species, the bulk contribution

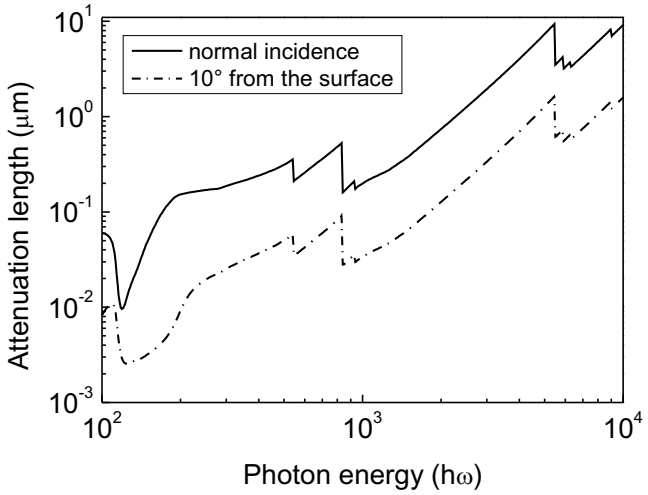

Fig. 1.2: Simulated attenuation length of x-ray in a model cuprate, La_2CuO_4, as a function of the photon energy ranging from 100 eV to 10 keV. The simulations were carried out from the CXRO online simulator of the Lawrence Berkeley National Laboratory's [14].

to the spectrum due to other chemical elements becomes negligible and the combination of bulk sensitivity and chemical selectivity of RIXS allows one to study buried interfaces or multilayers, thus making the technique very flexible, as we will see also in Chapter 4. Moreover, the surface sensitivity can be also enhanced by playing with the experimental geometry, i.e. working in grazing incidence conditions: in fact, the attenuation length is estimated [14] to decrease of roughly an order of magnitude over the whole energy range for x-rays at a glancing angle of 10° from the surface.

On the other hand, although x-rays penetrate enough to make the surface contribution negligible to the RIXS signal, this does not prevent from measuring tiny samples. As previously mentioned in fact RIXS has recently challenged inelastic neutron scattering (INS), thanks to the strength of the interaction between x-rays and matter and the much higher fluxes reached nowadays at synchrotrons compared to neutron sources. Differently from INS, that requires massive samples, RIXS is capable to work well even on very small amounts of material, such as nano-sized structures or thin films. In particular, this is the case of layered cuprates, which are often available only under these forms and could not be properly studied with neutron-based techniques because of the weakness of the signal, as it will be more clear in

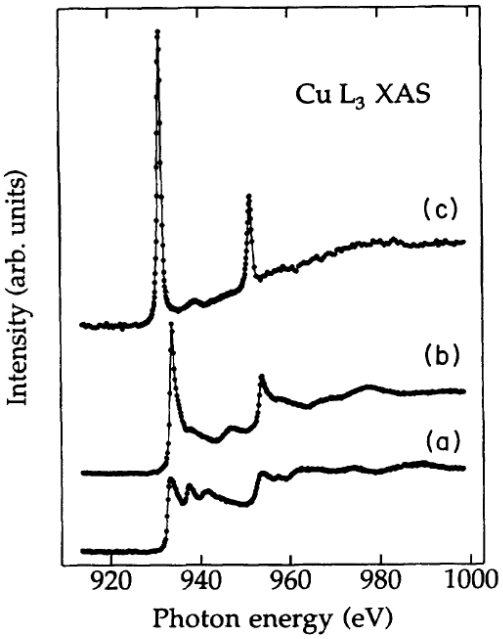

Fig. 1.3: Cu $L_{2,3}$ edge XAS of (a) copper metal, (b) Cu_2O (Cu^{1+}) and (c) CuO (Cu^{2+}) [15]. The different oxidation states of the Cu ions in these compounds give a sizable variation of the corresponding absorption edge energies.

Chapter 3 and Chapter 4.

As already above mentioned, an other profitable characteristic of RIXS is the *element (or chemical) selectivity*, based on the resonance with an absorption edge. As very well known an edge is a sharp discontinuity in the absorption spectrum of x-rays that occurs when the photon energy resonates with the excitation energy needed to promote a core electron above the Fermi level. Absorption edges represent then a signature for a given element. To measure a RIXS spectrum the incoming photon energy is tuned on purpose on a desired absorption edge, thus privileging the scattering from the corresponding element. In this respect RIXS allows one to excite selectively an element and study elementary excitations while "sitting" on that specific element. Moreover, since the chemical environment influences shape and energy of the absorption edge, one can discriminate between the same atomic specie with different oxidation states or coordination symmetries, as long as the corresponding absorption edges are sufficiently well separated in energy.

This is exemplified in Fig. 1.3, where the Cu $L_{2,3}$ edge absorption spectra of (a) copper metal, (b) Cu_2O (Cu^{1+}) and (c) CuO (Cu^{2+}) [15] are shown: the different oxidation states of Cu ions in the three compounds give a sizable

variation in the corresponding edge energies. If the studied system presents a mixture of these contribution, by tuning precisely the incoming photon energy, one can selectively probe the fraction of Cu ions with the corresponding oxidation state. In this sense, RIXS may be also considered to some extent a site-selective technique. We note here that the possibility to arbitrarily tune the incoming photon energy on a desired edge implies the use of synchrotron beamlines (see Chapter 2).

Finally, although it is usually considered negligible for visible light, photons carry a momentum that is inversely proportional to their wavelength (λ) and that becomes not-negligible for x-rays where $\lambda \approx 1$ Å, i.e. comparable with the interatomic distances in solids. This means that a sizable fraction of the Brillouin Zone of solids can be typically probed, contrarily to experiments using optical photons, which are restricted to a region very close to the Γ point.

1.3 Excitations accessible to Cu L_3 RIXS

The excitations probed by RIXS are related to the charge, spin, and orbital degrees of freedom of the studied system, and also to its lattice dynamics. As said in the previous section RIXS probes only neutral excitations that do not change the total net charge of the sample. In particular in the following chapters of this thesis it will become clear that high resolution RIXS is a powerful tool to measure both ligand field (dd) and magnetic excitations in cuprates, as we have recently demonstrated both theoretically and experimentally [3, 5, 16, 17].

When performed at Cu L_3 edge the RIXS process follows the steps exemplified in the sketch of Fig. 1.4. Let us consider a total energy scheme of the system with the Cu d states split by the symmetry breaking introduced by the presence of ligands atom and thus of a ligand field (we will return on this fundamental splitting later in Chapter 3). Since copper ions in the CuO_2 planes of cuprates are usually in a $3d^9$ configuration, i.e. they have just one hole in the d shell, we can reason in terms of this unique hole for the sake of simplicity. First the resonant absorption of a photon moves the hole from the highest d state to the $2p_{3/2}$ core level, bringing the system from the initial ground state to a highly excited intermediate one. Then the system rapidly decays by emitting one photon and the hole moves back to the d states. What can happen is that the final d state is not the same intial one and as a consequence the system will appear in an excited final state, i.e. the process was not elastic. The energy difference between the final and initial

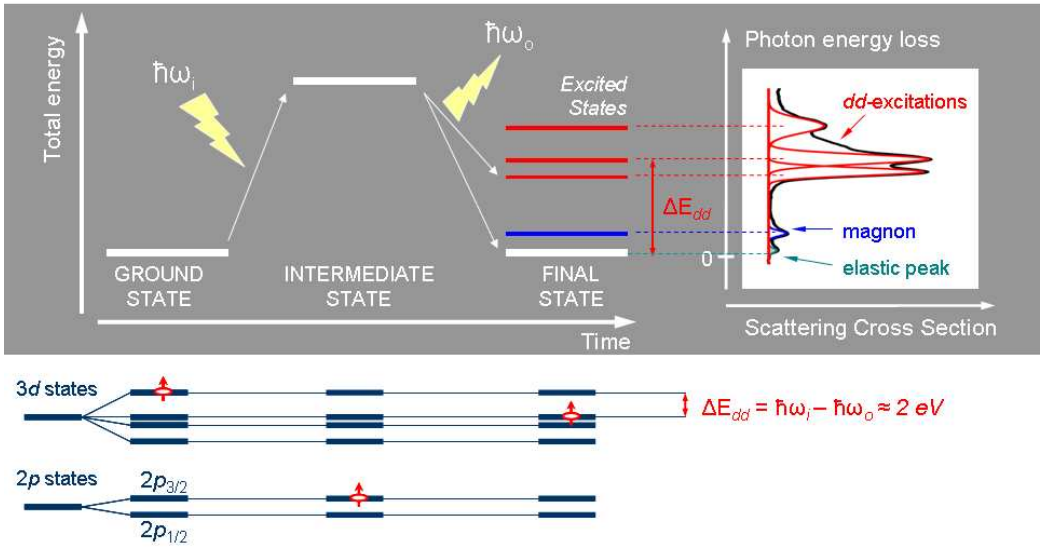

Fig. 1.4: Total energy scheme of copper at the various stages of a Cu L_3 RIXS process and associated typical RIXS spectrum of a cuprate. Note how the Cu $3d^9$ hole (open red circle) makes two dipole allowed transitions making possible a dipole forbidden dd-excitation of energy ΔE_{dd}.

d states is the energy of a so-called dd- (or ligand field) excitation (usually around 2 eV). In principle this is a transition not allowed by dipole (since $\Delta l = 0$), however with two dipole-allowed transitions having $\Delta l = \pm 1$ (d-to-p and p-to-d) RIXS makes it possible.

Moreover Cu L_3 RIXS gives access to magnetic excitations, such as single and multiple magnons. As well known a magnon is a wave-like collective excitation of the electrons' spin structure in a crystal lattice. As it will be recalled more in detail in Chapter 3, an antiferromagnetic order of the spin-1/2 Cu^{2+} sites in the CuO_2 planes always characterizes the ground state of cuprates. Starting from this situation in a Cu L_3 RIXS process a single magnon can be excited due to the strong spin-orbit interaction in the $2p$ core hole present in the intermediate state. A multiple magnon instead is formed by a few single magnons propagating simultaneously in different directions. In the intermediate state in fact the temporary $3d^{10}$ configuration with spin 0 makes the scattering Cu site a "non-magnetic" impurity. This impurity quenches the superexchange locally in the antiferromagnetic lattice and the consequent screening by neighboring sites can result in the generation of a multiple magnon. In general if the multiple magnon is formed by an even (odd) number of departing spin-waves the total spin moment of the system is (not) conserved; in any case finite energy and momentum have been trans-

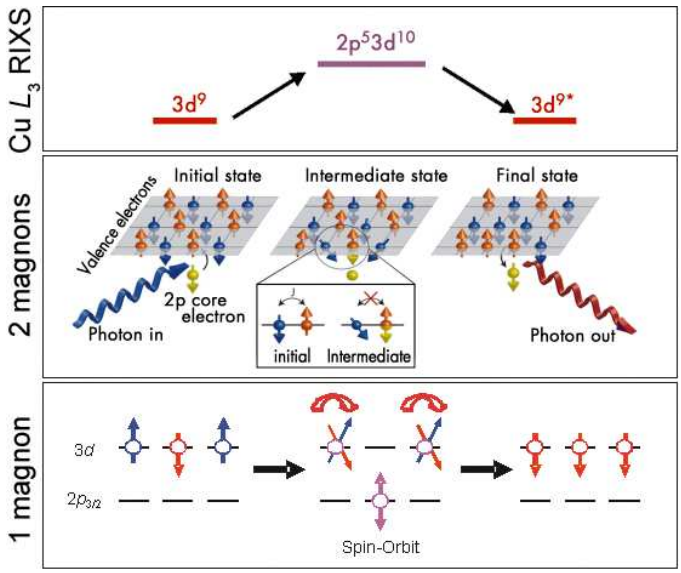

Fig. 1.5: Schematics of the excitation of a magnon and of a bimagnon in a Cu L_3 RIXS process.

ferred from the scattered photon to the system itself. Fig. 1.5 shows the scheme of a Cu L_3 RIXS excitation for a magnon and a bimagnon, i.e. a multiple magnon based on two spin waves.

The above presented excitations are the most important among the ones probed by RIXS with respect to the experimental results described in this thesis. However in more general terms one can use energy-, momentum-, and polarization-dependence in order to recognize and classify all different excitations probed by RIXS performed at different edges. Let us try to deepen these dependences, which are useful also for the understanding of the measurements that will be presented later on.

First of all some advantages are given by the possibility to study how a RIXS feature changes when the incoming photon energy ($\hbar\omega_i$) is slightly varied across the chosen absorption edge. In fact this allows one to distinguish between Raman-like features, i.e. the ones associated to elementary excitations that are found at constant energy loss (E_{loss}=$\hbar\omega_i$-$\hbar\omega_o$) in the spectra, and non-Raman features, i.e. the ones usually referred as *fluorescence* and associated to photons emitted at constant outgoing energy $\hbar\omega_o$, independently from $\hbar\omega_i$. The last are less important because they correspond to the decay of an electron that has already relaxed, losing the information about the RIXS intermediate state of the system. Magnons and *dd*-excitations belong to the first family and in this thesis we will focus only on Raman features. In

general, the intensity of both Raman and non-Raman features changes when $\hbar\omega_i$ is varied across the chosen absorption edge, because of both absorption cross-section effects and possible differences in the scattering paths. As a consequence, the $\hbar\omega_i$-dependence can also be used to determine at which energies the different features resonate.

Secondly, as mentioned in the previous section, in RIXS experiments a finite momentum $\hbar\mathbf{q} = -(\hbar\mathbf{k}_o - \hbar\mathbf{k}_i)$ is transferred to the system, depending on the scattering geometry. One can thus study the evolution of Raman-like features when the momentum transfer is changed and in such a way discriminate between *local* and *collective* excitations. In general terms, collective modes can be labelled with a wave-vector $\mathbf{q}^{exc} = \mathbf{q}$ and they show a dispersion, usually symmetric to the $\mathbf{q} \to -\mathbf{q}$ inversion, that can be mapped in the reciprocal space. On the other hand, for localized excitations $\mathbf{q}^{exc}$ does not represent a good quantum number and no dispersion is found. For instance in cuprates *dd*-excitations are known to have a local character [3] while magnons have a dispersive nature, as it will be shown more in detail in Chapter 3 and 4. We note here that independently from the nature of the excitation the intensity of the corresponding feature usually changes with $\mathbf{q}$, because of cross-sections variations that might be due to simple geometrical factors, rather than to an explicit $\mathbf{q}$-dependence. Moreover, there are also excitations having an hybrid character, in that they involve more than one site, but do not show any clear dispersion: this is the case of charge-transfer excitations, i.e. the ones associated to an electron transfer from an ion to its ligands.

Finally one can think to use the polarization-dependence of RIXS features to gain further information about them. The polarization of a photon determines its angular momentum so that ingoing and outgoing photon polarization $\boldsymbol{\varepsilon}_i$ and $\boldsymbol{\varepsilon}_o$ are subject to the selection rules imposed by the conservation of the total angular momentum of the system. Moreover $\boldsymbol{\varepsilon}_i$ and $\boldsymbol{\varepsilon}_o$ are vectorial entities that can be varied by changing the scattering geometry, in order to infer about the symmetry of the electronic wave-function in the initial and final states. As a consequence one would like to measure $\boldsymbol{\varepsilon}_o$, having fixed $\boldsymbol{\varepsilon}_i$. Unfortunately, while in the hard x-ray regime the measurement of the polarization of the scattered photons is nowadays feasible because Bragg optics are intrinsically polarization selective, in the soft x-ray energy range this is much more complicated because one has to rely upon multilayered mirrors, with very low reflectivity and polarization sensitivity. For this reason at present most of RIXS experiments fully exploit only the $\boldsymbol{\varepsilon}_i$-dependence. This is made possible by nowadays synchrotrons, where new-generation insertion devices

allow the full control of the polarization (linear or circular) of the emitted radiation (see Chapter 2). The outgoing polarization $\boldsymbol{\varepsilon}_o$ is known to lie in the plane perpendicular to $\mathbf{k}_o$, but it is not determined precisely.

However very recently our group has implemented a solution, based on a multilayered mirror, on the AXES spectrometer at the ESRF (described in Section 2.3), in order to add a partial polarization detection in the case of the linear polarization components of the scattered beam in soft RIXS [12, 13]. More details on this protoytpe of *polarimeter* will be given in a dedicated section (2.3.2) in Chapter 2. Although we did not use this polarimeter for the measurements presented in this thesis, we note here that in the case of Cu L_3 edge RIXS on undoped and superconducting layered cuprates we exploited the $\boldsymbol{\varepsilon}_i$-dependence of the low-energy excitations in the spectra, in order to distinguish magnetic and charge excitations and to discriminate between magnons of different orders, as it will become clear later.

1.4 RIXS cross-section

Before to get to the instrumentation needed for RIXS (described in the next Chapter), in this Section we recall and derive the expression for the RIXS cross-section, along the lines of Ref. [10] and references therein. In order to do so one has first to write the Hamiltonian of the system. We describe the incident x-rays by an electromagnetic field, with wave-vector potential $\mathbf{A}(\mathbf{r}, t)$, that will be coupled to the electrons according to the quantum electrodynamics theory. In the non-relativistic case and in the limit that the potentials related to electrons and photons in the system are small compared to twice the mass of the electron ($e\phi/2mc^2$, $e|\mathbf{A}|/2mc \ll 1$), the Hamiltonian for a system with N electrons interacting with an electromagnetic field is written in SI units as:

$$\begin{aligned}\mathcal{H} = &\sum_j^N \frac{\left[\mathbf{p}_j + e\mathbf{A}\left(\mathbf{r}_j\right)\right]^2}{2m} - \sum_j^N e\phi\left(\mathbf{r}_j\right) + \sum_j^N \frac{e\hbar}{2m}\boldsymbol{\sigma}_j \cdot \mathbf{B}\left(\mathbf{r}_j\right) + \\ &+ \sum_j^N \frac{e\hbar}{2\left(2mc\right)^2}\boldsymbol{\sigma}_j \cdot \left\{\mathbf{E}\left(\mathbf{r}_j\right) \times \left[\mathbf{p}_j + e\mathbf{A}\left(\mathbf{r}_j\right)\right] - \left[\mathbf{p}_j + e\mathbf{A}\left(\mathbf{r}_j\right)\right] \times \mathbf{E}\left(\mathbf{r}_j\right)\right\} + \\ &+ \sum_j^N \frac{e\hbar^2\rho\left(\mathbf{r}_j\right)}{8\left(mc\right)^2\varepsilon_0} + \int d\mathbf{k} \sum_{\boldsymbol{\varepsilon}} \hbar\omega_{\mathbf{k}} \left(c^\dagger_{\boldsymbol{\varepsilon},\mathbf{k}} c_{\boldsymbol{\varepsilon},\mathbf{k}} + \frac{1}{2}\right), \end{aligned} \tag{1.3}$$

where $\mathbf{p}_j$, $\mathbf{r}_j$ and $\boldsymbol{\sigma}_j$ are the momentum and the position operators and the Pauli matrices acting on the electron j, respectively. $\mathbf{A}(\mathbf{r})$ is the vector

potential, $\mathbf{E}(\mathbf{r}) = -\nabla\phi(\mathbf{r}) - \partial\mathbf{A}(\mathbf{r})/\partial t$ the electric field and $\mathbf{B}(\mathbf{r}) = \nabla \times \mathbf{A}(\mathbf{r})$ the magnetic field. $c^\dagger_{\boldsymbol{\varepsilon},\mathbf{k}}$ ($c_{\boldsymbol{\varepsilon},\mathbf{k}}$) creates (annihilates) a photon in the mode with wave-vector $\mathbf{k}$, energy $\hbar\omega_{\mathbf{k}} = c|\mathbf{k}|$ and polarization vector $\boldsymbol{\varepsilon}$.

The first two terms of $\mathcal{H}$ are the electrons kinetic and potential energy in the presence of an electromagnetic field, the third term gives the Zeeman splitting and the fourth accounts for the spin-orbit coupling. The fifth term, proportional to $\rho(\mathbf{r})$, is called the Darwin term. This changes the effective potential at the nucleus, smearing out the electrostatic interaction between electron and nucleus due to the rapid quantum oscillations of the electron. It shifts only the energy of s orbitals, i.e. the only ones overlapping with the charge density of the nucleus, in contrast with the spin-orbit term which affects all but the s states. Finally, the last term gives the energy of the radiation as the sum of all the modes, each having energy $\hbar\omega_{\mathbf{k}}$. The interaction of electrons with other electrons and nuclei is omitted.

In order to derive the scattering cross-section, it is convenient to split the Hamiltonian $\mathcal{H}$ into an electron-photon interaction part ($\mathcal{H}'$), and in the remaining terms, which describe the electron ($\mathcal{H}_{el}$) and photon ($\mathcal{H}_{em}$) dynamics in the absence of electron-photon interaction. In such a way it is possible to treat $\mathcal{H}'$ as a perturbation to $\mathcal{H}_0 = \mathcal{H}_{el} + \mathcal{H}_{em}$. Given that $\mathcal{H}_0$ does not contain electron-photon interactions, its eigenfunctions can be written as the product of eigenstates of $\mathcal{H}_{el}$ and eigenstates of $\mathcal{H}_{em}$.

We build the photon-field wavefunction by using the creation operator $c^\dagger_{\boldsymbol{\varepsilon},\mathbf{k}}$ on the vacuum state $|0\rangle$, for which

$$c_{\boldsymbol{\varepsilon},\mathbf{k}}|0\rangle \equiv 0 \qquad \forall\boldsymbol{\varepsilon},\mathbf{k}. \tag{1.4}$$

To calculate the RIXS cross-section, we assume that there is a single photon in the initial state with momentum $\hbar\mathbf{k}_i$, energy $\hbar\omega_{\mathbf{k}_i}$ and polarization $\boldsymbol{\varepsilon}_i$, that is subsequently scattered to $\hbar\mathbf{k}_o$, $\hbar\omega_{\mathbf{k}_o}$, $\boldsymbol{\varepsilon}_o$. Therefore the ground state wavefunction is $|\mathrm{g}\rangle = |g; 1_{\boldsymbol{\varepsilon}_i,\mathbf{k}_i}\rangle$, i.e. the product of the ground state wavefunction of the material $|g\rangle$ and the one-photon wavefunction $|1_{\boldsymbol{\varepsilon}_i,\mathbf{k}_i}\rangle = c^\dagger_{\boldsymbol{\varepsilon}_i,\mathbf{k}_i}|0\rangle$, while the final state wavefunction is denoted by $|\mathrm{f}\rangle = |f; 1_{\boldsymbol{\varepsilon}_o,\mathbf{k}_o}\rangle$. The states $|\mathrm{g}\rangle$ and $|\mathrm{f}\rangle$ are eigenstates of $\mathcal{H}_0$ with energies $E_\mathrm{g} = E_g + \hbar\omega_{\mathbf{k}_i}$ and $E_\mathrm{f} = E_f + \hbar\omega_{\mathbf{k}_o}$, respectively.

The Fermi golden rule to the second order gives the transition rate w for the scattering process as:

$$w = \frac{2\pi}{\hbar}\sum_\mathrm{f}\left|\langle \mathrm{f}\,|\mathcal{H}'|\,\mathrm{g}\rangle + \sum_n \frac{\langle \mathrm{f}\,|\mathcal{H}'|\,n\rangle\langle n\,|\mathcal{H}'|\,\mathrm{g}\rangle}{E_g + \hbar\omega_{\mathbf{k}_i} - E_n}\right|^2 \cdot\delta\left((E_f + \hbar\omega_{\mathbf{k}_o}) - (E_g + \hbar\omega_{\mathbf{k}_i})\right), \tag{1.5}$$

where n runs over the intermediate states $|n\rangle$, eigenstates of the unperturbed Hamiltonian $\mathcal{H}_0$ with energies E_n.

The first order amplitude generally dominates the second order, but when the incoming photon energy matches an absorption edge of the studied material, it becomes $E_g+\hbar\omega_{\mathbf{k}_i} \approx E_n$, the denominator of the second term gets very small and the second term becomes large. As a consequence in first approximation the first term yields only non-resonant scattering while the second term contains resonant scattering. By classifying the terms of Eq. (1.3) as powers of $\mathbf{A}(\mathbf{r})$ and separating the contributions to the first order scattering from the ones to the second order resonant scattering, it can be demonstrated that actually the resonant scattering can occur both via a magnetic and a non-magnetic term. An estimate shows that the non-magnetic term dominates so that we can consider just this for the sake of simplicity.

In particular it can be shown that the resonant part of the second order amplitude is

$$\frac{e^2\hbar}{2m^2\mathcal{V}\varepsilon_0\sqrt{\omega_{\mathbf{k}_i}\omega_{\mathbf{k}_o}}}\sum_n\sum_{j,j'}^{N}\frac{\langle f|\boldsymbol{\varepsilon}_o^*\cdot\mathbf{p}_{j'}e^{-i\mathbf{k}_o\cdot\mathbf{r}_{j'}}|n\rangle\langle n|\boldsymbol{\varepsilon}_i\cdot\mathbf{p}_j e^{-i\mathbf{k}_i\cdot\mathbf{r}_j}|g\rangle}{E_g+\hbar\omega_{\mathbf{k}_i}-E_n+i\Gamma_n}, \tag{1.6}$$

where $\mathcal{V}$ is the volume of the system and Γ_n is a lifetime broadening for the intermediate states introduced in order to account for the usually short lifetime of the core hole. Moreover it is reasonable to assume that all Γ_n at a certain edge are equal, so that it can be taken $\Gamma_n = \Gamma$.

Substituting Eq. (1.6) into Eq. (1.5) gives the Kramers-Heisenberg expression for the RIXS cross-section.

In particular in the following we use the dipole approximation: in this limit one assumes $e^{i\mathbf{k}\cdot\mathbf{r}}$ to be approximately constant at the length scale of the atomic wavefunctions: $e^{i\mathbf{k}\cdot\mathbf{r}} = 1 + i\mathbf{k}\cdot\mathbf{r} + ... \approx 1$. Then the scattering amplitude becomes:

$$\begin{aligned}\frac{e^2\hbar}{2m^2\mathcal{V}\varepsilon_0\sqrt{\omega_{\mathbf{k}_i}\omega_{\mathbf{k}_o}}}\sum_n\sum_{j,j'}^{N}\frac{\langle f|\boldsymbol{\varepsilon}_o^*\cdot\mathbf{p}_{j'}|n\rangle\langle n|\boldsymbol{\varepsilon}_i\cdot\mathbf{p}_j|g\rangle}{E_g+\hbar\omega_{\mathbf{k}_i}-E_n+i\Gamma_n} \approx \\ \approx \frac{e^2\hbar}{2m^2\mathcal{V}\varepsilon_0}\sqrt{\omega_{\mathbf{k}_i}\omega_{\mathbf{k}_o}}\sum_n\sum_{j,j'}^{N}\frac{\langle f|\boldsymbol{\varepsilon}_o^*\cdot\mathbf{r}_{j'}|n\rangle\langle n|\boldsymbol{\varepsilon}_i\cdot\mathbf{r}_j|g\rangle}{E_g+\hbar\omega_{\mathbf{k}_i}-E_n+i\Gamma_n},\end{aligned} \tag{1.7}$$

obtained by substituting the operator $\mathbf{p}$ with the commutator $im[\mathcal{H}_0,\mathbf{r}]/\hbar$ and realizing that $\langle n|\boldsymbol{\varepsilon}_i\cdot[\mathcal{H}_0,\mathbf{r}]|g\rangle = \langle n|\mathcal{H}_0\boldsymbol{\varepsilon}_i\cdot\mathbf{r}|g\rangle - \langle n|\boldsymbol{\varepsilon}_i\cdot\mathbf{r}\mathcal{H}_0|g\rangle = (E_n - E_g)\langle n|\boldsymbol{\varepsilon}_i\cdot\mathbf{r}|g\rangle \approx \hbar\omega_{\mathbf{k}_i}\langle n|\boldsymbol{\varepsilon}_i\cdot\mathbf{r}|g\rangle$.

The double differential cross-section is finally obtained by multiplying w by the density of photon states in the solid angle $d\Omega$ ($\mathcal{V}\mathbf{k}_o^2 d|\mathbf{k}_o|d\Omega/(2\pi)^3$),

and dividing by the photon flux $c/\mathcal{V}$ [18]:

$$d^2\sigma(\omega, \mathbf{k}_i, \mathbf{k}_o, \boldsymbol{\varepsilon}_i, \boldsymbol{\varepsilon}_o) = w\frac{\mathcal{V}^2\mathbf{k}_o^2 d|\mathbf{k}_o|d\Omega}{c(2\pi)^3} = w\frac{\mathcal{V}^2\omega_{\mathbf{k}_o}^2 d\hbar\omega d\Omega}{\hbar c^4(2\pi)^3}, \tag{1.8}$$

which produces the following final expression for the RIXS cross-section in dipole approximation

$$\frac{d^2\sigma}{d\hbar\omega d\Omega} = r_e^2 m^2 \omega_{\mathbf{k}_i}\omega_{\mathbf{k}_o}^3 \sum_f \left| \sum_n \sum_{j,j'}^{N} \frac{\langle f|\boldsymbol{\varepsilon}_o^* \cdot \mathbf{r}_{j'}|n\rangle\langle n|\boldsymbol{\varepsilon}_i \cdot \mathbf{r}_j|g\rangle}{E_g + \hbar\omega_{\mathbf{k}_i} - E_n + i\Gamma_n} \right|^2 \delta(E_g - E_f + \hbar\omega), \tag{1.9}$$

where $r_e = e^2/(4\pi\varepsilon_0 mc^2)$ is the classical electron radius.

It has to be stressed that Eq. (1.9) holds in the dipole approximation only, i.e. when $\mathbf{k}\cdot\mathbf{r} \approx 2\pi r/\lambda \ll 1$, with $r \sim 1$ Å. This condition is easily fulfilled in the case of soft x-rays and therefore it is true for all the Cu L_3 RIXS measurements presented in Chapter 3, 4 and 5. On the other hand for hard x-ray photons one might need instead to consider also electric *quadrupole* transitions taking part to the RIXS process.

Let us discuss briefly the obtained Kramers-Heisenberg formula and its implications. Given that for a generic RIXS process both the radiative transitions are necessary, the two dipole operators need to be multiplied. As previously said, this product is divided by a factor which becomes very small in the case of resonance, increasing in this way the process' cross section. It is interesting to note that the presence of the imaginary term $i\Gamma_n$, due to the finite linewidth of each intermediate state $|n\rangle$, forbids a division by zero. The δ-function assures the respect of the law of conservation of energy, stating that the difference in photon energies equals the excitation energy of the system, as already mentioned. Consequently any spectral peak due to a well defined excitation of the sample is found at constant transferred energy. In particular energy loss peaks disperse linearly with incoming photon energies, providing a very simple criterion to distinguish them from any other spectral feature, such as fluorescence emission peaks. The energy of the last in fact is fixed by the atomic species in the sample and does not depend from the excitation energy. As already stated in Section 1.3, fluorescence features are generally less important than the Raman ones, because they correspond to the decay of an electron that has already relaxed, losing the information about the RIXS intermediate state of the system.

In general the intermediate states have a crucial role in RIXS. The presence of an intermediate state between two consecutive dipole transitions provides for instance the possibility to follow a path from the ground $|\mathrm{g}\rangle$ to the

final state $|f\rangle$ which in direct way is forbidden by dipole selection rules. An excitation in the same valence shell d (dd-excitation) is a typical example of process which can be observed using RIXS, despite it is prohibited as direct dipole transition, as already mentioned in Section 1.3. Moreover, as in many other optical processes, the path from $|g\rangle$ to $|f\rangle$ introduces a useful sensitivity to polarization, so that the knowledge of incoming and outgoing polarizations can allow to unravel the local symmetry of the excitations (in this connection see also Section 2.3.2).
In a realistic description of a generic RIXS process sets of degenerate intermediate and final states can be present. In particular when we consider the manifold of intermediate states, which are not observed directly, we must do a coherent sum and superimpose amplitudes taking into account relative phases. Only after this operation the total amplitude must be squared. Everything goes just like in an ideal Young's experiment with two slits where you can not know which slit the photon has gone through. In the case of final states instead, since they are actually observed, there is no need of these considerations.
In this connection the case of layered cuprates, as the ones studied in this thesis, is somewhat particular. In these systems in fact Cu ions are known to be mostly in the Cu^{2+} oxidation state [19], corresponding to a $3d^9$ electronic configuration. In the crudest approximation, one can only consider the atomic states of a Cu^{2+} ion. In such a case the RIXS process can be modeled in the following two steps. First one $2p_{3/2}$ electron is resonantly promoted into the $3d$ states by absorption of a photon (intermediate state). Because of the large $2p$ spin-orbit splitting (~ 20 eV), interference effects with the $2p_{1/2}$ states can be neglected. Then the second step is the radiative deexcitation of one $3d$ electron into the $2p_{3/2}$ levels. The only available intermediate state in this process is given by a fully occupied $3d$ shell and one hole in the four-fold degenerate $2p_{3/2}$ core level. This fact makes the calculations of Cu L_3 RIXS cross section much easier than in the presence of a manifold of intermediate states, as it happens in general (see Refs. [3] and [11] for more details on Cu L_3 RIXS calculations).

Finally it must be stressed that the resonance acts as a real amplifier increasing remarkably the cross section of the process and improving the sensitivity of the measurements. Due to the small matrix elements of the second order process in fact the intensity of RIXS signal is quite weak. This is the main reason behind the necessity to use high sensitive *ad hoc* instrumentation and sources with very high brilliance, such as the ones described in the following Chapter.

Chapter 2

Experimental set-up

As mentioned in the introduction of this thesis, RIXS is well known as spectroscopic technique since more than 30 years but has gone through a "Renaissance" only in the last 15 years. During this period indeed the construction of third generation radiation sources and the design of dedicated RIXS spectrometers have overcome the limitations due to the limited flux provided by old generation synchrotrons and the poor energy resolution achievable by the first experimental apparata. This has allowed physicists to really exploit RIXS to study elementary excitations, with remarkable results. Although hard and soft x-ray RIXS are similar to some extent from a physical point of view, they require very different experimental set-ups. Given that this thesis deals with soft x-ray RIXS performed at Cu L_3 edge, I will introduce only the instrumentation related to the experiments discussed hereafter.
In particular in this Chapter, I will briefly present the ID08 beam line of the European Synchrotron Radiation Facility (ESRF) in Grenoble and the ADRESS beam line of the Swiss Light Source (SLS) at Paul Scherrer Institut (PSI) in Villigen (CH), where the RIXS measurements have been carried out. We have used two dedicated RIXS spectrometers (AXES and SAXES), whose general layout will be described, together with a standard experimental geometry for RIXS measurements on cuprates. I will discuss resolution and performances offered by the two instruments, underlining the differences and introducing also a procedure to get rid of the background contribution due to randomly scattered light in acquired RIXS spectra.
I will briefly present the prototype *polarimeter* that we mounted and tested successfully on AXES, providing for the first time the possibility to detect the polarization of the scattered beam in energy resolved soft x-ray scattering.
Moreover I will make a short comparison between the RIXS spectrometers

and a typical diffractometer for energy-integrated resonant x-ray scattering (RXS) measurements, that is preparatory to the understanding of the results presented in Chapter 5, obtained with a combination of RIXS and RXS experiments.
Aspects related to the basics of synchrotron radiation and instrumentation are not discussed in details and can be found by the reader elsewhere.

Contents

2.1 Introduction

Before the brief but punctual analysis of the experimental set-up needed for a soft x-ray RIXS experiment, I underline here again that despite it is known since a long time [1], RIXS is a very young technique. Being based on a second order process, as we have seen in the previous Chapter, RIXS is extremely *photon-hungry*. For these reasons RIXS has been fully exploited only recently, after that specifically dedicated spectrometers have been designed, third generation synchrotron radiation sources, like the Swiss Light Source, have been built and other older sources, like the ESRF, have been upgraded.

The new possibilities given by RIXS have brought to remarkable and sometimes unexpected results, some of which are presented in the following Chapters of this thesis. Given these facts it becomes clear why at the time of writing many synchrotron facilities all over the world are planning to have or they have already designed advanced high resolution RIXS end-stations, scheduled to be fully operative in the years to come. Moreover among these facilities there are big expectations for x-ray free electrons lasers (XFEL) and their possible cross-fertilization with RIXS.

Herefater I will introduce two soft x-ray synchrotron beamlines, namely

ID08 at the ESRF and ADRESS [20] at the SLS, and the two RIXS spectrometers which are located at these beamlines and have been used to perform the experiments described in this thesis, i.e. AXES [21, 22] and SAXES [23]. These two instruments share the same optical layout and they have the best resolution available at present date. In particular SAXES, which is the evolution of AXES, is working since July 2007 and it holds the world record of resolving power, providing a combined resolution around 130 meV at the Cu L_3 edge ($\sim$ 930 eV).

2.2 Two soft x-ray synchrotron beamlines

2.2.1 ID08 at the ESRF

The European Synchrotron Radiation facility (ESRF) is a synchrotron light source funded and operated by 19 countries since 1994 in Grenoble, France [24]. Its 41 experimental stations allow more than 6000 scientists every year to conduct forefront science experiments. The storage ring has a circumference of 844 m. The energy of the electrons is 6 GeV, the current in the ring can reach 200 mA and it is sustained with periodical re-injections. ESRF is conceived to work mostly in the hard x-ray regime and its uniqueness is that it holds the highest brightness in this energy range of the spectrum. Moreover it maintains its reputation through reinvestment and by continually improving its beamlines with technical upgrades. In particular the entire synchrotorn is currently undergoing a major upgrade programme started in 2009, which includes the development of a totally new dedicated RIXS endstation.

The ID08 beamline is actually the only soft x-ray beamline of the ESRF. This means that the x-ray path has to be kept in ultra high vacuum (UHV), differently from all other hard x-ray beamlines of the ESRF. More in detail ID08 works in a photon energy range from about 300 to 1600 eV, that is not the one for which the machine has been optimized. We will return on this fact later. ID08 is devoted to the study of the electronic and magnetic properties of materials, covering in particular the K edges of O and N, the $L_{2,3}$ edges of $3d$ transition-elements compounds and the $M_{4,5}$ edges of rare earth compounds. It is principally used to probe magnetism in these systems, with x-ray magneto-optical techniques, and to study the electronic structure of materials, using x-ray and photoelectron emission spectroscopies. In particular the principal techniques available at ID08 are x-ray absorption

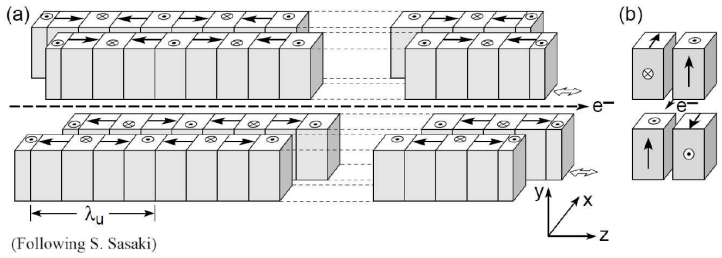

Fig. 2.1: Schematic view of an undulator for the generation of arbitrarily polarized radiation. (a) Isometric view showing two fixed rows (upper right and lower left) and two axially movable rows (upper left and lower right), shown displaced forward by one quarter period. (b) End-view in a midplane of the magnet structure in a configuration that produces both horizontal and vertical magnetic fields on axis, which will result in a helical electron motion and the concomitant emission of elliptically polarized radiation [25, 26]. Figure reproduced from Ref. [27].

spectroscopy (XAS) and x-ray magnetic circular dichroism (XMCD), spin polarized and angle resolved x-ray photoelectron spectroscopy (SPXPS and ARXPS, respectively), soft x-ray resonant magnetic scattering (SXRMS) and finally x-ray emission spectroscopy (XES) and especially RIXS.

Two APPLE II undulators [25], each 1.6 m long, constitute the source of the beam line. They adopt the Apple-type scheme in which the polarization as well as energy can be changed by variation of 4 moveable permanent magnet arrays. A pictorial illustration of their structure is given in Fig. 2.1. The two undulators provide 100% controllable polarization, both linear and circular, of the emitted radiation. In the synchrotron community it is tradition to define the spectral brightness of a system in terms of photons per second and in terms of a relative spectral bandwidth of 10^{-3}, often written as 0.1%BW. The flux of the emitted radiation at ID08 is 1.4×10^{15} ph/s/0.1%BW at the maximum ring-current of 200 mA at 1 keV.

A sketch of the ID08 beamline layout is shown in Fig. 2.2. A series of optical elements, based on properly machined mirrors operating at grazing incidence ($\sim 1^\circ - 3^\circ$), deflect and shape the beam, before it enters the so-called Dragon monochromator. This is the heart of ID08 and, accordingly to a design proposed by C. T. Chen [28] in 1987, is composed by three parts: an entrance slit, a single dispersive optical element (grating) and an exit slit. The aperture of the entrance slit (typically ~ 10 μm) defines the position and the size of the source seen by the grating. Since the entrance slit-to-grating distance is fixed, the entrance arm of the grating (r_i) is also fixed, and so is the incidence angle α.

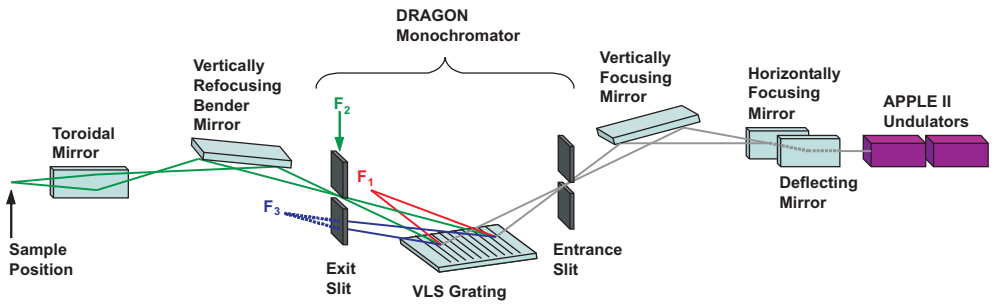

Fig. 2.2: Sketch of the optical layout of the ID08 beam line of ESRF. Note how the Dragon monochromator disperses and focuses different energies at different positions, i.e. F_1, F_2 and F_3, imposing the use of a movable exit slit and, as a consequence, of a bendable mirror (*bender*) in the refocusing system, in order to allow a wide range of working energies. For details on the optical elements, distances and incidence angles, see Tab. 2.1.

The grating is the active optical element that disperses photons with different energies. It is spherically shaped with a radius of curvature of 57.3 m and has a groove density of 1200 lines/mm, although secondary gratings with less lines/mm can be used, depending on the working energy of the experiment. Finally, the exit slit spatially filters the desired photons, substantially defining the energy resolution of the beam line: indeed the narrower the slit, the better the spatial filtering and the energy resolution. Obviously closing the slit has the cost of a reduction in flux, that is approximately linear with the apertures of the entrance and exit slits. Given that the exit arm r_o changes with the energy of the photons to be selected, the exit slit position has to be changed accordingly so to match the focusing distance for a given photon energy, as sketched in Fig. 2.2.
At the L_3 edge of Cu (~ 930 eV), the energy resolution $\Delta E/E$ of the Dragon monochromator is about 2×10^{-4}, with apertures of the entrance and exit slits of 10 μm.
Downstream the monochromator there are the various end-stations. Among these, the RIXS spectrometer needs a further refocusing of the x-ray beam, since the the spot size on the sample influences the energy resolution of the measurements (see Section 2.3). This is done by means of a refocusing system based on two optical elements: a bendable mirror, i.e. a spherical mirror with adjustable radius of curvature by means of piezo-actuators, and a toroidal mirror, that focus the beam sagittally in the vertical direction and tangentially in the horizontal direction.

The spot size at the sample is measured by imaging the visible light generated by the x-ray beam on a phosphor screen at the bottom of the sample

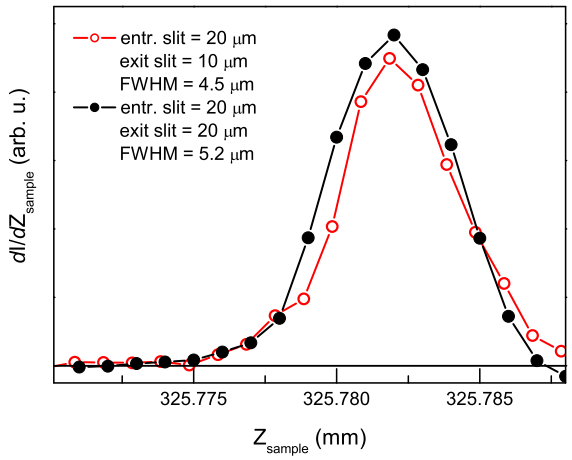

Fig. 2.3: Results of two razor blade scans vs. the manipulator z-coordinate for two different apertures of the exit slit of the Dragon monochromator. The razor blade is mounted at the bottom of the sample holder, which is electrically insulated, and the drain current is measured while the razor blade is scanned through the beam in steps of 1 μm. The curves represent the derivative of the drain current with respect to the z-coordinate and give the FWHM of the vertical focus. Note that the narrower the exit slit, the smaller is the focus.

holder, by using two lenses and a CCD camera,. The image on the CCD gives the shape and the horizontal size, that is routinely ~ 50 μm. T. Unfortunately the spatial resolution of the available optical system is not enough to judge a focus smaller than 15 μm, as it is the vertical focus. Therefore a razor blade, mounted below the phosphor screen on the sample holder, is used to measure more accurately the spot width in the vertical direction. This is done by scanning the razor blade in steps of 1 μm and by taking the derivative of the drain current signal from the blade itself with respect to the z-coordinate. The best FWHM of the vertical focus achieved on ID08 is around 5 μm (see Fig. 2.3).

2.2.2 ADRESS at the SLS and comparison

The Swiss Light Source (SLS) at the Paul Scherrer Institut is a third generation synchrotron light source that they have inaugurated in October 2001 in Villigen, Switzerland [29]. It is a competitive and in continuous progress machine, which provides highly brilliant and intense radiation to its 15 operational beamlines. The storage ring has a circumference of 288 m, much smaller than the ESRF. The energy of the electrons is 2.4 GeV, lower than ESRF, since SLS has been optimized to work in the soft x-ray regime. The current in the ring reaches 400 mA in top-up, an operation mode which keeps the intensity of the circulating electron beam approximately constant by frequent injections. The synchrotron light gives thus a constant heat load on the optical components such as mirrors, detectors etc. enhancing dramatically the stability of the photon beams used in the experimental areas. Moreover the elevated stability of the electron beam is one of the most outstanding properties of SLS. In particular an elaborate diagnostic equipment with a fast feedback system makes sure that the stability is better than 1 μm.

The ADvanced RESonant Spectroscopies (ADRESS) beamline at SLS is built to deliver soft x-ray radiation with energy range from 400 to 1800 eV and to assure high resolution in this whole operational range. The beamline has two end stations: one for Angle-Resolved Photoelectron Emission (ARPES) and the other for RIXS. The ADRESS beamline layout is shown in Fig. 2.4. The source of radiation is one 3.5 m long UE44 undulator which adopts an Apple-type scheme very similar to the one of the undulators of ID08 (see Fig. 2.1) and allows to choose between circular and 0-180^o variable linear polarization. The provided flux is about 2×10^{14} ph/s/0.01%BW at the maximum ring-current of 400 mA at 1 keV. A toroidal Collimating Mirror Unit (CMU) deflects the beam generated by the undulator and make it collimated in vertical direction with an infinity focus. In particular the angle of deflection assures that unwanted high energy photons are very weakly

	Deflecting mirror	Horizontally focusing mirror	Vertically focusing mirror	Grating	Vertically refocusing mirror	Toroidal mirror
Source plane distance (cm)	2941.25	28.7500	400.625	200.000	348.069*	59600.0
Image plane distance (cm)	28.7500	400.625	755.000	430.931*	250.000	150.000
Incidence angle (°)	88.0000	88.0000	88.5600	87.9757*	88.4400	8800.00
Reflection angle (°)	88.0000	88.0000	88.5600	86.1243*	88.4400	8800.00
Orientation (°)	90.0000	180.000	90.0000	180.000	180.000	90.0000
Shape	plane	spherical	spherical	spherical	spherical	toroidal
Type	mirror	mirror	mirror	grating	mirror	mirror
R (cm)	∞	92300.0	50127.7	5730.00	10689.0*	8596.11
r (cm)	-	-	-	-	-	8.36465
Slope error (μrad)	2.6	1.8	0.7	$\lesssim$1	2	5

Tab. 2.1: Main parameters for the optical elements of the ID08 beam line at the ESRF when operated at $\hbar\omega = 930$ eV.

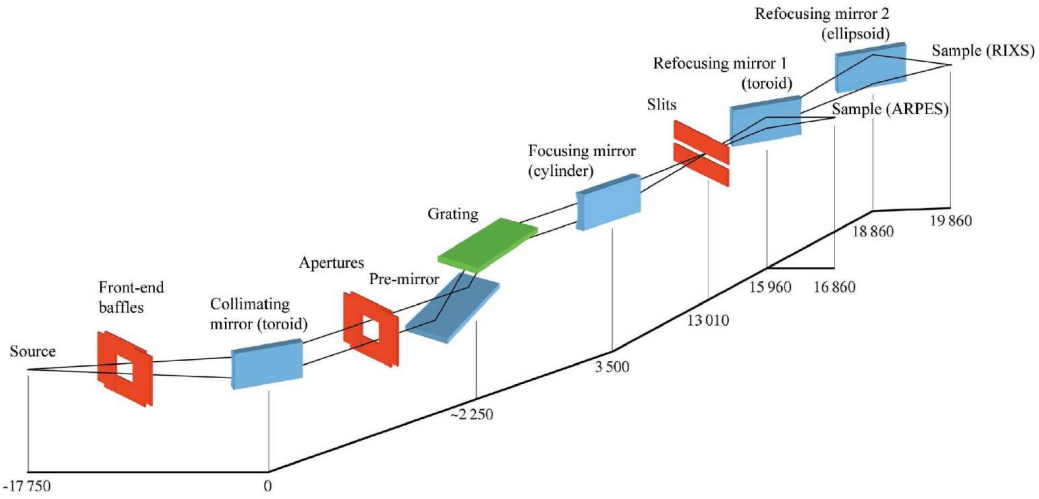

Fig. 2.4: Optical layout of the ADRESS beamline. The optical scheme is the collimated-light PGM. The dimensions are in mm. Figure reproduced from Ref. [20].

reflected by CMU.
Then the beam enters the Aperture Unit (AU) of the monochromator. Horizontal and vertical dimensions of AU are adjustable. The monochromator contains three optical elements: a plane Pre-Mirror (PM), a Plane Grating (PG) which disperses different photon energies and a Focusing Mirror Unit (FMU). More in detail there are three selectable gratings with constant groove densities of 800, 2000 and 4200 lines/mm to provide even coverage of the beamline resolution and transmission parameters (see below). With appropriate orientations of PM and PG the the dispersed collimated beam is focused on the monochromator exit slit by using the FMU. This is a cylinder that in the horizontal (non-dispersive) plane, has no focusing properties so that the beam coming from the undulator is horizontally focused onto the exit slit directly by the CMU, producing a stigmatic focus. No other optical element needs to be moved. The now monochromatic radiation is focused on the samples by means of a Refocusing Mirror Unit (RMU) mounted on hexapod mechanics, allowing most precise adjustment. Actually each of the two end stations has its own RMU. In particular the RMU_2 used for the RIXS end station have an ellipsoidal shape and provides a gaussian spot with FWHM of 52 μm horizontal $\times$ 4 μm vertical, comparable to that of the ID08 beamline. To judge the goodness of this vertical focus there is no need to scan a razor blade as for ID08. Indeed the long stroke of the mechanics of the RIXS spectrometer located at ADRESS (SAXES, presented in next

Section) allow to use the spectrometer itself as an x-ray reflection microscope to measure the actual size of the beam spot on the sample. This is done by using the grating of the spectrometer at the zeroth diffraction order, i.e. in specular reflection. Given that the magnification of SAXES is known, it is sufficient to measure the size of the image on the detector to get that of the beam spot on the sample. This is a very simple way to obtain this information and it does not require the use of other instruments.

There are 4 main differences in ADRESS with respect to the ID08 beamline: i) the absence of an entrance slit; ii) the monochromator based on multiple optical elements; iii) the constant focal distance provided by the plane monochromator; and iv) the use of an ellipsoidal mirror as ultimate refocusing system. Let us discuss shortly the consequences of these differences in the perspective of a soft x-ray RIXS experiment.

The absence of an entrance slit together with the optimization of the ring for the soft x-ray energy range result in excellent flux performances of the ADRESS beamline because the whole central cone of undulator radiation is captured. This helps in having higher counting rates and therefore better statistics in shorter times in RIXS spectra measured at ADRESS with respect to ID08. We will return later on this fact. On the other hand the entrance slit of the Dragon monochromator at ID08 ensures a stable source, filtering out the instabilities of the ring, that are not unusual and might degrade the energy resolution of the beamline and, as a consequence, of the experiment. It is also true that the above mentioned fast feedback system of SLS should avoid this kind of instabilities, but still an entrance slit is a safer guarantee for a stable measurement.

The force of the Dragon monochromator design is the use of a single (spherical) optical element: this fact allows for fast scans of the sole spherical grating without the need of any time-consuming re-alignemt of other nearby mirrors, as it is the case for a monochromator based on multiple optical elements. In the perspective of a RIXS experiment one important consequence of this fact is the possibility to carry out fast periodical x-ray absorption measurements, by scanning the grating and collecting the drain from the sample. These scans constitute a fundamental diagnostic to check that the incoming photon energy is actually on the absorption resonance chosen to perform RIXS. This might not be the case if slow thermal drifts of the optics have occurred or if a delicate sample has suffered some sort of radiation damage which has altered its properties. On the other hand the collimated light operation of the ADRESS plane grating monochromator (PGM) brings an important additional flexibility: one can in fact steer the PGM through different operation modes characterized by high resolution, high flux or maximal high-order suppression by tuning the cosine ratio C_{ff}

$= \cos\beta/\cos\alpha$ between the incidence and exit angles at the grating, α and β. Moreover the use of the PGM ensures a constant focal distance at the exit slit position, which is then fixed, contrarily to that of the Dragon monochromator. This fact eliminates the technicalities related to the broad movement of the exit slit in ultra high vacuum along the exit arm direction.

The possibility of using an ellipsoidal mirror is a consequence of the constant focal distance guaranteed by the PGM. An ellipsoidal curve has the unique property of connecting two foci, provided that the object and the image positions are fixed. In the case of ID08 it is the bendable mirror that provide a fixed intermediate focus and the use of an ellipsoidal mirror would not be precluded. However the use of a toroidal refocusing mirror at ID08 has shown to provide a spot size at the sample position (5 μm) very similar to that of the ADRESS beamline. This is probably a consequence of the smaller vertical source size and divergence with respect to those of the ADRESS beam line ($\sigma_y = 9.9$ μm, $\sigma'_y = 28$ μrad versus $\sigma_y = 33$ μm, $\sigma'_y = 33$ μrad). At ID08, unfortunately, whenever the working photon energy is changed, the monochromator exit slit moves accordingly, and the focus has to be re-optimized by acting on the radius of the bendable mirror and/or the positioning of the toroidal mirror.

The performances of the two beam lines in terms of their contribution to the overall energy resolution of the RIXS experiments is summarized in Fig. 2.10, as a function of the photon energy. It is seen that the ADRESS beam line (800 lines/mm grating) has a resolving power a factor ~ 1.5 better than that of ID08 at high photon energies, but almost comparable in the low energy range.

2.3 A RIXS spectrometer

Herefater I introduce the two RIXS spectrometers, located at the above presented beamlines, that have been used to perform the experiments described in this thesis. Both spectrometers have been entirely designed and built in Milan by my group leaded by prof. L. Braicovich and prof. G. Ghiringhelli. AXES, which stands for Advanced X-ray Emission Spectrometer, is working at the ID08 beamline since 1995 (Fig. 2.6(a)) and its evolution SAXES, i.e. Super AXES, is at the ADRESS beamline since 2006 (Fig. 2.6(b)). As before mentioned these two instruments provide the best resolution available at present date for soft x-ray RIXS experiments. Given that they also share the same optical layout I will describe it only once, highlighting the main differences between the two systems. A dedicated Subsection on resolution and performances of the two instruments will complete the comparison.

Among the different possible approaches to the design of a RIXS spectrometer the group of Milan has chosen to privilege *simplicity* and *reliability*. In particular they have combined the best current technologies in order to obtain the highest possible resolution in the soft x-ray range, where different difficulties arise. In principle in fact short wavelength electromagnetic radiation is analyzed by use of crystals. Unfortunately in nature there are no crystals which are suitable for the wavelength of soft x-rays, so that in this energy range it is necessary to use gratings which also have low efficiency. In this connection a RIXS spectrometer can be seen as a monochromator. In fact, their common aim is to separate the components constituting a polychromatic beam according to their energy and in both cases this is done by using dispersive optical elements, i.e. gratings, operating at grazing incidence. Finally, as a consequence of the approach based on "simplicity first", the two spectrometers are always open to possible upgrading without the need to disrupt the existing layout. This fact has been crucial for AXES during the past 15 years and it will be for SAXES in the years to come, in order to maintain the spectrometer competitive.

Fig. 2.5 shows the scheme of how a RIXS spectrometer works. According to above considerations the layout is simple and essential: the radiation emitted by the sample enters the spectrometer through an input slit and hits at grazing incidence a concave diffraction grating. This grating is the only optical element in the spectrometer. Other systems combine a concave mirror with a plane grating in order to separate the dispersing and focusing actions. The latter configuration should provide greater angular acceptance at the cost of more complicated assembly and operations. Instead, the choice of a single optical element layout is done not only to privilege simplicity but also to have a system where the minimization of all the higher order optical aberrations is easily obtained over the whole energy range. In fact, by using variable line spacing (VLS) gratings with fixed radius of curvature, it is possible to minimize the linewidth broadening due to the high order optical aberrations, by repositioning (in terms of incidence angle) the grating. The principal aim of the grating is to disperse and focus the radiation onto a position sensitive charge coupled device (CCD) detector, so that the position of photons on the CCD surface is in direct correspondence with their energies, as detailed below.

The source of the spectrometer is the light spot on the sample, whose size S_1 is given either by the width of the spectrometer entrance slit or by the height of the illuminated spot on the sample. As seen both in the case of AXES and SAXES, the vertical spot size is ~ 5 μm so that it is possible to work also in slit-less conditions, as it is routinely done. Samples are mounted on a sample holder and stay inside a chamber where a ionic pump

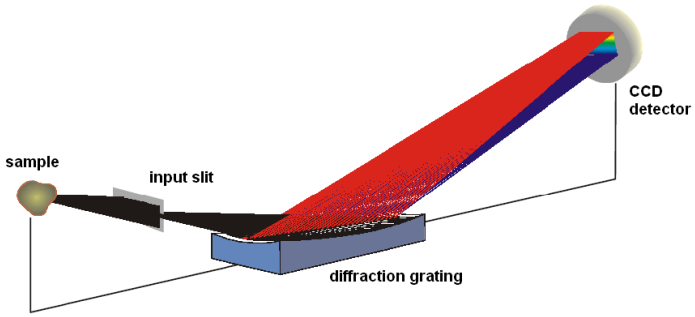

Fig. 2.5: Sketch of the optical layout of the AXES and SAXES spectrometers.

Fig. 2.6: Pictures of the AXES (a) and SAXES (b) spectrometers. AXES [21], installed at the ID08 beam line of the ESRF, is about 2.2 m long. SAXES [23] is a 5 m instrument, installed at the ADRESS [20] beam line of the SLS.

assures ultra high vacuum conditions (UHV, 10^{-10} mbar). The requirement to work in UHV comes from the use of soft x-rays and the need to protect beamline optical elements upstream of the sample. There is in fact a direct cross talking between these and the sample chamber. In the last the sample holder is mounted on a manipulator, which allows to move the sample in the three spatial directions and to rotate it around an axis perpendicular to the floor. In particular this rotation and the horizontal movements permit respectively to control the incidence angle of incoming photons and the portion of illuminated surface of the sample seen by the spectrometer. Furthermore, given that different samples can be piled up onto a single sample holder, it is possible to rapidly pass from a sample to another during an experiment by translating the holder vertically.

As above mentioned, in both spectrometers VLS gratings are used, with an average groove density $a_0 = 2400$ and 3200 lines/mm for AXES and SAXES, respectively. Their first aim is to spatially separate different energy components of the beam, thanks to these grooves which are perpendicular to the photons direction. The second function of the grating is to focus the different energy components of the beam onto the CCD, so that the vertical position of photons on its surface is in direct correspondence with their energies. In first approximation the isoenergetic lines of the image are horizontal and parallel among each other. More in detail, lines due to high energy photons will be in the lower region of the image and lines ascribable to low energy photons in the upper region. Therefore the position of the image in the space depends on the photon energy. This means that it is necessary to locate the detector in the right place in the space in order to have on focus energy windows centered around different incoming photon energies. The spatial resolution of the CCD detector determines the virtual exit slit of the spectrometer. The effective spatial resolution of modern CCD detectors (S_2) is around 25 μm, irrespective of the pixel size, as a consequence of split events [22]. In fact each photon which hits the wafer causes the release of a number of charges, so that a single photon results in a charge cloud shared by a number of neighboring pixels and only very seldom the whole charge is in a single pixel. The only way to gain in spatial resolution is thus to mount the CCD at grazing incidence (at an angle γ) so that the effective exit slit width $S_2 \sin\gamma$ becomes of the same order as the source size S_1 (see Fig.2.7).

Finally, the length of the spectrometer (L) and the horizontal dimension of the detector (D) determine the angular acceptance of the instrument and the uncertainty on the direction of the momentum transfer $\mathbf{q}$ (both proportional to D/L). In particular in AXES, the entrance and the exit arms are long 0.6 and 1.6 m, respectively, for a total length of the instrument of about 2.2 m at a fixed scattering angle of 130°. SAXES, instead, is 5 m long

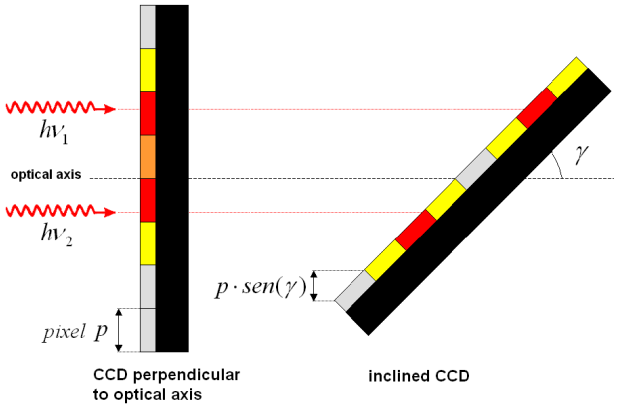

Fig. 2.7: Sketch of the improvement in the effective spatial resolution for an inclined CCD. The gain in spatial resolution is equal sen(γ), with γ angle between the detector surface and the optical axis of the spectrometer.

with an input arm of 1.1 m (roughly a factor 2 bigger than AXES) and it is mounted on a movable platform, which allows the scattering angle (and therefore the momentum transfer $\mathbf{q}$) to be changed. This fact is crucial to allow the study of elementary excitations probed by RIXS vs. $\mathbf{q}$ in 3 dimensions, so that their evolution in the k-space can be mapped out. However it has to be stressed that the possibility to change the scattering angle has never been exploited for the RIXS experiments discussed in this thesis, making the use of AXES and SAXES totally equivalent to study k-dependences of excitations in cuprates. Indeed the case of cuprates is somewhat special due to their quasi-2D nature. In fact, given that the physics interesting for superconductivity takes place in the CuO_2 planes, the meaningful quantity in the experiments is actually the projection of the transferred momentum $\mathbf{q}$ onto the sample ab-plane, $\mathbf{q}_{\parallel}$.

A typical experimental layout valid for all the RIXS measurements presented in this thesis is shown in Fig. 2.8. With the same convention used in Ref. [3] the incoming beam hits the sample surface (parallel to the ab plane) at incident angle θ_i and the outgoing beam is collected at the angle θ_o. The scattering angle 2θ is fixed, whereas the incident angle can be changed, thanks to the rotation of the sample holder. Together they define δ, the angle between the sample $c-$axis and the transferred momentum $\mathbf{q}$ (red arrow). Obviously as the photon momentum $\boldsymbol{k}$ is dictated by the energy of the chosen resonant transition, the scattering angle determines the maximum transferred momentum $\mathbf{q}$. Although this is fixed, δ and consequently $\mathbf{q}_{\parallel}$ can be easily changed by rotating the sample around an axis perpendicular to

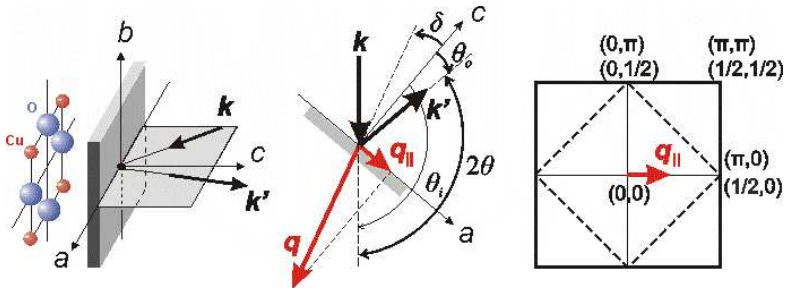

Fig. 2.8: Sketch of the typical experimental layout for RIXS measurements on cuprates and 2D Brillouin zone for cuprates. See the text for details.

the scattering plane, allowing to measure dispersing features. In this way, one can study the evolution of a given excitation along a chosen direction of the square 2D Brillouin zone (BZ) of cuprates (also shown on the right in Fig. 2.8).

2.3.1 AXES vs. SAXES: resolution and performances

In a RIXS spectrometer, such as the above described ones, there are three major contributions to the resolution that come from i) the finite size of the source ΔE_{S_1}, ii) the spatial resolution of the detector ΔE_{S_2}, and iii) the grating with its slope error ΔE_{SE}. Actually also the contribution coming from coma aberrations ΔE_{Ab} should be included, but, as already mentioned, this can be minimized at all energies by using a VLS grating and adjusting its position, so that in first approximation this contribution can be neglected. Unfortunately in the case of AXES the grating is fixed and coma aberrations are not negligible. In general, however, coma aberrations depend on the footprint length of the beam on the grating. Given this fact both AXES and SAXES are equipped with masks positioned just before the grating. These masks provide different apertures to select only a portion of the grating, reducing the footprint and limiting the undesired effects of aberrations.
One has to consider also the contribution coming from the beamline ΔE_{BL}, i.e. the linewidth of the monochromator, in order to understand which is the resolution limit of the entire system formed by beamline and spectrometer together. The actual combined resolving power of beamline and spectrometer is in fact given by the quadratic sum of all the listed contributions.

As shown in Fig. 2.9, the overall energy resolution is usually evaluated by measuring elastic peaks on a polycrystalline graphite. In fact non-resonant spectra from polycrystalline graphite do not show inelastic features, allowing a very straightforward assessment of the resolving power by measuring the

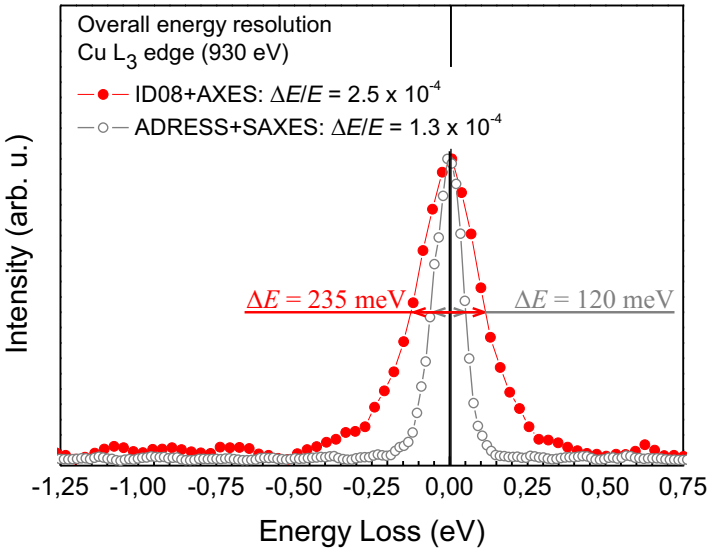

Fig. 2.9: Elastic peaks measured on polycrystalline graphite in order judge the instrumental energy resolution. The red dotted curve refers to the AXES spectrometer, while the grey dotted to SAXES. For the sake of clarity intensities have been normalized to the same value.

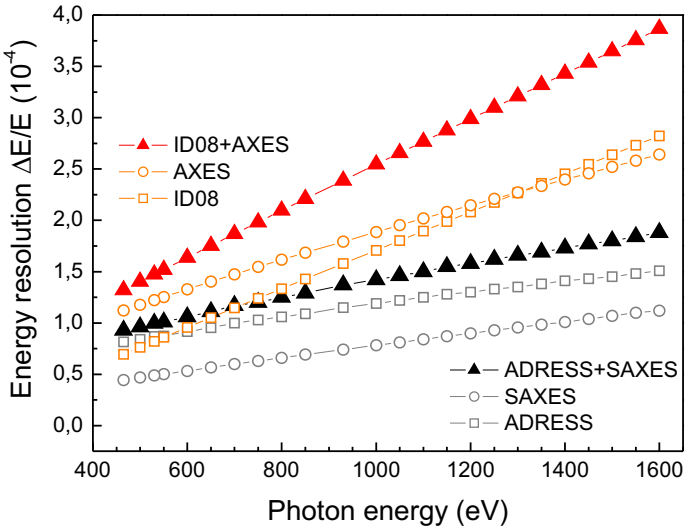

Fig. 2.10: Energy resolution of the AXES and SAXES apparata. The contributions of the beamlines (ID08 and ADRESS, respectively) and of the spectrometers alone are also shown individually. One needs to sum them up quadratically to obtain the combined energy resolution of RIXS experiments at the two facilities. Figure reproduced from Ref. [11].

full width at half maximum (FWHM) of the peak. Moreover, spectra on graphite are also periodically taken during RIXS experiments, in order to precisely calibrate the energy loss scale of the spectra. Indeed the isoenergetic line of the detector corresponding to the peak from graphite represents also the zero energy loss.

The resolving power of AXES is comparable to that of the Dragon monochromator (at 930 eV) and this results in a combined energy resolution of ~ 235 meV at the Cu L_3 edge, i.e. a resolving power $\Delta E/E = 2.5 \times 10^{-4}$. The combined energy resolution of SAXES and the ADRESS beam line at the same energy is instead around 120 meV, that means $\Delta E/E = 1.3 \times 10^{-4}$, i.e. roughly a factor 2 better, due primarily to the fact that the instrument is roughly twice longer than AXES. The overview of the resolution for the entire working range of photon energies is summarized in Fig. 2.10. The contributions of the beam lines (ID08 and ADRESS, respectively) and of the spectrometers are shown individually and also sum up to give the combined resolution of RIXS experiments at the two facilities.

An other fundamental parameter to judge the performances of a RIXS dedicated system is the counting rate of the spectra, that is related to the available flux and thus depends on both the characteristics of the beamline and the properties of the spectrometer. More in detail, as we have seen in the previous Section, SLS has some advantages in terms of intensity for two main reasons: on one side the machine is optimized for soft x-rays and on the other the choice of a plane grating monochromator for the beamline leaves open the possibility to choose a high flux configuration for the C_{ff} parameter. In general, as we have seen, in the synchrotron community the spectral brightness of a system is defined in terms of photons per second and in terms of the relative spectral bandwidth 0.1%BW. To specialize this to the case of a RIXS experiment is not so easy. It fact in RIXS it is essentially impossible to obtain absolute intensities from the experiment, because the overall detection efficiency can change over time for many different technical reasons. As we will see later usually it is thus necessary to use a spectral feature as reference, in order to make comparisons between spectra from different samples. In particular the most reasonable choice for the case of cuprates is to use *dd* excitations, which largely dominate all Cu L_3 RIXS spectra (see Fig. 2.11). Nevertheless it is worthy to look at a typical RIXS spectrum, in order to understand at least some typical numbers for AXES and SAXES, so to provide a phenomenological comparison of the performances in terms of intensity at the two facilities. To this purpose Fig. 2.11 shows two raw Cu L_3 spectra, as measured in identical working conditions with AXES and SAXES, on the very same sample of $CaCuO_2$, an antiferromagnetic insulator with a simple stacking of CuO_2 planes [30] intercalated by Ca that makes it a convenient

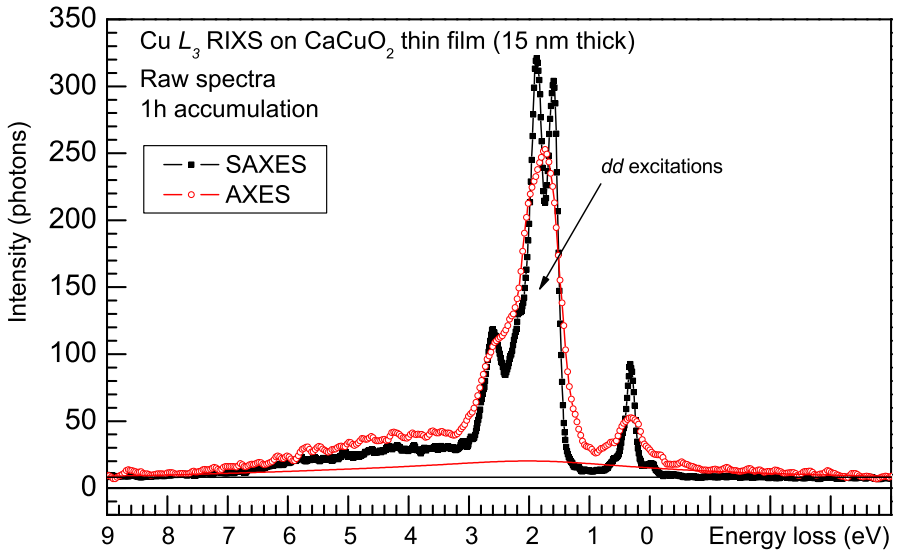

Fig. 2.11: Typical Cu L_3 RIXS spectra measured in identical working conditions with AXES (red open circles) and SAXES (black full squares) on the very same sample of $CaCuO_2$, a 15 nm thick film. Thin solid lines with the same color code represent the backgrounds mostly due to randomly scattered light. Note how in the case of AXES this is higher due to the use of an older grating with higher roughness than the one in SAXES.

model system [31, 32] for cuprates and also for the measurements discussed in this thesis. The sample is a thin film (150 Å thick) grown on a (100) $SrTiO_3$ substrate and it has been measured with linear horizontal (π) polarization at low temperature ($\sim$ 15 K) to reduce thermal scattering. The incidence of x-rays is at 110° from the surface and the emission is grazing (20° from the surface). The highest peaks around 2 eV of energy loss are *dd*-excitations. Each spectrum is the result of 1 hour total accumulation (12 partial spectra of 5 minutes). The intensity is given in number of accumulated photons per energy loss, i.e. by counting and summing the photons impinging on the CCD along the same isoenergetic lines. The counting is based on the conversion from number of electron generated by the events to number of photons and it simply requires the knowledge of the photon energy and of the gap of the Si-based CCD, which is the very same device in the two spectrometers. What we can see at a glance is that the overall intensity is comparable while the better energy resolution of the spectrum measured with SAXES (black full squares) stands out against the one of AXES (red open circles). Along the lines of the usual definition of brightness at the Cu L_3 edge energy ($\sim$ 930 eV) both the spectrometers are characterized by an average flux of $\sim$ 200 ph/hour/eV, i.e. roughly 3 ph/min/eV, on *dd*-excitations, which are the ones with the highest cross section. In this connection the definition of RIXS as an extremely *photon-hungry* technique becomes much more clear. On the other hand, by integrating in the low energy region (from 0 to 1 eV of energy loss), where are located many other interesting elementary excitations, the intensity goes down to $\sim$ 35 ph/hour/eV, i.e. less than 0.5 ph/min/eV, making evident the need for high flux sources and high throughput beamlines already mentioned many times.

On top of this fact one has to consider the backgrounds of the spectra in the two spectrometers, represented by the thin solid lines with the same color code in Fig. 2.11. While in SAXES (black thin solid line) the background can be assumed as essentially uniform over the entire energy range of the spectrum and brings a constant contribution of $\sim$ 8–10 ph/hour/eV, in the case of AXES the situation is more complicated. Indeed the VLS grating used in AXES, and produced in 1994, is much holder than the one of SAXES, realized more than ten years later. During this period polishing techniques for the production of gratings have made enormous improvements and, as a consequence, the VLS grating of SAXES has a much lower roughness. The non-flat shape of the background in AXES comes directly from the light randomly scattered by the old grating, which makes higher the background contribution by roughly a factor 2 on average over the entire spectrum.

Luckily this non-flat background bg_m can be obtained and subtracted by using a procedure based on a previous measurement of a single elastic line

spectrum, as the ones obtained by polycrystalline graphite. Indeed the resulting spectrum in that case can be considered as the response function of the AXES system to a Dirac-δ input. This response can be fitted by using a combination of one high Gaussian lineshape (with the instrumental FWHM) to fit the peak and one broad lower function (based on a Lorentzian lineshape) to fit the tails due the scattered light background. Once that the background bg_δ for a δ-input is known, it can be convoluted with the "clean spectrum" s that one would obtain in absence of randomly scattered light, so to get the non-flat background bg_m of the actual measured spectrum m, i.e. $bg_m \equiv m - s \equiv s * bg_\delta$. Obviously the "clean spectrum" s is not available but it can be approximated at the zero-th step by the real measured one m, so that $s_0 = m$ and $bg_{m,0} = m * bg_\delta$. If we do so, however, we end up to have an approximation of s better than s_0 and given by

$$s_1 = m - bg_{m,0} = m - s_0 * bg_\delta = m - m * bg_\delta. \tag{2.1}$$

By iterating this process restarting from s_1 we will have

$$s_2 = m - bg_{m,1} = m - s_1 * bg_\delta = m - (m - m * bg_\delta) * bg_\delta = m - m * bg_\delta + m * bg_\delta * bg_\delta \tag{2.2}$$

By continuing the recursive procedure following the rule $s_{i+1} = m - bg_{m,i}$ one obtains better and better approximations of the ideal clean spectrum s and therefore of the non-flat background $bg_m \equiv m - s$. Actually simulations show that after 6 steps there is already a good convergence of the series of convolutions, at least within the uncertainties introduced with the first Lorentzian fit of bg_δ. The red thin solid line in Fig. 2.11 has been obtained with the presented procedure. In particular this has been implemented in the Matlab code that is used to extract the spectra from the CCD images of AXES, so that the background subtraction is not time-consuming at all: it just requires to push a button and check on the screen the goodness of the result.

Finally, to complete the phenomenological comparison of a typical RIXS measurement at the two facilities, one should also note that although it seems that the overall intensity with AXES and SAXES is comparable, actually there is still an important parameter to take into account, i.e. the horizontal angular acceptance of the two spectrometers. As above mentioned this is defined by $\varphi = D/L$, where L is the length of the spectrometer and D is the horizontal dimension of the detector. Given that $L_{SAXES} \sim 2 \cdot L_{AXES}$ and $D_{SAXES} = D_{AXES}$, since the two spectrometers use the same model of CCD, we can conclude that $\varphi_{AXES} \sim 2\varphi_{SAXES}$. This means that in order to have similar accumulated intensities in the same amount of time as it is, the flux at the sample of the ADRESS beamline has to be roughly twice the one

provided by ID08, confirming the excellent flux performances of ADRESS.

Although the above presented results give a "tangible form" to the expression *photon-hungry* technique, Cu L_3 RIXS has quickly challenged inelastic neutron scattering (INS), in particular for the study of magnetic fluctuations in cuprates, thanks to the exceptional enhancement provided by the resonance and to the possibility to measure spin-flip excitations. Indeed, despite the low counting rates, Cu L_3 RIXS sensitivity remains many orders of magnitude higher than the one of INS, so that experiments can be made on sub millimeter crystals and thin films [4, 6, 7] like the one of Fig. 2.11.

2.3.2 Polarimeter of AXES

In order to complete the comparison between AXES and SAXES it has to be said that the former offers the unique possibility of measuring also the polarization of the scattered photons, thanks to a prototype *polarimeter* that I have personally mounted and tested with my group and I will briefly describe in the following.

In scattering experiments the control of polarization is often very valuable. As already mentioned in Section 1.3, by knowing how the photon polarization gets modified in the scattering one gets information on the symmetry of the excited state left after in the sample. In Raman experiments this is a current practice, because polarizing the incident radiation and measuring its polarization state after it has been diffused by the sample is practically very easy. For x-rays, synchrotron radiation sources are always highly polarized, but measuring the polarization of the outgoing beam is usually very challenging. In the hard x-ray range Bragg optics are intrinsically polarization selective, and fully polarized RIXS experiments have been already performed in the past [33]. On the other hand, for soft x-rays one has to rely upon multilayers (ML), whose reflectivity and polarization sensitivity are extremely low. This is why the scattered photon polarization has been measured up to date only in energy integrated experiments [34, 35].

The AXES spectrometer at the ID08 beamline of ESRF is the only existing instrument that offers a prototype solution to add a partial polarization detection in energy resolved soft RIXS, at least in the case of the linear polarization components of the scattered beam [12, 13]. In the initial phase we decided to finalize the apparatus to work only at the Cu L_3 edge. As reflecting element we used a ML (B_4C/W) grown at the ESRF by C. Morawe, mounted 30 cm before the CCD detector of AXES and deflecting the beam by 40° in a plane perpendicular to the grating dispersing direction, as sketched in Fig. 2.12. In this way the ML does not degrade the resolution of AXES and we can exploit the different reflectivity for the π

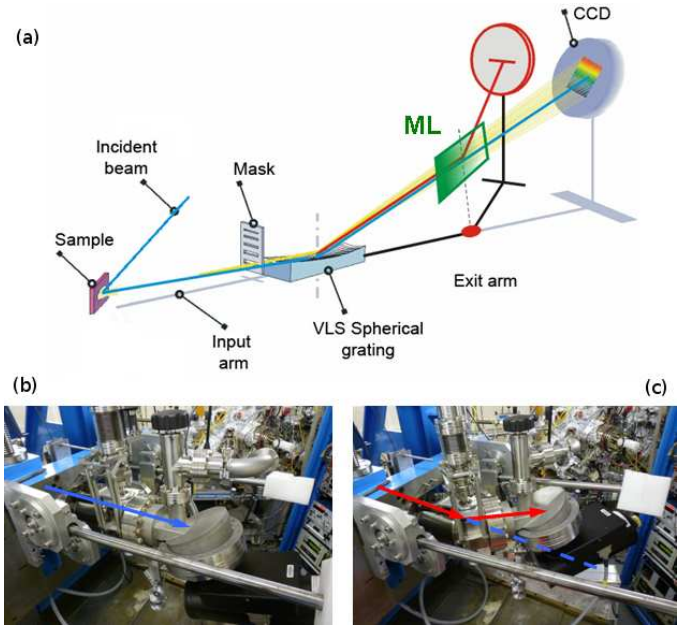

Fig. 2.12: (a) Sketch of the polarimeter based on a multilayer (ML) and installed on the AXES spectrometer at the ID08 beamline of the ESRF. The setup allows the insertion of the ML and the lateral displacement of the detector, to catch the filtered scattered beam, without breaking the vacuum. Thus it is easy to switch between the traditional (b) and the polarimetric (c) configuration of the exit arm of AXES.

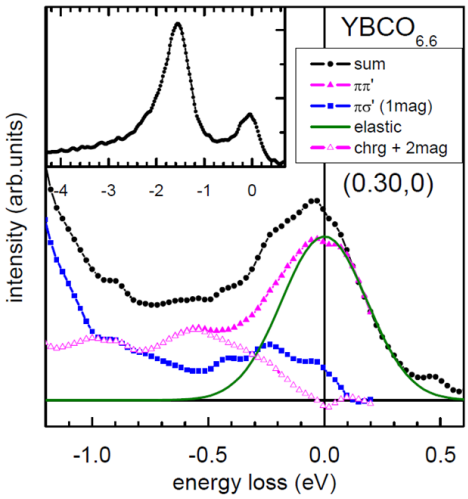

Fig. 2.13: Example of decomposition of a spectrum of $YBa_2Cu_3O_{6.6}$ (π incident polarization) obtained by properly combining the measurements with and without the polarimeter. The polarimeter has higher reflectivity for the crossed polarization scattering channel $\pi\sigma$. This is the single magnon channel. The $\pi\pi$ spectrum (magenta filled triangles) is further decomposed in the (quasi-)elastic component (resolution limited Gaussian, solid green line) and in the contributions from bimagnons and charge excitations (magenta open triangles).

and the σ polarization components (respectively parallel and perpendicular to the reflection plane of the ML mirror). The reflectivity ratio R_π/R_σ has been previously measured at the same beam ID08 line. The setup is based on a bending bellow (special delivery by Comvat) supported by a cage and it allows the insertion of the ML and the lateral displacement of the detector without breaking the vacuum: as a consequence it is easy to switch between the traditional configuration (Fig. 2.12(b)) and the polarimetric one (Fig. 2.12(c)). This is particularly important since the data analysis is based on a proper combination of four spectra, with two incident linear polarizations (horizontal and vertical in the laboratory space), and with and without the polarimeter.

To show the usefulness of this approach to disentangle different excitations in RIXS, we provide a recent result on a doped cuprate ($YBa_2Cu_3O_{6.6}$), measured by my group in collaboration with M. Le Tacon and N. B. Brookes. Considering the relative orientation the incident and scattered photon linear polarizations, the polarimeter allowed us separate the crossed and parallel polarization channels in the spectral region of magnetic excitations. We have

seen in Section 1.3 that single and multiple magnons can be seen with Cu L_3 RIXS in layered cuprates. We will return much more in detail on the measurements of magnetic excitations in Chapter 3. For now we just need to recall that in general in RIXS the conservation of angular momentum implies that single magnons ($\Delta S^{tot} = \pm 1$) are accompanied by a crossing of the ingoing and outgoing polarizations. This means that an incoming σ polarized photon generates a spin-flip transition in the outgoing π channel only, and viceversa, as one unit of angular momentum has to be exchanged between the photon and the sample. This fact can be generalized to all magnetic excitations of odd order. On the other hand, multi-magnons with even character such as bimagnons ($\Delta S^{tot} = 0$) conserve the polarization over the scattering process, and the same holds for elastic scattering, phonons, and charge excitations. Thus we can exploit this simple selection rule: the crossed polarization spectrum provides the single magnon energy distribution; the non-crossed channel is given instead by all the other contributions. The result is shown in Fig. 2.13. We chose on purpose an experimental geometry in which magnon and bimagnon have comparable spectral weights, thus making their separation difficult without polarimeter.

Due to the small reflectivity of the ML, the measurement of one spectrum with the polarimeter inserted can take up to 12–14 hours, because the count rate is unavoidably much smaller than in traditional measurements (typically a factor of 15). Therefore one should use this type of advanced polarization analysis only in well selected cases. Anyways the device can be of great help for the interpretation of RIXS spectra, in particular in doped cuprates, where the continuum of charge excitations due to extra charge carriers can hinder low energy losses features. With a polarimter in fact it will be possible to disentangle the evolution of the spin excitations from that of charge contribution, allowing in the future to give an absolute value of the magnetic intensity measured in the RIXS experiments.

Further successful new tests at L edges of other elements (not shown here) have confirmed the feasibility and usefulness of the device. Although this has been not used for the experiments presented in the following Chapters of this thesis (most of which were carried out before the final commissioning of the polarimeter), a number of scientific cases could be brought for polarimetric RIXS. As a consequence, an evolution of the polarimeter tested on AXES will be mounted on a new dedicated RIXS spectrometer, called ERIXS, that will be built at the new ID32 beamline of ESRF, in the framework of the current upgrade program of the synchrotron.

2.3.3 RIXS spectrometer vs. RXS diffractometer

The results which will be discussed in Chapter 5 have been obtained with a combination of RIXS and resonant elastic x-ray scattering (REXS) experiments. We notice here that for the sake of simplicity REXS is commonly abbreviated in RXS and actually this second definition is more precise, as it will be clear in a while. Being devoted to x-ray scattering experiments a RIXS spectrometer is not so different from a x-ray diffractometer used for RXS, however there are some big differences that deserve to be explained, in view of the combined use of the two instruments on which are based the results described in Chapter 5.

Fig. 2.14 shows a picture of a typical RXS diffractometer, namely the one at the UE46-PGM1 beamline of the Helmholtz-Zentrum Berlin at the BESSY II synchrotron that has been used to perform the above cited RXS measurements. BESSY II is a third generation synchrotron, more similar in size and performances to the SLS than the ESRF. The energy of the electrons is 1.72 GeV and the current is 300 mA. It is currently being upgraded to allow for the top-up operation and it is optimized to work in the soft-x-ray/ultra-violet regime. In the following I will not enter in the details of the machine and of the beamline, which is based on a layout very close to the one of ADRESS, because it is beyond the purpose of this subsection. The results described in Chapter 5 are related to the presence of a quasi-elastic resonance vs. transferred momentum $\mathbf{q}$ in the spectra of the superconductors $(Y,Nd)Ba_2Cu_3O_{6+x}$, ascribable to charge fluctuations in the CuO_2 planes of these compounds. Given that in first approximation this resonance is a modulation of the intensity of the elastic peak in principle it could be equivalently studied by using either RIXS or RXS, i.e. a spectrometer or a diffractometer respectively. This has been actually done, but with some caveats. In RXS in fact the detection of the scattered photons is simply based on the use of a photodiode. In connection to this fact there are two main differences between the two techniques: i) the possibility in RXS to change easily the scattering angle 2θ in a continuous way, by simply moving around the light photodiode, and ii) the energy-integrating nature of the same photodiode as opposite to the energy-resolved nature of RIXS spectra. Let us briefly discuss the consequences of these differences.

As above mentioned the change of the scattering angle is quite complicated in RIXS measurements since one has to move the entire spectrometer, as it is possible, at least in steps, with SAXES. However this fact is not a big issue for the study of layered cuprates: as we have seen in fact the meaningful quantity in that case is the projection of the transferred momentum $\mathbf{q}$ onto the sample ab-plane, $\mathbf{q}_{\parallel}$, that can be modified by simply rotating the

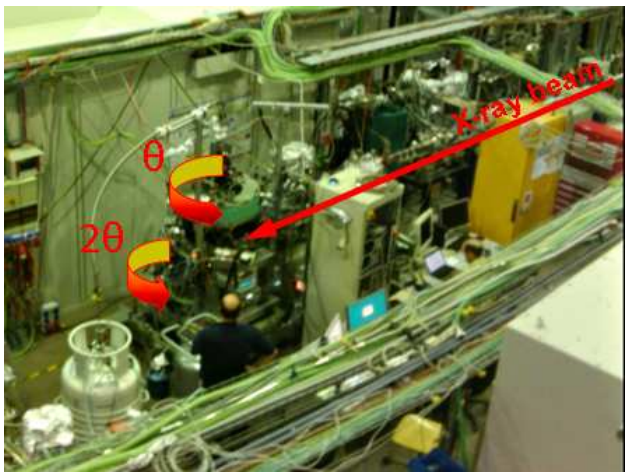

Fig. 2.14: RXS diffractometer at the UE46-PGM1 beamline of the BESSY II synchrotron. Arrows show the incoming beam and the two moving stages that allow to change both the angle of incidence on the sample θ and the scattering angle 2θ.

sample around an axis perpendicular to the scattering plane. In the case of an RXS experiments devoted to the exploration of a given direction in the 2D Brillouin Zone (BZ) of a layered cuprate one has therefore the freedom to choose between a measurement with fixed scattering angle and based on the simple rotation of the sample holder, as in RIXS, and a measurement in which the rotation of the sample is combined with that of the photodiode detector (possible only in RXS). In the latter case, if the two movements are in proper concert, the transferred momentum vector $\mathbf{q}$ is varied and meanwhile forced to lay entirely along the studied direction of the 2D BZ. In the first RIXS-like layout instead the vector $\mathbf{q}$ is fixed in modulus and in the laboratory space and, while the angle of incidence is changed by rotating the sample, for each projected $\mathbf{q}_{\parallel}$ there is also a component of the momentum $\mathbf{q}_{\perp}$ that is perpendicular to the BZ plane and varies as the scan is performed. Given the quasi-2D nature of cuprates the two ways of measurement should give the same result and this is usually the case, however it is an important fact to keep in mind in the case of incoherent outcomes.

On the other hand, if one is interested in the study of an elastic feature vs. momentum, much more difficulties arise from the energy-integrated nature of RXS spectra, due to the fact that the photodiode accumulates scattered photons over a wide energy range. In fact, although RXS signal unavoidably contains an inelastic component in this range, the results are always interpreted only in terms of elastic scattering only, at most considering the

inelastic contribution as a disturbing background signal. In this connection RIXS spectra, much more difficult to measure as they require a high resolution spectrometer, can be used to single out the true elastic component thanks to their energy-resolved nature. In general the elastic peak is often considered as a nuisance in RIXS experiments because it might hinder the very low energy loss spectral features. This situation is extreme at Cu L_3 edge for cuprates where the inelastic component, given mainly by *dd* excitations, is greatly enhanced and is overwhelmingly dominant over the elastic signal. The latter in fact represents only the 5% of the total valence emission, as it is evident from the spectra in Fig. 2.11. This circumstance is favorable for RIXS spectroscopy but it complicates dramatically RXS experiments based on a common diffractometer: in fact in the absence of any energy filtering the signal-to-background ratio is very low.

In this connection it has to be stressed that the results presented in Chapter 5 were first detected on the energy-resolving RIXS spectrometers with signal-to-background ratio at least one order of magnitude higher than RXS, where the large diffuse inelastic background dominates the signal. Actually in the past few years some RXS experiments were carried out by different groups in order to look for traces of the same quasi-elastic resonance but this was not found and null results were reported [36]. In our case we managed to observe it with RXS, by careful optimization of all experimental parameters, only once that we knew where to look, thanks to the previous RIXS results.

On the other hand it has to be said that, despite the above cited limitations, RXS has also many advantages. These are mainly related to the flexibility on angles typical of a diffractomer and the short time needed to record a scan vs. momentum. Faster scans are possible thanks to the higher photon flux available with respect to RIXS, where the more strict focusing conditions and the use of an energy-selective grating with very low efficiency drastically reduce the counting rate. For these reasons we combined the RIXS experiments with RXS measurements to study different directions and also bi-dimensional maps in the 3D reciprocal space, as it will be shown in Chapter 5.

Finally above considerations makes more clear the initial statement on the subtle difference between definitions: although usually elastic signals in resonant diffraction are so strong that allow to use the acronym REXS, there are some cases, as we have seen, in which this is not so true anymore, and RXS is a more honest definition. Therefore in Chapter 5 we will refer to the experiments carried out with the diffractometer as RXS measurements.

Chapter 3

Cuprates and magnetic fluctuations in CuO_2 planes

This Chapter gives a concise introduction to general aspects of insulating and superconducting layered cuprates and their properties of strongly correlated electron systems are briefly discussed.
Since their discovery in late 1986 cuprates superconductors have attracted a lot of attention due to the many potential technological applications allowed by their high critical temperature. However most part of the large variety of phenomena occuring in these systems has still to be understood and the mechanism behind high-T_c superconductivity (HTS) remains substantially unknown. In this respect RIXS can provide crucial information on magnetic and charge fluctuations in CuO_2 planes, which constitute the set in which superconductivity emerges, thus giving a crucial help in gathering together the pieces of the high-T_c puzzle.
In particular in the search for the mechanism of HTS, intense research has been focused on the evolution of the spin excitation spectrum on doping from the antiferromagnetic insulating to the superconducting state of layered cuprates. Because of technical limitations, the experimental investigation of doped cuprates has been largely focused on low-energy excitations in a small range of momentum space. In the second part of this Chapter the discussion is then restricted to a few RIXS experiments that overcome these difficulties and some general aspects of the magnon contribution to RIXS spectra are discussed. In particular, after a brief recall of the work done on undoped insulating cuprates, parent compounds of the superconducting ones, we show that a large family of superconductors, encompassing underdoped $YBa_2Cu_4O_8$ and overdoped $YBa_2Cu_3O_7$, exhibits damped spin excitations (*paramagnons*) with dispersions and spectral weights closely similar

to those of magnons in undoped samples. The comprehensive experimental description of this surprisingly simple spectrum enables quantitative tests of magnetic Cooper pairing models. A numerical solution of the Eliashberg equations for the magnetic spectrum of $YBa_2Cu_3O_7$ reproduces its superconducting transition temperature within a factor of two, a level of agreement comparable to that of Eliashberg theories of conventional superconductors.

Contents

3.1 High-T_c cuprate superconductors

Since the discovery, made and published by Bednorz and Müller in late 1986 [8], that the superconducting transition in cuprates can occur at temperatures well above the limits imposed by the BCS theory for traditional phonon-mediated superconductivity [9], a colossal amount of efforts has been devoted to the study of these materials. However, after more than 25 years of experiments and thousands of published results, the mechanism behind the phenomenon of high-T_c superconductivity still remains substantially unknown, although some experimental evidences seem to give strong indications in favor of some scenario more than others, as it will become more clear later. This endless crusade to understand high-T_c cuprate superconductors was strongly pushed by the potential technological applications allowed by the critical temperature of these materials that exceeds the boiling one of liquid N_2. Fig. 3.1 shows a synopsis of the critical temperatures of several superconducting compounds discovered in the last century. It is evident that layered cuprates represented a an enormous breakthrough in the physics of superconductivity with a maximum T_c of 138 K in $Hg_{0.2}Tl_{0.8}Ca_2Ba_2Cu_3O_{8+\delta}$ (138 K) [37]. A few years ago, in 2008, a new class of high-temperature superconductors has been discovered in layered iron arsenic compounds [38, 39], but still the highest critical temperatures belong to cuprates.

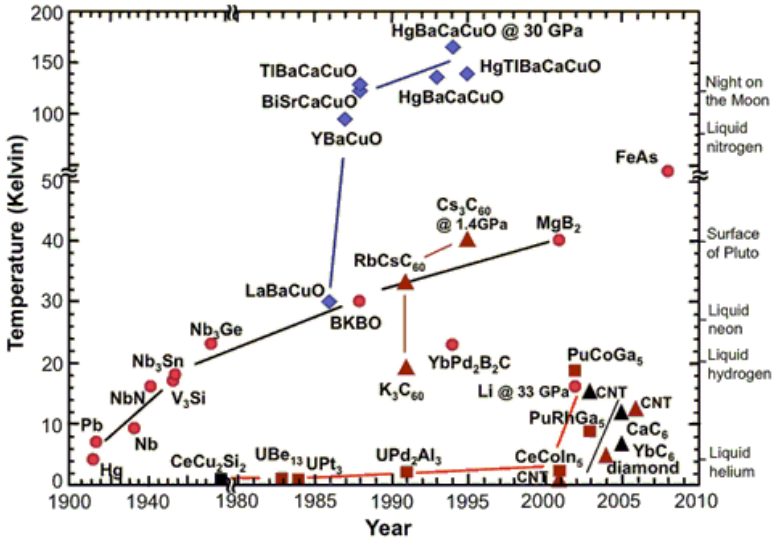

Fig. 3.1: Transition temperatures of several superconducting compounds. Note the breaks in both the horizontal and vertical axis. Fig. reproduced from Ref. [40].

There are many aspects of the copper oxide superconductors that makes them different from other $3d$ transition-element oxides from a chemical, structural, and electronic point of view. Even when we consider conducting oxides [41], in the most part of them electrons move around in energy bands based on the $3d$ orbitals of the transition-element present in the compound. In cuprates instead the energy difference between oxygen and transition-element states is so tiny that also the bands with oxygen character play a crucial role in the vicinity of the highest occupied electronic states, so that O is involved in conductivity as well as Cu. The heart of cuprates is constituted by the CuO_2 planes in which Cu^{2+} ions are in a $3d^9$ electronic configuration, i.e. nine of the ten available d orbitals are filled. These orbitals are non-degenerate in energy and the splitting of the associated electronic states depends on the geometrical coordination of the ligands, typically oxygens, surrounding each copper atom. The presence of these ligands in fact generates a so-called *ligand* (or *crystal*) *field* that lowers the spherical symmetry of the isolated ion and removes the initial degeneracy of the d orbitals. Usually every Cu ion has four in-plane near neighbors oxygens that form a square plaquette. Cu-O polyhedra are formed by adding one (pyramid) or two (octahedron) apical oxygens to this plaquette and they are usually elongated along the z direction, i.e. the $Cu\text{-}O_{plane}$ distance is $\simeq$ 1.91-1.94 Å while the $Cu\text{-}O_{apical}$ distance is $\simeq$ 2.3-2.7 Å [42]. As a consequence, among all d orbitals shown in Fig. 3.2,

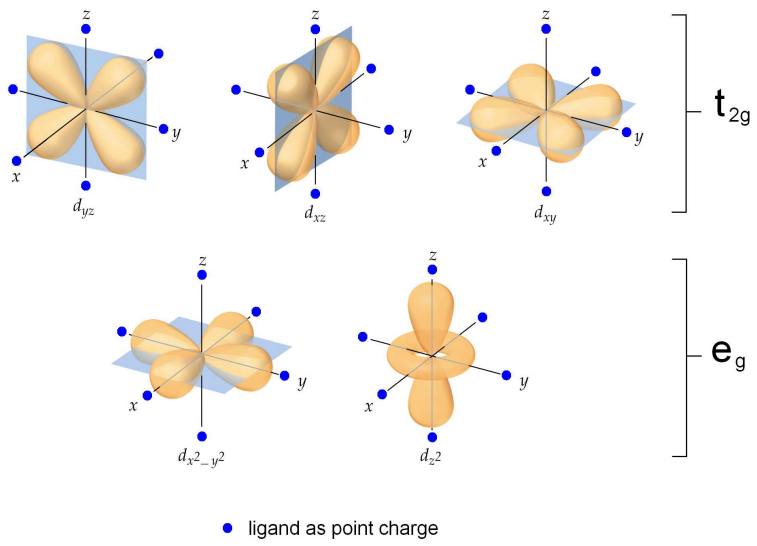

Fig. 3.2: Schematic representation of Cu d orbitals and of ligands, typically oxygens, as point charges in octahedral coordination. Note that the absence of one or two apical oxygens along the z direction would leave the Cu ion respectively in a pyramidal or *infinite-layer* coordination, i.e. surrounded only by the four oxygens in the xy plane.

it is energetically convenient to first fill completely (with six electrons) the three t_{2g} orbitals, i.e. the ones not directed towards oxygens and therefore lower in energy. Between the two e_g orbitals pointing toward oxygens is then preferable to fill the one pointing to the apices, that has lower repulsion from the O orbitals, given the elongated shape of the polyhedra. The result is that the nine-electrons configuration has one unpaired electron and one hole in the $d_{x^2-y^2}$ orbital, which points toward the in-plane oxygens. For this reason, and for the sake of simplicity, the electronic states of cuprates are often described by reasoning in terms of the single $3d^9$ hole and, as a consequence, the order of the energy levels has to be reversed, being the $d_{x^2-y^2}$ the more convenient to put a hole.

Given above considerations, one could expect a metallic behavior, due to the presence of electrons in a partially filled band with available energy states close-by. Instead copper oxides are electrical insulators that cannot be described by the standard one-electron picture for the electronic properties of solids. The standard scenario assumes that electrons in a solid are weakly interacting with each other, so that a single electron propagates in the periodic field due to the nuclei of the atoms and an *average* Coulomb field due to the other electrons. In this mean-field picture a compound with the out-

ermost electron shells not completely filled should be conductive. However, already in 1937, De Boer and Verwey [43] pointed out that some systems have properties that cannot be reconciled with one-electron calculations and that their failure relies in the mean-field approximation. In particular in the case of cuprates the addition of a second electron to the $d_{x^2-y^2}$ orbital takes a significant amount of extra energy, the on-site Coulomb repulsion energy U, due to the electron already present. As a consequence the motion of one electron is strongly correlated to the presence of an other, so that cuprates can be considered one of the best examples of *strongly correlated electron systems*.

In undoped cuprates, the insulating parent compounds of the high T_c superconductors, the Cu^{2+} spin 1/2 ions in the CuO_2 planes are ordered antiferromagnetically at low temperatures via super-exchange interaction, i.e. the exchange mediated by oxygen. This coupling between Cu spins is exceptionally strong, with super-exchange constants J of the order of 100 meV and common Néel ordering temperatures T_N of ~ 300 K, a value misleadingly low because also a small interlayer coupling has to be taken into account. In general insulating layered cuprates can be considered a good realization of a 2D Heisenberg antiferromagnet, i.e. a model system in which the interactions of spins at each site of a 2D lattice are treated quantum mechanically. Upon doping the long-range spin order is destroyed and the superconducting phase appears. However, as it will become more clear later, this does not mean that magnetic fluctuations are unimportant for superconductivity. Even without a strict long-range order, the spin correlation length can be large enough in the superconducting phase to promote a local arrangement of magnetic moments that at short distances differs very little from that observed below T_N in the insulating regime. Actually, many ideas have been discussed in the literature relating antiferromagnetism and superconductivity [44]. In particular the hypothesis that magnons instead of phonons could be the "glue" behind the pairing mechanism in cuprates has recently received the support of several experimental evidences, including the ones coming from the RIXS measurements presented hereafter in this Chapter.

What does exactly happen when electrons are added to or taken away from the electronic ground state of cuprate superconductors? Up to date this crucial question has remained unanswered. Between CuO_2 planes in cuprates there are other layers, usually named "charge reservoir" or "blocking" layers. Their function is to control, through chemistry, the number of electrons in the available electronic states in the CuO_2 planes and to electronically connect or isolate the CuO_2 planes with each other. Superconductivity is induced when the net charge of the network formed by copper and oxygen ions is changed starting from one electron per Cu site, i.e. when the formal valence

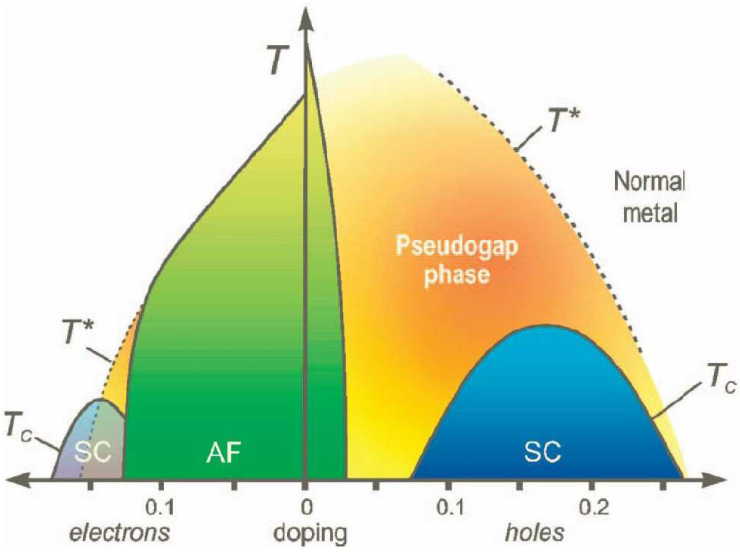

Fig. 3.3: Schematic doping phase diagram of electron and hole-doped high-T_c superconductors showing, in particular, the superconducting (SC) and antiferromagnetic (AF) phases. Fig. reproduced from Ref. [45].

Cu^{2+} is forced to become higher or lower. This is accomplished through the manipulation of the charge reservoir layer, either by adding oxygen or by partial substitution of one atom of higher or lower valence for another. Fig. 3.3 shows the phase diagram of electron and hole-doped high-T_c superconductors and in particular, the superconducting (SC) and antiferromagnetic (AF) phases. Upon adding either holes or electrons in the CuO_2 planes, cuprates originally insulating eventually become superconducting and T_c increases to reach a maximum, at a doping defined as *optimal*, before decreasing at higher doping concentrations, for which the system behaves in first approximation as a metal. The region with doping less (more) than optimal is known as underdoped (overdoped) region. We underline here that superconductivity is just one aspect of an exceptionally rich phase diagram, that should be understood in its totality [46]. In particular the region of the phase diagram above the superconducting dome is known as the *pseudogap phase*, since it is characterized by the presence of a "partial" energy gap near to the Fermi energy. This means that around the Fermi level there is a pronounced minimum in the density of states, very similar to an actual gap (in which there are no states at all). The pseudogap phase has been under intense study since it exhibits many unusual properties and ordering phenomena, such as uniaxially modulated antiferromagnetism combined with charge order or bidimensional charge density waves like the ones that will be discussed in

Chapter 5. Actually, when considering that region, physicists often use the term pseudogap regime since it is not even a well-defined phase and a precise finite-temperature phase boundary has never been found. In this respect the dashed line drawn in Fig. 3.3 should be considered as a crossover.

In most cases, and in all the superconducting samples measured in this thesis, the doping is by holes so that we should consider what happens to these holes when they are added to the electronic bands of a given cuprate. The most common belief is that every doping hole occupies oxygen states and gets delocalized on the four oxygens surrounding the Cu atom in a plaquette. The system becomes less magnetic on doping because the hole in the oxygen states has also a spin in the opposite direction with respect to the one of copper so that they cancel each other out. In this connection the doping hole can be considered as a magnetic impurity that locally quenches the superexchange. This entity with zero net spin and one more hole is called Zhang-Rice singlet [47] and has to move through a magnetic lattice of strongly antiferromagnetically coupled Cu spins. The common belief is that this exotic conduction process is the key to the whole problem and that somehow, at just the right concentration of these entities in the CuO_2 plane, their complex interactions can result in superconductivity.

Actually any successful theory for the mechanism behind HTS should require a detailed understanding of both the spin and charge correlations in the normal state from which superconductivity emerges. For this reason it is of paramount importance to study first the parent compounds, and the situation in absence of doping, and, subsequently, how this situation evolves upon doping, in order to understand the electronic and magnetic properties of the CuO_2 planes and their evolution in more complicated superconducting and/or artificial compounds. This is also the logical scheme behind the RIXS experiments presented hereafter in this thesis.

We note here that the nature of this thesis is extremely experimental and all results will be presented with a strongly phenomenological approach. When we will use models and calculations to support and quantitatively assess the experimental findings, we will provide qualitative descriptions of the theoretical background and references to get deeper insights in the used models. However we will not enter in details on theories for cuprates, since this is well beyond the purpose of an experimental thesis.

3.2 Magnons in undoped cuprates

As already mentioned in section 1.3, Cu L_3 edge RIXS gives direct access to magnetic excitations associated to a spin-flip. However it is well known that

a spin flip is not an eigenstate of the bidimensional antiferromagnetic ordered CuO_2 planes of layered cuprates. Therefore spin waves, namely *magnons*, are actually measured by Cu L_3 RIXS. Spin waves are coherent collective magnetic excitations, which involve more than one site in the same CuO_2 plane of the scatterer. Actually there can be also modes propagating perpendicularly to the CuO_2 planes, due to the weak (but finite) coupling among them, but these will not be addressed here. The collective behavior of a magnon is probed by the **q**-dependence of the RIXS signal. As already seen in Section 2.3, for bidimensional systems such as quasi-2D layered cuprates, it is sufficient to change the projection of the momentum transfer onto the sample CuO_2 planes ($\mathbf{q}_{\parallel}$) by rotating the sample around an axis perpendicular to the scattering plane. In such a way magnon dispersion as a function of $\mathbf{q}_{\parallel}$ and magnon spectral weight can be studied across almost the entire Brillouin Zone (BZ). In particular it can be demonstrated that Cu L_3 RIXS probes magnetic excitations in all cases but the very special one of Cu spins aligned along the [001] direction [5]. Moreover, it turns out that the orientation of the spin within the *ab* plane has no influence on the spin-flip cross-section. This makes it simpler to measure the magnon dispersion in samples with multiple magnetic domains.

The possibility to study single and multiple magnons with RIXS has enormous implications. In the last decades indeed the magnetic properties of cuprates have been studied primarily if not exclusively with inelastic neutron scattering (INS), providing a huge amount of experimental information [48]. However INS can be used only on massive samples (hundreds of mm^3 or more) and, although it provides an exceptional energy resolution (down to a few meV), it is restricted to the study of magnetic excitations with low energies (< 200 meV) in a small area around each corner of the BZ, as shown in the inset of Fig. 3.4. On the other hand RIXS can be used on tiny amounts of material (down to a few μm^3 in volume) and provides spectral information up to high-excitation energies, where the use of neutrons is experimentally very demanding. It is true that the very low energy scale (below ~ 50 meV at present) remains the domain of neutrons, because of the limited RIXS energy resolution, however, the spectacular progress made on spectrometers in recent years (see Chapter 2.3) has lead to a fruitful cross-fertilization of RIXS and INS. In particular this is the case of those samples that are hardly measurable with neutrons (because only thin films or single crystals of very small dimensions can be produced) at high transferred momentum (where the energy of magnetic excitations is higher), such as the doped (Y,Nd)$Ba_2Cu_3O_{6+x}$ samples presented later on in this Chapter.
Before to get to the RIXS measurements on doped superconducting cuprates, following the logical scheme presented at the end of the previous Section, it

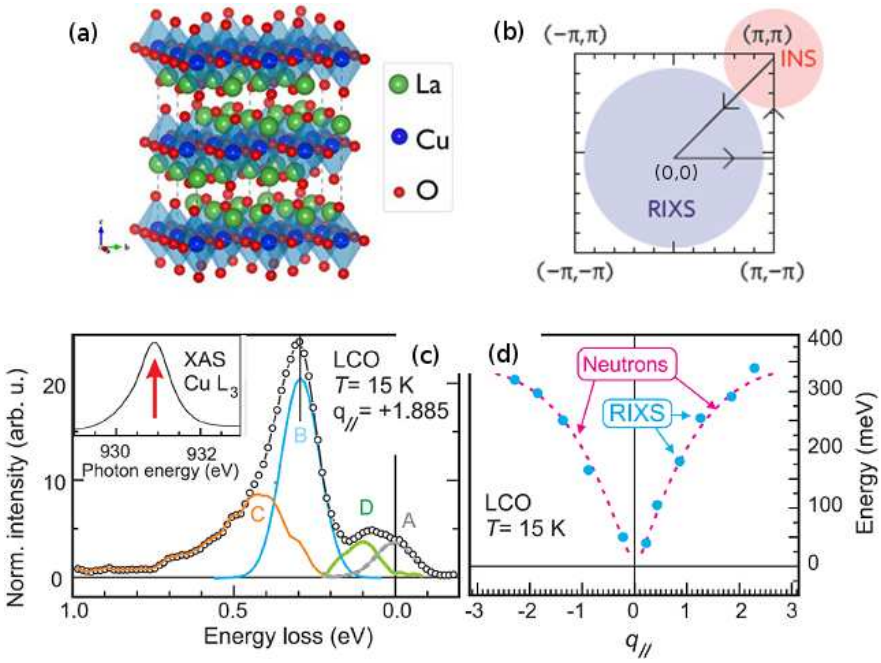

Fig. 3.4: (a) Crystal structure of La_2CuO_4 (LCO) showing octahedral coordination of Cu ions. (b) Accessible regions of 2D Brillouin Zone of cuprates for Cu L_3 RIXS and inelastic neutron scattering (INS). (c) Decomposition of the RIXS spectrum of LCO at $\mathbf{q}_{\parallel}$=1.85 Å showing elastic (A) and single magnon peaks (B); multiple magnon (C) and optical phonons (D) spectral features. (d) Single magnon dispersion extracted by various RIXS spectra not shown (blue dots) and determined by INS (dashed purple line from [49]). Panel (c) and (d) are reproduced from Ref. [16].

is useful to briefly recall the work already done with RIXS to study magnetic excitations in undoped antiferromagnetic insulating cuprates, i.e. the parent compounds of high-T_c superconductors, in order to get familiar with the problem and with some typical results.

My group first showed in 2009 [16] that RIXS can measure magnons by studying La_2CuO_4 (LCO). This is one of the most extensively studied parent compounds, so that it can be considered as a benchmark, and has the the crystal structure sketched in panel (a) of Fig. 3.4. Panel (c) shows a zoom on the low energy region of a RIXS spectrum (0 to 500 meV energy loss) measured on LCO with the standard experimental layout displayed in Fig. 2.8. It can be decomposed in several contributions: in principle by studying their dependence upon polarization, scattering geometry ($\mathbf{q}_{\parallel}$), temperature, etc., one can determine their origin. In particular if one tracks the energy

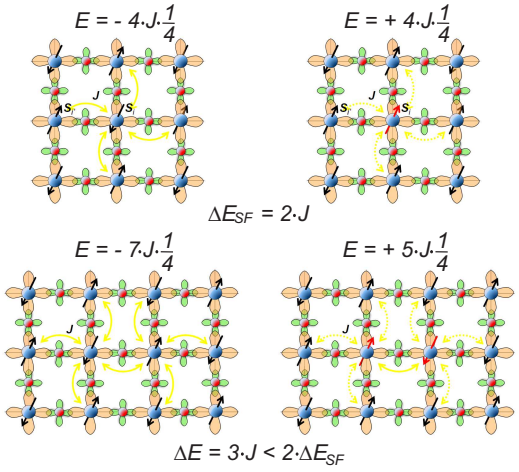

Fig. 3.5: Top panels: in a 2D antiferromagnet reversing a spin to start a spin wave (single magnon) costs an energy of $\Delta E_{SF} = 2J$, because it involves the breaking of four magnetic bonds. Lower panels: when reversing two neighboring spins (bimagnon) only six bonds are broken and the energy costs is $3J < 2\Delta E_{SF}$. A bimagnon is then possible only if the two spin-flip processes occur at neighboring ions. Figure reproduced from Ref. [11]

position of peak B as a function of $\mathbf{q}_{\parallel}$, a symmetric dispersion-like behavior is found, as shown in panel (d). If we take the INS data [49, 50] for a single magnon measured around the (π, π) point of the BZ and we report them at the (0,0) point where RIXS works, it turns out that the dispersion curve of peak B follows perfectly that inferred by INS data. Given that magnon dispersions at the center and at the corner of the BZ are superimposable, this direct comparison confirm that peak B is a single magnon. For this reason it can be fitted using a Gaussian lineshape with the FWHM of the instrumental resolution (given that the broadening due to magnon lifetime is negligible, if any). This result is the first experimental demonstration that Cu L_3 RIXS is able to probe single magnons in undoped cuprates, as supported by the theoretical arguments published in the same year [5]. The other features in Fig. 3.4(c) are the elastic peak (A) and the optical phonons contributions (D). The former is centered at zero energy loss and its FWHM defines the energy resolution of the measurement while the latter lie at about 80 meV. The feature C was identified as a bimagnon (section 1.3) and its dispersion was mapped in the reciprocal space for the first time in Ref. [16], since previous detections by optical absorption [51, 52] and Raman scattering [53, 54] were

restricted at zero momentum. It is interesting to underline that the energy of a bimagnon is higher than that of a single magnon, but still lower than that of a double spin-flip transition because of magnon-magnon interaction. This is shown in Fig. 3.5. In a 2D Heisenberg antiferromagnet, reversing a spin to start a spin wave costs an energy of $\Delta E_{SF} = 2J$, because it involves the breaking of four magnetic bonds. For a bimagnon instead two neighboring spins are reversed but only six bonds are broken (the bond connecting the two sites is left unchanged), so that the energy cost is $3J < 2\Delta E_{SF}$. Moreover the two interacting magnons must have their momentum coupled in such a way that $\mathbf{q}_{\parallel,1} + \mathbf{q}_{\parallel,2} = \mathbf{q}_{\parallel}$, where $\mathbf{q}_{\parallel,1(2)}$ is the momentum carried by the two interacting magnons, individually. Since there is an infinite number of ways of combining the two vectors $\mathbf{q}_{\parallel,1}$ and $\mathbf{q}_{\parallel,2}$ to give a fixed $\mathbf{q}_{\parallel}$, the width of the bimagnon peak is intrinsically broader than that of a single magnon and actually bimagnons form a continuum. We note here that also higher order magnetic excitations might be present at bigger energy losses, however these have usually a much lower intensity so that they are hardly detectable.

After the demonstration that RIXS can be used to study magnons, in order to address different issues related to magnetic excitations, and also better understand the capabilities of the technique, my group carried out other experiments on undoped cuprates [17, 55, 6]. Among these, for the sake of brevity, I will just mention the ones in which I was directly involved and/or propaedeutic to the understanding of the RIXS measurements presented in this thesis.

In particular to further establish RIXS as a viable technique we investigated the momentum and incident photon polarization dependence of the single-magnon spectral weight in a variety of layered undoped compounds, such as $SrCaCuO_2$ (SCCO) (that can be prepared in this form only as thin films on $SrTiO_3$) and $NdBa_2Cu_3O_{6+\delta}$ (NdBCO), beyond LCO [17]. This was done to have a proper understanding of the intensity of the magnetic RIXS signal in different geometries of measurement.

For all samples magnon intensities were extracted from the data (with the same procedure used in Ref. [16] and shown in Fig. 3.4) and compared to theoretical calculations for the atomic cross sections [3, 11]. As already stated in Section 2.3.1, in RIXS absolute intensities cannot be obtained from the experiment and the overall detection efficiency can change over time for technical reasons. Therefore we normalized experimental and theoretical single magnon intensities to the area of *dd* excitations, which largely dominate the Cu L_3 RIXS spectra. This procedure might slightly underestimate (5%) the single magnon intensity in the measured data, since a weak contribution from the charge transfer excitations (not included in our theory) is superimposed to the *dd* peaks. Two main precautions are important in handling the data:

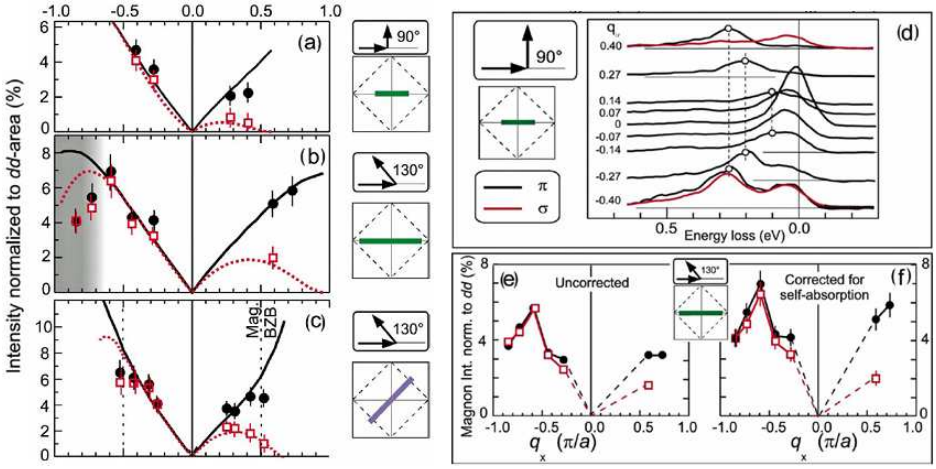

Fig. 3.6: Panels (a)-(c): comparison of the measured intensities in LCO with the theory in the scattering conditions shown by the icons at the right. In all panels of the figure full circles and hollow squares are for π an σ polarization respectively and intensities are normalized to the *dd* area put equal to 100. Panel (d): example of dispersion of the magnetic excitations in LCO for scattering angle $2\theta = 90$, note that the intensities are not symmetric with respect to $\mathbf{q}_{\parallel}$=0. Panel (e) and (f): raw data (e) and self-absorption corrected data (f) for 2θ =130. All panels are reproduced from Ref. [17].

i) we did not attempt to determine intensities at small $\mathbf{q}_{\parallel}$ where the superposition with other excitations such as phonons makes the spectral decomposition difficult as far as the intensities are concerned and ii) we corrected the measured intensities for self-absorption. In particular this is relevant only at grazing emission, i.e., at large positive $\mathbf{q}_{\parallel}$ where the scattered outgoing photons undergo a long path inside the strongly reabsorbing material. Fig. 3.6 show the results on measurements on LCO and the comparison with calculations. The agreement of experimental and theoretical results bolsters the assignment of RIXS spectral features to single magnons and the detailed analysis allows to disentangle single-magnon scattering from other spectral contributions. Moreover we showed that single magnons are enhanced and dominate over bimagnons if one works around normal incidence conditions with π polarization (while bimagnons are stronger with σ polarization). As a consequence this is the experimental layout in which one should work when interested in studying single magnon contributions or akin features as the ones that will be presented hereafter.

On the other hand, if one is interested in bimagnons, the polarization dependence of magnetic excitations can be exploited to extract the two-magnon

contribution from RIXS spectra [55], even without using a polarimeter like the one described in Subsection 2.3.2. In order to study bimagnons in fact one can also work, with some more complication, at different incoming photon energies, performing RIXS at the K edges of copper ($\sim$ 9 keV) and oxygen ($\sim$ 530 eV). The latter lies in the soft x-ray energy range so that measurements can be carried out with the instruments described in Chapter 2, while for hard x-ray RIXS ($>$ 1.5 keV) a different experimental set-up is needed. As already mentioned in Subsection 2.3.2, in general in RIXS the conservation of angular momentum implies that single magnons and all magnetic excitations of odd order ($\Delta S^{tot} = \pm 1$) are accompanied by a crossing of the ingoing and outgoing polarizations. On the other hand, magnetic excitations with even character such as bimagnons ($\Delta S^{tot} = 0$) conserve the polarization over the scattering process, and the same holds for elastic scattering and phonons. Given that at the K edges the spin orbit coupling is absent, the total spin of the system has to be conserved throughout the scattering process ($\Delta S^{tot} = 0$). As a consequence, the single magnon is forbidden and in RIXS spectra it becomes easier to recognize the bimagnon, i.e. the lowest order magnetic excitation left. In particular at Cu K edge bimagnons are not excited by directly promoting an electron into the magnetic $3d$ states. The final state of the K edge transition is in fact $4p$ and the process exciting the bimagnon is indirect: the super-exchange coupling between neighboring $3d$ electrons is altered by the $1s$ core-hole potential and therefore Cu K RIXS couples to even multimagnons [56, 57, 58, 59, 60]. Also at the O K edge the excitation is indirect but in that case oxygen $2p$ orbitals play an important role. The single magnon excitation is still forbidden and the bimagnon is seen when one excites tuning the incident photon energy at the first XAS feature. In particular in Ref. [55] we have shown that at Cu K and Cu L_3 edges the observed bimagnon has a strong dependence on momentum starting from zero energy at zero momentum, while with O K edge has little dispersion and starts from 430 meV at zero momentum. These results can be explained in terms of a different sampling of the bimagnon density of states made by the RIXS process at the three different edges [55, 61, 62].

3.3 *Paramagnons* in doped cuprates

The work presented in this Section has been published as "*Intense paramagnon excitations in a large family of high-temperature superconductors*", by M. Le Tacon, G. Ghiringhelli, J. Chaloupka, M. Moretti Sala, V. Hinkov, M. W. Haverkort, M. Minola, M. Bakr, K. J. Zhou, S. Blanco-Canosa, C. Monney, Y. T. Song, G. L. Sun, C. T. Lin, G. M. De Luca, M. Salluzzo, G.

Khaliullin, T. Schmitt, L. Braicovich and B. Keimer, Nature Physics **7**, 725 (2011)

In the previous Section we have seen that RIXS can probe magnetic excitations and their dispersions in undoped layered cuprates. In the following the same technique is applied to the study of how these excitations evolve upon doping in high-temperature superconductors (HTS).

Despite more than 25 years of experiments on these systems, the mechanism behind high-T_c superconductivity remains substantially unknown. After the discovery of an unconventional (d-wave) symmetry of the Cooper-pair wavefunction in the cuprates, the thrust of research had been focused on the role of repulsive Coulomb interactions between conduction electrons, which would naturally explain this pairing symmetry [63]. However given that simple models based on repulsive interactions did not provide a full solution, physicists started to doubt that such interactions alone can generate high-temperature superconductivity. In this connection a complementary, more empirical approach has proposed that antiferromagnetic spin fluctuations, that are a generic consequence of Coulomb interactions, could mediate Cooper pairing in analogy to the phonon-mediated pairing mechanism in conventional superconductors [64]. Therefore intense efforts have been focused on the evolution of magnetic excitations on doping from the antiferromagnetic insulating to the superconducting state of layered cuprates.

Although the role of magnons for high-T_c superconductivity is not yet totally clear a huge amount of experimental information has already been collected using inelastic neutron scattering (INS) [48]. This extensive experimental campaign has shown the presence of low-energy spin fluctuations in doped cuprates and it has also revealed signatures of a coupling between spin and charge excitations [65] that is apparently strong enough to mediate superconductivity in underdoped cuprates [66]. Together with the above cited results, the appearance of a neutron spin resonance signaling an unconventional superconducting state in cuprates and other materials, such as the Fe-based pnictides and chalcogenides, has lead physicists to propose that "spin-fluctuation mediated pairing is the common thread linking a broad class of superconducting materials", as stated by D.J. Scalapino in a very recent rewiev [67]. Upon cooling below T_c in fact the magnetic peak detected by INS (with energy ~ 60 meV) is enhanced in the model system $HgBa_2CuO_{4+\delta}$ and in other HTS, suggesting a cooperative behavior of magnons to get to superconductivity (see Ref. [67] and references therein).

Unfortunately INS experiments are limited to a narrow range of excitation energies up to ~ 100 meV and they only cover a small portion of the BZ

($\sim$ 10 %) around the antiferromagnetic ordering wave vector $\mathbf{q}_{\parallel}^{AF} = (\pi, \pi)$ (see Fig. 3.4(b)). As a consequence the energy- and momentum-integrated intensity of magnetic excitations observed with neutrons constitutes only a few percent of the spectral weight of spin waves in antiferromagnetically ordered cuprates [65, 68] and is thus clearly insufficient to support high-T_c superconductivity.
Moreover these results are also strongly influenced by the the small cross-section of magnetic neutron scattering in combination with the weak primary flux of currently available high-energy neutron sources. In fact these constraints in intensity impose the use of single-crystal samples with volumes of even $\sim$ 10 cm^3, very difficult to prepare, in order to detect spin waves in antiferromagnetically ordered cuprates. These complications are particularly pronounced for the compounds that show the most robust superconducting states and reach critical temperatures $\geq$ 90 K, such as $YBa_2Cu_3O_{6+x}$, that can be grown only as thin films or single crystals of very small size. On top of these facts doping further reduces the intensity of the INS profiles and exacerbates the above cited difficulties. In order to support the scenario of a magnon-mediated high-T_c superconductivity in fact one should document the existence of well-defined magnetic fluctuations in the entire superconducting range of the cuprate phase diagram, i.e. for hole concentrations $5\% \leq p \leq 25\%$ per copper atom, well outside the narrow stability range of antiferromagnetic long-range order ($0 \leq p \leq 2\%$).

Proven that RIXS can see magnetic excitations in undoped cuprates with sizable intensity over much of the accessible reciprocal space, and even on very small sample volumes, hereafter we exploit these capabilities to study doped superconducting cuprates. My group had already made some preliminary RIXS experiments on doped samples of LCO, namely $La_{2-x}Sr_xCuO_4$ with x=0.125=1/8. These had revealed a complex magnetic contribution based on two components extending in energy up to about 350 meV [69]. This was somewhat a special case: the presence of two branches was attributed to phase separation between the superconducting state and another state with incommensurate spin and charge order, that is particularly favored at doping 1/8. We will return on these incommensurate ordering much more in detail in Chapter 5.

In the following we apply the same method in the widely studied $YBa_2Cu_3O_{6+x}$ family, that is much less affected by doping-induced disorder and does not show any static phase separation [70]. We do this in order to explore with a systematic approach the doping dependence of magnetic excitations in a wide energy-momentum window that is largely inaccessible by INS (see Fig. 3.4(b)). The major outcome of this extensive experiment is the

demonstration that spin-wave-like dispersive magnetic excitations, hereafter named *paramagnons*, exist deep inside the electron-hole spin-flip continuum (up to ~ 300 meV), for all investigated doping levels. Moreover their spectral weights is comparable to those of magnons seen with RIXS in the undoped parent compounds and thus sufficient to support the hypothesis of a magnon-mediated high-T_c superconductivity.

3.3.1 Experimental

The RIXS measurements presented in the next Section have been obtained on thin films of $Nd_{1+x}Ba_{2-x}Cu_3O_7$ (NdBCO) and on millimeter-sized single crystals of $YBa_2Cu_3O_{6+x}$ (YBCO) far below the volume requirements of INS. All the samples share the same crystal structure in which Cu atoms are accomodated both in the usual CuO_2 planes (ions labelled as Cu2) and in the copper-oxygen chain layer (label Cu1), as shown in Fig 3.7(a). In YBCO the doping level p, i.e. the hole concentration per Cu atom, is adjusted through the density and arrangement of oxygen atoms in the Cu1 chain layer: this means that by varying x in the chemical formula $YBa_2Cu_3O_{6+x}$ one can pass from the "empty" chains of an undoped sample (x=0, $YBa_2Cu_3O_6$) to the fully oxygenated chains of an overdoped sample (x=1, $YBa_2Cu_3O_7$). Moreover when chains in a given specimen are oriented along only one direction the sample is defined as *untwinned* (or *detwinned*), whereas it is called *twinned* if there are different domains with chains oriented along both directions. Usually crystals are mechanically detwinned by heating under uniaxial stress, when samples with ordered chains are needed. On the other hand in thin films of $Nd_{1+x}Ba_{2-x}Cu_3O_7$ the Cu1 chains are fully oxygenated and p is simply controlled through the Nd/Ba ratio, but it is also possible to lower the doping level reducing the oxygen concentration by annealing.

For this RIXS experiment in particular we used 3 YBCO and 2 NdBCO specimens.
Two samples were untwinned $YBa_2Cu_3O_{6.6}$ and $YBa_2Cu_3O_7$ single crystals (abbreviated in YBCO6.6 and YBCO7 hereafter) of volume about $3 \times 3 \times 0.5$ mm^3, with superconducting transition temperatures T_c of 61 K and 90 K ($\Delta T_c = 2$ K), respectively, determined for each crystal by SQUID magnetometry. We used also one $YBa_2Cu_4O_8$ single crystal ($T_c = 80$ K) grown with KOH flux under ambient pressure in a box furnace. The source material was conventionally prepared polycrystalline $YBa_2Cu_3O_7$ mixed with CuO in a molar ratio of 1:1 [71, 72]. The peculiarity of this YBCO with different stoichiometry is the presence of a double chain layer, which results in a longer lattice parameter c and a greater distance between different pairs of coupled CuO_2 planes. It must be said that although this compound shows greater

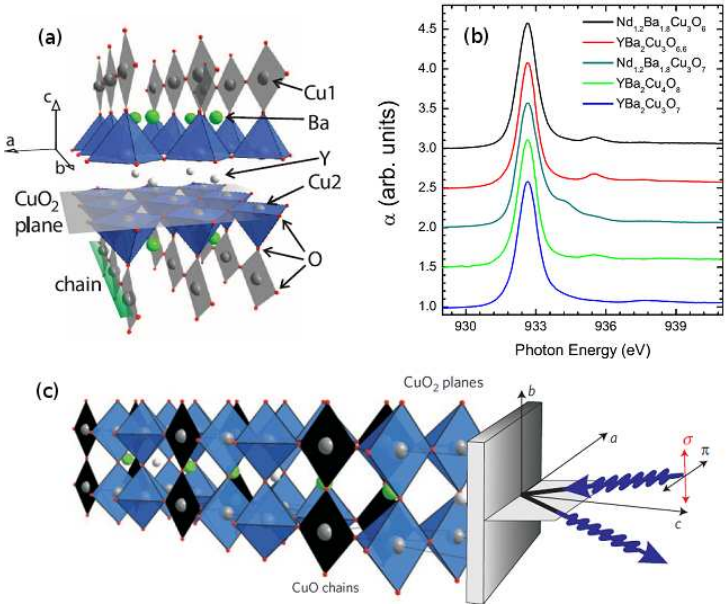

Fig. 3.7: (a) Crystal structure of $YBa_2Cu_3O_{6+x}$ and $Nd_{1+x}Ba_{2-x}Cu_3O_7$: note that copper atoms are both in CuO_2 planes (Cu2) and Cu-O chains (Cu1). (b) Cu L_3 edge x-ray absorption spectra of all the investigated samples measured with total electron yield (normal incidence, π polarization). The spectra have been vertically shifted by 0.5 for clarity. (c) Schematic representation of the experimental layout.

Tab. 3.1: Lattice parameters and transition temperatures of thin films and single crystals investigated.

Sample	a	b	c	Transition Temp.
$Nd_{1.2}Ba_{1.8}Cu_3O_6$	3.905 Å	3.905 Å	11.85 Å	$T_N > 300$ K
$Nd_{1.2}Ba_{1.8}Cu_3O_7$	3.885 Å	3.92 Å	11.7 Å	$T_c = 65$ K
$YBa_2Cu_3O_{6.6}$	3.82 Å	3.87 Å	11.7 Å	$T_c = 61$ K
$YBa_2Cu_3O_7$	3.817 Å	3.884 Å	11.681 Å	$T_c = 90$ K
$YBa_2Cu_4O_8$	3.84 Å	3.87 Å	27.25 Å	$T_c = 80$ K

thermodynamical and structural stability than $YBa_2Cu_3O_{6+x}$, its production is still challenging and requires a special apparatus and peculiar considerations [72]. As a consequence the crystal size was smaller, i.e. $0.8 \times 0.8 \times 0.2$ mm^3.

NdBCO films of thickness 100 nm were deposited on $SrTiO_3$ (100) single crystals by diode high-pressure oxygen sputtering. One undoped antiferromagnetically ordered $Nd_{1.2}Ba_{1.8}Cu_3O_6$ film (AF NdBCO6) was obtained by annealing as-grown $Nd_{1.2}Ba_{1.8}Cu_3O_7$ samples (NdBCO7) in Argon atmosphere (10 mbar) for 24 hours. The AF NdBCO6 was used as insulating reference, while the NdBCO7 adds another doping level to the experiment. The films had an area of approximatively 5×5 mm^2. Details of the films growth and characterization can be found in Ref. [73]. The superconducting transition temperature was determined by DC four-point transport and by magnetic susceptibility measurements. Tab. 3.1 lists the lattice parameters and transition temperatures of all samples.

All RIXS measurements were performed at the ADRESS beamline of the Swiss Light Source (Paul Scherrer Institut, Switzerland) using the SAXES spectrometer described in Section 2.3 with a combined resolution of 130 meV. The experimental geometry is the standard one already presented in the same Section and reported also in Fig. 3.7(c).

The resonant conditions were achieved by tuning the incoming photon energy to the maximum of the Cu L_3 absorption peak ($\sim$ 932 eV, see Fig. 3.7(b)). The maximum momentum transfer allows to cover about 85% of the first Brillouin zone along the [100] direction. Momentum transfers are given in units of the reciprocal lattice vectors a^*, b^* and c^* where $a^* = 2\pi/a$, $b^* = 2\pi/b$, and $c^* = 2\pi/c$.

We remind that the in-plane momentum transfer $\mathbf{q}_{\parallel}$ is in direct correspondence with the angle δ between the sample $c-$axis and the total transferred momentum $\mathbf{q}$ (see Section 2.3 for details of the conventions). Some of the

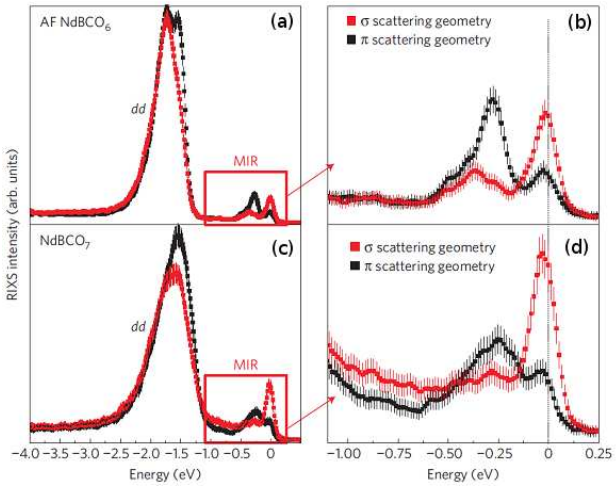

Fig. 3.8: Typical RIXS spectra of undoped antiferromagnetic (AF) $Nd_{1.2}Ba_{1.8}Cu_3O_6$ (a,b) and superconducting underdoped $Nd_{1.2}Ba_{1.8}Cu_3O_7$ (c,d), obtained at $T = 15$ K and $\mathbf{q}_{\parallel} = 0.37$ r.l.u., with both π (black squares) and σ (red squares) incident photon polarizations.

figures in the following sections report both the values of $\mathbf{q}_{\parallel}$ and δ.
The exact position of the elastic (zero energy loss) line was determined by measuring, for each momentum transfer $\mathbf{q}_{\parallel}$, a non-resonant spectrum of polycrystalline graphite. All data where recorded at $T = 15$ K, i.e. well below T_c and in the superconducting regime for all doped samples. Each spectrum is the result of 30 to 180 minutes total accumulation (sum of partial spectra of 5 min).

3.3.2 Dispersing magnetic excitations

Fig. 3.8 shows Cu L_3 RIXS spectra obtained on undoped $Nd_{1.2}Ba_{1.8}Cu_3O_6$ (panel (a)), that is insulating and antiferromagnetic (AF), and underdoped superconducting $Nd_{1.2}Ba_{1.8}Cu_3O_7$ (panel (c)), for incident photon polarizations π (black) and σ (red) and $\mathbf{q}_{\parallel} = 0.37$ r.l.u.. For both polarizations, on top of a continuum of charge-transfer excitations there is an intense peak located around 1.7 eV energy loss. This is ascribable to *dd* excitations, that, as explained in Section 1.3, are due to transitions of the unpaired hole of Cu^{2+} ions between the ligand field split *d* states of copper.

The low energy region is expanded for both compounds in panels (b) and (d) of Fig. 3.8: an inelastic feature centred around 250 meV and a resolution-limited elastic peak are present for both samples. For energy losses < 500 meV we can decompose the spectrum of undoped NdBCO6 following the

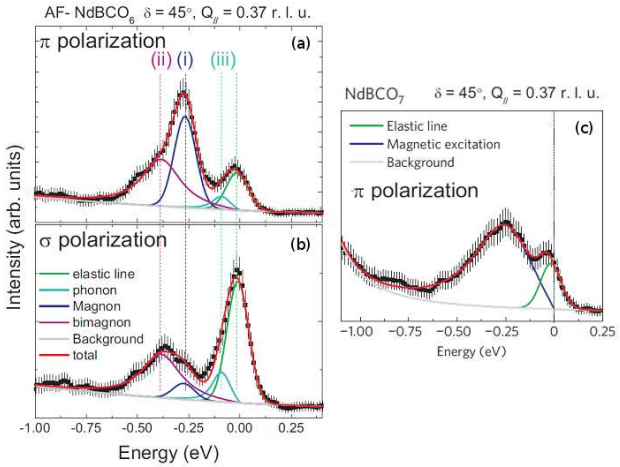

Fig. 3.9: Detail of the fitting procedure for the spectra measured on the AF parent compound NdBCO6, for π (a) and σ (b) incident photon polarizations, and on underdoped superconducting NdBCO7 for π polarization. See text for details. Note that the positions and widths of the various features are identical in both polarizations and only their relative intensities differ.

method employed in Fig. 3.4 for LCO. In the case of π polarization reported in Fig. 3.9(a) this leads to i) an intense resolution-limited magnon peak around 250 meV, ii) a high-energy tail of this peak ($\sim$ 400 meV), associated with higher-order spin excitations, and iii) a weak low-energy contribution around 100 meV due to phonons. The only difference between the two polarizations arises from the relative intensities of the features, whereas the widths and positions are identical in the two cases (compare panels (a) and (b) of Fig. 3.9). The magnetic nature of the peak at 250 meV is confirmed by the fact that working at positive $\mathbf{q}_{||}$ the peak is enhanced with π polarization while it is strongly suppressed with σ polarization, as expected for a single magnon [17, 5]. Moreover this assignment is further confirmed by the disappearance of this low energy inelastic response as the incoming photon energy is moved away from the Cu L_3 resonance (not shown here).

If we now focus on the doped NdBCO7 (Fig. 3.9(c)) we see that the magnetic peak is both damped and intrinsically broader than in the undoped case and, as a consequence, it can not be fitted with a lineshape that has the full width at half maximum (FWHM) of the instrumental resolution. This is consistent with the fact that we expect a strong damping of magnetic excitations in the continuum of incoherent electron–hole excitations that characterize the metallic nature of doped superconducting cuprates. On top of this fact higher-order excitations are expected to broaden even more

so that the separation between single- and multiple-magnon contributions that is apparent in the undoped case goes lost in the doped samples. One needs therefore to make a different choice of fitting and in this case we have decided to use Voigt profiles, that are the result of the convolution of the Lorentzian lineshape of excitations with finite lifetime with the Gaussian resolution function (FWHM = 130 meV). It can be demonstrated that at the Cu L_3 edge the RIXS intensity for magnetic excitations can be expressed as the product of a local structure factor (a quantity that depends only on the x-ray absorption spectra and the scattering geometry and is therefore momentum dependent) with the imaginary part of the systems spin susceptibility $\chi"(\mathbf{q},\omega)$ (see Supplementary Information of Ref. [7]). In particular the Lorentzian lineshape used to fit $\chi"$ in doped samples need to be antisymmetrized in order to take into account the finite lifetime of the magnetic excitations and also causality, which requires $\chi"$ to be an odd function of the energy transfer $\hbar\omega$. As a consequence the fitting Lorentzian is written as:

$$\chi"(\mathbf{q},\omega) = \frac{\Gamma_q}{(\omega-\omega_q)^2+(\Gamma_q^2)} - \frac{\Gamma_q}{(\omega+\omega_q)^2+(\Gamma_q^2)}, \tag{3.1}$$

This simple fitting procedure yields excellent results (blue solid lines in Figures 3.9(c) and 3.10) and enabled us to extract both the energies and the half-widths at half maximum (HWHMs) of the magnetic excitation as a function of momentum, as it is shown in the following.

Fig. 3.10 provides a synopsis of the experimental spectra measured at different momenta $\mathbf{q}_\parallel$ and fitted accordingly to above described procedures for all investigated compounds. These span a wide range of doping levels starting from the undoped NdBCO6 and including strongly underdoped NdBCO7 and YBCO6.6 (T_c = 65 K and 61 K, respectively), weakly underdoped $YBa_2Cu_4O_8$ (T_c = 80 K) and finally weakly overdoped YBCO7 (T_c = 80 K). In particular, given their stoichiometric composition and electronic homogeneity, the latter two systems have served as model compounds in the experimental literature on high-T_c superconductivity, but except from the 'resonant mode' observed in YBCO7 below T_c [74], their magnetic excitation spectra were unkwown before this experiment. The main message of Fig. 3.10 is that broad inelastic features are present at all doping levels in the same energy range as the single-magnon peak in undoped NdBCO6. As these features obey the same polarization dependence of single magnon in undoped cuprates, they can be assigned to magnetic excitations.

The energy of the magnetic feature in all samples strongly depends on $\mathbf{q}_\parallel$, as highlighted by the vertical inclined arrows that guide the eye along each stack of spectra. This means that the two fitting procedures described above for undoped and doped samples can be used to obtain the magnon

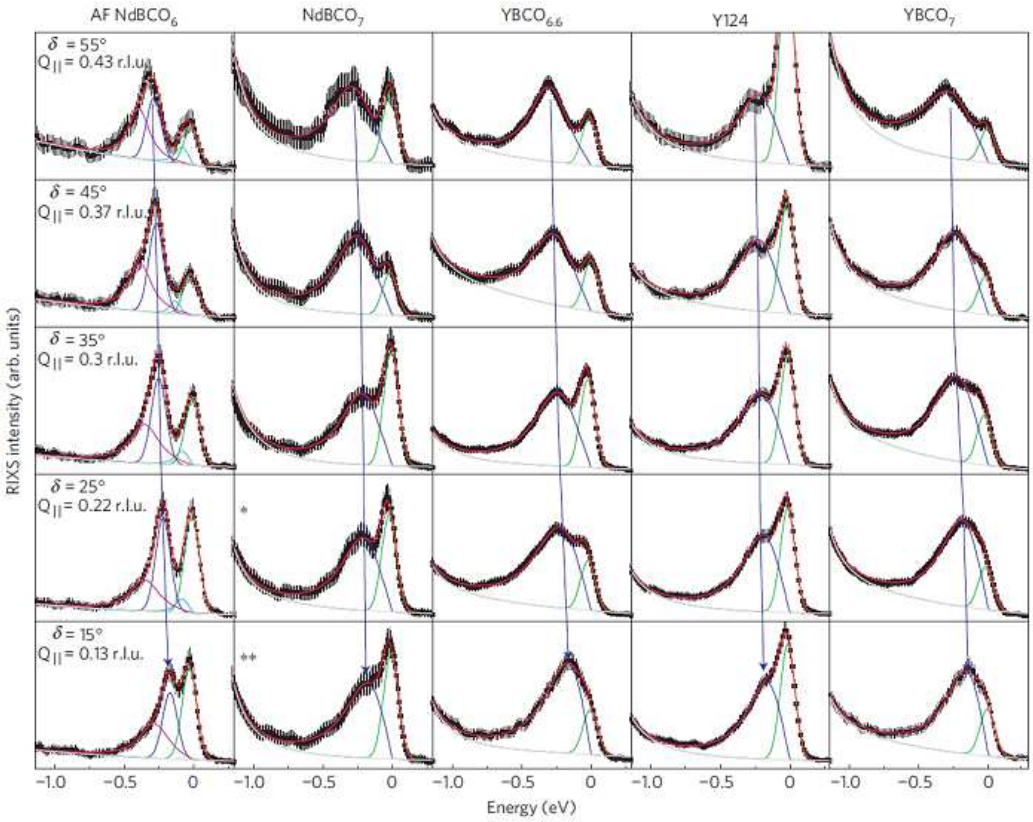

Fig. 3.10: RIXS response of undoped AF NdBCO6, underdoped NdBCO7, YBCO6.6, $YBa_2Cu_4O_8$ and slightly overdoped YBCO7 for various momentum transfers at $T = 15$ K. Note that the spectra for NdBCO7 labelled with an asterisk (two asterisks) were actually recorded for $\mathbf{q}_{\parallel} = 0.26$ (0.18) r.l.u.. Vertical inclined arrows guide the eye to follow the magnetic peak dispersion along each stack of spectra.

dispersion relations. The result for the undoped NdBCO6 is reported in Fig. 3.11(a) while the ones for the superconducting compounds are shown in Fig. 3.11(b). For an undoped cuprate having the crystal structure of (Y,Nd)BCO, with two antiferromagnetically coupled CuO_2 planes per unit cell, one expects two magnon branches [75, 76, 77], differently from the single sinusoidal branch observed in La_2CuO_4 [16, 49], in which there is only one plane per unit cell. In particular one should observe an acoustic branch with intensity $\propto sin^2(d\mathbf{q}_\perp/2)$, where $\mathbf{q}_\perp$ is the momentum transfer perpendicular to the CuO_2 layers and d is the spacing between the two coupled CuO_2 planes, and an optical branch with intensity $\propto cos^2(d\mathbf{q}_\perp/2)$. However from the calculations of the relative intensities of these two branches for our scattering geometry it turns out that the gapped optical branch dominates close to the Brillouin zone center, as shown in the inset of Fig. 3.11(a).

We have fitted the momentum dependence of the single-magnon energy position of NdBCO6 using the spin-wave dispersion calculated for a bilayer in the framework of a simple Heisenberg model [75, 76, 77], based on the intra- and inter-layer exchange constants $J_\parallel$ and $J_\perp$ respectively. We will not enter in details on this since it is just an extension to the case of a bilayer of the Heisenberg Hamiltonian for a single CuO_2 plane that will be described and used later in Section 4.4. For NdBCO6 we find $J_\parallel$ and $J_\perp$ in excellent agreement with the values obtained in antiferromagnetic $YBa_2Cu_3O_{6+x}$ [76, 77].

The magnetic excitation energies of the doped samples are extracted from the fitting based on the Voigt lineshapes. The typical error in the excitations energy depends on the momentum, and ranges from 20 meV at high momenta ($\mathbf{q}_\parallel \geq 0.3$ r.l.u) to $\pm$ 45 meV for the lowest measured $\mathbf{q}_\parallel$ (0.13 r.l.u.) due to limited resolution. Within these error bars the message is clear: the magnetic excitation energies of NdBCO7, YBCO6.6 and YBCO7 at the Brillouin-zone boundary are nearly identical to the ones found in the undoped NdBCO6. This means that the intra-layer, i.e. in-plane, exchange constant $J_\parallel$ is approximately doping independent.
Moreover this finding is not affected by the much bigger uncertainties associated with previous attempts to extract $J_\parallel$ for doped cuprates by extrapolating INS data at much lower energies [81, 82, 83, 79]. One difference with respect to the undoped sample is a steeper dispersion in the doped compounds moving towards the Γ point ($\mathbf{q}_\parallel = 0$).

Despite the fact that 0 and $\mathbf{q}_\parallel^{AF} = (\pi, \pi)$ are no longer equivalent in the absence of magnetic long-range order, one can take take the low-energy dispersion previously extracted from INS data around $\mathbf{q}_\parallel^{AF}$ and report it at Γ: it turns out that the RIXS data on YBCO6.6 nicely extrapolate the "hour-glass" dispersion found with INS on identical samples [78]. Moreover

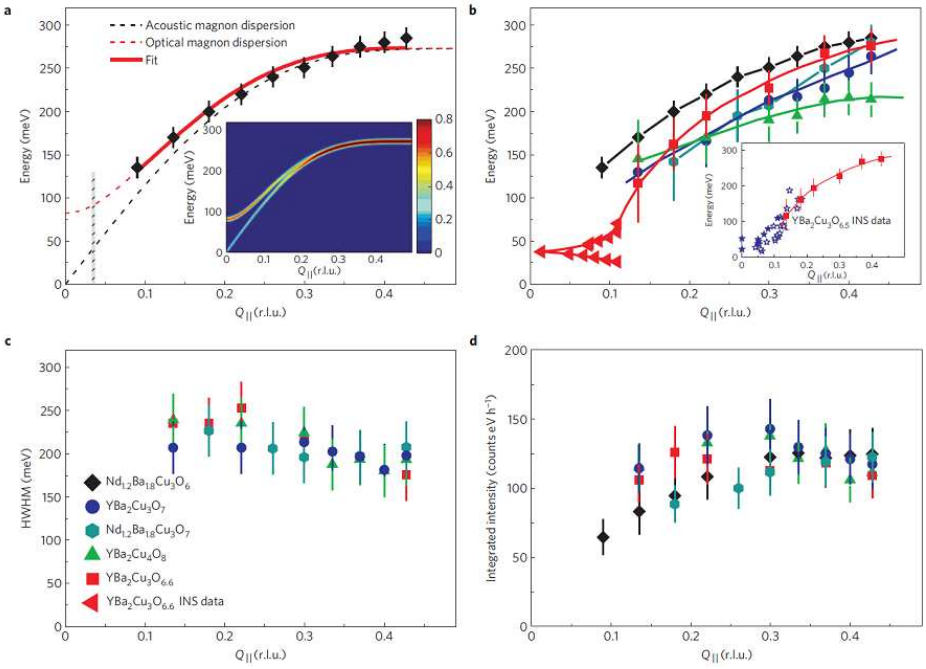

Fig. 3.11: (a) Experimental magnon dispersion along the 100 direction in AF NdBCO6 at $T = 15$ K, fitted using the spin-wave dispersion of a bilayer from Ref. [75] (thick red line). The dashed lines are the acoustic (black) and optical (red) spin-wave dispersions calculated using the fitting parameters. The grey thick vertical line represents the energymomentum resolution of this RIXS experiment. Inset: relative intensities of the acoustic and optical magnons for the scattering geometry used. (b) Experimental magnon dispersion along the 100 direction in AF NdBCO6, underdoped NdBCO7, YBCO6.6, $YBa_2Cu_4O_8$ and YBCO7 at $T = 15$ K. Low-energy INS data recorded around $\mathbf{q}_{\parallel}^{AF}$ for YBCO6.6 [78] are also shown around Γ. Lines are guides to the eye. Inset: data on YBCO6.5 from Ref. [79] (open stars) and [80] (filled stars) extrapolated by RIXS data (red squares). (c) HWHMs of magnetic excitations in NdBCO7, YBCO6.6, $YBa_2Cu_4O_8$ and YBCO7. (d) Integrated inelastic intensities. The error bars reflect the accuracy of the fitting procedure detailed in the text.

the same RIXS data are consistent with recent high-energy INS data on YBCO6.5 [79, 80].

We note here that the overall picture is slightly different for $YBa_2Cu_4O_8$, whose dispersion is flatter in general and significantly reduced close to the zone boundary compared with the other systems ($\sim$ 210 meV instead of $\sim$ 300 meV). This fact could be the signature of different $J_{\parallel}$ and $J_{\perp}$, probably due to the double chain structure peculiar of this compound (see Section 3.3.1), and will deserve further investigations (not addressed here).

Panels (c) and (d) of Fig. 3.11 provide the intrinsic HWHM and the integrated inelastic intensities of all measured compounds. The HWHM of doped samples ($\sim$ 200 meV) is much larger than the instrumental resolution and comparable to the magnon energies, indicating a strong doping-induced damping that does not change substantially with momentum or with doping.

As already explained (see Section 2.3.1), it is not possible to obtain absolute magnetic intensities from RIXS spectra. However we can extract the relative intensity of the RIXS profiles by integrating the inelastic signal in the low energy region. Remarkably, the integrated intensity normalized over time obtained in this way is conserved on doping from the antiferromagnetic insulator to the slightly overdoped superconductor. We note that we have a typical error of about 30 meV on the HWHM (mostly due to the background determination), which leads to an estimated uncertainty of about 15% in the integrated intensities. Moreover since the absorption profiles are essentially identical between the different samples, the self-absorption corrections are not at all critical to make relative comparisons of intensities and the high-energy *dd* excitations peak (visible in Fig. 3.8(a,c)) provides an additional calibration standard.

Finally we mention here that recent unpublished RIXS spectra on an other YBCO sample strongly overdoped with Ca ($Y_{0.85}Ca_{0.15}Ba_2Cu_3O_7$, T_c = 75 K) seem to confirm that the damped magnetic peak survive well beyond optimal doping with unchanged width and spectral weight. A preliminary analysis of the low energy region for this sample measured at $\mathbf{q}_{\parallel} = 0.37$ and 0.43 r.l.u., i.e. towards the border of the BZ, is reported in Fig. 3.12, showing a 400 meV broad magnetic peak with intensity comparable to the other investigated samples.

The major result of this systematic RIXS experiment at several dopings is the demonstration that damped but well-defined dispersive magnetic excitations continue to exist deep inside the continuum of incoherent electron–hole excitations of cuprates, with doping levels beyond optimal doping. Their spectral weights are similar to those of spin waves in the undoped, antiferromagnetically ordered parent compounds. Therefore we define them as *paramagnons*, to recall the fact that are akin of the single magnons ob-

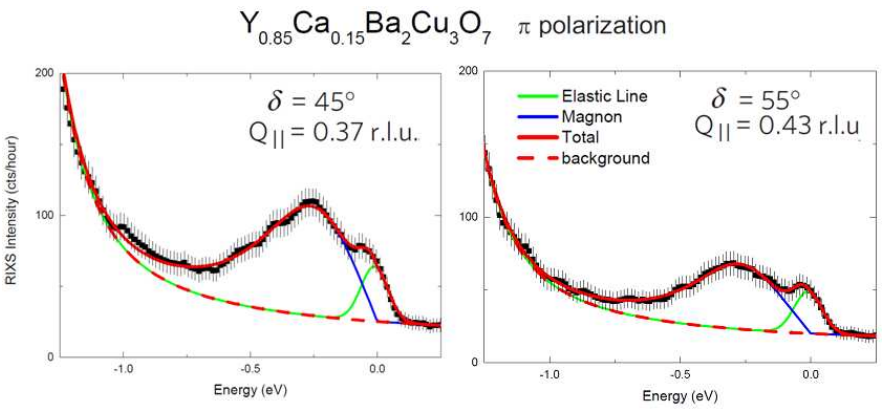

Fig. 3.12: Detail of the low energy region of a strongly overdoped $Y_{0.85}Ca_{0.15}Ba_2Cu_3O_7$ single crystal, measured with π polarization at $T = 15$ K and $\mathbf{q}_{\parallel} = 0.37$ and 0.43 r.l.u, and fitted using Voigt profiles for the magnetic peak. See also Fig. 3.9 for comparison.

served in the insulating samples. These excitations had thus far not been observed by INS, due to the much less favorable counting rates and signal-to-background ratios that characterize INS experiments on doped cuprates [74, 78, 79, 81, 82, 83, 84, 85, 86, 87].

3.3.3 Model calculations

In order to make a quantitative assessment of the results presented in the previous Subsection, we have i) carried out exact-diagonalization calculations of the $t - J$ Hamiltonian on finite-sized clusters, based on the method proposed in Refs. [88, 89, 44] and ii) self-consistently solved the Eliashberg equations to estimate the critical temperature T_c generated by a magnon mediated Cooper-pairing. For both calculations, before to go to the numerical results, we briefly recall the theoretical background.

The $t - J$ model represent a possible interpretation of the strong coupling limit of the well-known and more general Hubbard model, named after John Hubbard [90]. The two models together are considered as the simplest ones that capture the physics of strongly correlated systems, such as cuprates [46]. In particular the Hubbard model has been widely used as a benchmark for theories of copper oxides and contains two contributions: a kinetic term characterized by a hopping energy t between nearest-neighbor Cu sites, and a potential energy term which depends on the energy U, that is the penalty for double occupancy on a given site. In fact, as already mentioned in Section 3.1, the addition of a second electron to the $d_{x^2-y^2}$ ground

state orbital of a Cu ion rises the energy of the system by U, i.e. the on-site Coulomb repulsion energy due to the electron already present. The Hubbard Hamiltonian is written down as:

$$\mathcal{H} = -t \sum_{\langle i,i'\rangle,\sigma} \left(d^\dagger_{i\sigma} d_{i'\sigma} + d_{i\sigma} d^\dagger_{i'\sigma} \right) + U \sum_i n^d_{i\uparrow} n^d_{i\downarrow}, \tag{3.2}$$

where $n^d_{i\sigma} \equiv d^\dagger_{i\sigma} d_{i\sigma}$ and $d^\dagger_{i\sigma}$ ($d_{i\sigma}$) creates (annihilates) a d electron (or hole) on site i with spin σ ($\uparrow$ or $\downarrow$) and $\langle i, i'\rangle$ denotes a nearest-neighbor pair. Depending on the U/t ratio a system with a half-filled band can either be metallic or insulating. For small U and/or big t the hopping is favored and the system is metallic. On the other hand in the case of $U \gg t$, as for cuprates, it is very unfavorable for two electrons to be at the same lattice site, so that in the ground state each site is forced to be occupied by exactly one electron, which cannot move easily to other sites. The electron are thus fully localized and the system is insulating. As a bonus the insulating state is also magnetic: it is in fact favorable for neighboring electrons to have opposite spins, so that one electron can be virtually excited to a neighboring site, a process that would be otherwise forbidden by the Pauli principle for two electrons with parallel spins. This situation with large U, antiferromagnetic ordering, and electrons almost entirely localized is that of cuprates and it is usually referred to as strong coupling limit.

Unfortunately, the Hubbard model is difficult to solve and exact solutions are known only for 1D systems. The more appealing 2D and 3D cases remain to be solved exactly. Moreover we have seen in Section 3.1 that upon doping in cuprates the added holes go mainly in the bands with p character given by the oxygen lying in the CuO_2 planes. In order to take into account also the role of oxygen, one has to consider the possibility of a charge fluctuation between Cu and O and introduce the charge-transfer gap Δ, that is the energy cost to move one electron (or hole) from a Cu ion to one of the surrounding ligands, i.e. oxygens. Many expansions of the Hubbard model have been proposed to account for the peculiarities of the strong coupling limit of cuprates. Among the alternatives the $t-J$ model introduced by P. W. Anderson [91] in 1987 is the simplest that takes into account simultaneously the magnetic interactions and the presence of holes in the antiferromagnetic CuO_2 planes. In particular the $t-J$ Hamiltonian is defined as:

$$\mathcal{H} = J \sum_{\langle i,i'\rangle} \mathbf{S}_i \cdot \mathbf{S}_{i'} - t \sum_{\langle i,i'\rangle,\sigma} \left[d^\dagger_{i\sigma} (1 - n_{i\bar{\sigma}})(1 - n_{i'\bar{\sigma}}) d_{i'\sigma} \right], \tag{3.3}$$

where $t = t^2_{pd}/\Delta$ and $J = 4t^4_{pd}/\Delta^3$ are the two main parameters, corresponding to the effective hopping integral and magnetic coupling constant between

unpaired electrons in nearest-neighbor Cu sites. Both t and J take into account explicitly the role of oxygen through their dependences on t_{pd}, i.e. the hopping between Cu d and O p orbitals, and on the charge-transfer gap Δ, that substitutes the U of the Hubbard model and plays the same role.

For $t-J$ calculations on YBCO we used $J = 0.3t$ and clusters with 18 and 20 spins arranged in various shapes to map the (H, K, 0) reciprocal plane with sufficient momentum resolution. The combination of different cluster shapes shown in panel (c) of Fig. 3.13 provides access to the momentum points displayed in panel (d). The resulting spectra have been convoluted by a Gaussian lineshape with FWHM $0.2t$ to simulate the experimental resolution. Fig. 3.13 shows the calculated imaginary part of the spin susceptibility for different hole concentrations. The two peaks obtained in the undoped case correspond respectively to the single-magnon excitation (stronger feature) and the higher-order multimagnon processes (weaker feature). The single-magnon peak disperses as it should, although its energy is slightly above the value expected from linear spin-wave theory (dotted lines), due to the finite size of the cluster. The insets of Fig. 3.13(a) report the calculated energy-integrated magnetic intensity in the (H, K, 0) reciprocal plane at different dopings. The intensity in the undoped situation is strongly peaked at $\mathbf{q}_{\parallel}^{AF} = (\pi, \pi)$ and more uniformly distributed in the rest of the plane. Upon doping of the clusters, the magnetic spectral weight strongly decreases only around (π, π), remaining essentially constant everywhere else. This is clear also from Fig. 3.13(b), in which the imaginary part of the energy-integrated spin susceptibility for different momentum points is displayed as a function of doping. The calculated and experimental data are thus in excellent agreement.

In order to estimate the superconducting transition temperature that would be reached if the experimentally detected spin fluctuations play the role of bosonic glue in the Cooper-pairing mechanism, we have self-consistently solved the equations of Eliashberg theory [92, 93]. This has been very successful in explaining the physical properties of most traditional low-temperature superconductors, such as their critical temperature T_c. Indeed the Eliashberg theory is an extension of the BCS, the original microscopic theory of conventional superconductivity named after Bardeen, Cooper and Schrieffer [9]. As a consequence the standard Eliashberg equations [92, 93] were derived for superconductors with an energy gap of s-wave symmetry and assuming that the electron-phonon interaction is the mechanism for superconductivity. In particular Eliashberg theory makes use of two non-linear coupled equations: the first, referred to as the *renormalization channel*, describes the effect of the electron-phonon interaction on the properties of both normal and superconducting states, while the second equation, called *the pairing channel*, deals

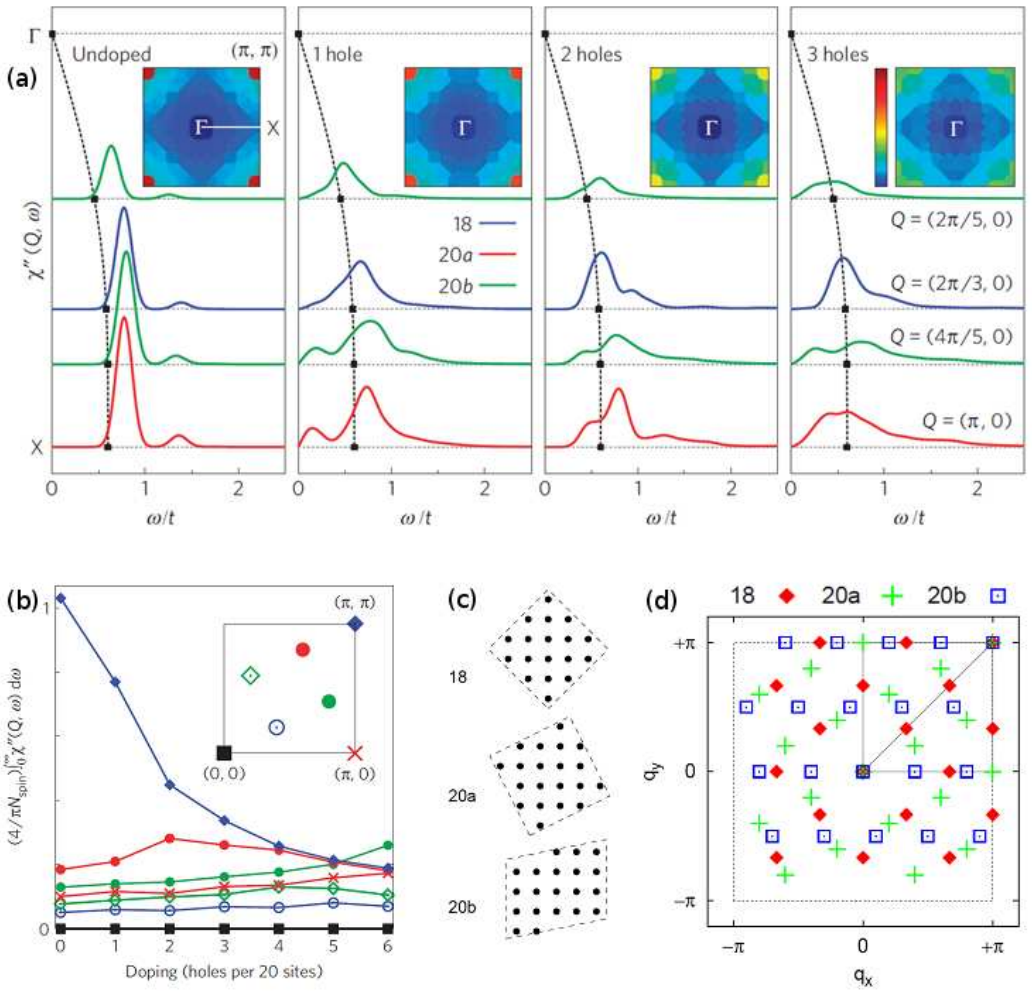

Fig. 3.13: (a) Imaginary part of the spin susceptibility $\chi"(\mathbf{q},\omega)$ resulting from exact diagonalization of the tJ model with $J = 0.3t$ on small clusters. Results from 18-site and two 20-site clusters are combined to cover the $0X$ line. The spectra are broadened using a Gaussian with FWHM $= 0.2t$. Dashed lines correspond to the linear spin-wave dispersion with the same J. Insets: Brillouin-zone maps of energy-integrated $\chi"$ with a common color scale. (b) Energy-integrated $\chi"$ of the 20-site cluster, normalized to the number of electrons on the cluster, as a function of doping. The seven accessible non-equivalent momentum points for this cluster are shown in the inset. (c) Cluster shapes used to compute the spectra of panel (a). (d) Non-equivalent momentum points in the BZ accessible to calculations on the different clusters.

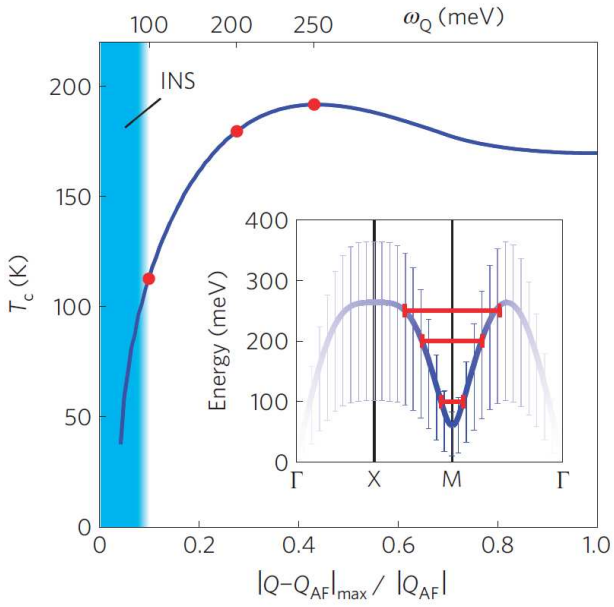

Fig. 3.14: Superconducting transition temperature T_c as resulting from the Eliashberg calculation for the measured spin fluctuations spectrum of YBCO7 shown in the inset. Vertical bars account for the experimentally determined linewidth of the excitations. Horizontal red lines indicate the momentum-space cutoffs limiting the maximum distance from $\mathbf{q}_{\parallel}^{AF} = (\pi, \pi)$ = M for which $\chi(\mathbf{q}, \omega)$ is included in the calculation. Red full circles indicate the T_c obtained from these cutoffs.

directly with the superconducting energy gap, so that is identically zero in the normal-state. In principle, these equations can be easily generalized to include the *d*-wave symmetry of the energy gap of cuprate superconductors [63] by an appropriate extension (i.e. a dependence on orientation of the electron momenta) of the charge carrier-exchange boson interaction spectral density. This in fact contains all the relevant information about the coupling of the charge carriers to the exchange bosons. However, since the microscopic mechanism leading to high-T_c superconductivity is not yet known, one has to use an appropriate experimental data set to get information on the charge carrier-exchange boson interaction spectral density, making a phenomenological hypothesis on the boson nature. In such a way it is possible to have a complete description of the problem, even in the case of cuprates, and to estimate fundamental physical parameters, such as T_c.

Our calculations presented in the following are based on above considerations and on the conjecture that, in our collected data set, paramagnons

are the exchange bosons. In particular the solution to Eliashberg equations for YBCO has been obtained by using the vertex function of the $t-J$ model [94] (for $t = 400$ meV and $J = 130$ meV) and the experimental paramagnon spectrum of YBCO7, reported in the inset of Fig. 3.14, without adjustable parameters. More details on the actual calculations are given in the Supplementary Information of Ref. [7]. The results are displayed in Fig. 3.14: the estimated T_c is similar to the maximum one observed in cuprates and also to another recent estimate based on the comparison of INS and photoemission data on underdoped $YBa_2Cu_3O_{6+x}$ [66]. The agreement within a factor of two with the experimentally measured T_c of YBCO7 ($T_c = 90$ K) could seem poor at first sight, but actually it is more than satisfactory, in view of all corrections and simplifying assumptions in the calculations. Moreover the outcome of Eliashberg estimations for conventional low-T_c superconductors show a similar level of quantitative agreement [93].

We have also introduced different momentum cutoffs around $\mathbf{q}_{\parallel}^{AF}$ in the calculation (horizontal red lines in the inset of Fig. 3.14), in order to better understand the relative contribution to the pairing strength due to the high-energy part of the spin susceptibility revealed by RIXS and to the same region around (π, π), whose magnetic spectral weight is strongly doping-dependent. It turns out that both low- and high-energy spin fluctuations contribute substantially to the pairing. However, in underdoped cuprates, with lower gaps and stronger antiferromagnetic correlations, corrections are expected to become essential, reducing the T_c values calculated here and suppressing the coupling to magnons close to (π, π). This would leave only the higher-energy paramagnon excitations detected with RIXS to give their vital contribution to Cooper pairing.

3.3.4 Conclusions

The results presented in this Chapter show that high resolution RIXS can provide crucial information on magnetic fluctuations in CuO_2 planes, in both undoped insulating parent compounds and doped superconducting cuprates, thus adding crucial pieces to the puzzle of high-T_c superconductivity (HTS).

In particular Cu L_3 RIXS has allowed us to make a detailed and systematic assessment of the evolution of spin fluctuations upon doping in a large family of superconductors, namely the ones showing the most robust superconducting states, with critical temperatures up to 90 K. The major outcome of this study, that goes from underdoped to strongly overdoped samples, is the existence in all superconducting samples of paramagnons, i.e. damped but well-defined spin excitations with dispersions and spectral weights closely similar to those of magnons in undoped cuprates. Being available deep in

the superconducting regime of the phase diagram, these paramagnons could play the crucial role of bosonic glue for the Cooper's pairs of HTS. Because of a series of physical and technical limitations, these excitations had never been observed before with inelastic neutron scattering, that was so far the elective technique for the study of magnetic fluctuations in strongly correlated electron systems.

Our systematic approach has lead to a comprehensive experimental description of the magnetic spectrum of cuprates, which turns out to be surprisingly simple and unchanged upon doping. This finding, supported also by $t-J$ model calculations, has enabled quantitative tests of magnetic Cooper pairing models. More in detail we have applicated to the model case of $YBa_2Cu_3O_7$ an extended Eliashberg theory, based on the conjecture that paramagnons are the exchange bosons leading to high-T_c superconductivity. The solution of Eliashberg equations reproduces the superconducting transition temperature of YBCO within a factor of two, a level of agreement comparable to the one found applying the same theoretical scheme to conventional superconductors.

Our findings complete and enlarge the horizons of the results obtained with INS on doped cuprates in the last two decades, showing the presence of low-energy spin fluctuations coupled to charge excitations [65] and the appearance of neutron spin resonances in the superconducting state, and give more credit to the picture that sees spin-fluctuation-mediated pairing as the common thread linking a broad class of high-temperature superconductors [67].

However, although all these evidences seem to make the overall picture of HTS more neat, a lot of work is still required: indeed we have just demonstrated that magnetic fluctuations are available for Cooper pairing, but it remains largely unknown whether this resource is actually utilized. In this connection the results presented in this Chapter are a strong boost for further experiments to address this question. In particular a change of the RIXS magnetic response at the onset of the superconducting state could provide a stronger proof that paramagnons are really the "smoking gun" behind the HTS mechanism, along the lines of a recent Raman experiment on the model single-layer system $HgBa_2CuO_{4+\delta}$ [95]. Upon cooling this compound in fact our collaborators and co-workers have observed an amplitude enhancement of the "two-magnon" peak associated to high-energy magnetic fluctuations. This enhancement occurs in concert with the development of the superconducting gap and can be understood as a high-energy feedback effect, analogous to the resonant mode observed at low energies by INS, and indicating a contribution of the high-energy magnetic fluctuations to the pairing interaction. For reasons of symmetry Raman can see only bi-magnons,

so that it would be interesting in a close future to make a broader systematic study with RIXS of the temperature evolution of magnetic fluctuations in the search of similar feedback effects.

Finally it must be said that in any case the completion of the high-T_c puzzle might still be far. According to some theoretical physicists, like S. A. Kivelson, in fact the description of HTS based on the extension of the conventional concept of Cooper pairing, by solely changing the bosonic glue, could be an oversimplification of the HTS problem, which would be instead characterized by an "ineluctable complexity" [96]. In this respect all the above presented evidences could just be correlations between different effects, that are not necessarily related to each other through causality, and are instead the manifestations of inner-lying inter-twined ordering phenomena from which superconductivity can emerge. We will return on these ordering phenomena in Chapter 5.

Chapter 4

CuO_2 planes at the interfaces of cuprate-based superlattices

A part of the work presented in this Chapter has been published in "*Magnetic and ligand field properties of copper at the interfaces of $(CaCuO_2)_n$/$(SrTiO_3)_n$ superlattices studied with high resolution Resonant Inelastic X-ray Scattering*", by M. Minola, D. Di Castro, L. Braicovich, N. B. Brookes, D. Innocenti, M. Moretti Sala, A. Tebano, G. Balestrino, and G. Ghiringhelli, Phys. Rev. B **85**, 235138 (2012)
and in
"*Occurrence of a high-temperature superconducting phase in cuprate/ titanate $(CaCuO_2)_n/(SrTiO_3)_m$ superlattices*", by D. Di Castro, M. Salvato, A. Tebano, D. Innocenti, C. Aruta, W. Prellier, O. I. Lebedev, I. Ottaviani, N. B. Brookes, M. Minola, M. Moretti Sala, C. Mazzoli, P.G. Medaglia, G. Ghiringhelli, L. Braicovich, M. Cirillo, and G. Balestrino, Phys. Rev. B **86**, 134524 (2012).

Using high resolution RIXS excited at the Cu L_3 edge we have investigated the ligand field (dd) and magnetic excitations in $(CaCuO_2)_n/(SrTiO_3)_m$ superlattices, both insulating and superconducting, and compared them to those of a 14 nm thick $CaCuO_2$ film. The dd excitation spectrum reveals a pyramidal coordination of Cu ions at the $CaCuO_2/SrTiO_3$ interfaces. In all insulating samples spin excitations are in the form of dispersing magnons. In particular in the SLs magnons have similar spectral intensity but reduced dynamics with respect to pure $CaCuO_2$. By fitting the dispersions within linear spin wave theory we have obtained the leading term of the in-plane superexchange parameters: $J = 127$ meV, 138 meV and 157 meV

for $n = m = 2$, $n = m = 3$ SLs and $CaCuO_2$ respectively. These results demonstrate that the antiferromagnetic order is preserved in the insulating SLs down to very small cuprate layer thickness and despite the chemical and structural alterations at the interface. On the other hand the superconducting SLs exhibit dispersing paramagnons, similarly to the case of superconducting $YBa_2Cu_3O_{6+x}$presented in Section 3.3. These findings open the way to the production of new, artificial high temperature superconductors based on cuprate/noncuprate SLs where the charge reservoir layer is constituted by the interface itself.

Contents

4.1 Introduction

In Chapter 3, we have focused on the study of magnetic fluctuations in the inner layers of bulk doped cuprates and we have discovered that the magnetic peak, although damped and broader, is still present in the form of paramagnon over a wide range of doping, possibly supporting the Cooper's pairs formation in those systems. Hereafter in this Chapter we use again Cu L_3 RIXS to assess the effects (if any) on magnetic fluctuations when CuO_2 planes are close to the interfaces of an artificial cuprate-based heterostructure. In fact the proximity of interfaces could in principle affect magnons in different ways, due to the unavoidable presence of chemical and structural alterations of the cuprate system when it is combined with an another compound. Incidentally, the information on *dd* excitations and associated ligand field provided by RIXS can help to get deeper insights into these alterations and on the local coordination of Cu ions close to the interfaces of these artificial systems.

Cuprate-based heterostructures are just one example of the many superlattices (SLs) that have been grown and studied over the last few years.

Recently the high pace technical progress in epitaxial growth has indeed lead to the discovery of a panoply of exceptional magnetic and transport properties in artificial heterostructures of $3d$ transition metal oxides in general. The most cited case is the formation of two-dimensional electron gas at the $LaAlO_3/SrTiO_3$ interface [97, 98]. Electronic, lattice and orbital reconstruction occurring at the interfaces can in fact influence the charge transfer between the different oxides (often inducing a doping of the interface layers), while the modified dimensionality can affect the magnetic properties of the oxides. What makes particularly interesting the study of cuprate-based SLs among these heterostructures is the fact that they can be considered as new, artificial materials belonging to the family of high T_c superconductors (HTS). In particular they offer the opportunity to assemble in an original combination the two building blocks of HTS, i.e., the superconducting CuO_2 plane and the charge reservoir layer that provides the extra charge needed to dope the planes and make them superconduct. By epitaxial growth we can thus explore the physics of HTS over a broader range of conditions, with a bottom-up approach, overcoming the thermodynamic limitations governing the chemical stability of bulk materials.

The production of cuprate-based heterostructures is an ongoing work started more than 20 years ago: the very first steps towards artificial HTS were made by Triscone *et al.* [99], who produced SLs of $YBa_2Cu_3O_7$ and $DyBa_2Cu_3O_7$ (both superconductors) and then substituted Dy with Pr [100] to study the coupling between superconducting $YBa_2Cu_3O_7$ layers separated by an insulator with a very similar structure ($PrBa_2Cu_3O_7$). Later the goal rapidly became to produce superconducting SLs consisting of materials (metals and/or insulators) which are not superconducting by themselves. The ultimate double goal is to better understand the charge transfer mechanisms and, hopefully, to increase T_c above what is possible with bulk materials. For example Balestrino *et al.* [101, 102] first found $T_c = 80$ K by alternating undoped and overdoped cuprates in the $(CaCuO_2)_2/(BaCuO_2)_2$ SL; the same scheme was used by Gozar *et al.* [103] with La_2CuO_4 and $La_{1.55}Sr_{0.45}CuO_4$ ($T_c = 30$ K). Clearly the key process there is the charge transfer at the interface between the materials, so that the correct amount of holes move to the originally undoped CuO_2 planes to give rise to superconductivity in a sort of "remote" chemical doping across the interface. How far does the charge transfer extends from the interface? In other words, is superconductivity confined at the interface or is it a property of several unit cells in the vicinity of the interface?

X-ray absorption spectroscopy and x-ray scattering have been used to answer these key questions. Aruta *et al.* [104] have studied the hole redistribution and symmetry in $CaCuO_2/BaCuO_2$, Smadici *et al.* [105] used

resonant soft x-ray scattering to determine the hole distribution along the SL profile, and Logvenov *et al.*, after showing that superconductivity can occur within a single CuO_2 plane [106], made a comprehensive study of interface superconductivity [107] in the $La_2CuO_{4+\delta}/La_{1.55}Sr_{0.45}CuO_4$ system. However, a general understanding of the charge redistribution across the interfaces is more difficult to reach in the above mentioned examples, due to the presence of copper in both building blocks. In fact the two cuprates are both susceptible to becoming superconductors. Moreover resonant x-ray techniques can hardly differentiate between Cu sites of the two layers, leading to ambiguous results.

To overcome those practical difficulties we have studied a new type of cuprate SL, made of few unit cells of infinite layer $CaCuO_2$ alternated by the perovskite insulator $SrTiO_3$. The chemical formula is $(CaCuO_2)_n/(SrTiO_3)_m$, where n and m are the number of unit cells (u.c.) of $CaCuO_2$ (CCO) and $SrTiO_3$ (STO), respectively. $SrTiO_3$ is at the basis of the emerging field of oxide electronics, due to the occurrence of exotic, two-dimensional phases of electron matter at the interface with other oxides [108, 109, 110, 111]. $CaCuO_2$ is an antiferromagnetic insulator [30] and it is considered the simplest parent compound of HTS [112]: in this compound the CuO_2 planes, where superconductivity can occur, are separated by bare Ca atoms in a pure infinite layer (IL) structure [30]. These SLs, constituted of two insulating materials, are normally not superconducting and they simply show a relatively low sheet resistance at room T. However very recently Di Castro *et al.* reported superconductivity in strictly similar SLs grown in a highly oxidizing atmosphere [113], demonstrating that these cuprate-based heterostructures can actually be thought as artificial HTS and are indeed of very high interest. In particular they provided evidences that, when $CaCuO_2$ and $SrTiO_3$ are brought together to form the SL, superconductivity with a maximum $T_c = 40$ K (zero resistance temperature), is achieved, with the interfaces working as charge reservoir to inject holes in the inner CuO_2 planes of the $CaCuO_2$ block, making the SLs superconducting, although based on two insulators.

In order to understand what's happening at the interfaces of these SLs we have exploited the capability of RIXS of working very well on thin films. First we have measured insulating SLs to observe in which way the usual antiferromagnetic order of $CaCuO_2$ is affected by the alterations at the interfaces. Then, once the simpler undoped case was known, we have studied superconducting SLs, to understand how magnetic fluctuations evolve with doping and if a (para)magnon-mediated superconductivity could in principle still be possible in these artificial HTS.

4.2 Experimental

Our collaborators have used pulsed laser deposition (PLD) to synthesize several superlattices $(CaCuO_2)_n/(SrTiO_3)_m$ made by 10 to 20 repetitions of n unit cell of CCO and m unit cells of STO, on different substrates, namely $LaAlO_3$ (100) (LAO) and $NdGaO_3$ (110) (NGO). Actually NGO is the most suitable substrate to grow both CCO and STO, having a pseudocubic in-plane lattice parameter ($a = 3.87$ Å) just in the middle between CCO ($a = 3.84$ Å) and STO ($a = 3.91$ Å).

In the following discussion I will first present the RIXS results on the non-superconducting SLs. These are two $(CaCuO_2)_n/(SrTiO_3)_m$ SLs with $n = m = 2$ and $n = m = 3$ and they are respectively 340 ± 10 Å and 460 ± 10 Å thick films, epitaxially grown by Pulsed Laser Deposition (PLD) on (100) $LaAlO_3$ substrate. The bulk $CaCuO_2$ used as reference is a 145 ± 10 Å thick film, also grown by PLD, on (100) $SrTiO_3$ substrate. While bulk $CaCuO_2$ is insulating the SLs show a low sheet resistance at room T. The structural characterization was performed by x-ray diffraction (XRD) measurements in a $\theta - 2\theta$ Bragg-Brentano geometry. The presence of sharp superlattice satellite peaks SL_{-i} and SL_{+i} around the mean structure peak SL_0 in the XRD patterns (Fig. 4.2) on both SLs clearly indicate a good quality of the heterostructures consistent with the layer scheme of Fig. 4.1(a). n unit cells of $CaCuO_2$, each containing one CuO_2 plane, are alternated to n unit cells of $SrTiO_3$ and the $(CaCuO_2)_n/(SrTiO_3)_n$ block is repeated 22 times. In particular, in order to retrieve all information on these multilayered heterostructures, one has to combine the position of the satellite peaks $SL_{-1}(\theta_{+1})$ and $SL_{+1}(\theta_{-1})$ with that of the average structure peak SL_0 in the XRD spectra. The thickness of the supercell $\Lambda = n \times c_{CCO} + m \times c_{STO}$, where c_{CCO} is the c-axis lattice parameter of CCO and c_{STO} the one of STO, is given by $\Lambda = \lambda/[sin(\theta_{+1}) - sin(\theta_{-1})]$, where λ is the wavelength of the incident radiation. On the other hand the value of the mean c-axis lattice parameter $c_m = (n \times c_{CCO} + m \times c_{STO})/(n + m)$ is obtained by the Bragg law $c_m = \lambda/[2sin(\theta_0)]$ using the position θ_0 of the peak SL_0.

The superconducting SLs were grown on NGO at about 600°C in a mixture of oxygen and 12% ozone atmosphere at a pressure of about 1 mbar. The growth was followed by a quenching at an oxygen pressure of about 1 bar. In Fig. 4.3(a) the x-ray diffraction (XRD) spectrum of a superconducting SL $(CCO)_n/(STO)_m$, with nominal composition $n = 3$ and $m = 2$, reveals the presence of sharp satellite peaks around the average structure one, indicating the formation of a high quality superlattice with a period $\Lambda = 19.5(5)$ Å, $n = 3.5(5)$, and $m = 2.0(5)$. To better evaluate the structural quality of CCO/STO SLs, we recorded a HRTEM image on an identical sample along

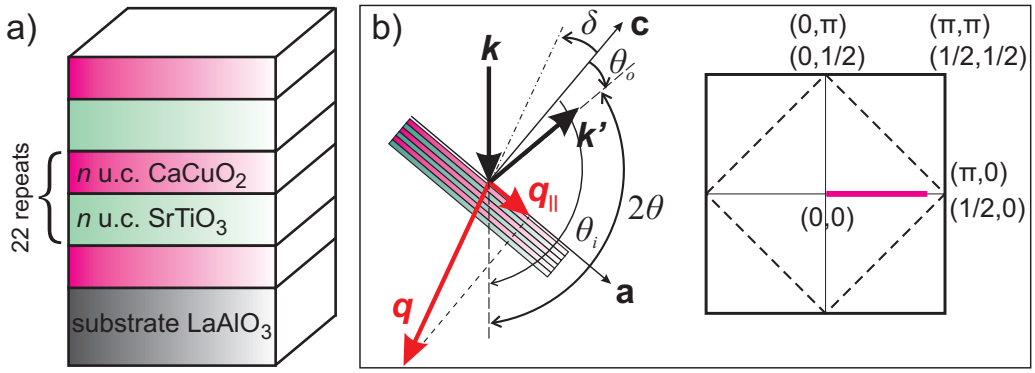

Fig. 4.1: (a) Schematic view of $(CaCuO_2)_n/(SrTiO_3)_m$ structure with $n = m$. Each block contains n unit cells of $CaCuO_2$ ($SrTiO_3$) and therefore n CuO_2 (TiO_2) planes. (b) Layout of the experimental setup and indication of the reciprocal space region (magenta thick line) spanned inside the first Brillouin zone.

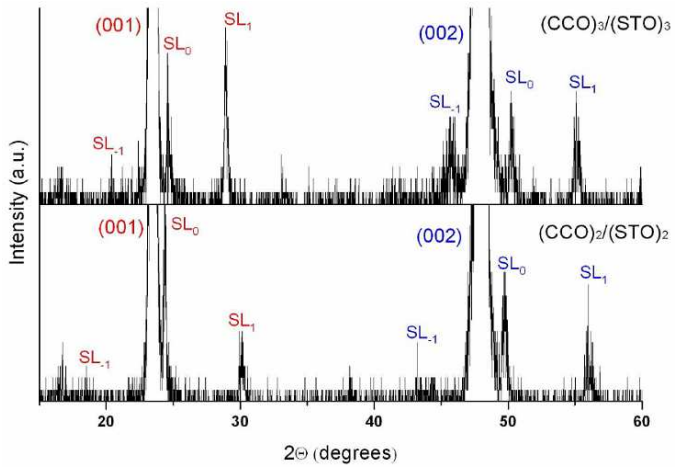

Fig. 4.2: Diffraction patterns of $(CaCuO_2)_n/(SrTiO_3)_m$ SLs with $n = m = 3$ (a) and $n = m = 2$ (b). In order to retrieve the information on the SL structure one has to combine the position of the satellite peaks $SL_{-1}(\theta_{+1})$ and $SL_{+i}()$ with that of the average structure peak SL_0. See the text for details.

the [110] direction of the $NdGaO_3$ substrate. The image (Fig. 4.3(b)) shows a heteroepitaxial superlattice film growth and a series of stacked layers with different contrast, regularly alternate thicknesses and sharp interfaces. The high quality of the SL is confirmed by the Fourier Transform (FT) pattern (inset of Fig. 4.3(b)), where, beside the intense reflections associated with the CCO and STO substructures, satellite lower intensity reflections are observed in the growth direction (i.e. [001] direction). These reflections are associated to the periodic structure generated by the regular stacking of CCO and STO. The stacking can be described as an average of 3.5 u.c. of CCO and 2 u.c. of STO, with a superlattice period 19 Å, in agreement with the XRD analysis. This means that the number of CCO u.c. varies from 3 to 4.
This assignment is confirmed by the analysis of the filtered HRTEM image (see Fig. 4.3(c)), where it is possible to precisely determine the layers stacking, as illustrated in the color circles model structure in the inset.

Our collaborators observed that the conductivity of $(CCO)_n/(STO)_m$ SLs slightly varies with varying n and m, but increases substantially with increasing the oxidizing power of the growth atmosphere, till the occurrence of superconductivity. In particular, they found that for a weakly oxidizing growth atmosphere (oxygen pressure lower than 0.1 mbar) the SLs show always a semiconductor-like temperature dependence of the resistance, even if the film is quenched to room temperature in high (about 1 bar) oxygen pressure. An insulator to metal transition occurs only when a highly oxidizing growth atmosphere is used (oxygen plus 12% ozone at a pressure of about 1 mbar) and the film is rapidly quenched to room temperature at high oxygen pressure (about 1 bar). Under these conditions, the SL is metallic, and, in the best case, the resistance goes to zero at about 40 K (see inset of Fig. 4.11). Thus, strong oxidation is a key ingredient to obtain superconducting samples. The RIXS measurements that will be shown hereafter have been carried out on only four superconducting SLs: these were CCO_m/STO_n heterostructures respectively with $n = 13$, $m = 2$, $T_c = 12$ K (thick CCO layer); $n = 7$, $m = 2$, $T_c = 16$ K (intermediate CCO layer); $n = 3$, $m = 2$, $T_c = 25$ K (thin CCO layer); and $n = 3$, $m = 5.5$, $T_c = 12$ K (thick STO layer).

The RIXS experiments were performed at the ID08 beam line of the European Synchrotron Radiation Facility using the AXES spectrometer (presented in Chapter 2). The combined resolution of the beam line Dragon monochromator and the spectrometer for this experiment was 260 meV. The incident x-rays were tuned to the maximum of the Cu L_3 absorption peak and we used π polarized x-rays (i.e. linearly polarized parallel to the scattering plane) which enhance the magnon peak at positive in-plane momentum $\mathbf{q}_{\parallel}$ (i.e. around normal incidence), as we have demonstrated in Ref. [17] and shown in Section 3.2.

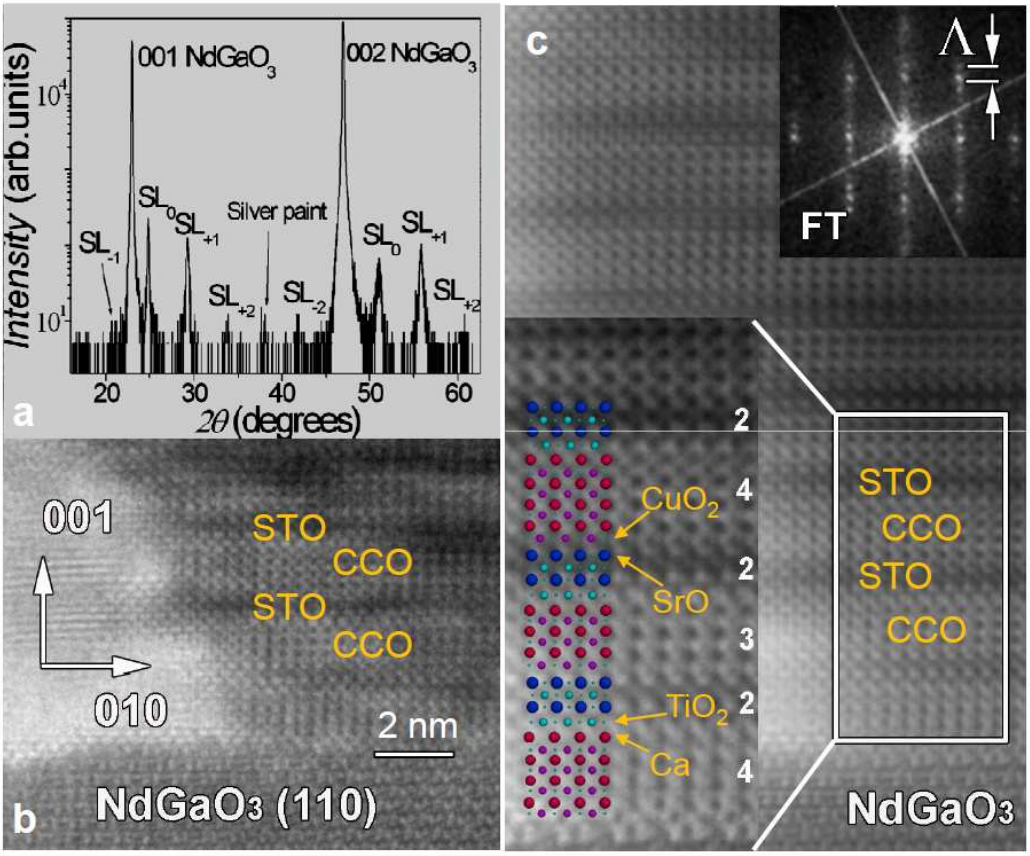

Fig. 4.3: (a) XRD pattern (intensity in log scale) from $(CaCuO_2)_{3.5}/(SrTiO_3)_2$ SL. SL_i mark the satellite peaks, around the average structure peak SL_0. (b) HRTEM image of an identical SL taken along the [110] orientation of the $NdGaO_3$ substrate. (c) filtered HRTEM image. Bottom inset: enlargement of the area marked by white rectangle close to substrate with the atomic model of STO-CCO sequences (dark blue: Sr; light blue: Ti; small light blue: O; red: Ca; purple: Cu). Top inset: Fourier Transform (FT) pattern where superlattice spots are clearly visible along [001] growth direction.

The experimental layout is shown in Fig. 4.1(b) and is the one already described in Section 2.3. Given that the photon momentum $\boldsymbol{k}$ is dictated by the energy of the Cu $2p \rightarrow 3d$ resonant transition, the scattering angle $2\theta = 130°$ determines the maximum transferred momentum $\mathbf{q}$. Although this is fixed, its projection onto the ab-plane $\mathbf{q}_{\parallel}$, i.e. the meaningful quantity in the experiment, can be easily changed by rotating the sample around an axis perpendicular to the scattering plane, allowing to measure dispersing features. In this way, the region of the 2D reciprocal space indicated by the thick magenta line can be covered (Fig. 4.1(b)). The maximum reachable $\mathbf{q}_{\parallel}$ is 0.7 Å^{-1}, corresponding to 0.435 r.l.u.. All RIXS spectra were measured at low T (20 K, the minimum allowed by the cryostat). Each spectrum is the result of 1 hour total accumulation (12 spectra of 5 minutes). The exact position of the zero on the energy loss scale was determined by measuring for each $\mathbf{q}_{\parallel}$ a non-resonant spectrum from polycrystalline graphite.

4.3 Ligand field excitations

In this and in the following Section we will focus only on insulating CCO/STO heterostructures compared with CCO. Since the non-superconducting SLs that we measured have the same number of CCO and STO u.c. per layer, i.e. they have the chemical formula $(CaCuO_2)_n/(SrTiO_3)_m$ SLs with $n = m$ hereafter we will just refer to the number n of u.c.

The RIXS spectra of bulk $CaCuO_2$ and insulating SLs at $\mathbf{q}_{\parallel} = 0.375$ r.l.u. and T = 20 K are presented in Fig. 4.4(a). The peaks at high energy loss (from 1 to 3.5 eV) correspond to dd-excitations, i.e. transitions between the ligand field split d states of Cu ions. As already mentioned in section 2.3 in RIXS it is not possible to obtain absolute intensities from the experiment, the overall detection efficiency can change over time for technical reasons and thus it is necessary to use a spectral feature as reference. The most reasonable choice for cuprates is to use dd excitations, which largely dominate all Cu L_3 RIXS spectra. Therefore the intensity of each spectrum is normalized to the area of the dd peaks (ranging from 1 eV to 3.5 eV) put equal to 100. In particular we notice here that the highest dd peak in bulk $CaCuO_2$ comes out by chance equal to 100, while the peaks of the SLs are slightly lower. This is simply due to some broadening in the case of SLs, more affected by disorder than bulk $CaCuO_2$.

In past experiments we have already calculated the theoretical cross sections for dd excitations in a pure ionic picture and used them to fit the experimental spectra of bulk $CaCuO_2$ with excellent agreement [3, **?**]. Later these results have been supported also by ab initio quantum chemical calcu-

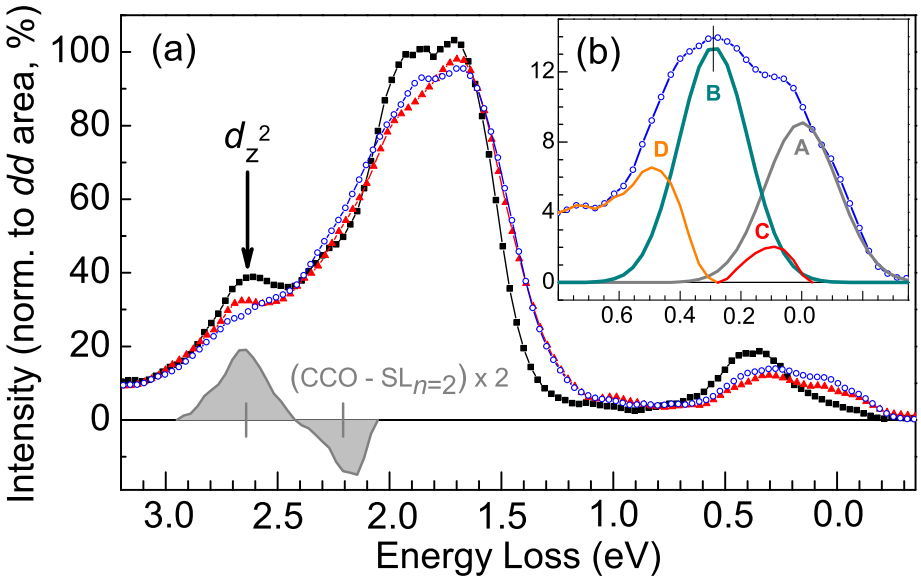

Fig. 4.4: (a) RIXS raw spectra at Cu L_3 edge of bulk $CaCuO_2$ (black filled squares) and $(CaCuO_2)_n/(SrTiO_3)_n$ SLs with $n = 3$ (red filled triangles), $n = 2$ (blue open circles) at $\mathbf{q}_{\parallel} = 0.375$ r.l.u. and $T = 20$ K using π incident polarization. Intensities are normalized to the dd area put to 100. The shaded area under the gray solid line represents the difference between the bulk $CaCuO_2$ and the SL with $n = 2$ multiplied by 2. The ticks at 2.65 and 2.2 eV indicate respectively the center of mass of the resulting positive and negative peaks. Note how the spectral weight of the d_{z^2} peak moves towards lower energy loss passing from bulk $CaCuO_2$ to the SL. (b) decomposition of SL $n = 2$ spectrum in the low energy region: elastic (A) and magnon (B) peaks; optical phonon (C) and multiple magnons (D) spectral features.

lations [114]. Consistently with previous measurements here we recognize in the peaks at 1.65 eV, 1.95 eV and 2.65 eV the transitions of the Cu $3d^9$ hole respectively to the d_{xy}, $d_{xz/yz}$, and the d_{z^2} orbital, starting from the $d_{x^2-y^2}$ ground state.
Both spectra of SLs present essentially these same three features with two main differences: *dd*-excitations peaks are broader than in bulk $CaCuO_2$ and the d_{z^2} peak changes drastically in the SLs, going under a suppression which is stronger in the case $n = 2$. The former difference, as we have seen, has a general nature and we consider it as the fingerprint of possible defects, which arise more probably in the artificial heterostructure of the SLs than in bulk $CaCuO_2$. On the contrary the marked change in the d_{z^2} peak is likely related to a structural and orbital reconstruction that can be readily explained. In the infinite layer configuration of bulk CCO copper ions have no apical oxygens and this is also the reason behind the peculiar strong separation in energy of the d_{z^2} peak from other *dd*-peaks in $CaCuO_2$, as pointed out also in Ref. [114].
If we introduce an apical oxygen, modifying the infinite layer structure of $CaCuO_2$, the d_{z^2} peak associated to the copper ions with the new coordination moves towards lower energy loss, resulting in a significant decrease of the spectral weight of the peak at 2.65 eV. This is what happens in the case of SLs: in particular, as reported in Fig. 4.4(a), the difference between bulk $CaCuO_2$ and the SL with $n = 2$ shows that the missing spectral weight moves towards 2.2 eV energy loss. RIXS spectra of the SLs are thus consistent with the presence of some apical oxygens, i.e. a portion of Cu ions has a pyramidal coordination, instead of the infinite layer one of bulk $CaCuO_2$. These copper ions are much likely located in the CuO_2 planes at the interfaces with $SrTiO_3$. We also note that, even with the formation of pyramids at the interfaces, the ground state of the system maintains the $3d^9$ hole in the $d_{x^2-y^2}$ orbital, as it is readily confirmed by the unchanged assignment of the *dd*-peaks in the SLs with respect to the bulk $CaCuO_2$. In order to understand how pyramids are built up, two types of $CaCuO_2/SrTiO_3$ interfaces can be envisaged, as shown in Fig. 4.5.

If we consider a TiO_2 layer, in between this and the first CuO_2 plane we can have either a plane of Ca^{2+} ions (Fig. 4.5(a)) or a neutral SrO plane (Fig. 4.5(b)). In the second case oxygens of the SrO plane act as apical for the nearby copper ions (thin dashed line in the structure), causing a loss of spectral weight at 2.65 eV. Moreover, as shown in Fig. 4.4(a), the reduction of this peak passing from bulk $CaCuO_2$ to the SLs is bigger in the the SL with $n = 2$. In a simple picture in the SL $n = 3$ only two out of three copper ions are at the interfaces, while in the SL $n = 2$ all copper ions have in principle the possibility to have apical oxygens and this will depend on the

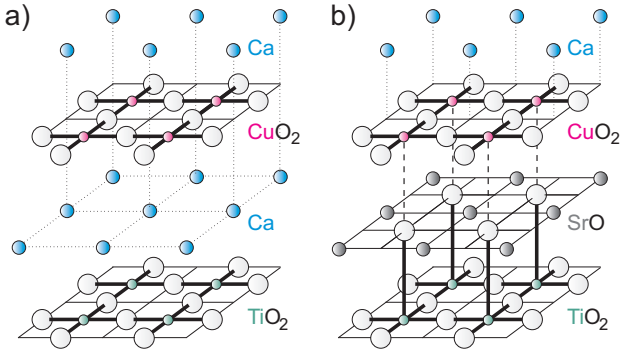

Fig. 4.5: Schematic representation of the possible interfaces in $(CaCuO_2)_m/(SrTiO_3)_n$ SLs starting from a TiO_2 layer. Thick lines highlights bondings while thin lines guide the eye. Note that Cu ions at the interface can either maintain the infinite layer coordination (a) or gain an apical oxygen (thin dashed line) from a SrO plane (b).

type of interface. As a consequence, in the case $n = 2$ a bigger portion on the total amount of Cu atoms is expected to have pyramidal coordination with respect to the case $n = 3$, resulting in a stronger suppression of the d_{z^2} peak, in excellent agreement with the data.

We note here that very likely the real interfaces are given by a mixture of the two types proposed in Fig. 4.5 and also CaO planes can be envisaged at the interfaces (with Ca substituting Sr in Fig. 4.5(b)) so that, depending on the growth conditions, different overall oxygen contents can be reached. Indeed, as shown above, the interface layers have a double nature: either infinite-layer-like (Fig. 4.5(a)) or perovskite-like (Fig. 4.5(b)). If the SL is grown in high oxygen pressure the perovskite–like nature will prevail so that we can have both CaO_x and SrO_y interfaces with overall oxygen content at the interfaces $x+y > 1$. This leaves open the door to a possible doping of the SL system. In particular, as already mentioned, our collaborators [113] have shown that under strongly oxidizing conditions high temperature superconductivity can be achieved. As previously said, the SLs presented here are *not* superconducting but they show a relatively low sheet resistance at room T. This fact is much likely related to a very small oxygen-doping coming from the interfaces: indeed both spectra of the SLs present a spectral weight slightly higher than bulk $CaCuO_2$ in the region around 1 eV of energy loss, that is where one can usually see the charge contribution in doped cuprates [4].

Further support for a slight doping and for previous considerations comes also from x-ray absoprtion spectroscopy (XAS) measurements. Fig. 4.6 shows

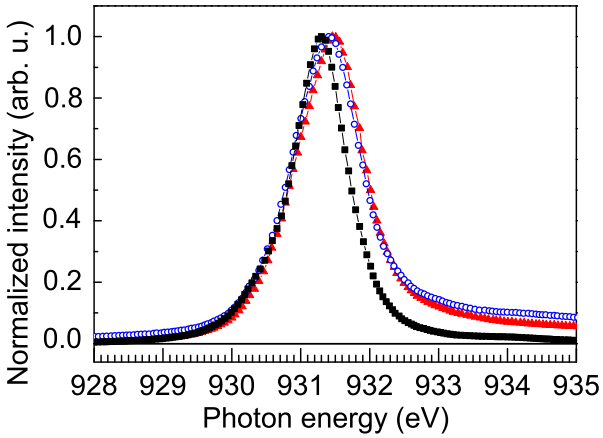

Fig. 4.6: XAS spectra at Cu L_3 edge of bulk $CaCuO_2$ (black filled squares) and $(CaCuO_2)_n/(SrTiO_3)_n$ SLs with $n = 3$ (red filled triangles), $n = 2$ (blue open circles) measured at $T = 20$ K using σ incident polarization. Intensities are normalized to the main peak.

the Cu L_3 absorption spectra of bulk $CaCuO_2$ and $CaCuO_2/SrTiO_3$ SLs measured in total electron yield for σ polarized incoming x-rays. After a linear background subtraction (fitted to the pre-edge region of the L_3 edge) for each sample XAS spectrum has been normalized so that the intensity of the peak is 1. The measurements have been done in grazing incidence geometry (10 $^\circ$ from surface) so that the electric vector lies in the CuO_2 planes when using σ incident polarization. This geometry enhances the sensitivity to in-plane doping charge. In both the SLs the L_3 peak is slightly shifted and broader with respect to bulk $CaCuO_2$. In particular there is some additive spectral weight distributed just above the main peak, around 932.7 eV. This is much likely due to the contribution of charge carriers, similarly to the case of $YBa_2Cu_3O_{6+x}$ [115]. Consistently with this picture the effect becomes much bigger in the case of the superconducting $CaCuO_2/SrTiO_3$ SLs, on which we will return later. Indeed we will show that for doped SLs the main XAS peak moves to slightly higher energy than in the undoped film.

4.4 Dispersing magnetic excitations

Let us now focus on the low energy spectral region. As expected a magnon peak around 400 meV is clearly visible in the raw spectrum of bulk $CaCuO_2$,

enhanced by our choice of π incident polarization and positive transferred momentum $\mathbf{q}_{\parallel}$. Remarkably also both raw spectra of SLs show a magnon peak, slightly damped and shifted by roughly 50 meV to lower energies with respect to bulk $CaCuO_2$. In Fig. 4.4(b) an expansion of the low energy region is shown only for the SL $n = 2$. Following the same procedure as in our previous work [4] the raw spectrum is decomposed into an elastic peak A and a magnon peak B, both with the full width at half maximum of the instrumental resolution. This operation leaves a residual inelastic spectrum which is composed by a low-energy (100 meV) peak C and a high-energy broader feature D. Within our uncertainties on the energy loss scale the former is assigned to a well-known optical phonon [116, 117], while the feature D is due to higher-order magnetic excitations, namely, multi-magnons. The assignment of the peak B to a magnon excitation also in the case of SLs is straightforward and supported both by the energy of the excitation and by the empirical fact that the peak B show a clear dispersion for both SLs, very similar to that of bulk $CaCuO_2$. Moreover the intensity and the shape of the dispersions are consistent with the expected behaviour of a magnon [17] when using the incident polarization (π) and the scattering angle (130°) chosen for this experiment.

Fig. 4.7 shows RIXS spectra for the bulk $CaCuO_2$ and the SL with $n = 2$, at selected $\mathbf{q}_{\parallel}$ along the (1/2,0) direction (see Fig. 4.1(b)). For each spectrum a resolution-limited Gaussian lineshape has been used to fit the elastic (already subtracted in the figure) and the magnon peak. The thin solid guiding lines highlight the magnon peak dispersion. The complete dispersions, as resulting from the decomposition of all spectra of all samples, are shown in Fig. 4.8. Error bars in the figure have been estimated from a sensitivity analysis of the Gaussian fittings and are ≤ 30 meV. We underline here that the magnon fittings based on the resolution-limited Gaussian lineshapes work very well, exactly as it happens in other undoped cuprates known to have a static long range anti-ferromagnetic order [4]. This fact is a clear signature of spin excitations on top of an anti-ferromagnetic lattice. Dynamical magnetic fluctuations indeed would imply significantly larger energy broadening and damping of the magnon peak, such as the ones observed for doped YBCO in Section 3.3. In that case the width of magnetic peaks is much bigger than the resolution, making much more tough the use of resolution-limited Gaussians. Given these considerations in the following we will discuss magnetic excitations reasoning in terms of spin waves.

Looking at Fig. 4.8 we observe that the dynamics of the dispersion is reduced in the SLs, i.e. when the number of CuO_2 layers is lowered, but does not collapse. This fact means that in the CuO_2 layers of the SLs there is a decrease of the superexchange coupling with respect to the case of bulk

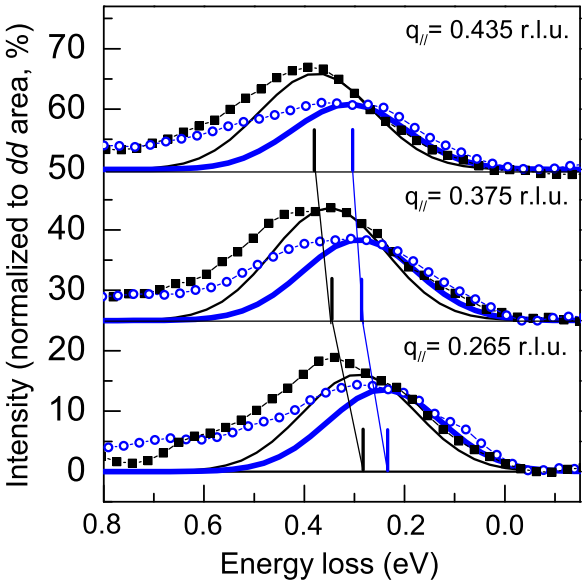

Fig. 4.7: Selected RIXS spectra for bulk $CaCuO_2$ (black filled squares) and $(CaCuO_2)_n/(SrTiO_3)_n$ SL with $n = 2$ (blue open circles), after the substraction of the elastic peak, measured at different $\mathbf{q}_{\parallel}$. Solid lines (thinner for bulk $CaCuO_2$) with the same color code represent the magnon peak simulated by a resolution limited Gaussian lineshape. Ticks and vertical lines are guides for the eye to follow the magnon dispersion.

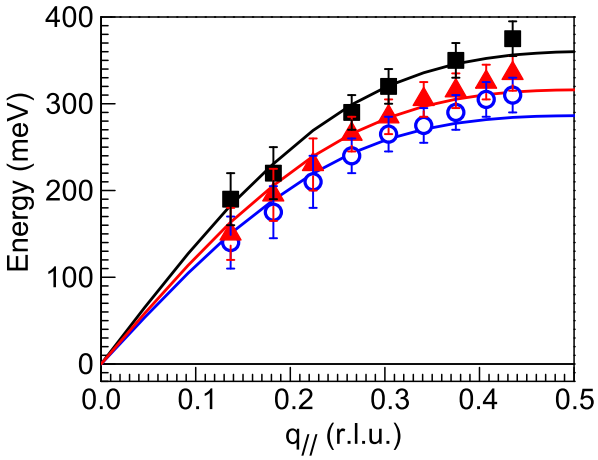

Fig. 4.8: Magnon dispersion determined by RIXS for $CaCuO_2$ (black filled squares) and $(CaCuO_2)_n/(SrTiO_3)_n$ SLs with $n = 2$ (blue open circles), $n = 3$ (red filled triangles) at T=20 K. Solid lines with the same color code represent the relative fittings according to the linear spin wave theory for $\mathbf{q}_{\parallel} \leq 0.375$ (see text for details).

$CaCuO_2$, i.e., the average in-plane magnetic coupling is weakened. However the antiferromagnetic order is not destroyed, also in the case of all CuO_2 layers at the interfaces ($n = 2$). The last fact is remarkable when considering the Mermin-Wagner theorem [118], which states that thermal fluctuations prohibit the existence of long range magnetic order at non-zero temperature in a striclty two-dimensional isotropic system, such as a single CuO_2 plane of a cuprate. Here we have the experimental evidence that adding a second CuO_2 plane is sufficient to establish a magnetic order, probably due to the coupling between the two layers, on a range long enough to allow the measurement of magnon dispersion.

Moreover very recently a RIXS experiment carried out by Mark Dean *et al.* [119] on an other type of SLs have lead to strictly similar results, providing and indepedent confirmation of the possibility to have a Néel-ordered state with just two copper oxide planes. The authors of that work studied insulating heterostructures based on the high-T_c parent compund La_2CuO_4 (LCO) and on $LaAlO_3$ (LAO). In particular they measured RIXS spectra on two $(LCO)_p/(LAO)_p$ SLs with number of u.c. $p = 1$, 2 (see panel (b) of Fig. 4.9) and compared the spectra with those of bulk LCO. Note that, differently from CCO where there is one copper oxide plane per u.c., in the

case of La_2CuO_4, 1 u.c. contains two CuO_2 layers, making their SL with $p = 1$ strictly comparable to our insulating SL with $n = m = 2$. Using RIXS they found that even in LCO layers only a single unit cell thick, a coherent, bulk-like magnon is a reasonable description of the magnetic excitations and this magnon has a dispersion very similar to that of bulk La_2CuO_4 along two directions in the BZ, i.e., from (0,0) to (π/2,0) and (π/2,π/2) respectively. Thus, it is possible to use linear spin wave theory (LSWT), which is based on an ordered Néel state, to describe properly the spin response of a 1 u.c. LCO layer such as that of our CCO/STO SLs. This is feasible despite the fact that the Néel-ordered state is predicted to be suppressed in the limiting case of an isolated two-dimensional Heisenberg antiferromagnet [120].

The dispersions for the two $(LCO)_p/(LAO)_p$ SLs with $p = 1$, 2 and bulk LCO, as extracted from RIXS spectra with the same procedure used by us, are shown, together with inelastic neutron scattering data [50], in Fig. 4.9, which is directly taken from Ref. [119]. Moreover in the figure a calculation based on resonance valence bond (RVB) theory [121] is also reported (dotted line). The authors claim in fact that their results answer the key question whether a 1 u.c. layer of LCO hosts a more RVB-like state, or whether it obeys the expectations of the Heisenberg model with renormalized classical correlations. RVB is a well known theoretical model, proposed by P. W. Anderson in 1987 [91], that attempts to describe high-T_c superconductivity in cuprates. The theory states that in copper oxide lattices, electrons from neighboring Cu atoms interact to form a valence bond, which locks them in place. However, when the system is doped, the same electrons can act as mobile Cooper pairs and are able to superconduct. Since RVB models predict a much lower energy at (π/2,0) than at (π/2,π/2) and in contrast Fig. 4.9(c) shows no such downturn, the results on LCO/LAO SLs strongly support the second scenario of the Heisenberg antiferromagnet. Although we cannot make the same comparison between the dispersions along the two directions for our samples (since we spanned just one direction of the BZ) we note here that also in the case of CCO/STO SLs the dispersion towards (π/2,0) does not show any downturn. As a consequence, we can safely extend the Heisenberg picture also to the case of CCO/STO heterostructures.

Let us now come back to the data collected on our SLs. Since, as seen above, we are dealing with spin waves that can be described properly by LSWT we have fitted the magnon dispersion using this model, as done also by Coldea *et al.* [49, 50] for inelastic neutron scattering data of La_2CuO_4. In that case they interpreted their results (actually covering a broader set of points in the Brillouin zone than what we present here for our samples) including also the higher-order magnetic coupling parameters, besides the nearest neighbor superexchange interaction J, in the Heisenberg Hamilto-

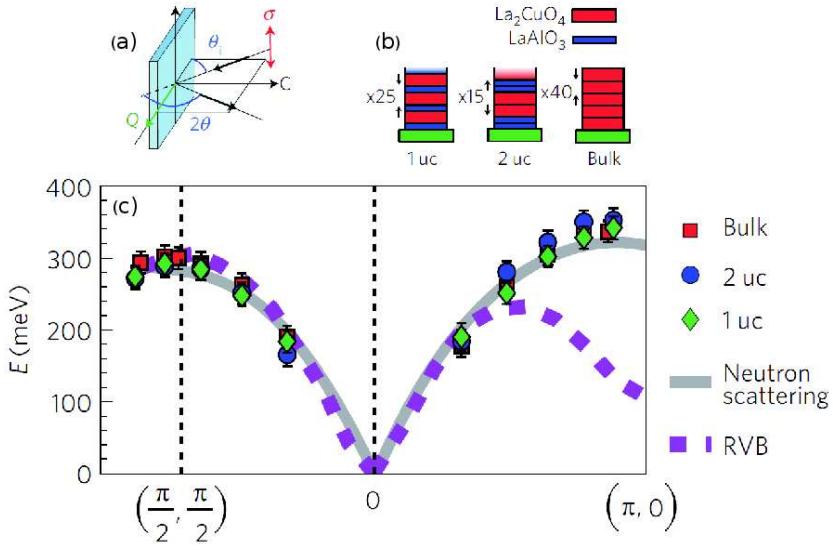

Fig. 4.9: Panel (a) The experimental scattering geometry used by Mark Dean *et al.* similar to the one used for CCO/STO SLs. Differently from us however they used σ-polarized X-rays. Panel (b) The multilayer films studied, composed of 13.2 Å La_2CuO_4 (LCO) layers (red blocks), each containing two CuO_2 planes, and 3.8 Å $LaAlO_3$ (blue blocks). The films are labelled, on the basis of the thickness of LCO, as 1 uc, 2 uc and bulk. The arrows denote the repeat unit of the films ($\times$25, $\times$15, $\times$40) Panel (c) The peak energy dispersion in bulk (red squares), 2 uc (blue circles) and 1 uc LCO (green diamonds). The solid grey line is the result from neutron scattering measurements of bulk LCO [50]; the dotted purple line are calculations for an RVB model. All panels in this figure are taken from Ref. [119].

nian. This is:

$$\mathcal{H} = J \sum_{<i,j>} \mathbf{S}_i \cdot \mathbf{S}_j + J' \sum_{<i,i'>} \mathbf{S}_i \cdot \mathbf{S}_{i'} + J'' \sum_{<i,i''>} \mathbf{S}_i \cdot \mathbf{S}_{i''} + \\ + J_c \sum_{<i,j,k,l>} \{(\mathbf{S}_i \cdot \mathbf{S}_j)(\mathbf{S}_k \cdot \mathbf{S}_l) + (\mathbf{S}_i \cdot \mathbf{S}_l)(\mathbf{S}_k \cdot \mathbf{S}_j) - \\ -(\mathbf{S}_i \cdot \mathbf{S}_k)(\mathbf{S}_j \cdot \mathbf{S}_l)\}, \tag{4.1}$$

In particular J' and J'' are second and third nearest neighbor exchange energies while J_c is the ring exchange interaction coupling for four spins (labeled clockwise) at the corners of a square plaquette. In the 2D reciprocal space indexed by h and l, the dispersion relation is given then by

$$\hbar\omega(h,l) = 2Z_c\sqrt{A_{q_\parallel}^2 + B_{q_\parallel}^2},$$

where $A_{q_\parallel} = J - J_c/2 - (J' - J_c/4)[1 - \nu(h)\nu(l)] - J''\{1 - \frac{1}{2}[\nu(2h) + \nu(2l)]\}$ and $B_{q_\parallel} = (J - J_c/2)\frac{1}{2}[\nu(h) + \nu(l)]$, with $\nu(x) = \cos(\pi x)$. Z_c is a normalization factor that includes the effect of quantum fluctuations. We have maintained the same $Z_c = 1.18$ used in Ref. [49].

In order to reduce arbitrariness, given the restricted nature of our data set, we have decided to reduce the number of the fitting parameters by exploiting the dependence of the magnetic exchanges on the two energy parameters at the basis of the Hubbard Hamiltonian [90]. As already explained in Section 3.3.3, this contains two main contributions: the kinetic term associated to the hopping energy t between nearest-neighbor Cu sites, and the potential energy term that depends on U, i.e. the energy cost for double occupancy on a given site. Given that $J = 4t^2/U - 24t^3/U^3$, $J_c = 80t^4/U^3$, $J' = J'' = 4t^4/U^3$ we could reduce the number of fitting parameters from 4 to 2. Then for each fixed hopping parameter t (chosen in a range of reasonable values), U has been numerically optimized. However we found that the error ($\sim$ 10 meV) is little sensitive to the value of t and all fittings are equally good for 250 meV $\leq t \leq$ 320 meV for the SLs and 300 meV $\leq t \leq$ 360 meV for bulk $CaCuO_2$.

We notice that for all three samples the quality of the fitting gets worse closer to the magnetic Brillouin zone boundary in (1/2,0). This general fact is probably due to the effect of quantum fluctuations, which linear spin wave theory can not catch comprehensively by just introducing the renormalization factor Z_c. We have thus decided to fit only data points for $\mathbf{q}_\parallel \leq 0.375$. Best fittings with this caveat are shown in Fig. 4.8 as solid lines and clearly support the evidence of magnon dispersion also in the case of SLs.

The parameters obtained to fit the data of Fig. 4.8 are summarized in Table 5.1. We notice that t, U and J increase passing from SLs to bulk

Tab. 4.1: Fitting results (in meV) within linear spin wave theory for magnon dispersion as measured on SLs and bulk $CaCuO_2$ by RIXS; they are compared to those given for La_2CuO_4 in Ref. [49]. From t and U obtained by numerical error minimization, the values of nearest neighbor superexchange interaction parameters J, J', J'' and J_c are obtained (see text for details).

	SL(n=2)	SL(n=3)	$CaCuO_2$	La_2CuO_4
U	1970	2720	3010	2200
t	250	320	360	300
J	127	138	157	138
J_c	41	42	49	38
$J' = J''$	2	2	2	2

$CaCuO_2$ but they are always relatively close to the values found for La_2CuO_4. The case of bulk $CaCuO_2$ appears somehow special, with $J = 157$ meV, higher than in La_2CuO_4 (138 meV) [49, 50] and in $Sr_2CuO_2Cl_2$ (130 meV) [6]. In the SLs, although evidently smaller than in the infinite layer, the in-plane magnetic coupling is still very strong, comparable to that of most HTS parent compounds.

4.5 Superconducting SLs: ligand field

The RIXS spectra of the superconducting $(CaCuO_2)_n/(SrTiO_3)_m$ SLs at $\mathbf{q}_{\parallel} = 0.375$ r.l.u. and $T = 20$ K are presented in Fig. 4.10 together with that of bulk $CaCuO_2$, as done before for the insulating samples. They correspond respectively to the SLs with $n = 13$, $m = 2$, $T_c = 12$ K (thick CCO layer); $n = 7$, $m = 2$, $T_c = 16$ K (intermediate CCO layer); $n = 3$, $m = 2$, $T_c = 25$ K (thin CCO layer).

We can see at a glance that there some similarities and some major changes with respect to the case of the non-superconducting SLs. Let us focus first on ligand field and *dd* excitations. The d_{z^2} peak has a trend similar to the one observed in the insulating heterostructures and decreases monotonically as the interfaces are made more dense, i.e. as the number n of CCO u.c. is lowered. As explained in Section 4.3, this effect is the signature of Cu ions with apical oxygens, whose portion with respect to the total number of copper atoms gets smaller as the thickness of the CCO layer gets bigger. Moreover the more n decreases, the higher is the T_c of the sample. This fact is consistent with the idea that the interfaces are working as charge reservoir

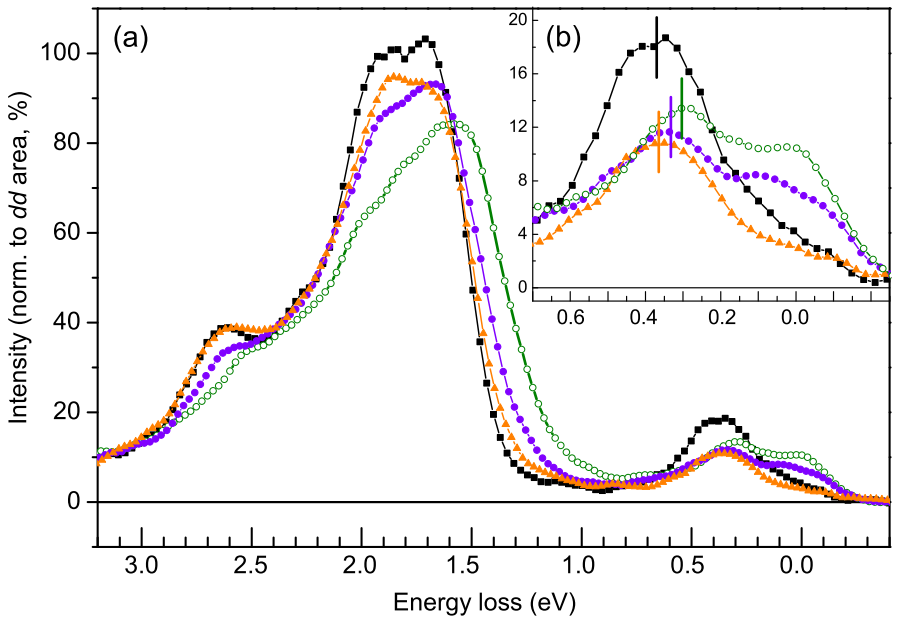

Fig. 4.10: Panel (a) RIXS raw spectra at Cu L_3 edge of bulk $CaCuO_2$ (black filled squares) and $(CaCuO_2)_m/(SrTiO_3)_n$ superconducting SLs with $n = 13$, $m = 2$, $T_c = 12$ K (thick CCO layer, orange filled triangles); $n = 7$, $m = 2$, $T_c = 16$ K (intermediate CCO layer, violet filled circles); $n = 3$, $m = 2$, $T_c = 25$ K (thin CCO layer, open green circles) at $\mathbf{q}_{\parallel} = 0.375$ r.l.u. and $T = 20$ K using π incident polarization. Intensities are normalized to the *dd* area put to 100. Note how the spectral weight of the d_{z^2} peak decreases and moves towards lower energy loss when the number n of CCO u.c. is lowered. Panel (b) Zoom on the low energy excitations region for the same 4 spectra. The vertical solid ticks highlight the shift of the magnon peak when the interfaces are made more dense passing from bulk CCO to the SLs.

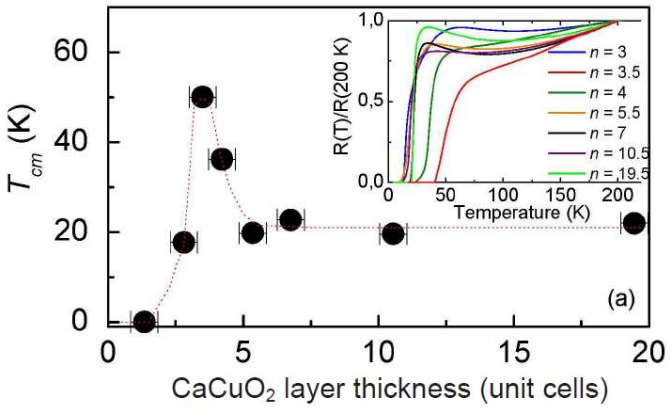

Fig. 4.11: T_{cm}, defined as the midpoint of the resistive transitions shown in the inset, as a function of the number n of CCO unit cells. The number of STO u.c. is kept fixed at $m = 2$. The dotted line is a guide for the eye. Inset: $R(T)$ normalized at $T = 200$ K for the same SLs as in the main panel.

and the apical oxygens gained by Cu ions close to the interfaces are providing the doping holes, which are transferred to the CuO_2 planes, giving rise to superconductivity. Indeed the thicker becomes the CCO layer, the lower the ratio between apical oxygens and Cu ions and the more it is difficult that the doping holes get transferred to the inner copper-oxide planes.

An independent proof of this model comes from the comparison of a series of SLs, produced by our collaborators and not all measured with RIXS, where the number of STO u.c. is kept fixed at $m = 2$ and the number of CCO u.c. is varied from $n = 1.5$ to $n = 20$. We saw that superconductivity shows up when n becomes larger than 2, and T_{cm}, defined as the transition midpoint in the R(T) curves (inset to Fig. 4.11), reaches the maximum value for n between 3 and 4, as shown in Fig. 4.11. For higher values of n, T_{cm} decreases and for $n \geq 5$ remains almost constant up to the thickest sample ($n = 20$). This behavior confirms that superconductivity is confined within few unit cells from the interface.

Furthermore looking at the overall *dd* spectrum it is easy to notice that it gets broader the more n is lowered, i.e. the more the SL is doped. In particular, when the interfaces are made more dense, we observe an increase of spectral weight between 1 and 1.5 eV of energy loss, together with a tendency of the overall shape of the *dd* peak to become more and more triangular. These effects have been already observed in doped cuprates [4] and can be readily explained, at least qualitatively. The spectral weight associated to the extra charges is known to show up around 1 eV of energy loss and above, while the the additional degrees of freedom coming from the doping charges

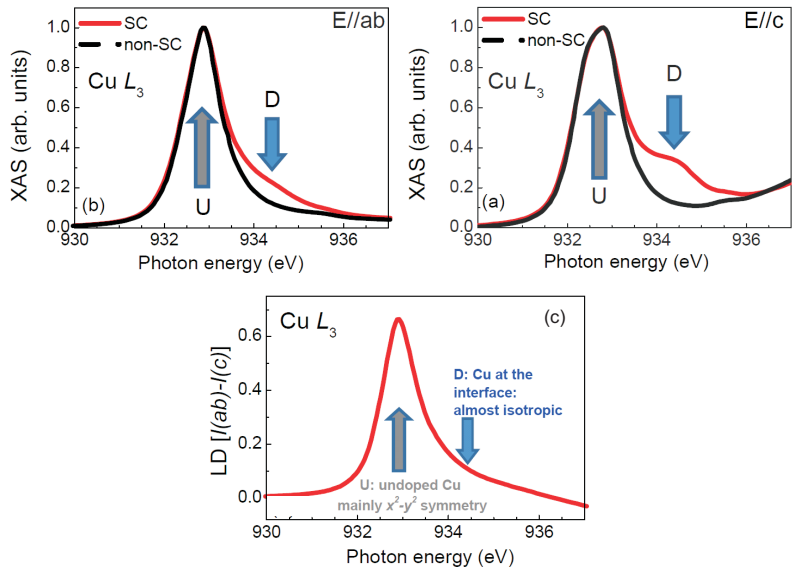

Fig. 4.12: Cu L_3 XAS for superconducting (SC) (full line) and not-superconducting (dashed line) $(CCO)_3/(STO)_2$ SL measured with the electric field of the incident x-rays parallel to the to the ab-plane (E$\|ab$, panel (a)) and to the c-axis (E$\|c$, panel (b)) . All measurements are performed at $T =$ 20 K and the spectra are normalized to the maximum height intensity of the L3 edge. Panel (c): linear dichroism for the SC sample.

are known to further complicate the electronic situation of the system.
As a consequence, the ligand field split $3d$ states that one would observe in the insulating parent compound get closer to each other and mix, similarly to what would happen if one reduces the ligand field and the associated degree of anisotropy that characterize the environment of every Cu ion. The result is a "contraction" of the associated dd peaks that merge together in a single triangle-shaped broad peak, which is common to all doped cuprates. Moreover in the case of these superconducting CCO/STO SLs there is a second contribution that makes dd transition energies closer to each other: indeed the apical oxygens makes more isotropic the surroundings of copper atoms at the interfaces, lowering the ligand field splitting and changing the purely planar oxygen coordination of these Cu ions in a pyramidal one, i.e. closer to spherical symmetry.

Further support to these considerations comes again from absoprtion measurements. We collected XAS spectra at the Cu L_3 edge on the best superconducting SL with with $n = 3$, $m = 2$, $T_c = 25$ K, and on a twin

sample that was not grown in a highly oxidizing atmosphere and therefore is not superconducting. Figs. 4.12(a) and (b) show the XAS spectra taken at the Cu L_3 edge for the two samples normalized so that the intensity of the main peak is 1. We carried out XAS measurements with the electric field of the incident radiation parallel both to the c-axis (E$\|c$) and to the ab-plane (E$\|ab$), by measuring in grazing incidence geometry and using π and σ polarized x-rays, respectively. We use U to indicate the L_3 peak at 932.8 eV, in Fig. 4.12 associated to the transition from the $3d^9$ ground state to a $\underline{c}3d^{10}$ state, where $\underline{c}$ stands for a Cu $2p$ core hole. We assign the U peak to the absorption by an undoped Cu site [104, 122, 123]. The feature about 1.5 eV above the main peak U is instead associated to the absorption by doping holes and to the process $3d^9\ \underline{L} \rightarrow \underline{c}\ 3d^{10}\underline{L}$, where $\underline{L}$ refers to an additional oxygen ligand hole arising from the Cu $3d$ O $2p$ hybridization, mainly with an O $2p$ character [104, 124, 122]. Thus we labelled this feature as D. The major differences between the spectra of superconducting and insulating SL are in the region around D. With both polarizations, this region acquires spectral weight in the case of the superconducting sample. This ia a clear indication of an increased concentration of holes delocalized on the in-plane and out-of-plane O $2p$ bands [104, 122, 123]. We note also that the presence of out-of-plane ligand holes has been already observed in some HTS [125, 126] and the debate about their role in superconductivity is still open.

The clear support to the idea that Cu ions at the interfaces are characterized by a reduced anisotropy actually comes from the linear dichroism (LD) of the features U and D. The XAS LD, showed in Fig. 4.12(c), is defined as the difference between the XAS contributions from the two polarizations: LD = I(E$\|ab$) – I(E$\|c$) and therefore it can be considered as a measure of the anisotropy of the environment around selected ions. In the CCO/STO SLs we can essentially distinguish two distinct Cu sites: i) Cu(1) sites in the CuO_2 planes closest to the STO (interface sites), which can have apical oxygen; ii) Cu(2) sites in all other CuO_2 planes, that are all characterized by a purely planar oxygen coordination. We expect the majority of Cu(1) sites in the doped SL to have an apical oxygen because of the additional oxygen atoms accumulating in the interface planes when the sample is grown in highly oxidizing conditions. Since the c-axis of CCO is about 3.19 Å, we also expect that the out-of-plane Cu(1)-O distance is not much different from the in-plane one, as it has been also shown in some doped CCO samples (where superconductivity was reported and explained by the random insertion of planar defects in the infinite layer structure [127]). For these reasons we can expect to have an isotropic orbital population at Cu(1) sites. Recalling that the main peak U is ascribed to the absorption by undoped Cu sites and the feature D to the absorption by delocalized doping holes, we observe that D

is just weakly anisotropic (low LD). Consistently with our picture we assign D to the doped isotropic Cu(1) sites hybridized with both in-plane (holes with $3d_{x^2-y^2}$ character) and out-of-plane (holes with $3d_{z^2}$ character) oxygen orbitals. On the other hand, the presence in the spectrum of Fig. 4.12(c) of spectral weight with large LD in the region about 1 eV above U, can be ascribed to the absorption by doping holes with in-plane $3d_{x^2-y^2}$ character at the Cu(2) sites, that have purely planar oxygen coordination.

Our picture is thus consistent: when oxygen is added at the interfaces, the doping holes, are mainly confined at the Cu(1) sites that are characterized by a more isotropic pyramidal coordination, with respect to the planar one of Cu(2) sites. As a consequence, the bigger the ratio of Cu(1) sites on the total number of copper atoms, the more the d_z^2 peak decreases and its spectral weight moves towards lower energy loss, while all dd excitations are getting closer in energy and mixed. Although mostly localized at Cu(1) sites the doping holes can get transferred to the neighboring $Cu(2)O_2$ planes, so that they give rise to an interface-driven superconductivity.

4.6 Superconducting SLs: paramagnons

Let us now focus again on Fig. 4.10 and in particular on the zoom of the low energy spectral region in panel (b). We note here that we chose to measure RIXS spectra using again π incident polarization and positive transferred momentum $\mathbf{q}_{\parallel}$, in order to enhance possible magnetic excitation. Similarly to what we observed in the two insulating samples, also the raw spectra of all the superconduting SLs show a magnon peak, slightly damped and monotonically shifted to lower energies for decreasing n, with respect to the magnon peak at 400 meV of bulk $CaCuO_2$. At this point one would like to make the same decomposition of the spectra that has been made for the insulating SLs, in order to isolate the magnetic peak and possibly study its dispersion vs. transferred momentum.

However in the case of the superconducting SLs we find that the magnon peak cannot be considered as a resolution-limited feature, as done for the case of the insulating samples. This fact is exemplified in Fig. 4.13, where we have reported a comparison between the RIXS spectra of bulk CCO, an insulating SL and a superconducting SL, zoomed in the low energy excitations region, after the subtraction of the elastic peak. The spectra have been normalized so to have the same height on the magnon peak and the spectrum of bulk CCO has been also slightly shifted in energy for the sake of clarity. It is clear that full width half maximum (FWHM) of the instrumental resolution (red solid line) used to fit the data of CCO and insulating SLs is not enough large

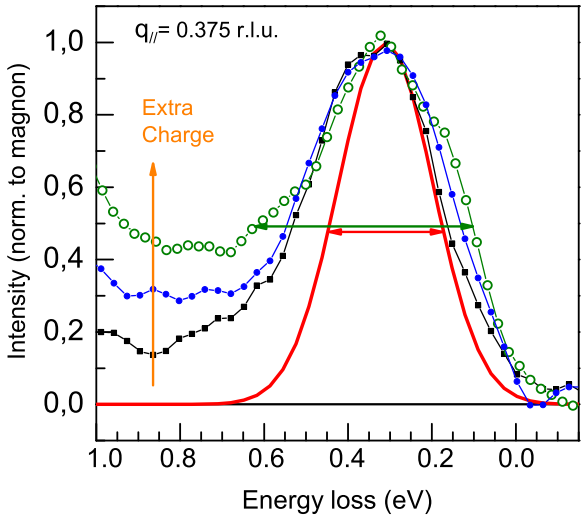

Fig. 4.13: RIXS raw spectra at Cu L_3 edge of bulk $CaCuO_2$ (black filled squares) and $(CaCuO_2)_n/(SrTiO_3)_m$ SLs with $n = 3$, $m = 2$, $T_c = 25$K (open green circles) and $n = m = 2$ insulating (blue filled circles), at $\mathbf{q}_{\parallel} = 0.375$ r.l.u. and $T = 20$ K after the subtraction of the elastic peak (resolution-limited Gaussian). Intensities are normalized so to have the same height on the magnon peak, put equal to 1. The red solid line represent the resolution-limited Gaussian used to decompose the data of CCO and insulating SLs. Note how the FWHM of the low energy peak of the superconducting SL (green horizontal double arrow) is larger than the resolution width, supporting the hypothesis of a damped, broader magnetic excitation, i.e. a paramagnon. Note also the growth of the high energy tail passing from bulk CCO to the doped SL, ascribable to the contribution of extra doping charges.

to allow a proper fit of the magnetic peak for the superconducting sample, even taking into account the contributions of phonons and multimagnons. The magnetic peak indeed is not only damped but also intrinsically broader: this implies that we are dealing with dynamical magnetic fluctuations, i.e. *paramagnons*, similar to the ones observed in $YBa_2Cu_3O_{6+x}$ and described in Chapter 3. This also means that the actual lineshape of the magnetic peak is not precisely known anymore and we have to keep this fact in our mind, whatever kind of fitting we want to use to fit the data. For the sake of simplicity in this case we have decided to use a Gaussian lineshape with a larger FWHM (300 meV) and we have extracted the dispersion, as done for the case of the insulating samples, although with slightly higher uncertainties. The lower resolution, with respect to the one of the results presented in Section 3.3.2 and fitted with Voigt profiles, allows in fact the use of Gaussian lineshapes, without the need to introduce an antisymmetrized Lorentzian to account for the finite lifetime of the magnetic excitations and causality. The Gaussian instrumental width is indeed so large that dominates over the Lorentzian one and it can be safely used to directly fit the paramagnons with good results. In particular we have estimated from a sensitivity analysis that we can assign magnetic peaks with uncertainties in between 30 meV and 40 meV. In particular the closer is the measurement to the Γ point of the BZ, the more difficult it becomes to separate magnetic contributions from the elastic line.

Fig. 4.14 reports magnon dispersions, as extracted from the only two superconducting SLs for which we have measured several spectra at different transferred momenta. They correspond respectively to the heterostructures with $n = 13$, $m = 2$, $T_c = 12$ K (thick CCO layer, orange filled triangles)and $n = 3$, $m = 2$, $T_c = 25$ K (thin CCO layer, green open circles). As said before here we are dealing with paramagnons and therefore the use of linear spin wave theory (LSWT) would not be strictly correct. However with this caveat in mind we can think to compare the dispersions of the superconducting SLs with those of the insulating samples, which are instead describable by LSWT. In particular the solid lines reported in Fig. 4.14 behind the experimental data points are taken from Fig. 4.8 and represent the three fittings based on LSWT that have been done for the two insulating SLs and for bulk CCO. We can see at a glance that, if we restrict ourselves to the region of transferred momentum $\mathbf{q}_{\parallel} \leq 0.375$, for the same reasons mentioned in the Section 4.4, the fittings for bulk CCO and SL with $n = m$=2 are following very well the dispersions of the superconducting SLs with thick and thin CCO layers respectively.

We note here that, also when started from scratch on the two new data sets, the numerical optimizations of U for each fixed hopping parameter t

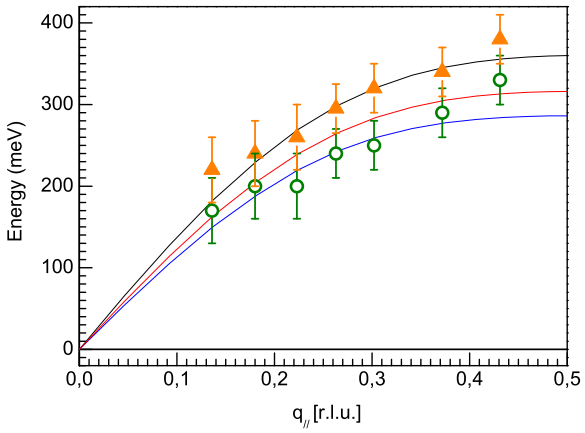

Fig. 4.14: Magnon dispersion determined by RIXS for the superconducting $(CCO)_n/(STO)_m$ SLs with $n = 13$, $m = 2$, $T_c = 12$ K (thick CCO layer, orange filled triangles) and $n = 3$, $m = 2$, $T_c = 25$ K (thin CCO layer, green open circles) at $T = 20$ K. Solid lines are taken from Fig. 4.8 and represent the fittings based on the linear spin wave theory for $\mathbf{q}_{\parallel} \leq 0.375$ (see text for details) relative to the insulating samples (SL $n = m = 2$ in blue, $n = m = 3$ in red and bulk CCO in black).

(see Section 4.4 for fitting details) give the same fittings obtained for the two insulating samples within uncertainties. Despite the above mentioned caveat on the LSWT approach, these results are consistent with the general experimental picture: indeed the sample with 13 u.c. thick blocks of CCO, i.e., 11 out of 13 CuO_2 planes not at the interfaces, can be considered as a bulk with good approximation and, consistently, the paramagnon dispersion is reminescent of that observed in the undoped bulk film. On the other hand the best superconducting SL ($T_c = 25$K) has a dispersion with reduced dynamics. In particular, although it has 3 u.c per block of CCO, it seems to mimic more the trend of the non-superconducting sample with only 2 u.c. per block and all CuO_2 planes close to the interfaces. This could be also due to the fact that when the number n of CCO u.c. becomes small, there are more copper oxide planes at the interfaces and the effect of doping gets more important, affecting both the shape and dispersion of the magnetic peak and the reliability of our Gaussian fittings.

Independently from these considerations the clear message here is that again the average in-plane magnetic coupling is weakened when the interfaces are made more dense, but still the antiferromagnetic order is not destroyed, even in the presence of the alterations introduced in the electronic structure by the presence of the extra doping charges coming from apical oxygens. Moreover if we consider the magnetic coupling parameters obtained from the LSWT fittings of the data for the superconducting SLs ($J = 157$ meV and $J = 127$ meV for $n = 13$ and $n = 3$ respectively) they indicate that the superexchange J is strong enough to support what we have seen in Chapter 3 on $YBa_2Cu_3O_{6+x}$[7] on the possible role of magnetic fluctuations in high temperature superconductors.

4.7 Conclusions

High resolution Cu L_3 RIXS has allowed us to make a univocal assessment on the orbital and magnetic properties of Cu ions in $(CaCuO_2)_n/(SrTiO_3)_m$ superlattices with various periods. For $n = 2$ we can consider that all the Cu ions belong to an interface with the perovskite buffer layer $SrTiO_3$. For $n = 3$ only one third of the Cu ions belong to the genuine infinite layer of $CaCuO_2$ and this ratio grows when the number n of CCO u.c. per block is increased. When the SLs are grown in highly oxidizing conditions they gain more apical oxygens at the interfaces. These oxygens provide the extra charges that are transferred into the nearby CuO_2 planes and make the system superconducting. In conclusion we can highlight two main results.

The first one is brought by the study of *dd* excitations, which are directly

related to the ligand field at Cu sites. In both insulating and superconducting SLs the strong modifications to the chemical environment at the interface leads to a drastic modification of the z^2 $3d$ orbital energy as referred to the $x^2 - y^2$ ground state: the spectral weight at energy 2.65 eV of normal $CaCuO_2$ is decreased monotonically when the number n of CCO u.c. is lowered and moves towards 2.2 eV (or even less) for the $CaCuO_2/SrTiO_3$ interface. The lowering of the z^2 energy can be explained by the presence of apical oxygen at the interface, i.e., a pyramidal coordination of Cu with 5 ligands. We notice that the Cu-O_{apical} distance is likely to be comparable if not shorter than Cu-O_{plane} $\simeq$ 1.92 Å. We have thus the formation of "short" pyramids at the interface, in contrast with the usual elongated pyramidal coordination (Cu-O_{plane} $\simeq$ 1.91-1.94 Å, Cu-O_{apical} $\simeq$ 2.3-2.7 Å) [42] or absence of apical ligand in all bulk HTS. This fact has two important consequences. The hybridization between Cu and O along the c axis is likely to be much stronger than usual, favoring the charge transfer across the interface to the inner cooper oxide planes, and thus opening the opportunity of hole doping $CaCuO_2$ by coupling it to $SrTiO_3$. On the other hand the ground state might not be anymore of almost pure x^2-y^2 symmetry anymore, with possible negative effects on d-wave superconductivity at interfacial CuO_2 planes.

The second result concerns the modifications of the in-plane antiferromagnetic short- and mid range order typical of all HTS cuprats. This 2D magnetic lattice is always associated to spin excitations, whose dispersion we have studied here with RIXS. We have found that spin excitations are present in both insulating and superconducting heterostructures with energy and strength very close to those of bulk $CaCuO_2$. This means that at the interface the modified structural and chemical environment only marginally affects the robustness of the antiferromagnetic order. This fact is all but obvious, especially when considering the SLs with a very small number of CuO_2 planes per $CaCuO_2$ layer, which is separated from the rest of the sample by the magnetically dead $SrTiO_3$. Moreover even when the electronic structure of the system is further complicated by the insertion of extra doping holes, magnetic excitations, which are probably the best candidates as pairing glue in HTS, are still present in the system. This fact is remarkable since it supports what we have found on $YBa_2Cu_3O_{6+x}$ on the role of magnetic fluctuations in HTSs (see Chapter 3).

Finally the results presented in this Chapter are a strong boost for the search of new, artificial HTSs based on cuprate/noncuprate SLs, because they demonstrate that the cuprate layer preserves most of its properties at the interface (in particular magnetism), even when its electronic and charge properties are modified by a different chemical environment.

Chapter 5

Charge fluctuations in the CuO_2 planes of 123 cuprates

The work presented in this Chapter has been published as "*Long-Range Incommensurate Charge Fluctuations in (Y,Nd)$Ba_2Cu_3O_{6+x}$*", by G. Ghiringhelli, M. Le Tacon, M. Minola, S. Blanco-Canosa, C. Mazzoli, N. B. Brookes, G. M. De Luca, A. Frano, D. G. Hawthorn, F. He, T. Loew, M. Moretti Sala, D. C. Peets, M. Salluzzo, E. Schierle, R. Sutarto, G. A. Sawatzky, E. Weschke, B. Keimer, and L. Braicovich, Science **337**, 821 (2012)

In parallel to the observation of magnetic fluctuations described in Chapter 3, working with RIXS on underdoped (Y,Nd)BCO, we found a very strong resonance of the elastic peak around incommensurate wave vectors (0.31,0,L) and (0,0.31,L). Systematic further investigations revealed that this enhancement of the elastic scattering could be the signature of a charge ordering that coexists with the superconducting state. The concept that superconductivity coexists and/or competes with other orders in cuprate superconductors has become increasingly apparent and widely studied in recent years, especially in the case of the so-called "214 cuprates" [with composition $La_{2-x-y}(Sr,Ba)_x(Nd,Eu)_yCuO_4$], whose CuO_2 planes are characterized by charge stripes combined with uniaxially modulated antiferromagnetism. Unfortunately obtaining direct evidence of these ordering phenomena with bulk-sensitive probes is really challenging and so far, despite theoretical predictions and lots of experiments, similar charge orders had never been detected in "123 cuprates", that are the ones with the composition and crystal structure of RBCO (where R stands for Rare Earth).
In this Chapter we show how we have used resonant soft x-ray scattering to

assign the observed elastic resonance to two-dimensional charge fluctuations in the copper-oxide planes of the superconductors (Y,Nd)$Ba_2Cu_3O_{6+x}$, with hole concentrations p of 0.09 to 0.13 per planar Cu ion. Over this entire range of doping, the charge fluctuations have a constant incommensurate periodicity of ∼3.2 lattice units, different from the one observed for static stripes in 214 cuprates and till now considered "universal". Moreover the elusive nature of the incommensurate peak is probably due to the non-static nature of charge fluctuations, impossible to seize by techniques slower than x-ray scattering. The intensity and correlation length of the fluctuation signal increase strongly upon cooling down to the superconducting transition temperature (T_c); further cooling below T_c abruptly reverses the divergence of the charge correlations and the signal starts to die out as superconductivity emerges. As a consequence these data indicate an incipient *charge density wave* instability, that seem to compete with superconductivity.

Contents

5.1 Introduction

As we have already stated, in order to try to understand the mechanism behind HTS one should study first the normal-state from which superconductivity emerges and in particular the pseudo-gap regime, on top of the superconducting dome in the phase diagram of cuprates, and its unusual physical properties [46]. Any successful theory for HTS should in fact require a detailed understanding of all the correlations present in the normal-state of cuprates and related to their spin, orbital and charge degrees of freedom. In recent years, the evidence of ordering phenomena, in which these correlations might assume particularly simple forms, has become more clear [128, 129], but much work remains to be done. Indeed, despite intense efforts,

at the time of writing only two clear ordering phenomena have been reported for cuprates: i) the well-known uniform 2D antiferromagnetism at the basis of magnetic excitations presented in Chapter 3 and ii) a uniaxially modulated antiferromagnetism combined with charge order [130, 131] in the CuO_2 planes of the underdoped 214 cuprates, i.e. compounds of chemical composition $La_{2-x-y}(Sr,Ba)_x(Nd,Eu)_yCuO_4$. In particular the latter evidence is often referred to as "stripe order" and a long-standing debate has evolved around the questions of whether this order is a generic feature of the copper oxides and if stripe fluctuations are essential or counter-productive for superconductivity. Indeed the study of what happens to the charges that are added to the system to make it superconduct could be crucial to get deeper insights in the mechanisms at the origin of the onset of HTS. For these reasons, before to tackle the problem of stripes in the wide family of 123 cuprates [$RBa_2Cu_3O_{6+x}$ with R = Y or another rare earth element], where ordering phenomena have been so far elusive, we will briefly recall what is known about stripe order in the most studied model case of the 214 materials.

5.1.1 214 cuprates and stripes

Back in the 1990s physicists used INS to show for the first time that stripe correlations of spins and holes were a common feature of 214 materials [132, 133, 134, 130, 135], confirming previous theoretical predictions and shedding some light on the long-standing mysteries associated with the anomalous suppression of superconductivity around doping $p = 1/8$ in these compounds [136]. Stripe ordering in fact occurs around this very same doping. In order to understand the reasons behind these phenomena and what happens when doping holes are added to the CuO_2 planes of a 214 system, in the following we make use of the model proposed by J. Lorenzanza and G. Seibold [137, 138].

It can be demonstrated that the compromise between the energy needed to break the superexchange between nearest neighbor Cu ions (each doping hole is a magnetic impurity in the 2D AF lattice) and the Coulomb repulsion between the added holes, makes energetically convenient for the extra charge carriers to arrange themselves in stripes. To evaluate the stability of these stripes one can compute the energy per added hole e_h for N_h holes added to the system with N CuO_2 units. This is defined as $e_h = [E(N + N_h) - E(N)]/N_h$, where $E(N + N_h)$ $[E(N)]$ is the total energy of the doped [undoped AF] solution. If one defines the filling of the stripes $\nu = N_h/(N_s L)$ as the number of added hole per Cu site along a L-long stripe, it can be shown that e_h is always minimized for half filled stripes

($\nu = 0.5$, i.e. 1/2 hole per Cu ion) and that, upon increasing doping, it is more convenient to increase the density of stripes than their filling, as exemplified in Fig. 5.1(a)–(d). Actually it turns out that this is valid only until the stripes get so close to be separated by just 4 lattice parameters. This situation is usually referred to as $d = 4$ stripes, with d dimensionless number indicating the lattice parameters between one stripe and the next. Further doping of $d = 4$ stripes results in higher filling ratios ν, instead of stripes with shorter period d.

Let us focus on this special case of $d = 4$ half filled stripes. There is a superlattice modulation on top of the real space lattice (panel (a) of Fig. 5.2), characterized by a spin periodicity that is twice that of the charge modulation. The positions of the Bravais superlattice are given by $\mathbf{R} = n_1\mathbf{a}_1 + n_2\mathbf{a}_2$ with n_i integer, i.e. the Bravais lattice is generated by combining the elementary translations $\mathbf{a}_1$ and $\mathbf{a}_2$. From these same translation vectors we can obtain the generators $\mathbf{b}_i$ of the reciprocal superlattice, defined by the relation $\mathbf{a}_i \cdot \mathbf{b}_j = 2\pi\delta_{ij}$, and construct the associated magnetic Brillouin zone, reported in Fig. 5.2(b). The black spots in the same figure correspond to the new reflections, induced by the superlattice modulation, that should be seen with a diffraction experiment sensitive to spin ordering, such as INS.

This indeed was the case for neutron-based experiments carried out in the 1990s [132, 133, 134, 130, 135]: instead of finding the typical in-plane reflection, due to bi-dimensional antiferromagnetic order, at $\mathbf{q}^{AF} = (\pi, \pi)$, physicists found incommensurate peaks at a distance δ from (π, π), that were the signature of a uniaxial magnetic ordering in the CuO_2 planes.
More recently, in the last decade, the signature of stripes in 214 compounds was seen also with x-rays [131, 139, 140]. X-ray scattering experiments are sensitive to charge modulations (being x-rays scattered by electrons, rather than nuclei as INS) and, as a consequence, researchers found peaks around Γ at a wavevector that is twice that of INS measurements, given the above cited factor two in the periodicities of charge and spin. These findings confirm the validity of the above presented model of uniaxial spin and charge ordering. Moreover the evolution of stripe density vs. doping described by the model is in excellent agreement with the experimental findings.

Let us define the distance of the INS peak from $\mathbf{q}^{AF}$ in the reciprocal space as *incommensurability* $\delta = 1/(2d)$, inversely proportional to the period d of the stripes in real space. The outcome of INS experiments is that stripes get denser and δ increases linearly with hole concentration p ($\delta(p) = p$) until it is reached the limit situation of $d = 4$ stripes, corresponding to a doping $p = 1/8 = 0.125$. The famous plot by Yamada [135], reported in Fig. 5.1(e), sums up the situation and underlines the criticality of the 1/8 doping, around which is observed the anomalous suppression of superconductivity in

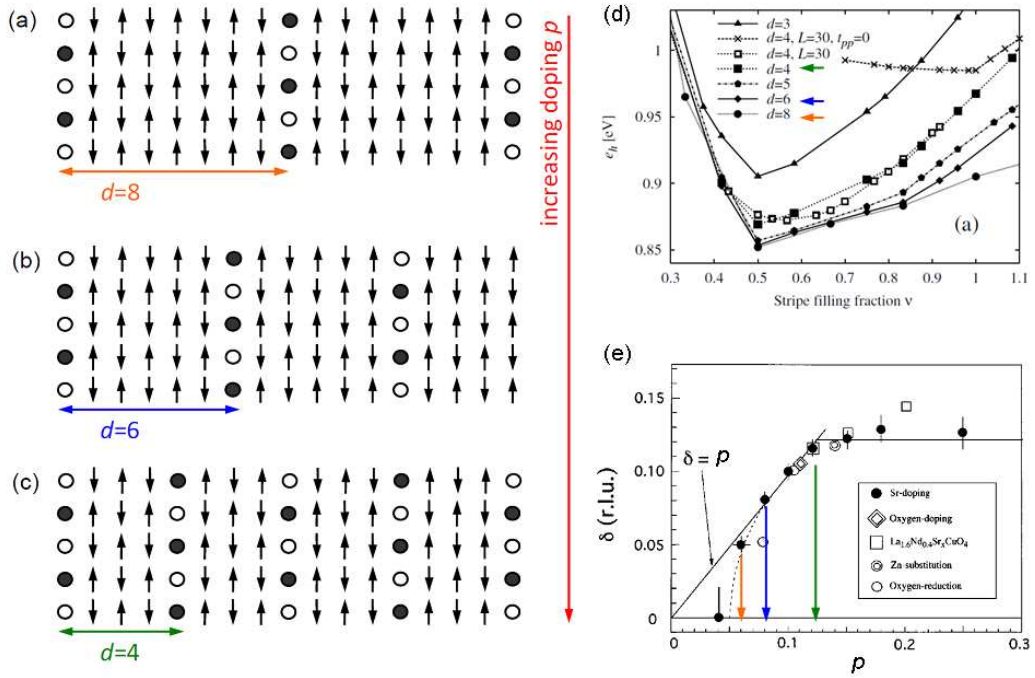

Fig. 5.1: Schematic representation of half filled stripes in a CuO_2 plane of a 214 cuprate, where doping holes (circles) represent magnetic impurities in the 2D AF-ordered lattice of Cu spins (arrows). Filled and empty circles represent the half filling along the stripe (1/2 of the sites is actually doped). As the doping increases, passing from panel (a) to (c), stripes get closer to each other until they reach the limit situation of a 4 lattice units period ($d = 4$, panel (c)). (d) Energy per added hole e_h as a function of the stripe filling ratio ν, as resulting from the calculations made in Ref. [137]. Note that, independently from the period d, the energy is always minimized for half filled stripes ($\nu = 0.5$, 1/2 hole per Cu ion). (e) Doping dependence of the incommensurability $\delta = 1/(2d)$ of the spin fluctuations for different samples, as reported in Ref [135]. The black thin solid line is a guide for the eye, highlighting the linear dependence and the plateau, respectively before and after the critical doping $p = 1/8 = 0.125$. In panels (d) and (e) colored arrows indicate the situations corresponding to panel (a)–(c). For more details see text and Refs. [137, 135].

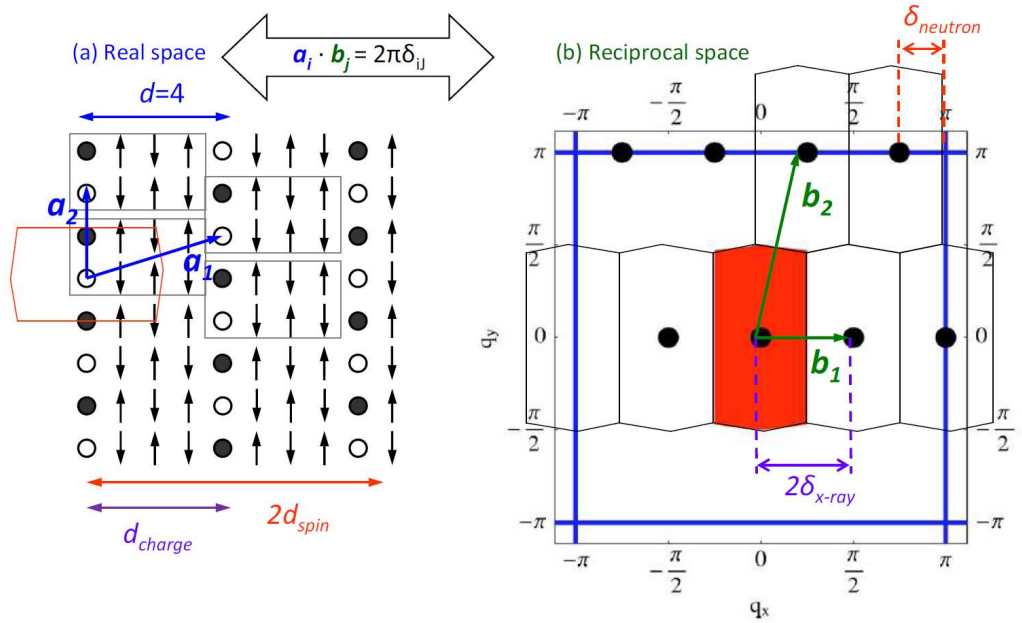

Fig. 5.2: (a) Schematic representation of half filled $d = 4$ stripes for a CuO_2 plane of a 214 cuprate in real space. Note the factor two in the periodicities of spin and charge modulations. (b) Corresponding reciprocal space: the central orange polygon is the first magnetic Brillouin zone for $d = 4$ stripes, constructed starting from the generator vectors $\mathbf{b}_i$. Blue thick lines enclose the extended Brillouin zone (EBZ). The black dots are a set of magnetic reciprocal superlattice vectors that define a set of higher magnetic Brillouin zones with total volume equal to the EBZ volume. Black dots correspond also to the reflections visible with a diffraction experiment sensitive to spin (charge) ordering, such as neutron (x-ray) scattering. Actually in real experiments neutrons can explore regions around $\mathbf{q}^{AF} = (\pi, \pi)$ and x-rays around $\Gamma = (0,0)$.

214 cuprates [136] (See Fig. 5.3(a)). On the other hand incommensurate spin fluctuations with $p \neq 1/8$ [84] have been interpreted as evidence of fluctuating stripes [141].

Further experiments confirmed this overall scenario in 214 materials, giving credit to the universality of the "Yamada plot" and showing that in some cases the stripe order can be stabilized for structural reasons. For example in $La_{2-X}Ba_xCuO_4$ (LBCO) with $x = 0.125$, a low-temperature tetragonal phase appears and stabilizes a static stripe-like order [142], due to the corrugated pattern of the in-plane lattice potential [143], and similar static order has been reported also for $La_{1.6-x}Nd_{0.4}Sr_xCuO_4$ (LNSCO), where the corrugation of the CuO_2 plane is more pronounced, due to the smaller ionic radius of Nd compared to La [130, 144]. Moreover if ones replaces Nd by even smaller Eu ions, in $La_{1.8-x}Eu_{0.2}Sr_xCuO_4$ (LESCO) the magnetic stripe order is so stable that replaces almost completely the superconducting range between $x = 0.08$ and 0.2 [145] (yellow area in Fig. 5.3(a)).

Although the overall phenomenology of stripes in 214 cuprates is quite well known, it must be stressed that a still lasting debate has evolved about the questions of whether this stripe order is a generic feature of the cuprates, and whether stripe fluctuations are essential or counterproductive for superconductivity, and a unified answer is still missing. In this connection physicists looked for similar evidences in other compounds, and in particular in the 123 cuprates, as discussed in the next subsection.

5.1.2 123 cuprates... and stripes?

In the search of a universal presence of stripes in cuprates recent attention has focused on the 123 family, that is well known to exhibit substantially lower chemical disorder and higher maximal T_c than the 214 systems. Physicist have in fact proposed that the anomalous *plateau* around doping $p = 1/8$ in the superconducting dome of 123 cuprates [146] (see Fig. 5.3(b)) could be a signature of stripe order or fluctuations analogous to the ones found in 214 materials [147]. The same argument would hold for the large in-plane anisotropies of the transport properties [148, 149] found in 123 samples.

However, differences in the spin dynamics in the two families of cuprates have cast some doubt on these interpretations. In particular, inelastic neutron scattering studies of underdoped 123 compounds have revealed a gap ≥ 20 meV in the magnetic excitation spectrum [150, 151, 81, 78], whereas 214 compounds with similar hole concentrations exhibit nearly gapless spin excitations [84], as shown in Fig. 5.4. Obviously, to detect the diffraction peak associated with the periodicity of any kind of magnetic ordering, one needs a signal in the elastic scattering channel, i.e. at zero transfer energy in

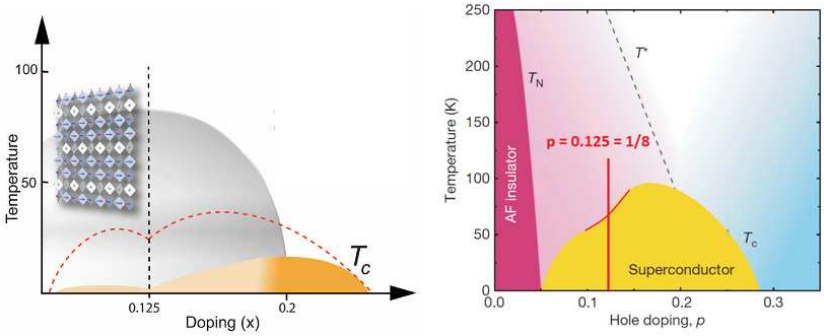

Fig. 5.3: (a) Schematic phase diagram for 214 cuprates, with chemical composition $La_{2-x-y}(Sr,Ba)_x(Nd,Eu)_yCuO_4$. In particular the red dashed curve marks the boundary for the superconducting dome in compounds of the type $La_{2-x}Sr_xCuO_4$, while the yellow area indicate superconductivity quenched at all doping levels (gray area) below 0.2, emerging only at very low temperatures in $La_{1.8-x}Eu_{0.2}Sr_xCuO_4$ (LESCO). At 0.125 doping, a static 1D modulation of charges and spins, the stripe state, emerges in the planes. This stripe phase is stabilized by a structural distortion associated with a corrugation of the CuO_2 planes (see inset) in LESCO. (b) Phase diagram of the 123 cuprates, i.e. $RBa_2Cu_3O_{6+x}$ with R = Y or another rare earth element. Note the different temperature scale and the pit in the superconducting dome around the same critical doping $p = 0.125 = 1/8$ of 214 materials.

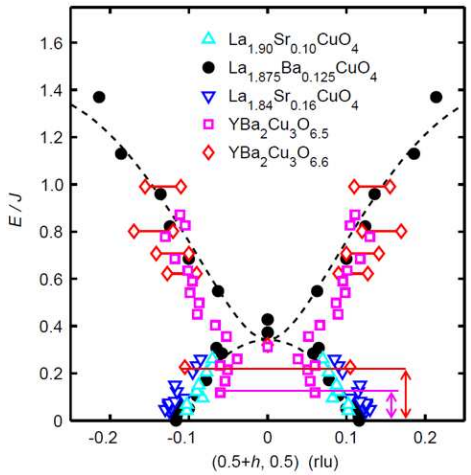

Fig. 5.4: Comparison of measured dispersions around $\mathbf{q}^{AF} = (\pi, \pi) = (0.5$ r.l.u., 0.5 r.l.u.) for 214 and 123 cuprates. Data on 214 materials include $La_{2-x}Sr_xCuO_4$ with $x = 0.10$ (up triangles) and 0.16 (down triangles) from Christensen *et al.* [152], and $La_{1.875}Ba_{0.125}CuO_4$ (filled circles) from Ref. [153]. For 123 cuprates, data on $YBa_2Cu_3O_{6+x}$ with $x = 0.5$ (squares) from Stock *et al.* [81] and 0.6 (diamonds) from Hayden *et al.* [85] are shown. The energy has been scaled by the superexchange energy J for the appropriate parent insulator. The doubled symbols with bars indicate two different ways of interpolating the results. Note that, while for 214 materials the dispersions approach the zero energy line, giving incommensurate elastic peaks around $\mathbf{q}^{AF}$, due to uniaxial spin ordering, the data of 123 cuprates show a gap (vertical double arrows with the same color code). Figure reproduced from Ref. [48].

the INS spectra, as it happens for 214 compounds. If the magnetic spectrum shows a gap, as in 123 cuprates, there is no elastic signal at all so that it becomes legitimate to ask: how could it be possible to have a spin ordering, if no elastic peak related due to its periodicity can be detected? Although this argument could actually rule out the presence of magnetic stripes, it does not impose any limitations to the existence of charge ordering.

In this connection further questions have been raised by some recent experiments on 123 cuprates immersed in a magnetic field large enough to weaken or obliterate superconductivity. In quantum oscillation experiments on underdoped 123 compounds N. Doiron-Leyraud *et al.* [154] have in fact discovered some small Fermi pockets, that other researchers have attributed to a Fermi surface reconstruction due to a magnetic field-induced stripe order [147]. Although some physicists have argued that even the high magnetic

fields applied in these experiments cannot be capable of closing the spin gap, still a biaxial *charge* ordering could explain well the quantum oscillation data [155]. On top of these facts recent nuclear magnetic resonance (NMR) experiments on $YBa_2Cu_3O_{6.5}$ have shown evidence of a magnetic field-induced uniaxial charge modulation [156]. However the NMR measurements do not provide any information about electronic fluctuations outside a very narrow energy range of ~ 1 μeV. On the other hand, scattering experiments to determine the periodicity of this modulation and/or to characterize its dynamics are currently hardly performable, at least under the extreme experimental conditions required to stabilize a high-magnetic-field phase.

Obviously, if charge ordering is present also in the absence of a magnetic field and/or spin ordering, its signatures should be visible in x-ray scattering experiments (as mentioned in the previous Subsection), but actually their detection turned out to be really challenging for a series of reasons, which will become more clear later on in this Chapter and partly have been already discussed in Section 2.3.3. As a consequence, despite theoretical predictions and several experimental trials, only null results have been reported so far [36] and both the nature of the leading electronic instability of doped 123 materials and its relation to superconductivity and stripe order remain largely unknown.

In the following we show how we have used resonant soft x-ray scattering to assess these issues and identify two-dimensional charge fluctuations in the CuO_2 planes of the superconductors (Y,Nd)$Ba_2Cu_3O_{6+x}$, with hole concentrations per planar Cu ion in the range $0.09 \leq p \leq 0.13$. The intensity and correlation length of the signal increase strongly upon cooling down to the superconducting transition temperature (T_c), while further cooling below T_c abruptly reverses the divergence of the charge correlations. In combination with the above cited observations of a large spin gap in these compounds, these data indicate an incipient *charge density wave* (CDW) instability, that seems to compete with superconductivity, and, for the first time, we have the evidence that the anomalously low T_c found in underdoped cuprates is likely due to CDW, and not other phenomena.

5.2 Experimental

The resonant soft x-ray scattering measurements presented in the following Sections have been carried out on both thin films and millimeter-sized single crystals of $Nd_{1+x}Ba_{2-x}Cu_3O_7$ (NdBCO) and $YBa_2Cu_3O_{6+x}$ (YBCO), all belonging to the 123 family of cuprates. Tab. 5.1 lists chemical formulas, lattice parameters, superconducting transition temperatures and hole concentration

Tab. 5.1: Composition, lattice parameters (a, b, c), transition temperature (T_c) and doping (p holes per planar Cu2 atom) of the systems investigated in the search of charge density wave.

Sample	a (Å)	b (Å)	c (Å)	T_c (K)	p
$YBa_2Cu_3O_{6.35}$	3.845	3.871	11.781	10	0.06
$YBa_2Cu_3O_{6.45}$	3.839	3.875	11.761	35	0.08
$Nd_{1.2}Ba_{1.8}Cu_3O_7$ (50 nm)	3.905	3.905	11.7	56	0.09
$YBa_2Cu_3O_{6.5}$	3.829	3.875	11.731	60	0.11
$Nd_{1.2}Ba_{1.8}Cu_3O_7$ (100 nm)	3.885	3.92	11.7	65	0.11
$YBa_2Cu_3O_{6.6}$	3.82	3.87	11.7	61	0.12
$YBa_2Cu_3O_{6.7}$	3.826	3.880	11.709	69	0.13
$YBa_2Cu_4O_8$	3.84	3.87	27.25	80	0.14
$YBa_2Cu_3O_7$ (100 nm)	3.82	3.88	11.68	91	0.16
$NdBa_2Cu_3O_7$ (100 nm)	3.86	3.92	11.74	92	0.16
$YBa_2Cu_3O_7$	3.817	3.884	11.681	90	0.17
$Y_{0.85}Ca_{0.15}Ba_2Cu_3O_7$	3.89	3.88	11.695	75	0.21

per planar Cu ion of all the investigated samples, in order of increasing doping. Details of the samples type, growth and characterization have been already described in Section 3.3.1. In addition to the processes listed there, YBCO single crystals were also polished in air to obtain a flat and shiny (001) surface. All NdBCO samples are thin films but for this experiment we had also a thin film of YBCO. More in detail $Nd_{1.2}Ba_{1.8}Cu_3O_7$ films of thickness 50 nm and 100 nm and NdBa2Cu_3O_7 and YBa2Cu_3O_7 films of thickness 100 nm were deposited on $SrTiO_3$ (100) substrates. In the former two cases the underdoping is determined by the 1.2/1.8 ratio in the Nd to Ba relative contents. However the two effective doping levels and different T_c are a consequence of the different film thickness, as explained in Ref. [73]. The optimally doped films were instead thick enough to neglect the influence of the substrate, that forces the thinner films to grow pseudo-tetragonally. All films had an area of approximatively 5×5 mm^2. The oxygen content and the hole concentration p were determined from the known doping dependence of the out-of-plane lattice parameter c and of T_c, according to the relations described in Ref. [146]. For all samples, XAS and resonant x-ray scattering measurements were performed without any in-vacuum surface preparation.

As it will be detailed in the next Sections we found a very strong resonance of the elastic peak around incommensurate wave vectors (0.31,0,L) and (0,0.31,L) in the RIXS spectra of some of the above listed samples. In

order to further investigate this finding we used a combination of resonant elastic and inelastic x-ray scattering measurements, conventional RXS and RIXS respectively. Given that this resonance is a modulation of the intensity of the elastic peak in fact it can be equivalently studied by using either RIXS, and looking at the elastic channel of scattering, or RXS, that is resonant or anomalous diffraction. More in detail this can be done but one has to keep in mind some caveats: indeed, although these two scattering techniques are very similar, RIXS measurements are energy-resolved, while RXS measurements are energy-integrated. As a consequence in RIXS one can discriminate between the elastic (or quasi-elastic) signal coming from charge density fluctuations and the dominant inelastic contribution with a sensitivity on the elastic that is roughly one order of magnitude higher than that of conventional RXS experiments. These however provide more flexibility on angles and the possibility of faster scans vs. momentum transfer with respect to RIXS (see Section 2.3.3 for more details).

The energy-resolved (RIXS) measurements were performed both at the ADRESS beamline of the Swiss Light Source (Paul Scherrer Institute, Switzerland), using the SAXES spectrometer, and at the ID08 beamline of the European Synchrotron Radiation Facility (ESRF, Grenoble, France), using the AXES spectrometer. On the other hand the energy-integrated RXS measurements were performed at the UE46-PGM1 beamline of the Bessy-II storage ring (Helmholtz-Zentrum Berlin, Germany) using the XUV diffractometer. All these instruments, and the differences among them, have been already described in detail in Chapter 2.

The use of photons with energies resonant to the Cu L_3 edge greatly enhances the sensitivity of the scattering signal to the valence electron system, differently from non-resonant x-ray scattering, in which the ordering of the charges could be monitored only indirectly by the associated lattice distortion. In particular the resonant conditions were always achieved by tuning the energy of the incident x-ray to the maximum of the Cu L_3 absorption peak, around 931.5 eV. At that energy the absorption takes place mainly at the planar Cu2 sites of (Y,Nd)BCO with $3d^9$ electronic configuration (see Fig. 5.5(a)). Although a contribution from Cu1 sites in the chain layer is also present around the same photon energy, as demonstrated in Ref. [36], we can neglect it because its polarization dependence in the RXS process is expected to be different from the one that we found. This will be better explained in the following Section, using also XAS spectra recorded at the ID08 beamline of the ESRF with the fast scanning Dragon monochromator.

For all RXS measurements presented, unless otherwise stated, the scattering geometry is the standard one already presented in the Section 2.3 and reported here in Fig. 5.5(b). While keeping the scattering angle (2θ) fixed,

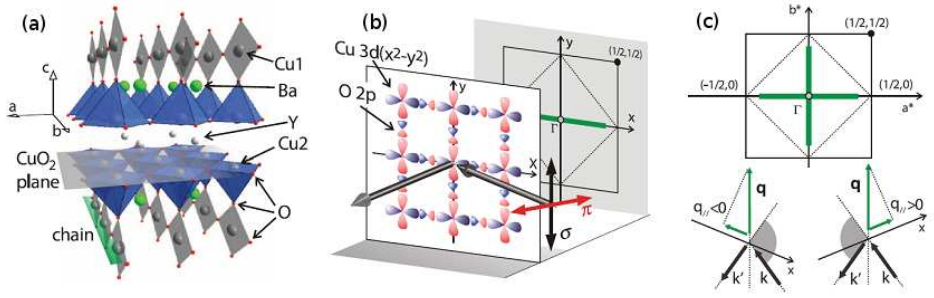

Fig. 5.5: (a) Crystalline structure of (Y,Nd)BCO superconductors, reproduced from Fig. 3.7. (b) Scattering geometry with the c and either a or b axes in the scattering plane. The incoming photon polarization is either parallel (π) or perpendicular (σ) to the scattering plane. The real and reciprocal spaces are sketched in the front and rear plane, respectively. In the real-space image, the Cu $3d_{x^2-y^2}$ and O $2p$ orbitals are shown. In the reciprocal-space image, the nuclear and magnetic first Brillouin zones are drawn with solid and dotted lines, respectively; the thick green line indicates the range covered by the experiments. Γ labels the (0,0) point, origin of the reciprocal space and center of the first Brillouin zone. (c) The in-plane momentum transfer $\mathbf{q}_{\parallel}$ ranges from 0.4 to +0.4 r.l.u. along the (1,0) or (0,1) direction when the sample is rotated around the y axis at a fixed scattering angle, indicated by the gray arcs (2θ).

the sample is turned around the y axis, perpendicular to the scattering plane, thus changing the projection $\mathbf{q}_{\parallel}$ of the transferred momentum $\mathbf{q}$ onto the direction x parallel to the CuO_2 plane. At 931.5 eV photon energy the total momentum transfer is $\mathbf{q} = 0.944 sin\theta$ Å^{-1}.
In the energy-resolved RIXS experiments $2\theta = 130°$, giving $\mathbf{q} = 0.855$ Å^{-1}, which allows one to cover about $\sim 85\%$ of the first Brillouin zone along the [100] direction (see green lines in Fig. 5.5). The total instrumental energy resolution for RIXS was about 130 meV with SAXES and 250 meV with AXES, both experimentally determined on a non-resonant elastic scattering spectrum of polycrystalline graphite. Each RIXS spectrum was measured for 5 minutes typically. In some cases with low signal we increased the statistics by accumulating for 10 minutes or more.
In the energy-integrated RXS experiments $2\theta = 154°$, $\mathbf{q} = 0.919$ Å^{-1}, $\mathbf{q}_{\parallel,max} = 0.44$ r.l.u..

Hereafter momentum transfers are given in reciprocal lattice units (r.l.u.), that is, in units of the reciprocal lattice vectors a^*, b^* and c^* where $a^* = 2\pi/a$, $b^* = 2\pi/b$, and $c^* = 2\pi/c$ (see Tab. 5.1 for the values of a, b, and c for each sample). The momentum resolution was ≤ 0.005 r.l.u. in all measurements. The conventional sign of $\mathbf{q}_{\parallel}$ is shown in Fig. 5.5(c): $\mathbf{q}_{\parallel} < 0$ ($\mathbf{q}_{\parallel} > 0$) for grazing incidence onto (emission from) the (001) surface.
In all experimental setups, the alignment of the crystallographic c axis to the scattering plane was made when mounting the sample to the holder, with no possibility of further adjustment in vacuum. This might lead to small inaccuracies when comparing measurements on different samples or along a^* and b^*.

5.3 Charge Density Waves

The observation at the basis of the investigations presented hereafter is clearly evident in the raw spectra of underdoped $Nd_{1+x}Ba_{2-x}Cu_3O_7$, shown in Fig. 5.6 as a function of both photon energy loss and $\mathbf{q}_{\parallel}$ along the horizontal direction (1,0) of the 2D Brillouin Zone, i.e. parallel to the Cu-O bonds in the CuO_2 planes. The inelastic portion of the spectrum comprises features around 100 to 300 meV, resulting from paramagnon excitations, and from 1 to 3 eV, due to dd excitations. These features depend weakly on $\mathbf{q}_{\parallel}$, whereas the response centered at zero energy loss exhibits a pronounced maximum around $\mathbf{q}_{\parallel} = (\pm 0.3,0)$. Scans around symmetry equivalent reciprocal-space points (see green lines in Fig. 5.5) on multiple NdBCO and YBCO samples (listed in the previous Section) have confirmed that the latter feature is generic to the 123 system and that its intensity maximum is at a wave vector

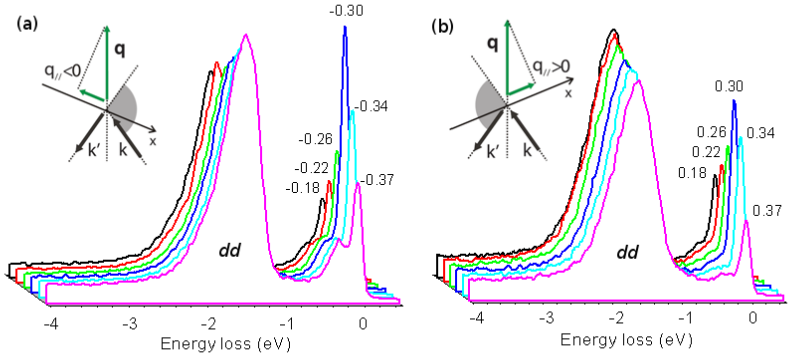

Fig. 5.6: Cu L_3 energy-resolved RIXS spectra of underdoped $Nd_{1.2}Ba_{1.8}Cu_3O_7$ (T_c = 65 K, T = 15 K, σ polarization) for $\mathbf{q}_{\|} < 0$ (a) and > 0 (b), showing that the quasi-elastic component has a maximum intensity around $\mathbf{q}_{\|} = \pm$ 0.3 r.l.u.. The dispersing paramagnons are visible next to the quasi-elastic peak while *dd* excitations around 2 eV carry most of the spectral weight.

distinctly different from the commensurate position (1/3,0). More in detail careful scans vs. momentum transfer assign the peak to the incommensurate in-plane wavevectors (0.31,0) and (0,0.31).

As another example, in Fig. 5.7 we have plotted the raw RIXS intensity for the $YBa_2Cu_3O_{6.6}$ sample for three different momentum transfers: $\mathbf{q}_{\|}$ = 0.31 r.l.u. (on the resonant peak) and $\mathbf{q}_{\|}$ = 0.28 r.l.u. and 0.35 r.l.u. (away from it). The differences between the former and each of the latter spectra are displayed in panels (b) and (c). These three spectra were measured at $T \sim T_c$ = 61 K, where the signal is maximal. We will return later on the temperature dependence of the signal. Despite the limited energy resolution, we can safely place an upper bound of about 20 meV for the energy of the resonant contribution.

In the following we will refer to this feature as a resonant elastic x-ray scattering (REXS) peak, although, as shown below, it arises from low-energy fluctuations of the valence-electron charge density in the CuO_2 planes and, hence, is not strictly elastic. We also note here that, in order to evaluate the evolution of this (quasi)elastic intensity in RIXS spectra presented hereafter, we have fitted the zero-energy-loss feature with a Gaussian peak of width not exceeding 1.3 times the instrumental energy width, so to take into account

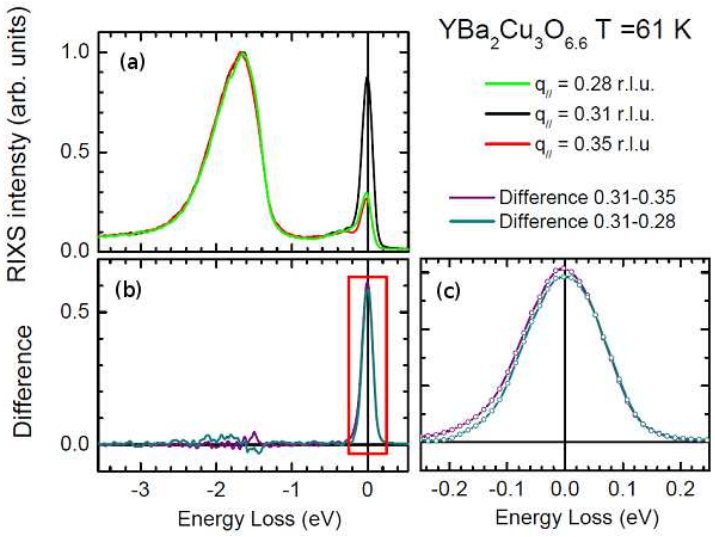

Fig. 5.7: (a) RIXS intensity at $\mathbf{q}_{\parallel} = 0.28$, 0.31 and 0.35 r.l.u. for the $YBa_2Cu_3O_{6.6}$ sample at $T \sim T_c = 61$ K. (b) Difference between the spectra measured at $\mathbf{q}_{\parallel} = 0.31$ and 0.28 r.l.u., and $\mathbf{q}_{\parallel} = 0{:}31$ and 0.35 r.l.u.. (c) Zoom on the low energy region of panel (b).

possible fluctuations of the energy resolution and uncertainties related to the count statistics. Then, to allow safe comparisons between different spectra and different samples, we have normalized this elastic intensity to the integral of the RIXS spectrum between 0 and 20 eV energy loss. Hereafter, unless otherwise stated, all results showing the intensity of the REXS peak come from energy-resolved measurements and have been treated in this way.

As shown in Fig. 5.5 the 123 crystal structure contains copper atoms in two different crystallographic sites: i) Cu2 atoms in the CuO_2 planes that are common to all high temperature cuprate superconductors and ii) Cu1 atoms in chains specific to the 123 system, that act as charge reservoirs with a doping capacity depending on their oxygen filling. Moreover empty and filled chains can be ordered in such a way to produce a pattern and usually samples showing this property are referred to as ortho-P, where P is a Roman numeral indicating the period of the superstructure. So, for example, in an ortho-VIII ordered YBCO, chains are ordered in a 11011010 pattern with a period of 8 lattice units (1 and 0 indicate filled and empty chains, i.e. the presence or absence of intercalated oxygen in a given chain). For these reasons it is crucial to distinguish between the copper in the chains and in the planes: in fact, if the REXS peak that we see arises from a charge modulation, one has to understand if this modulation is in the CuO_2 planes or it is related to some charge ordering in the chains. Luckily in x-ray absorp-

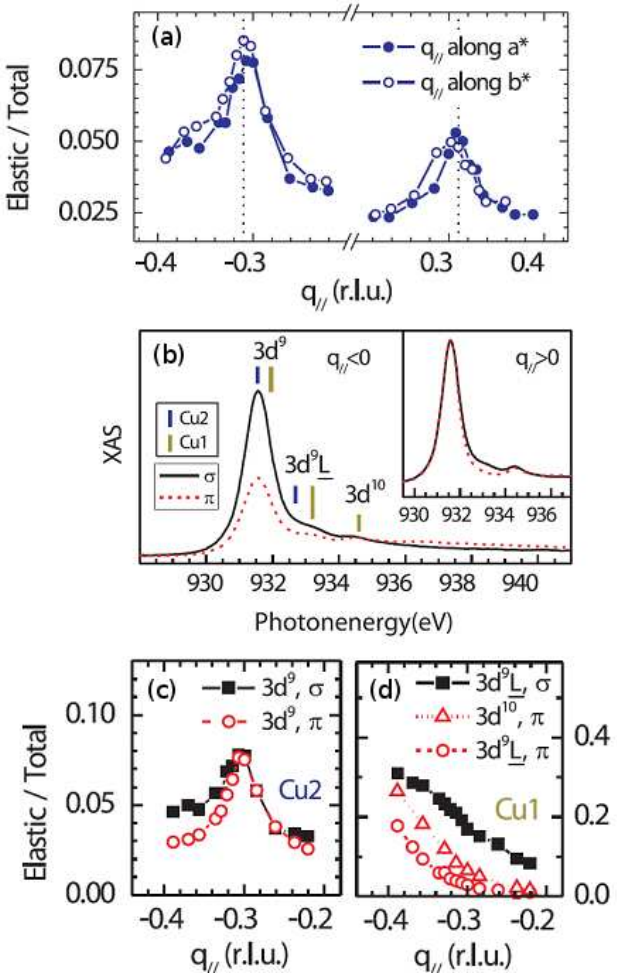

Fig. 5.8: (a) REXS scans measured at the Cu L_3 edge for positive and negative values of $\mathbf{q}_{\|}$ along (1,0) and (0,1), using σ polarization. (b) XAS spectra of $YBa_2Cu_3O_{6.6}$ with two polarizations and two geometries corresponding to negative and positive values of $\mathbf{q}_{\|}$, i.e. grazing and normal incidence respectively. The main contributions to the XAS peaks are indicated. RXS with photon energies at the main absorption peak of 931.5 eV selects signals arising from the Cu2 sites. (c)–(d) REXS scans show the REXS peak only when exciting at the Cu2 sites and show nothing but monotonic trends at higher excitation energies.

tion (XAS) and RXS experiments, signals arising from Cu1 and Cu2 sites can be differentiated by virtue of their distinct absorption resonance energy and photon polarization dependence, as it is shown in Fig. 5.8(b). Once that XAS features are safely assigned to the different crystallographic sites of copper, one can choose the site to excite in a selective way, by tuning the incoming photon energy at the corresponding XAS feature. More in detail we have found that the anomalous REXS peak is present only when the photon energy is tuned to the $3d^9$ configuration of Cu2 sites, as displayed in Fig. 5.8(c) and (d). Therefore the resonant peak can be unambiguously assigned to the copper in the CuO_2 planes.
Further confirmation for this assignment comes from a comparison of $\mathbf{q}_{\parallel}$ scans along the (0,1) and (1,0) directions (parallel and perpendicular to the chains, respectively) in untwinned $YBa_2Cu_3O_{6.6}$ crystals (Fig. 5.8(a)). In fact the presence of equally intense REXS peaks in the two directions is totally incompatible with a possible origin of the signal in the Cu1 chains, that in the untwinned samples are aligned along only one direction.

Having established that the REXS peak arises from an ordering in the planes, we now have to understand if it is due to a modulation of the charge or of the spin density in the CuO_2 layers. To tackle this issue we exploit the dependence of the RXS cross section on the polarization geometry. In particular, in order to separate the two possible scattering channels, we have measured the scattering intensity for σ (Fig. 5.8(a)) and π polarization of the incident beam and for the two opposite directions of $\mathbf{q}_{\parallel}$ along (1,0) and we have compared the RIXS results to model calculations for spin-flip and non-spin-flip RXS from Cu2 sites with $3d^9$ configuration, computed as explained in Ref. [3].

More in detail the non-spin-flip cross sections can be multiplied by the structure factor for a 2D antiferromagnetic lattice to obtain the RIXS intensities from spin waves [5] of parent compounds. The atomic cross sections have been calculated for a ground state with $(x^2-y^2)^{\downarrow}$ single hole symmetry and $(x^2-y^2)^{\downarrow}$ and $(x^2-y^2)^{\uparrow}$ final states, for the charge and spin-flip scattering channel respectively. The spin is assumed to be oriented along the (110) direction. In case of spin fluctuations bringing the spin to point in different directions, the results would not be very different: both channels in fact depend only on the angle θ_s between the spin and the c axis and not on the in-plane spin direction. In explicit we have:

$$\frac{I_{\pi}^{charge}}{I_{\sigma}^{charge}} = \frac{[4sin^2(\delta-\theta)+cos^2\theta_s]sin^2(\delta+\theta)}{4+cos^2\theta_s sin^2(\delta-\theta)}, \tag{5.1}$$

$$\frac{I_{\pi}^{spin}}{I_{\sigma}^{spin}} = \frac{sin^2(\delta+\theta)}{sin^2(\delta-\theta)}, \tag{5.2}$$

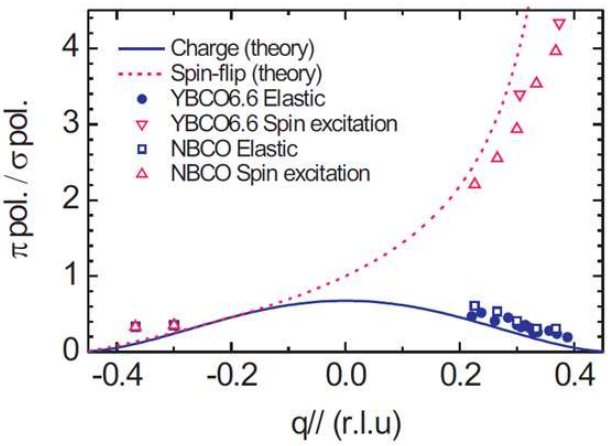

Fig. 5.9: Ratio between the REXS signal intensities obtained with π and σ polarizations. The experimental data of elastic and magnetic excitation signal (100- to 300-meV energy loss) for $YBa_2Cu_3O_{6.6}$ and $Nd_{1.2}Ba_{1.8}Cu_3O_7$ are compared to the model calculations (see text for details).

where δ is the angle between the c axis and $\mathbf{q}$ and θ is 1/2 of the scattering angle 2θ. In particular in Fig. 5.9 we report the π/σ ratios, in which the structure factor cancels out [17], because it is the same for the two incident polarizations for each final state. In this way we do not need to make any assumptions about the scattering structure factor, when trying to determine whether a given feature originates from spin or charge scattering.

Fig. 5.9 shows that, while the paramagnon feature around $\sim$ 200 meV follows the behavior expected for spin-flip scattering, already observed in cuprates (see Chapter 3), the polarization dependence of the REXS peak is that typical of charge scattering, confirming that we are dealing with a *charge* modulation in the CuO_2planes.

We now try to understand if this modulation is just in the planes and bidimensional or there is also some out-of-plane correlation. To do this we have used the diffractometer and measured the scattering map in the (a^*,c^*) plane of some samples showing the REXS peak, as for the case of $Nd_{1.2}Ba_{1.8}Cu_3O_7$ (T_c = 65 K) displayed in Fig. 5.10. The map confirms that there is little or no dependence of the scattering cross section along the c^* direction, as there is just a vertical rod, at least in the accessible region of the reciprocal space. Obviously we can not rule out short-range correlations extending over 1–2 unit cells along the c-axis. However this finding is a strong indication that the charge modulation has a substantial bidimensional nature. Moreover the comparison of energy-resolved data at scattering angle $2\theta = 130°$ with the energy-integrated data in the same conditions but $2\theta = 154°$ indicates that

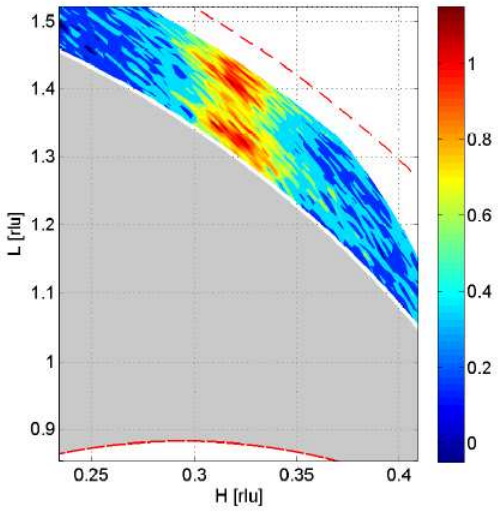

Fig. 5.10: Color map of the scattering intensity in the (a^*,c^*) plane measured at $T = 15$ K in the energy-integrated mode for $Nd_{1.2}Ba_{1.8}Cu_3O_7$, $T_c = 65$ K. A non constant background, equal to the intensity at 200 K, has been subtracted. The intensity is only weakly modulated along c^* (L index), and the maximum is at constant a^*, i.e. H, value, indicating that the charge modulation has intrinsic 2D nature. Hence $\mathbf{q}_{\|}$ is the meaningful wave vector in this experiment. The red dashed lines indicate the limits set by the maximum value of $\mathbf{q}$ (for $2\theta = 180°$ and the Bragg geometry limit for a (001) oriented surface, for photons of 931 eV energy). Actually the meaningful data collection region is set by the signal to noise ratio, drastically decreasing when moving away from backscattering geometry: the grey area indicates a severe diffuse contamination region for this specific sample, corresponding to $2\theta \leq 130°$.

the REXS peak is found at exactly the same in-plane momentum transfer $\mathbf{q}_{\parallel}$ [at wavevectors (0.31,0,1.29) and (0.31,0,1.44) respectively], irrespective of the different value of the momentum perpendicular to the CuO_2 planes. This fact confirms the intrinsic bidimensionality of the ordering phenomenon.

To sum up we have observed a resonating quasi-elastic superstructure peak, due to a bidimensional modulation of the valence charges of Cu atoms in the CuO_2 planes. This *charge density wave* (CDW) is generic to the 123 family of cuprates, so that it is worthy to study its evolution versus doping, as done in the next Subsection.

5.3.1 Doping dependence of CDW

Fig. 5.11 provides an overview of the REXS response in several 123 samples, namely the ones listed in Tab. 5.1. These include both single crystals of $YBa_2Cu_3O_{6+x}$, where the doping level p is adjusted through the density and arrangement of oxygen atoms in the Cu1 chain layer, and thin films of $Nd_{1+x}Ba_{2-x}Cu_3O_7$, where the Cu1 chains are fully oxygenated and p is controlled through the Nd/Ba ratio. The presence of closely similar charge-fluctuation peaks at $\mid \mathbf{q}_{\parallel} \mid = 0.31$ r.l.u. in all systems, in the range $0.09 \leq p \leq 0.13$, confirms that they are totally independent of the Cu1 chains and other details related to the doping mechanism and the sample type (film or crystal). Moreover the CDW peak position is constant for varying p, at least within experimental uncertainties, although its intensity is maximum at $p = 0.11$.

Samples outside this narrow p range do not show any evidence of the anomalous REXS response, in agreement with earlier RXS work [36]. This implies either an absence or much weaker charge fluctuations in samples at lower p, where some incommensurate magnetic order has been observed at low temperatures [157], and at higher p, where the superconducting T_c is maximal.

This doping dependence is totally different from the one observed in 214 cuprates and cast big doubts on the universality of the Yamada plot, at least for charge correlations. As displayed in Fig. 5.12(a) in fact the rectangular behavior versus p of the charge incommensurability 2δ for 123 systems is much different from that of 214 materials, strongly related to the static uniaxial spin ordering with incommensurability δ observed in those compounds (see Subsection 5.1.1).

Moreover it is instructive to compare the charge correlations revealed by our RXS experiments to the p evolution of the spin correlations previously determined by some magnetic neutron scattering experiments. As mentioned in Subection 5.1.2, $YBa_2Cu_3O_{6+x}$ samples exhibit a spin gap that precludes the possibility to observe any truly elastic scattering peak related to magnetic

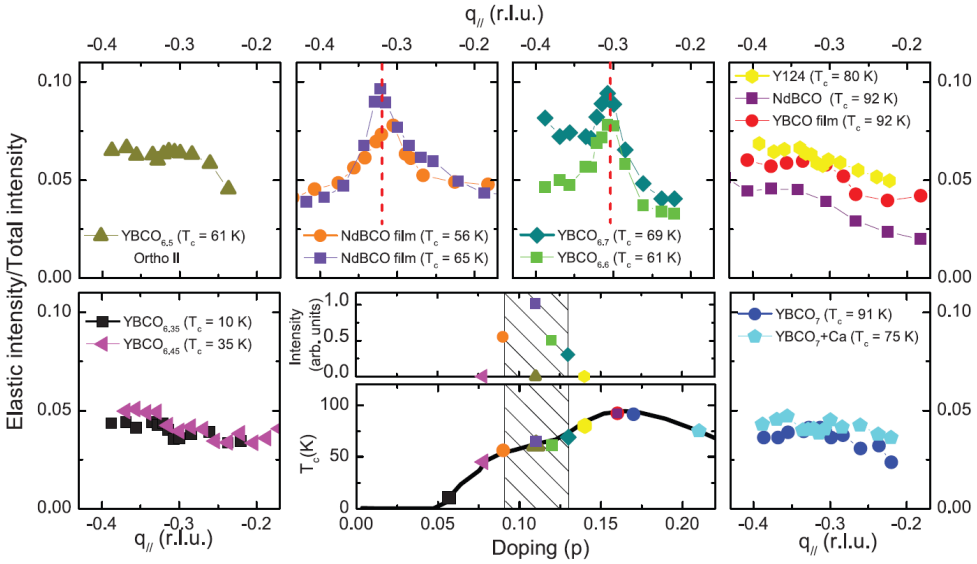

Fig. 5.11: Dependence of the CDW signal at 15 K on the entire doping range explored. The CDW signal is present in several $YBa_2Cu_3O_{6+x}$ and $Nd_{1+x}Ba_{2-x}Cu_3O_7$ samples, but only for $0.09 \leq p \leq 0.13$. In this doping range (shaded in the central panel), the T_c-versus-p relation of 123 cuprates exhibits a plateau. The CDW peak position does not change with p outside of the experimental error, but its intensity is maximum at $p = 0.11$.

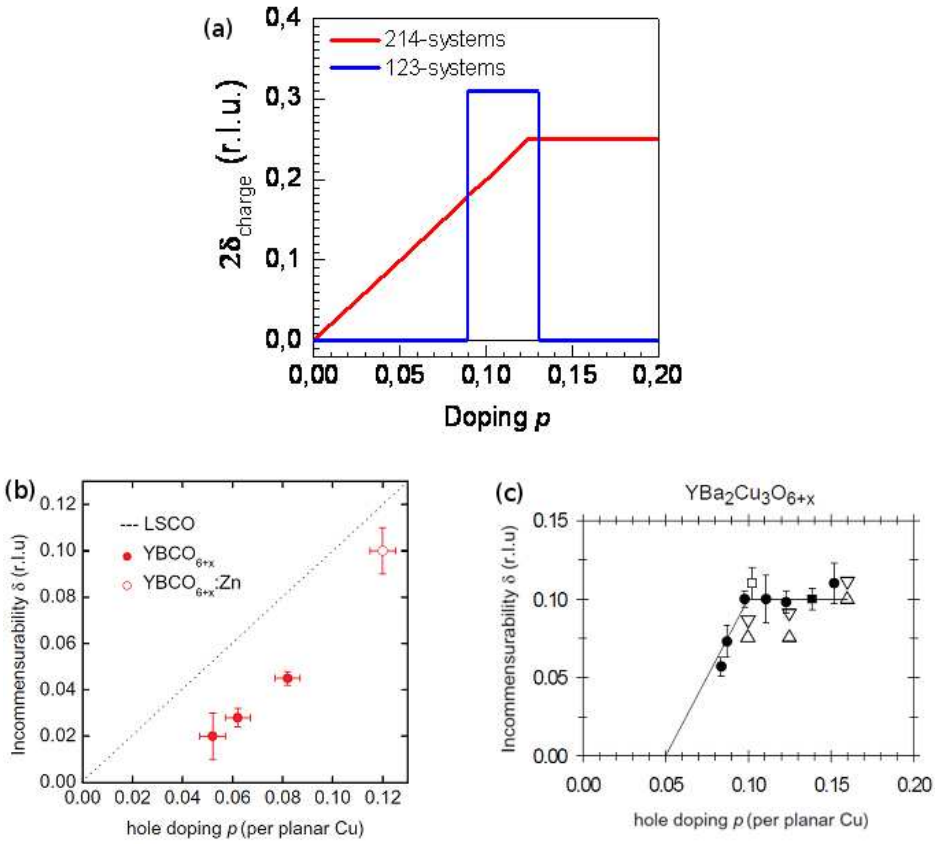

Fig. 5.12: (a) Schematic dependence of the CDW incommensurability 2δ on the hole doping p for 214 and 123 systems. (b) Doping dependence of the magnetic incommensurability δ for an energy transfer of E = 3 meV at low T for $YBa_2Cu_3O_{6.6}$ (filled circles) and Zn-doped $YBa_2Cu_3O_{6.6}$ (open circle) compared with the linear δ-versus-p relation for LSCO (dashed line). Panel reproduced from Ref. [157]. (c) Magnetic incommensurability δ in $YBa_2Cu_3O_{6+x}$ (circles and squares) measured just above the spin-gap energy. The triangles indicate the incommensurability at 20 meV (upper) and 30 meV (lower) for $La_{2-x}Sr_xCuO_4$ with $x = 0.10$ and 0.16 and $La_{1.875}Ba_{0.125}CuO_4$. Panel reproduced from Ref. [151].

ordering. However, given that the spin gap decreases with underdoping, in samples with low dopings it is possible to look at the incommensurability δ of quasi-elastic peaks at energies just above the spin gap, that is only a few meV wide. In particular, for $p \leq 0.08$, INS experiments have revealed incommensurate magnetic quasi-elastic ($E = 3$ meV) peaks at wave vectors ($0.5+\delta$, 0.5) [157], where the δ increases monotonically with p, with a trend vaguely resemblant of the Yamada one, as shown in Fig. 5.12(b). Our findings in Fig. 5.11 show that neither charge order nor low-energy incommensurate charge fluctuations are present in this doping range. For $p > 0.08$, the spin correlations remain constant, as in a Yamada-like picture, and centered at wave vectors similar to those at lower p, which bear no simple relation to the wave vector of our REXS peaks [151] (Fig. 5.12(c)). However, as above said, in this doping range the magnetic excitation spectrum develops a larger gap, that increases smoothly with p. This fact makes more difficult any comparison between our results and INS data, whose trend remains in stark contrast to the abrupt appearance and disappearance of the charge density correlations with increasing p. These considerations imply the important message that spin and charge order are decoupled in the 123 family, differently from what happens in the 214 family, where they coexist microscopically in the striped state.

Finally we note that the range in which the REXS peak is observed (shaded region in Fig. 5.11) coincides with the well-known plateau in the superconducting dome of the 123 system (see Fig. 5.3), suggesting that a competition between superconducting and charge density correlations might be responsible for the anomalously low T_c in this range. In order to get a deeper insight in this interplay between CDW and superconductivity it is useful to look at the temperature dependence of the CDW signal, which is presented in the next Subsection.

5.3.2 Temperature dependence of CDW

Fig. 5.13 shows the temperature dependence of the REXS peak, measured in the energy-resolved mode (panel (a)) and with the more traditional energy-integrated detection (panel (b)). The peak is present both above and below the superconducting critical temperature T_c. It grows in intensity and narrows continuously upon cooling toward T_c. Given that in first approximation the width of the peak is inversely proportional to the correlation length of the CDW, this means that there is a pronounced increase of the last, which reaches 16 ± 2 in-plane lattice units at T_c of $YBa_2Cu_3O_{6.6}$. This value has to be compared with domain sizes in the range of 40 to 66 lattice parameters for the case $La_{1.875}Ba_{0.125}CuO_4$, that shows static stripe-order [131, 144, 142].

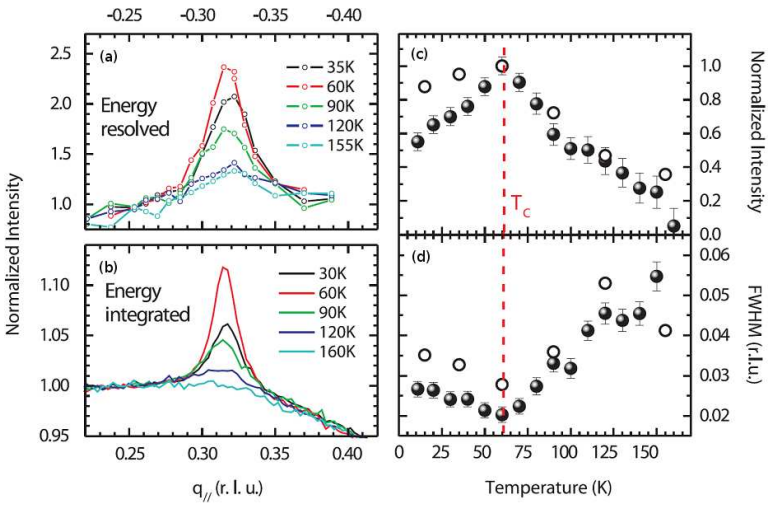

Fig. 5.13: (a) and (b) Comparison of RXS scans at selected temperatures, as obtained with an energy-resolving spectrometer and with a conventional diffractometer for soft x-rays on $YBa_2Cu_3O_{6.6}$. (c) and (d) T-dependence of the CDW intensity and full width at half maximum (FWHM) derived from the energy-resolved (open circles) and the energy-integrated data (solid circles) for σ polarization.

As a consequence, the observed temperature dependence of the correlation length is a strong proof that our REXS signal arises from charge density *fluctuations*, rather than a static CDW.

However the incipient CDW phase transition that seems to be heralded by the diverging correlation length is hampered by the onset of superconductivity, which manifests itself in an abrupt decrease of the intensity and correlation length of the REXS peak (Fig. 5.13(c),(d)). Using only the energy-integrated RXS, we have got similar results also in the cases of the underdoped $Nd_{1.2}Ba_{1.8}Cu_3O_7$ thin film and $YBa_2Cu_3O_{6.7}$ single crystal, displayed in Fig. 5.14: the maximum intensity is observed at T_c and the CDW signal starts to decrease as superconductivity emerges. These facts constitutes a strong evidence of a close competition between superconducting and incommensurate CDW states, supporting what was already suggested by the doping dependence of the REXS response (Fig. 5.11).

Finally, the determination of the high temperature where the CDW peak vanishes is complicated by the weakness of the dying signal, especially in the case of the energy integrated measurements with large fluorescent background. However we can at least say that the onset of charge fluctuations appears above $T = 150$ K for all investigated underdoped samples.

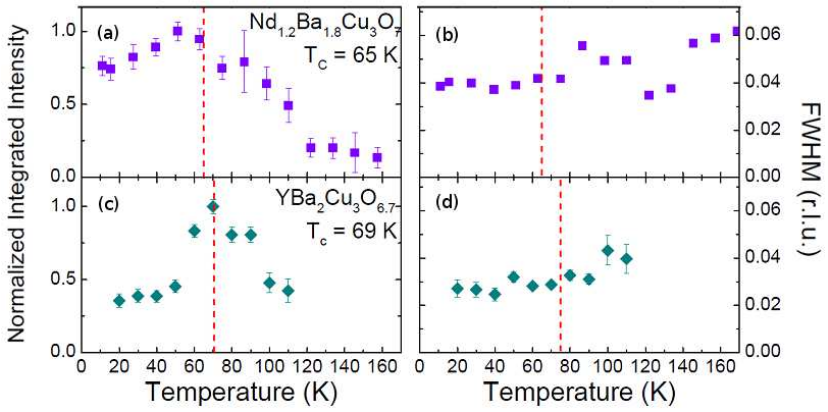

Fig. 5.14: Temperature dependence of the CDW signal intensity and FWHM in underdoped $Nd_{1.2}Ba_{1.8}Cu_3O_7$ (a, b) $YBa_2Cu_3O_{6.7}$ (c, d), measured using energy integrated RXS.

5.4 Conclusions and further works

We have observed fluctuating CDW in the CuO_2 planes of 123 systems with doping levels from 0.09 to 0.13, in strict correspondence with the anomalous plateau in the superconducting dome of these materials. Over this entire range of doping the charge modulation has a constant incommensurate periodicity of ~ 3.2 lattice units, different from the ubiquitous 4-lattice-units period observed for static stripes in 214 cuprates and till now considered "universal".
The doping- and T-dependence of the observed CDW suggests a close competition between high temperature superconductivity (HTS) and the fluctuating charge correlations, as already suggested for static stripes at 1/8 doping in 214 cuprates. However in the case of 123 compounds the evolution of the CDW with doping is totally different and, moreover, the charge and spin ordering phenomena seem to be totally decoupled.

On the side of methods, RXS has been proven to be a technique fast enough to seize in a "clean" experiment the non-static nature of these CDW, until now elusive in 123 materials. CDW correlations in fact were previously observed for example by scanning tunneling spectroscopy (STS) on the surface of superconducting $Bi_2Sr_2CuO_{6+\delta}$ [158] and $Bi_2Sr_2CaCu_2O_{8+\delta}$ [159, 160, 161], but one can get only limited information from STS on the temperature evolution of the CDW correlations, due to the intrinsically slow nature of scanning probe experiments.
In particular the energy-resolved RXS measurements, i.e. RIXS, has been

established as a highly sensitive probe of momentum-dependent static and quasi-static electronic correlations.

Our work provides the first clear evidence of CDW order in YBCO and, for this reason, it constitutes a crucial advance in the field that has already pushed physicists to make further inquiries. In fact, being YBCO one of the "cleanest" among cuprate materials, any ordering tendency is likely to be intrinsic, and not due, for example, to corrugations or particular structural phases. On top of this fact, our results shed light on many points but also raise several questions related to ordering phenomena in cuprates.

Remarkably the wave vector of the charge correlations revealed in our experiments is in good agreement with the nesting vector of the antibonding Fermi surface sheets predicted by density functional calculations for 123 cuprates [162]. The nesting vector is defined as that vector which connects those segments on the 2D Fermi surface that develop the maximal gap amplitude in the *d*-wave superconducting state. Given this correspondence of vectors, the observed CDW in 123 cuprates could be thought as a natural consequence of a Fermi surface instability competing with superconductivity [163]. Moreover the critical nature of the charge fluctuations, evidenced by their T-dependence, suggests the possibility of a CDW ground state for underdoped 123 materials immersed in magnetic fields sufficient to weaken or obliterate superconductivity. This ground state might be responsible both for the Fermi surface reconstruction shown by the quantum oscillation data [154] and for the results of the recent NMR study on YBCO [156] in high magnetic fields. As already mentioned in Section 5.1.2, both the experiments could in fact be explained with the presence of a field-induced CDW and this scenario agrees also with theoretical work on this issue [155, 163].
Actually in the case of the NMR measurements, the agreement with our incommensurate peak is only qualitative: they authors in fact explain their data by means of a uniaxial commensurate charge modulation with a period of 4 lattice units, similar to the one of 214 samples. The sample studied with NMR is a detwinned $YBa_2Cu_3O_{6.5}$ crystal, with oxygen-filled chains alternated to empty chains, so that they generate a charge pattern with a period of 2 lattice units (ortho-II) in the chain layers. For some unknown reason, in our experiment the untwinned $YBa_2Cu_3O_{6.5}$ has not shown a clear CDW peak, although its doping is included in the range from 0.09 to 0.13 (see Fig. 5.11). The most highly ordered case, with half of the chains filled, is thus somewhat particular. A possible explanation for this and maybe the key to reconcile the NMR data with our results could be the same long-range ortho-II oxygen order: its presence in fact might favor a uniaxial charge modulation with a period multiple of 2, like the one inferred from the authors, helped in its stabilization by the high field conditions.

In this connection an important message is brought by a very recent hard x-ray scattering experiment, come after ours and carried out by Chang *et al.* [164], on high quality ortho-VIII crystals of $YBa_2Cu_3O_{6.67}$. In fact the results of this independent study not only further corroborate the competition between CDW and HTS, but also demonstrate that the application of magnetic fields up to 17 T perpendicular to the planes produces a large enhancement of both the intensity and the correlation length of the CDW peak for $T < T_c$, "stabilizing and pinning" the charge fluctuations, as exemplified in Fig. 5.15 (in the same fashion used for Figs. 5.13 and 5.14). It is reasonable to presume that this enhanced CDW order is an indirect consequence of the magnetic-field-induced suppression of the superconducting order.

This picture of a field-enhanced charge order has been very recently confirmed even in the case of 214 cuprates. M. H*ü*cker and coworkers, have in fact reported hard x-ray diffraction experiments on $La_{2-x}Ba_xCuO_4$ for $0.095 \leq x \leq 0.155$ and fields up to 10 T, showing that also the charge stripe order typical of 214 materials can be enhanced in a broad range of doping by the application of a magnetic field [165]. More in detail the effect is particularly large in samples far away from $x = 1/8$, where the charge order is weak and bulk superconductivity is strong, and it is substantially absent close to $x = 1/8$, where static stripe order is already strong and bulk superconductivity suppressed (as seen in Subsection 5.1.1).

Moreover other extremely recent measurements carried out by our collaborators [166] has evidenced charge ordering also in the ortho-II state of $YBa_2Cu_3O_{6.55}$. The results reveal a nearly critical, biaxial CDW state with propagation vector akin to those presented in this Chapter, i.e. $| \mathbf{q}_{\parallel} | = 0.31$ r.l.u., but with reduced amplitude and width and a strong uniaxial anisotropy. The paper also underlines the decoupling bewteen incommensurate spin and charge orders in the 123 family, already mentioned in Subsection 5.3.1. In fact RXS experiments show that the CDW correlation length is strongly reduced in $YBa_2Cu_3O_{6.6}$ crystals with a dilute concentration of spinless (Zn) impurities known to nucleate incommensurate magnetic order, as compared to pristine crystals with the same doping level. These findings thus indicate that not only the spin and charge channels are decoupled in 123 cuprates but that there is a real three-phase competition between spin-modulated, charge-modulated, and superconducting states.

Along the same lines, another very recent hard x-ray diffraction study by Blackburn *et al.* [167] present similar findings for the ortho-II YBCO. The authors find also a field-enhancement of the incommensurate peak and propose an alternative explanation of the NMR data, supposing that an additional commensurate modulation appears in that case, due to the very high magnetic field.

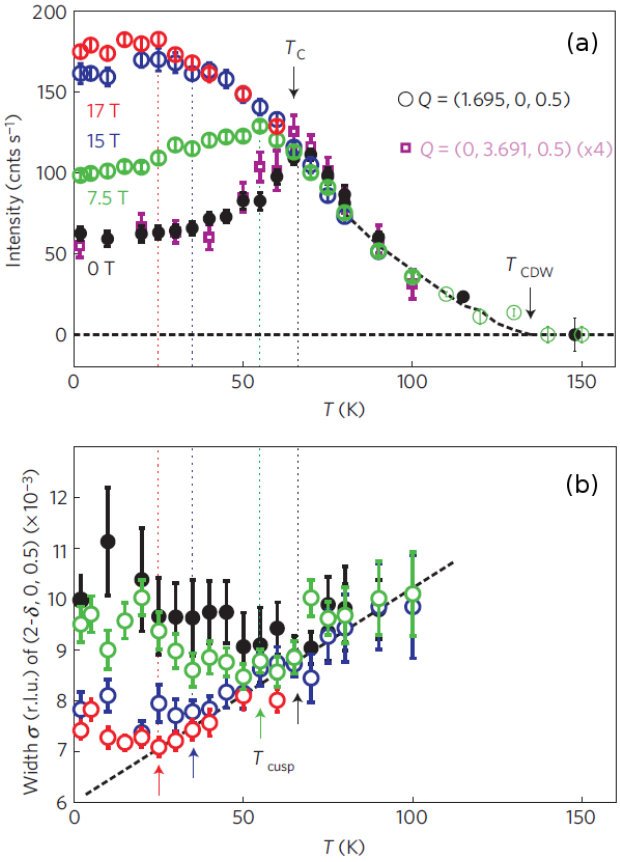

Fig. 5.15: (a) Temperature dependence of the CDW signal intensity in underdoped $YBa_2Cu_3O_{6.67}$ (c, d), measured with hard x-ray scattering at wavevectors (1.695, 0, 0.5) (circles) and (0, 3.691, 0.5) (squares) for different applied magnetic fields. The square data points have been multiplied by a factor 4. In the normal state, there is a smooth onset of the CDW peak that decreases in intensity below T_c. This trend can be reversed by the application of a magnetic field. (b) Gaussian FWHM of the (1.695, 0, 0.5) CDW modulation plotted versus temperature and field respectively. The raw linewidth, including a contribution from the instrumental resolution, is field-independent in the normal state above T_c. In contrast, the CDW order becomes more coherent below T_c, once a magnetic field is applied. Figure reproduced from Ref. [164].

To sum up, everything is consistent in the x-ray scattering data and also the special case of ortho-II YBCO fit the overall picture: the very low intensity of the REXS peak, barely visible above the back-ground, together with its small width, comparable to the the momentum resolution of the RIXS apparata [166], were much likely responsible for our initial null result on this particular sample. In this connection NMR would see something that is totally unconnected from the x-ray scattering results, given also that fluctuating CDWs are visible to x-rays much before they become slow enough to have strong effects on NMR, that is a relatively low-frequency technique.

Going back to our results, the small or absent intensity difference between the signal intensities at $\mathbf{q}_{\parallel} = (0.31,0)$ and $(0,0.31)$ (Fig. 5.8(a)) cast some doubts also on the interpretation, based on stripe fluctuations, of various transport anomalies in the normal state of underdoped 123 compounds [148, 149], at least in the doping range where we have seen the REXS peak. Indeed the isotropic intensity distribution of our CDW signal shows that the observed charge fluctuations cannot account for the strongly anisotropic resistivity and Nernst effect detected in the normal state. It this respect it is also true that further experiments are required to establish whether our isotropic REXS peak arises from an equal distribution of fluctuating domains of two uniaxial CDWs with mutually perpendicular propagation vectors or from a single CDW with biaxial charge modulation.

Finally, despite some materials-specific variations, our data imply that long-range CDW correlations are a common feature of underdoped cuprates, independently of the given chemical composition or crystal structure.
Moreover, although our results do not provide any final proof to state that the CDW ordering is either the cause or a derivative phenomenon of the pseudogap regime, the close similarity of the temperatures at play and the localization in the same region of the phase diagram suggest a single unifying physical reason for these phases. In this sense the presented results and the consistent findings by other groups could be used to state that the interplay between CDW and HTS is something more complex than just a competition, supporting the picture proposed by S. A. Kivelson that "all these phases arise together from one 'parent' state and that the various order parameters are 'intertwined'." [96]
In this connection detailed microscopic calculations are required to assess the relation of CDW with the pseudogap regime [128] and also with the unusual magnetic ordering detected very recently in this same regime in some of these materials, using Kerr effect measurements [168] and polarized elastic neutron scattering [169].
The extensive **q**-, p-, and T-dependent data set that we have reported in this Chapter constitutes an excellent basis and a strong boost for theoretical

work and further experiments on all these issues.

Conclusions

With the present thesis, we have demonstrated that Cu L_3 RIXS can provide a wealth of information on layered cuprates, that can be of great help in a full description of these compounds, adding crucial pieces to the high-T_c puzzle. In fact Cu L_3 RIXS has proven to be a unique tool for the study of magnetic, orbital and charge fluctuations in cuprates. More in detail we have shown that it can effectively probe the spin and charge orders in the CuO_2 planes, that constitute the set in which superconductivity emerges.

During the past decades the magnetic properties of cuprates have been studied almost exclusively with inelastic neutron scattering (INS), that has provided remarkable results but has a series of technical and physical limitations. RIXS has cross-fertilized with INS, opening new perspectives mostly due to the possibility of studying tiny amounts of material, up to high-energies of excitation, where the use of neutrons is experimentally too demanding. Thanks to the relatively large momentum carried by soft x-rays, we could study magnon dispersions over more than 2/3 of the first Brillouin Zone in several compounds, from single crystals to thin films: in particular the application of Cu L_3 RIXS to the wide family of superconducting (Y,Nd)BCO has shown that magnetic excitations survive up to optimal doping and beyond, in the form of damped magnons, with dispersions and spectral weights closely similar to those observed in undoped parent compounds. The comprehensive experimental description of these paramagnons, well described also in the framework of a $t-J$ model, has enabled quantitative tests of magnetic Cooper pairing models, based on a numerical solution of the Eliashberg equations. The experimental and theoretical results give credit to the scenario that sees magnons as the glue of Cooper's pairs in high temperature superconductors (HTS), complementing previous neutrons observations and filling the high-energy part of the magnetic spectrum with enough spectral weight to support a magnetic pairing.

A similar picture has been proposed also for spin excitations in the CuO_2 planes at the interfaces of $(CaCuO_2)_n/(SrTiO_3)_m$ superlattices (SLs). In that case RIXS has shown first that the antiferromagnetic order is preserved in the insulating SLs down to very small cuprate layer thickness and despite the chemical and structural alterations at the interface. The same holds for paramagnons in superconducting SLs grown in highly oxidizing atmosphere, that can be considered as artificial HTS, given the insulating nature of the two building blocks. Moreover the study of orbital (dd) excitations in these SLs has evidenced a pyramidal coordination of Cu ions at the $CaCuO_2/SrTiO_3$ interfaces, revealing where the extra doping oxygens are accomodated in the heterostructures. These findings pave the way to the production of new, artificial HTS based on cuprate/noncuprate SLs, where the charge reservoir layer is constituted by the interface itself.

Finally we have made a different use of soft RIXS aimed at clarifying the issue of ordering phenonema in the CuO_2 planes of cuprates, focusing our attention to the elastic part of the spectra. In particular, by combining RIXS with conventional RXS measurements, we have obtained direct evidence of two-dimensional incommensurate charge fluctuations in the copper oxide planes of 123 cuprates, indicating an incipient charge density wave (CDW) instability that competes with superconductivity. The energy-resolved nature of RIXS has been crucial to detect for the first time the elastic scattering associated with this until now elusive CDW. The presence of this charge ordering could be another signature of a single complex parent phase made of inter-twined orders, at the origin of high temperature superconductivity.

Although we do not have a definitive proof of a magnetic Cooper pairing, nor we can state that the charge modulation detected in 123 systems is universal among cuprates, our results surely stimulate more investigations in a fascinating field, providing an extensive basis of data for future theoretical work and further experiments.

Acknowledgments

There are several people that I have to thank for these long (and in a way short) four years.

First of all my gratitude goes to my two bosses, Prof. Giacomo Ghiringhelli and Prof. Lucio Braicovich, for which I have the greatest respect, as physicists and persons. With their two different but complementary approaches, Giacomo and Lucio have been my constant reference in these years, impressing me continuously with their eclectic competences and working out solutions to the most complicated problems, even when almost everyone else was about to give up. Giacomo, with his countless advices and his "magical touch" on instruments, and Lucio, with his apparently infinite knowledge and his mixture of endless patience and tough temper, have been together a wonderful guide along the path: I ought to them almost everything I know in physics. It's been a pleasure to make experiments with them and to share funny moments together. In a way or the other, they have always been helpful for me, even in hard times of my personal life, and hopefully they will be a reference also in the future. Thanks for all this.

Thanks to Dr. Nicholas Brookes, Nick, for giving me the possibility to stay at the ID08 beamline for one year and for his never-ending efforts to get always things working at their best on the beamline. Thanks to him and to the ID08 staff, Andrea and Violetta, for making me feel "a casa" even in France, Flora, with her several recommendations, Julio, who left for Brazil too early, and Kurt, for being the nicest office-*mate* that one could ask. All together they made my stay at the ESRF, as well as in Grenoble, more than comfortable.

Thanks to Carmela (Lina) Aruta, Valentina Bisogni, Daniele Di Castro, Gabriella De Luca, Alice Galdi, Alex Fraño, Claudio Mazzoli, Mathieu Le Tacon, Pasquale Orgiani, Marco Salluzzo and all the other several coworkers and collaborators, with whom I shared pleasant beam-times and crazy

sleepless night-shifts.

Thanks to all the people I've met along the way and the friends I've made during the HERCULES school and the conferences that I've attended. Many thanks in particular to the guys met in Grenoble: Baptiste, Carlotta, Eduardo, Giorgos, Isil, Jess, Marie, Lucia, Luca, Massimo, Peter, Radhika, Simone, Svetlana, Vitor and my "Dream Team", Emanuelle, Kamila, and Marianne. Special thanks to the students Greta Dellea and Ross Boulton and the (by now former) PhD students Marco Moretti, aka Marco Sala, and Christian Piovera. Without all of you guys my (not) working life wouldn't have been so funny and pleasant.

My endless gratitude goes to my friends of a life and the ones who came later, even only for being always there for me, no matter the distance in between. Many thanks in particular to Phab, Marci, Dany, Gabri, Moreno, Andre aka Qt, Rocco, St*é*phy, Ste, Valerio and to Ilaria. Everyone in his own way, you have always been my constants and I hope you will be the same for the rest of my life.

Thanks to my sisters, Marta and Matilde, for their fights and their love: I am so lucky to have you.

Thanks to my father, Massimo, who always supported me and believed in me.

Thanks to my mother, Annita. If I am the person who I am is because of you: there's no way I can pay you back but I hope to show you that I understand and to make you proud of me one day, wherever you are.

Bibliography

[1] C. J. Sparks, "Inelastic resonance emission of x rays: Anomalous scattering associated with anomalous dispersion," *Phys. Rev. Lett.*, vol. 33, p. 262, July 1974.

[2] A. Kotani and S. Shin, "Resonant inelastic x-ray scattering spectra for electrons in solids," *Rev. Mod. Physics*, vol. 73, pp. 203–246, 2001.

[3] M. M. Sala, V. Bisogni, C. Aruta, G. Balestrino, H. Berger, N. B. Brookes, G. M. D. Luca, D. D. Castro, M. Grioni, M. Guarise, P. G. Medaglia, F. M. Granozio, M. Minola, P. Perna, M. Radovic, M. Salluzzo, T. Schmitt, K. J. Zhou, L. Braicovich, and G. Ghiringhelli, "Energy and symmetry of dd excitations in undoped layered cuprates measured by Cu L_3 resonant inelastic x-ray scattering," *New Journal of Physics*, vol. 13, p. 043026, 2011.

[4] L. Braicovich, J. van den Brink, V. Bisogni, M. M. Sala, L. J. P. Ament, N. B. Brookes, G. M. D. Luca, M. Salluzzo, T. Schmitt, V. N. Strocov, and G. Ghiringhelli, "Magnetic excitations and phase separation in the underdoped $La_{2-x}Sr_xCuO_4$ superconductor measured by resonant inelastic x-ray scattering," *Phys. Rev. Lett.*, vol. 104, p. 077002, 2010.

[5] L. J. P. Ament, G. Ghiringhelli, M. Moretti Sala, L. Braicovich, and J. van den Brink, "Theoretical demonstration of how the dispersion of magnetic excitations in cuprate compounds can be determined using resonant inelastic x-ray scattering," *Phys. Rev. Lett.*, vol. 103, p. 117003, 2009.

[6] M. Guarise, B. D. Piazza, M. Moretti Sala, G. Ghiringhelli, L. Braicovich, H. Berger, J. N. Hancock, D. van der Marel, T. Schmitt, V. N. Strocov, L. J. P. Ament, J. van den Brink, P.-H. Lin, P. Xu,

H. M. Rønnow, and M. Grioni, "Measurement of magnetic excitations in the two-dimensional antiferromagnetic $Sr_2CuO_2Cl_2$ insulator using resonant x-ray scattering: Evidence for extended interactions," *Phys. Rev. Lett.*, vol. 105, p. 157006, 2010.

[7] M. L. Tacon, G. Ghiringhelli, J. Chaloupka, M. M. Sala, V. Hinkov, M. W. Haverkort, M. Minola, M. Bakr, K. J. Zhou, S. Blanco-Canosa, C. Monney, Y. T. Song, G. L. Sun, C. T. Lin, G. M. D. Luca, M. Salluzzo, G. Khaliullin, T. Schmitt, L. Braicovich, and B. Keimer, "Intense paramagnon excitations in a large family of high-temperature superconductors," *Nature Physics*, vol. 7, pp. 725–730, 2011.

[8] J. G. Bednorz and K. A. Müller, "Possible high-t_c superconductivity in the La-Ba-Cu-O system," *Z. Phys. B: Condens. Matter*, vol. 64, p. 188, 1986.

[9] J. Bardeen, L. N. Cooper, and J. R. Schrieffer, "Theory of superconductivity," *Phys. Rev.*, vol. 108, no. 5, pp. 1175–1204, 1957.

[10] L. J. P. Ament, M. van Veenendaal, T. P. Devereaux, and J. P. H. J. van den Brink, "Resonant inelastic x-ray scattering studies of elementary excitations," *Rev. Mod. Phys.*, 2011.

[11] M. M. Sala, *Magnetic and orbital resonant inelastic soft x-ray scattering.* PhD thesis, Politecnico di Milano, 2011.

[12] L. Braicovich, M. M. Sala, M. Minola, G. Trezzi, A. D. Natale, G. Ghiringhelli, F. Yakhou-Harris, C. Morawe, L. Eybert, A. Fondacaro, and N. B. Brookes, "Towards full polarisation control in resonant inelastic soft x-ray scattering." http://www.esrf.eu/news/spotlight/spotlight140/index_html/.

[13] L. Braicovich, N. B. Brookes, G. Ghiringhelli, M. Minola, G. Monaco, M. M. Sala, and L. Simonelli, "Resonant inelastic scattering at the esrf: hard and soft x-rays," *Synchrotron Radiation News*, vol. 25, p. 4, 2012.

[14] L. B. N. L. Center for X-Ray Optics, "X-ray interactions with matter." http://henke.lbl.gov/optical_constants/.

[15] M. Grioni, J. F. van Acker, M. T. Czyzcaronyk, and J. C. Fuggle, "Unoccupied electronic structure and core-hole effects in the x-ray-absorption spectra of Cu_2O," *Phys. Rev. B*, vol. 45, no. 7, p. 3309, 1992.

[16] L. Braicovich, L. J. Ament, V. Bisogni, F. Forte, C. Aruta, G. Balestrino, N. B. Brookes, G. M. D. Luca, P. G. Medaglia, F. M. Granozio, M. Radovic, M. Salluzzo, J. van den Brink, and G. Ghiringhelli, "Dispersion of magnetic excitations in the cuprate La_2CuO_4 and $CaCuO_2$ compounds measured using resonant x-ray scattering," *Phys. Rev. Lett.*, vol. 102, p. 167401, 2009.

[17] L. Braicovich, M. Moretti Sala, L. J. P. Ament, V. Bisogni, M. Minola, G. Balestrino, D. D. Castro, G. M. D. Luca, M. Salluzzo, G. Ghiringhelli, and J. van den Brink, "Momentum and polarization dependence of single-magnon spectral weight for Cu l_3-edge resonant inelastic x-ray scattering from layered cuprates," *Phys. Rev. B*, vol. 81, p. 174533, 2010.

[18] W. Schülke, *Electron dynamics by inelastic x-ray scattering.* Oxford University Press, Oxford, 2007.

[19] J. Ghijsen, L. H. Tjeng, H. Eskes, and G. A. Sawatzky, "Resonant photoemission study of the electronic structure of Cuo and Cu_2O," *Phys. Rev. B*, vol. 42, p. 2268, 1990.

[20] V. N. Strocov, T. Schmitt, U. Flechsig, T. Schmidt, A. Imhof, Q. Chen, J. Raabe, R. Betemps, D. Zimoch, J. Krempasky, X. Wang, M. Grioni, A. Piazzalunga, and L. Patthey, "High-resolution soft x-ray beamline ADRESS at the swiss light source for resonant inelastic x-ray scattering and angle-resolved photoelectron spectroscopies," *J. Synchrotron Rad.*, vol. 17, no. 5, pp. 631–643, 2010.

[21] C. Dallera, E. Puppin, G. Trezzi, N. Incorvaia, A. Fasana, L. Braicovich, N. B. Brookes, and J. B. Goedkoop, "Soft x-ray emission spectroscopy at ESRF beamline 26 based on a helical undulator," *J. Synchrotron Radiat.*, vol. 3, pp. 231–238, 1996.

[22] M. E. Dinardo, A. Piazzalunga, L. Braicovich, V. Bisogni, C. Dallera, K. Giarda, M. Marcon, A. Tagliaferri, and G. Ghiringhelli, "Gaining efficiency and resolution in soft x-ray emission spectrometers thanks to directly illuminated CCD detectors," *Nucl. Instrum. Methods Phys. Res., Sect. A*, vol. 570, p. 176, 2007.

[23] G. Ghiringhelli, A. Piazzalunga, C. Dallera, G. Trezzi, L. Braicovich, T. Schmitt, V. N. Strocov, R. Betemps, L. Patthey, X. Wang, and M. Grioni, "SAXES, a high resolution spectrometer for resonant x-ray

emission in the 4001600 eV energy range," *Rev. Sci. Instrum.*, vol. 77, p. 113108, 2006.

[24] "European Synchrotron Radiation Facility." http://www.esrf.eu.

[25] S. Sasaki, K. Kakunori, T. Takada, T. Shimada, K. Yanagida, and Y. Miyahara, "Design of a new type of planar undulator for generating variably polarized radiation," *Nucl. Instrum. and Meth. A*, vol. 331, p. 763, 1993.

[26] S. Sasaki, "Analysis for planar variably-polarizing undulator," *Nucl. Instrum. and Meth. A*, vol. 347, p. 83, 1994.

[27] D. Attwood, *Soft x-ray and extreme ultraviolet radiation. Principles and application.* Cambridge University Press, 1999.

[28] C. T. Chen, "Concept and design procedure for cylindrical element monochromators for synchrotron radiation," *Nucl. Instr. and Meth. A*, vol. 256, pp. 595–604, May 1987.

[29] "Swiss Light Source." http://http://www.psi.ch/sls/.

[30] T. Siegrist, S. M. Zahurak, D. W. Murphy, and R. S. Roth, "The parent structure of the layered high-temperature superconductors," *Nature*, vol. 334, pp. 231–232, 1988.

[31] S. Y. Savrasov and O. K. Andersen, "Linear-response calculation of the electron-phonon coupling in doped $CaCuO_2$," *Phys. Rev. Lett.*, vol. 77, p. 4430, 1996.

[32] P. Zhang, S. G. Louie, and M. L. Cohen, "Electron-phonon renormalization in cuprate superconductors," *Phys. Rev. Lett.*, vol. 98, p. 067005, 2007.

[33] K. Ishii, S. Ishihara, Y. Murakami, K. Ikeuchi, K. Kuzushita, T. Inami, K. Ohwada, M. Yoshida, I. Jarrige, N. Tatami, S. Niioka, D. Bizen, Y. Ando, J. Mizuki, S. Maekawa, and Y. Endoh, "Polarization-analyzed resonant inelastic x-ray scattering of the orbital excitations in $KCuF_3$," *Phys. Rev. B*, vol. 83, p. 241101, 2011.

[34] L. Braicovich, G. van der Laan, A. Tagliaferri, E. Annese, G. Ghiringhelli, and N. B. Brookes, "Resonant inelastic x-ray scattering from magnetic systems with angular resolutionand polarization analysis of the scattered beam: Results on metallic Co, Fe, and Co ferrite at the $L_{3,2}$ edges," *Phys. Rev. B*, vol. 75, p. 184408, 2007.

[35] U. Staub, V. Scagnoli, Bodenthin, Y. Bodenthin, M. Garcia-Fernandez, R. Wetter, A. M. Mulders, H. Grimmer, and M. Horisberger, "Polarization analysis in soft x-ray diffraction to study magnetic and orbital ordering," *Journ. of Synchr. Rad.*, vol. 15, pp. 469–476, 2008.

[36] D. G. Hawthorn, K. M. Shen, J. Geck, D. C. Peets, H. Wadati, J. Okamoto, S.-W. Huang, D. J. Huang, H.-J. Lin, J. D. Denlinger, R. Liang, D. A. Bonn, W. N. Hardy, and G. A. Sawatzky, "Resonant elastic soft x-ray scattering in oxygen-ordered $YBa_2Cu_3O_{6+\delta}$," *Phys. Rev. B*, vol. 84, p. 075125, 2011.

[37] P. Dai, B. C. Chakoumakos, G. F. Sun, K. W. Wong, Y. Xin, and D. F. Lu, "Synthesis and neutron powder diffraction study of the superconductor $hgca_2ba_2cu_3o_{8+\delta}$ by Tl substitution," *Physica C: Superconductivity*, vol. 243, pp. 201–206, Mar. 1995.

[38] Y. Kamihara, T. Watanabe, M. Hirano, and H. Hosono, "Iron-based layered superconductor $La[O_{1-x}F_x]FeAs$ ($x = 0.05 - 0.12$) with $t_c = 26$ K," *J. Am. Chem. Soc.*, vol. 130, pp. 3296–3297, Mar. 2008.

[39] X. H. Chen, T. Wu, G. Wu, R. H. Liu, H. Chen, and D. F. Fang, "Superconductivity at 43 K in $SmFeAsO_{1-x}F_x$," *Nature*, vol. 453, pp. 761–762, June 2008.

[40] Coalition for the Commercial Application of Superconductors. http://www.ccas-web.org/pdf/ccas_brochure_web.pdf.

[41] R. J. Cava, "Oxide superconductors," *J. Am. Ceram. Soc.*, vol. 82, no. 1, pp. 5–28, 2000.

[42] M. A. G. Aranda, "Crystal structures of copper-based High-T_c superconductors," *Advanced Materials*, vol. 6, pp. 905–921, 1994.

[43] H. J. de Boer and E. J. W. Verwey *Proc. Phys. Soc. London A*, vol. 49, p. 59, 1937.

[44] E. Dagotto, "Correlated electrons in high-temperature superconductors," *Rev. Mod. Phys.*, vol. 66, p. 763, July 1994.

[45] Ø. Fischer, M. Kugler, I. Maggio-Aprile, and C. Berthod, "Scanning tunneling spectroscopy of high-temperature superconductors," *Rev. Mod. Phys.*, vol. 79, p. 353, 2007.

[46] P. A. Lee, N. Nagaosa, and X. Wen, "Doping a Mott insulator: Physics of high-temperature superconductivity," *Rev. Mod. Phys.*, vol. 78, p. 17, Jan. 2006.

[47] F. C. Zhang and T. M. Rice, "Effective hamiltonian for the superconducting Cu oxides," *Phys. Rev. B*, vol. 37, p. 3759, 1988.

[48] J. M. Tranquada, *Handbook of High-Temperature Superconductivity.* Springer, New York, 2007.

[49] R. Coldea, S. M. Hayden, G. Aeppli, T. G. Perring, C. D. Frost, T. E. Mason, S.-W. Cheong, and Z. Fisk, "Spin waves and electronic interactions in La_2CuO_4," *Phys. Rev. Lett.*, vol. 86, p. 5377, 2001.

[50] N. S. Headings, S. M. Hayden, R. Coldea, and T. G. Perring, "Anomalous high-energy spin excitations in the high-t_c superconductor-parent antiferromagnet La_2CuO_4," *Phys. Rev. Lett.*, vol. 105, p. 247001, 2010.

[51] J. D. Perkins, J. M. Graybeal, M. A. Kastner, R. J. Birgeneau, J. P. Falck, and M. Greven, "Mid-infrared optical absorption in undoped lamellar copper oxides," *Phys. Rev. Lett.*, vol. 71, p. 1621, 1993.

[52] J. Lorenzana and G. A. Sawatzky, "Phonon assisted multimagnon optical absorption and long lived two-magnon states in undoped lamellar copper oxides," *Phys. Rev. Lett.*, vol. 74, pp. 1867–1870, 1995.

[53] K. B. Lyons, P. E. Sulewski, P. A. Fleury, H. L. Carter, A. S. Cooper, G. P. Espinosa, Z. Fisk, and S. Cheong, "High-energy spin and charge excitations in La_2CuO_4," *Phys. Rev. B*, vol. 39, p. 9693, May 1989.

[54] P. E. Sulewski, P. A. Fleury, K. B. Lyons, S. Cheong, and Z. Fisk, "Light scattering from quantum spin fluctuations in R_2CuO_4 (R=La, Nd, Sm)," *Phys. Rev B*, vol. 41, p. 225, Jan. 1990.

[55] V. Bisogni, L. Simonelli, L. J. P. Ament, F. Forte, M. M. Sala, M. Minola, S. Huotari, J. van den Brink, G. Ghiringhelli, N. Brookes, and L. Braicovich, "Bimagnon studies in cuprates with resonant inelastic x-ray scattering at the o K edge. i - assessment on La_2CuO_4 and comparison with the excitation at cu L_3 and cu K edges," *Phys. Rev. B*, vol. 85, p. 214527, 2012.

[56] J. P. Hill, G. Blumberg, Y.-J. Kim, D. S. Ellis, S. Wakimoto, R. J. Birgeneau, S. Komiya, Y. Ando, B. Liang, R. L. Greene, D. Casa, and T. Gog, "Observation of a 500 meV collective mode in $La_{2-x}Sr_xCuO_4$

and Nd_2CuO_4 using resonant inelastic x-ray scattering," *Phys. Rev. Lett.*, vol. 100, p. 097001, 2008.

[57] J. van den Brink, "The theory of indirect resonant inelastic x-ray scattering on magnons," *Europhys. Lett.*, vol. 80, p. 47003, 2007.

[58] T. Nagao and J. ichi Igarashi, "Two-magnon excitations in resonant inelastic x-ray scattering from quantum Heisenberg antiferromagnets," *Phys. Rev. B*, vol. 75, p. 214414, 2007.

[59] F. Forte, L. J. P. Ament, and J. van den Brink, "Magnetic excitations in La_2CuO_4 probed by indirect resonant inelastic x-ray scattering," *Phys. Rev. B*, vol. 77, p. 134428, 2008.

[60] D. S. Ellis, J. Kim, J. P. Hill, S. Wakimoto, R. J. Birgeneau, Y. Shvydko, D. Casa, T. Gog, K. Ishii, K. Ikeuchi, A. Paramekanti, and Y.-J. Kim, "Magnetic nature of the 500 meV peak in $La_{2-x}Sr_xCuO_4$ observed with resonant inelastic x-ray scattering at the Cu K-edge," *Phys. Rev. B*, vol. 81, p. 085124, 2010.

[61] V. Bisogni, *Local and collective excitations in cuprates investigated by high resolution resonant inelastic x-ray scattering*. PhD thesis, Politecnico di Milano, 2010.

[62] L. J. P. Ament, *Resonant inelastic x-ray scattering studies of elementary excitations*. PhD thesis, Universiteit Leiden, 2010.

[63] D. J. Scalapino, "The case for $d_{x^2-y^2}$ pairing in the cuprate superconductors," *Phys. Rep.*, vol. 250, no. 6, pp. 329–365, 1995.

[64] A. Abanov, A. V. Chubukov, and J. Schmalian, "Quantum-critical theory of the spin fermion model and its application to cuprates: Normal state analysis," *Adv. Phys.*, vol. 52, pp. 119–218, 2003.

[65] M. Eschrig, "The effect of collective spin-1 excitations on electronic spectra in high-t_c superconductors," *Adv. Phys.*, vol. 55, p. 47, 2006.

[66] T. Dahm, V. Hinkov, S. V. Borisenko, A. A. Kordyuk, V. B. Zabolotnyy, J. Fink, B. Bchner, D. J. Scalapino, W. Hanke, and B. Keimer, "Strength of the spin-fluctuation-mediated pairing interaction in a high-temperature superconductor," *Nat. Phys.*, vol. 5, p. 217, 2009.

[67] D. J. Scalapino, "A common thread: The pairing interaction for unconventional superconductors," *Rev. Mod. Phys.*, vol. 84, p. 1383, 2012.

[68] H.-Y. Kee, S. A. Kivelson, and G. Aeppli, "Spin-1 neutron resonance peak cannot account for electronic anomalies in the cuprate superconductors," *Phys. Rev. Lett.*, vol. 88, p. 257002, 2002.

[69] L. Braicovich, J. van den Brink, V. Bisogni, M. M. Sala, L. J. Ament, N. B. Brookes, G. M. D. Luca, M. Salluzzo, T. Schmitt, V. N. Strocov, and G. Ghiringhelli, "Magnetic excitations and phase separation in the underdoped $La_{2-x}Sr_xCuO_4$ superconductor measured by resonant inelastic x-ray scattering," *Phys. Rev. Lett.*, vol. 104, p. 077002, 2010.

[70] J. Bobroff, H. Alloul, S. Ouazi, P. Mendels, A. Mahajan, N. Blanchard, G. Collin, V. Guillen, and J. Marucco, "Absence of static phase separation in the high T_c cuprate $YBa_2Cu_3O_{6+y}$," *Phys. Rev. Lett.*, vol. 89, p. 157002, 2002.

[71] Y. T. Song, J. B. Peng, X. Wang, G. L. Sun, and C. T. Lin, "Ambient-condition growth of superconducting $YBa_2Cu_4O_8$ single crystals using KOH flux," *J. Cryst. Growth*, vol. 300, pp. 263–266, 2007.

[72] G. L. Sun, Y. T. Song, and C. T. Lin, "Investigation of $YBa_2Cu_4O_8$ single crystal growth by KOH flux," *Supercond. Sci. Technol.*, vol. 21, p. 125001, 2008.

[73] M. Salluzzo, G. M. de Luca, D. Marré, M. Putti, M. Tropeano, U. S. di Uccio, and R. Vaglio, "Thickness effect on the structure and superconductivity of $Nd_{1.2}Ba_{1.8}Cu_3O_z$ epitaxial films," *Phys. Rev. B*, vol. 72, p. 134521, 2005.

[74] H. F. Fong, B. Keimer, D. Reznik, D. L. Milius, and I. A. Aksay, "Polarized and unpolarized neutron-scattering study of the dynamical spin susceptibility of $YBa_2Cu_3O_7$," *Phys. Rev. B*, vol. 54, pp. 6708–6720, 1996.

[75] J. M. Tranquada, G. Shirane, B. Keimer, S. Shamoto, and M. Sato, "Neutron scattering study of magnetic excitations in $YBa_2Cu_3O_{6+x}$," *Phys. Rev. B*, vol. 40, pp. 4503–4516, 1989.

[76] D. Reznik, P. Bourges, H. F. Fong, L. P. Regnault, J. Bossy, C. Vettier, D. L. Milius, I. A. Aksay, and B. Keimer, "Direct observation of optical magnons in $YBa_2Cu_3O_{6.2}$," *Phys. Rev. B*, vol. 53, pp. R14741–R14744, 1996.

[77] S. M. Hayden, G. Aeppli, T. G. Perring, H. A. Mook, and F. Dogan, "High-frequency spin waves in $YBa_2Cu_3O_{6.15}$," *Phys. Rev. B*, vol. 54, pp. R6905–R6908, 1996.

[78] V. Hinkov, P. Bourges, S. Pailhes, Y. Sidis, A. Ivanov, C. D. Frost, T. G. Perring, C. T. Lin, D. P. Chen, and B. Keimer, "Spin dynamics in the pseudogap state of a high-temperature superconductor," *Nat. Phys.*, vol. 3, pp. 780–785, 2007.

[79] C. Stock, R. A. Cowley, W. J. L. Buyers, C. D. Frost, J. W. Taylor, D. Peets, R. Liang, D. Bonn, and W. N. Hardy, "Effect of the pseudogap on suppressing high energy inelastic neutron scattering in superconducting $YBa_2Cu_3O_{6.5}$," *Phys. Rev. B*, vol. 82, p. 174505, Nov. 2010.

[80] P. Bourges, H. F. Fong, L. P. Regnault, J. Bossy, C. Vettier, D. L. Milius, I. A. Aksay, and B. Keimer, "High-energy spin excitations in $YBa_2Cu_3O_{6.5}$," *Phys. Rev. B*, vol. 56, pp. R11439–R11442, 1997.

[81] C. Stock, W. J. L. Buyers, R. A. Cowley, P. S. Clegg, R. Coldea, C. D. Frost, R. Liang, D. Peets, D. Bonn, W. N. Hardy, and R. J. Birgeneau, "From incommensurate to dispersive spin-fluctuations: The high-energy inelastic spectrum in superconducting $YBa_2Cu_3O_{6.5}$," *Phys. Rev. B*, vol. 71, p. 024522, Jan. 2005.

[82] B. Vignolle, S. M. Hayden, D. F. McMorrow, H. M. Rønnow, B. Lake, C. D. Frost, and T. G. Perring, "Two energy scales in the spin excitations of the high-temperature superconductor $La_{2-x}Sr_xCuO_4$," *Nat. Phys.*, vol. 3, pp. 163–167, 2007.

[83] O. J. Lipscombe, B. Vignolle, T. G. Perring, C. D. Frost, and S. M. Hayden, "Emergence of coherent magnetic excitations in the high temperature underdoped $La_{2-x}Sr_xCuO_4$ superconductor at low temperatures," *Phys. Rev. Lett.*, vol. 102, p. 167002, 2009.

[84] R. J. Birgeneau, C. Stock, J. M. Tranquada, and K. Yamada, "Magnetic neutron scattering in hole-doped cuprate superconductors," *J. Phys. Soc. Jpn.*, vol. 75, p. 111003, 2006.

[85] S. M. Hayden, H. A. Mook, P. Dai, T. G. Perring, and F. Doğan, "The structure of the high-energy spin excitations in a high-transition-temperature superconductor," *Nature*, vol. 429, pp. 531–534, 2004.

[86] V. Hinkov, S. Pailhès, P. Bourges, Y. Sidis, A. Ivanov, A. Kulakov, C. T. Lin, D. P. Chen, C. Bernhard, and B. Keimer, "Two-dimensional geometry of spin excitations in the high-transition-temperature superconductor $YBa_2Cu_3O_{6+x}$," *Nature*, vol. 430, pp. 650–654, 2004.

[87] D. Reznik, J.-P. Ismer, I. Eremin, L. Pintschovius, T. Wolf, M. Arai, Y. Endoh, T. Masui, and S. Tajima, "Local-moment fluctuations in the optimally doped high-t_c superconductor $YBa_2Cu_3O_{6.95}$," *Phys. Rev. B*, vol. 78, p. 132503, 2008.

[88] T. Tohyama, P. Horsch, and S. Maekawa, "Spin and charge dynamics of the $t - J$ model," *Phys. Rev. Lett.*, vol. 74, pp. 980–983, 1995.

[89] R. Eder, Y. Ohta, and S. Maekawa, "Anomalous spin and charge dynamics of the $t - J$ model at low doping," *Phys. Rev. Lett.*, vol. 74, pp. 5124–5127, 1995.

[90] J. Hubbard *Proc. Roy. Soc. London A*, vol. 276, p. 238, 1963.

[91] P. W. Anderson, "The resonating valence bond state in La_2CuO_4 and superconductivity," *Science*, vol. 235, pp. 1196–1198, 1987.

[92] G. Eliashberg *Zh. Eksperim. i Teor. Fiz.*, vol. 38, p. 966, 1960.

[93] J. Carbotte, "Properties of boson-exchange superconductors," *Rev. Mod. Phys.*, vol. 62, p. 1027, 1990.

[94] P. Prelovšek and A. Ramšak, "Spectral functions and the pseudogap in the $t - J$ model," *Phys. Rev. B*, vol. 63, p. 180506(R), 2001.

[95] Y. Li, M. L. Tacon, M. Bakr, D. Terrade, D. Manske, R. Hackl, L. Ji, M. K. Chan, N. Barišic, X. Zhao, M. Greven, and B. Keimer, "Feedback effect on high-energy magnetic fluctuations in the model high-temperature superconductor $HgBa_2CuO_{4+\delta}$ observed by electronic raman scattering," *Phys. Rev. Lett.*, vol. 108, p. 227003, 2012.

[96] E. Fradkin and S. A. Kivelson, "High-temperature superconductivity: Ineluctable complexity," *Nature Physics*, vol. 8, pp. 864–866, 2012.

[97] A. Ohtomo and H. Y. Hwang, "A high-mobility electron gas at the $LaAlO_3/SrTiO_3$ heterointerface," *Nature*, vol. 427, pp. 423–426, 2004.

[98] J. Mannhart and D. Schlom, "Oxide interfaces an opportunity for electronics," *Science*, vol. 327, pp. 1607–1611, 2010.

[99] J. M. Triscone, M. G. Karkut, L. Antognazza, O. Brunner, and Ø. Fischer, "Y-Ba-Cu-O/Dy-Ba-Cu-O superlattices: A first step towards the artificial construction of high-T_c superconductors," *Phys. Rev. Lett.*, vol. 63, pp. 1016–1019, 1989.

[100] J. M. Triscone, Ø. Fischer, O. Brunner, L. Antognazza, A. D. Kent, and M. G. Karkut, "$YBa_2Cu_3O_7/PrBa_2Cu_3O_7$ superlattices: Properties of ultrathin superconducting layers separated by insulating layers," *Phys. Rev. Lett.*, vol. 64, pp. 804–807, 1990.

[101] G. Balestrino, S. Martellucci, P. G. Medaglia, A. Paoletti, G. Petrocelli, and A. A. Varlamov, "Dependence of the critical temperature on n in $(BaCuO_2)_2/(CaCuO_2)_n$ superlattices," *Phys. Rev. B*, vol. 58, pp. R8925–R8928, 1998.

[102] C. Aruta, G. Balestrino, S. Martellucci, A. Paoletti, and G. Petrocelli, "Artificially layered films of $CuBa_2(Ca_{1-x}Sr_x)_{n-1}Cu_nO_y$ grown using pulsed laser deposition," *J. Appl. Phys.*, vol. 81, p. 220, 1997.

[103] A. Gozar, G. Logvenov, L. F. Kourkoutis, A. T. Bollinger, L. A. Giannuzzi, D. A. Muller, and I. Bozovic, "High-temperature interface superconductivity between metallic and insulating copper oxides," *Nature*, vol. 455, pp. 782–785, 2008.

[104] C. Aruta, G. Ghiringhelli, C. Dallera, F. Fracassi, P. G. Medaglia, A. Tebano, N. B. Brookes, L. Braicovich, and G. Balestrino, "Hole redistribution across interfaces in superconducting cuprate superlattices," *Phys. Rev. B*, vol. 78, p. 205120, 2008.

[105] S. Smadici, J. C. T. Lee, S. Wang, P. Abbamonte, G. Logvenov, A. Gozar, C. D. Cavellin, and I. Bozovic, "Superconducting transition at 38 K in insulating-overdoped La_2CuO_4-$La_{1.64}Sr_{0.36}CuO_4$ superlattices: Evidence for interface electronic redistribution from resonant soft x-ray scattering," *Phys. Rev. Lett.*, vol. 102, p. 107004, 2009.

[106] G. Logvenov, A. Gozar, and I. Bozovic, "High-temperature superconductivity in a single copper-oxygen plane," *Science*, vol. 326, pp. 699–702, 2009.

[107] G. Logvenov, A.Gozar, V. Y. Butko, A. T. Bollinger, N. Bozovic, Z. Radovic, and I. Bozovic, "Comprehensive study of high-T_c interface superconductivity," *J. Phys. and Chem. of Solids*, vol. 71, pp. 1098–1104, 2010.

[108] N. Reyren, S. Thiel, A. D. Caviglia, L. F. Kourkoutis, G. Hammerl, C. Richter, C. W. Schneider, T. Kopp, A.-S. Retschi, D. Jaccard, M. Gabay, D. A. Muller, J.-M. Triscone, and J. Mannhart, "Superconducting interfaces between insulating oxides," *Science*, vol. 317, pp. 1196–1199, 2007.

[109] C. Cen, S. Thiel, J. Mannhart, and J. Levy, "Oxide nanoelectronics on demand," *Science*, vol. 323, pp. 1026–1030, 2009.

[110] E. Dagotto, "When oxides meet face to face," *Science*, vol. 318, pp. 1076–1077, 2007.

[111] N. Nakagawa, H. Y. Hwang, and D. A. Muller, "Why some interfaces cannot be sharp," *Nature Materials*, vol. 5, pp. 204–209, 2006.

[112] M. Azuma, Z. Hiroi, M. Takano, Y. Bando, and Y. Takeda, "Superconductivity at 110 K in the infinite-layer compound $(Sr_{1-x}Ca_x)_{1-y}CuO_2$," *Nature*, vol. 356, pp. 775–776, 1992.

[113] D. D. Castro, M. Salvato, A. Tebano, D. Innocenti, C. Aruta, W. Prellier, O. I. Lebedev, I. Ottaviani, N. B. Brookes, M. Minola, M. M. Sala, C. Mazzoli, P. Medaglia, G. Ghiringhelli, L. Braicovich, M. Cirillo, and G.Balestrino, "Occurrence of a high-temperature superconducting phase in cuprate/titanate $(CaCuO_2)_n/(SrTiO_3)_m$ superlattices," *Phys. Rev. B*, vol. 86, p. 134524, 2012.

[114] L. Hozoi, L. Siurakshina, P. Fulde, and J. van den Brink, "*Ab Initio* determination of cu $3d$ orbital energies in layered copper oxides," *Scientific Reports*, vol. 1, p. 65, 2011.

[115] D. G. Hawthorn, K. M. Shen, J. Geck, D. C. Peets, H. Wadati, J. Okamoto, S.-W. Huang, D. J. Huang, H.-J. Lin, J. D. Denlinger, R. Liang, D. A. Bonn, W. N. Hardy, and G. A. Sawatzky, "Resonant elastic soft x-ray scattering in oxygen-ordered $YBa_2Cu_3O_{6+\delta}$," *Phys. Rev. B*, vol. 84, p. 075125, 2011.

[116] G. Burns, M. K. Crawford, F. H. Dacol, E. M. McCarron, and T. M. Shaw, "Phonons in $CaCuO_2$," *Phys. Rev. B*, vol. 40, pp. 6717–6720, 1989.

[117] B. K. Agrawal and S. Agrawal, "Structural, dynamical, and electronic properties of $CaCuO_2$," *Phys. Rev. B*, vol. 48, pp. 6451–6455, 1993.

[118] N. Mermin and H. Wagner, "Absence of ferromagnetism or antiferromagnetism in one- or two-dimensional isotropic Heisenberg models," *Phys. Rev. Lett.*, vol. 17, pp. 1133–1136, 1966.

[119] M. P. M. Dean, R. S. Springell, C. Monney, K. J. Zhou, J. Pereiro, I. Bozovic, B. D. Piazza, H. M. Rønnow, E. Morenzoni, J. van den Brink, T. Schmitt, and J. P. Hill, "Spin excitations in a single La_2CuO_4 layer," *Nature Materials*, vol. 11, pp. 850–854, 2012.

[120] S. Chakravarty, B. Halperin, and D. Nelson, "Two-dimensional quantum Heisenberg antiferromagnet at low temperatures," *Phys. Rev. B*, vol. 39, pp. 2344–2371, 1989.

[121] T. C. Hsu, "Spin waves in the flux-phase description of the S = 1/2 Heisenberg antiferromagnet," *Phys. Rev. B*, vol. 41, pp. 11379–11387, 1990.

[122] A. Bianconi, A. C. Castellano, M. D. Santis, P. Rudolf, P. Lagarde, A. M. Flank, and A. Marcelli, "$L_2, 3$ XANES of the high T_c superconductor $YBa_2Cu_3O_7$ with variable oxygen content," *Solid State Commun.*, vol. 63, p. 1009, 1987.

[123] D. D. Sarma, O. Strebel, C. T. Simmons, U. Neukirch, and G. Kaindl, "Electronic structure of high-T_c superconductors from soft-x-ray absorption," *Phys. Rev. B*, vol. 37, pp. 9784–9787, 1988.

[124] J. Fink, N. Nucker, E. Pellegrin, H. Romberg, M. Alexander, and M. Knupfer, "Electron-energy-loss and x-ray absorption spectroscopy of cuprate superconductos and related-compounds," *J. Electron Spectrosc. Relat. Phenom.*, vol. 66, pp. 395–452, 1994.

[125] P. Srivastava, B. R. Sekhar, C. Gasser, F. Studer, K. B. Garg, C. T. Chen, and M. Pompa, "A polarized x-ray absorption spectroscopy study of O K and Cu L_3 edges in a Tl(2212) thin film," *J. Phys.: Condens. Matter*, vol. 10, p. 3417, 1988.

[126] R. K. Singhal, S. Dalela, D. Chaturvedi, B. Dalela, N. L. Saini, B. R. Sekhar, K. B. Garg, V. Beaumount, B. Mercey, C. T. Chen, H.-J. Lin, and T. Y. Huo, "An electronic structure study of *c*-axis oriented Nd-BCO (123) thin films using polarized soft x-ray absorption spectroscopy on Cu L_3 and O K edges," *J. Phys.: Condens. Matter*, vol. 13, p. 6865, 2001.

[127] H. Zhang, Y. Y. Wang, H. Zhang, V. P. Dravid, L. D. Marks, P. D. Han, D. A. Payne, P. G. Radaelli, and J. D. Jorgensen, "Identity of planar defects in the infinite-layer' copper oxide superconductor," *Nature*, vol. 370, pp. 352–354, 1994.

[128] M. Vojta, "Lattice symmetry breaking in cuprate superconductors: Stripes, nematics, and superconductivity," *Adv. Phys.*, vol. 58, pp. 699–820, 2009.

[129] R.-H. He, M. Hashimoto, H. Karapetyan, J. D. Koralek, J. P. Hinton, J. P. Testaud, V. Nathan, Y. Yoshida, H. Yao, K. Tanaka, W. Meevasana, R. G. Moore, D. H. Lu, S.-K. Mo, M. Ishikado, H. Eisaki, Z. Hussain, T. P. Devereaux, S. A. Kivelson, J. Orenstein, A. Kapitulnik, and Z.-X. Shen, "From a single-band metal to a high-temperature superconductor via two thermal phase transitions," *Science*, vol. 331, pp. 1579–1583, 2011.

[130] J. M. Tranquada, B. J. Sternlieb, J. D. Axe, Y. Nakamura, and S. Uchida, "Evidence for stripe correlations of spins and holes in copper-oxide superconductors," *Nature*, vol. 375, p. 561, 1995.

[131] P. Abbamonte, A. Rusydi, S. Smadici, G. D. Gu, G. A. Sawatzky, and D. L. Feng, "Spatially modulated "Mottness" in $La_{2-x}Ba_xCuO_4$," *Nat. Phys.*, vol. 1, p. 155, 2005.

[132] S.-W. Cheong, G. Aeppli, T. E. Mason, H. Mook, S. M. Hayden, P. C. Canfield, Z. Fisk, K. N. Clausen, and J. L. Martinez, "Incommensurate magnetic fluctuations in $La_{2-x}Sr_xCuO_4$," *Phys. Rev. Lett.*, vol. 67, pp. 1791–1794, 1991.

[133] T. R. Thurston, P. M. Gehring, G. Shirane, R. J. Birgeneau, M. A. Kastner, Y. Endoh, M. Matsuda, K. Yamada, H. Kojima, and I. Tanaka, "Low-energy incommensurate spin excitations in superconducting $La_{1.85}Sr_{0.15}CuO_4$," *Phys. Rev. B*, vol. 46, pp. 9128–9131, 1992.

[134] T. E. Mason, G. Aeppli, and H. A. Mook, "Magnetic dynamics of superconducting $La_{1.86}Sr_{0.14}CuO_4$," *Phys. Rev. Lett.*, vol. 68, pp. 1414–1417, 1992.

[135] K. Yamada, C. H. Lee, K. Kurahashi, J. Wada, S. Wakimoto, S. Ueki, H. Kimura, Y. Endoh, S. Hosoya, G. Shirane, R. J. Birgeneau, M. Greven, M. A. Kastner, and Y. J. Kim, "Doping dependence of the spatially modulated dynamical spin correlations and

the superconducting-transition temperature in $La_{2-x}Ba_xCuO_4$," *Phys. Rev. B*, vol. 58, pp. 6165–6172, 1998.

[136] A. R. Moodenbaugh, Y. Xu, M. Suenaga, T. J. Folkerts, and R. N. Shelton, "Superconducting properties of lanthanum barium copper oxide ($La_{2-x}Ba_xCuO_4$)," *Phys. Rev. B*, vol. 38, pp. 4596–4600, 1988.

[137] J. Lorenzana and G. Seibold, "Metallic mean-field stripes, incommensurability, and chemical potential in cuprates," *Phys. Rev. Lett.*, vol. 89, p. 136401, 2002.

[138] G. Seibold and J. Lorenzana, "Doping dependence of spin excitations in the stripe phase of high- T_c superconductors," *Phys. Rev. B*, vol. 73, p. 144515, 2006.

[139] J. Fink, E. Schierle, E. Weschke, J. Geck, D. Hawthorn, V. Soltwisch, H. Wadati, H.-H. Wu, H. A. Dürr, N. Wizent, B. Büchner, and G. A. Sawatzky, "Charge ordering in $La_{1.8-x}Eu_{0.2}Sr_xCuO_4$ studied by resonant soft x-ray diffraction," *Phys. Rev. B*, vol. 79, p. 100502(R), 2009.

[140] J. Fink, V. Soltwisch, J. Geck, E. Schierle, E. Weschke, and B. Büchner, "Phase diagram of charge order in $La_{1.8-x}Eu_{0.2}Sr_xCuO_4$ from resonant soft x-ray diffraction," *Phys. Rev. B*, vol. 83, p. 092503, 2011.

[141] S. A. Kivelson, I. P. Bindloss, E. Fradkin, V. Oganesyan, J. M. Tranquada, A. Kapitulnik, and C. Howald, "How to detect fluctuating stripes in the high-temperature superconductors," *Rev. Mod. Phys.*, vol. 75, pp. 1201–1241, 2003.

[142] M. Hücker, M. v. Zimmermann, G. D. G. Z. J. Xu, J. S. Wen, G. Xu, H. J. Kang, A. Zheludev, and J. M. Tranquada, "Stripe order in superconducting $La_{2-x}Ba_xCuO_4$ ($0.095 < x < 0.155$)," *Phys. Rev. B*, vol. 83, p. 104506, 2011.

[143] M. Fujita, H. Goka, K. Yamada, and M. Matsuda, "Competition between charge- and spin-density-wave order and superconductivity in $La_{1.875}Ba_{0.125-x}Sr_xCuO_4$," *Phys. Rev. Lett.*, vol. 88, p. 167008, 2002.

[144] S. B. Wilkins, M. P. M. Dean, J. Fink, M. Hücker, J. Geck, V. Soltwisch, E. Schierle, E. Weschke, G. Gu, S. Uchida, N. Ichikawa, J. M. Tranquada, and J. P. Hill, "Comparison of stripe modulations in $La_{1.875}Ba_{0.125}CuO_4$ and $La_{1.48}Nd_{0.4}Sr_{0.12}CuO_4$," *Phys. Rev. B*, vol. 84, p. 195101, 2011.

[145] H. Klauss, W. Wagener, M. Hillberg, W. Kopmann, H. Walf, F. J. Litterst, M. H*ü*cker, and B. B*ü*chner, "From antiferromagnetic order to static magnetic stripes: The phase diagram of $(La,Eu)_{2-x}Sr_xCuO_4$," *Phys. Rev. Lett.*, vol. 85, p. 4590, 2000.

[146] R. Liang, D. A. Bonn, and W. N. Hardy, "Evaluation of CuO_2 plane hole doping in $YBa_2Cu_3O_{6+x}$ single crystals," *Phys. Rev. B*, vol. 73, p. 180505, 2006.

[147] F. Laliberté, J. Chang, N. Doiron-Leyraud, E. Hassinger, R. Daou, M. Rondeau, B. Ramshaw, R. Liang, D. Bonn, W. Hardy, S. Pyon, T. Takayama, H. Takagi, I. Sheikin, L. Malone, C. Proust, K. Behnia, and L. Taillefer, "Fermi-surface reconstruction by stripe order in cuprate superconductors.," *Nat. Commun.*, vol. 2, p. 432, 2011.

[148] X. F. Sun, K. Segawa, and Y. Ando, "Metal-to-insulator crossover in $YBa_2Cu_3O_y$ probed by lowtemperature quasiparticle heat transport," *Phys. Rev. Lett.*, vol. 93, p. 107001, 2004.

[149] R. Daou, J. Chang, D. LeBoeuf, O. Cyr-Choinière, F. Laliberté, N. Doiron-Leyraud, B. J. Ramshaw, R. Liang, D. A. Bonn, W. N. Hardy, and L. Taillefer, "Broken rotational symmetry in the pseudogap phase of a high-T_c superconductor," *Nature*, vol. 463, pp. 519–522, 2010.

[150] H. F. Fong, P. Bourges, Y. Sidis, L. P. Regnault, J. Bossy, A. Ivanov, D. L. Milius, I. A. Aksay, and B. Keimer, "Spin susceptibility in underdoped $YBa_2Cu_3O_{6+x}$," *Phys. Rev. B*, vol. 61, p. 14773, 2000.

[151] P. C. Dai, H. A. Mook, R. D. Hunt, and F. Dogan, "Evolution of the resonance and incommensurate spin fluctuations in superconducting $YBa_2Cu_3O_{6+x}$," *Phys. Rev. B*, vol. 63, p. 054525, 2001.

[152] N. B. Christensen, D. F. McMorrow, H. M. Rønnow, B. Lake, S. M. Hayden, G. Aeppli, T. G. Perring, M. Mangkorntong, M. Nohara, and H. Takagi, "Dispersive excitations in the high-temperature superconductor $La_{2-x}Sr_xCuO_4$," *Phys. Rev. Lett.*, vol. 93, p. 147002, 2004.

[153] J. M. Tranquada, H. Woo, T. G. Perring, H. Goka, G. D. Gu, G. Xu, M. Fujita, and K. Yamada, "Quantum magnetic excitations from stripes in copper oxide superconductors," *Nature*, vol. 429, no. 6991, pp. 534–538, 2004.

[154] N. Doiron-Leyraud, C. Proust, D. LeBoeuf, J. Levallois, J.-B. Bonnemaison, R. Liang, D. A. Bonn, W. N. Hardy, and L. Taillefer, "Quantum oscillations and the Fermi surface in an underdoped high-T_c superconductor," *Nature*, vol. 447, pp. 565–568, 2007.

[155] N. Harrison and S. E. Sebastian, "Protected nodal electron pocket from multiple-Q ordering in underdoped high temperature superconductors," *Phys. Rev. Lett.*, vol. 106, p. 226402, 2011.

[156] T. Wu, H. Mayaffre, S. Krämer, M. Horvatic, C. Berthier, W. N. Hardy, R. Liang, D. A. Bonn, and M.-H. Julien, "Magnetic-field-induced charge-stripe order in the high-temperature superconductor $YBa_2Cu_3O_y$," *Nature*, vol. 477, p. 191, 2011.

[157] D. Haug, V. Hinkov, Y. Sidis, P. Bourges, N. B. Christensen, A. Ivanov, T. Keller, C. T. Lin, and B. Keimer, "Neutron scattering study of the magnetic phase diagram of underdoped $YBa_2Cu_3O_{6+x}$," *New J. Phys.*, vol. 12, p. 105006, 2010.

[158] W. D. Wise, M. C. Boyer, K. Chatterjee, T. Kondo, T. Takeuchi, H. Ikuta, Y. Wang, and E. W. Hudson, "Charge-density-wave origin of cuprate checkerboard visualized by scanning tunnelling microscopy," *Nat. Phys.*, vol. 4, pp. 696–699, 2008.

[159] J. E. Hoffman, E. W. Hudson, K. M. Lang, V. Madhavan, H. Eisaki, S. Uchida, and J. C. Davis, "A four unit cell periodic pattern of quasi-particle states surrounding vortex cores in $Bi_2Sr_2CaCu_2O_{8+\delta}$," *Science*, vol. 295, pp. 466–469, 2002.

[160] C. Howald, H. Eisaki, N. Kaneko, M. Greven, and A. Kapitulnik, "Periodic density-of-states modulations in superconducting $Bi_2Sr_2CaCu_2O_{8+\delta}$," *Phys. Rev. B*, vol. 67, p. 014533, 2003.

[161] C. V. Parker, P. Aynajian, E. H. da Silva Neto, A. Pushp, S. Ono, J. Wen, Z. Xu, G. Gu, and A. Yazdani, "Fluctuating stripes at the onset of the pseudogap in the high-T_c superconductor $Bi_2Sr_2CaCu_2O_{8+x}$," *Nature*, vol. 468, pp. 677–680, 2010.

[162] O. K. Andersen, A. I. Liechtenstein, O. Rodriguez, I. I. Mazin, O. Jepsen, V. P. Antropov, O. Gunnarsson, and S. Gopalan, "Electrons, phonons, and their interaction in $YBa_2Cu_3O_7$," *Physica C*, vol. 185–189, pp. 147–155, 1991.

[163] H. Yao, D.-H. Lee, and S. Kivelson, "Fermi-surface reconstruction in a smectic phase of a high-temperature superconductor," *Phys. Rev. B*, vol. 84, p. 012507, 2011.

[164] J. Chang, E. Blackburn, A. T. Holmes, N. B. Christensen, J. Larsen, J. Mesot, R. Liang, D. A. Bonn, W. N. Hardy, A.Watenphul, M. v. Zimmermann, E. M. Forgan, and S. M. Hayden, "Direct observation of competition between superconductivity and charge density wave order in $YBa_2Cu_3O_{6.67}$," *Nat. Phys.*, vol. 8, pp. 871–876, 2012.

[165] M. H*ü*cker, M. v. Zimmermann, Z. J. Xu, J. S. Wen, G. D. Gu, and J. M. Tranquada, "Enhanced charge stripe order of superconducting $La_{2-x}Ba_xCuO_4$ in a magnetic field.," *arXiv:1212.3575v1*, 2012.

[166] S. Blanco-Canosa, A. Frano, T. Loew, Y. Lu, G. Ghiringhelli, M. Minola, C. Mazzoli, L. Braicovich, E. Schierle, E. Weschke, M. L. Tacon, and B. Keimer, "Three-phase competition in underdoped $YBa_2Cu_3O_{6+\delta}$," *arXiv:1212.5580v1*, 2012.

[167] E. Blackburn, J. Chang, M. H*ü*cker, A. T. Holmes, N. B. Christensen, R. Liang, D. A. Bonn, W. N. Hardy, M. v. Zimmermann, E. M. Forgan, and S. M. Hayden, "Direct observation of charge density wave order at zero magnetic field in ortho-ii $YBa_2Cu_3O_{6.54}$," *arXiv:1212.3836v1*, 2012.

[168] J. Xia, E. Schemm, G. Deutscher, S. A. Kivelson, D. A. Bonn, W. N. Hardy, R. Liang, W. Siemons, G. Koster, M. M. Fejer, and A. Kapitulnik, "Polar Kerr-Effect measurements of the High-Temperature $YBa_2Cu_3O_{6+x}$ superconductor: Evidence for broken symmetry near the pseudogap temperature," *Phys. Rev. Lett.*, vol. 100, p. 127002, Mar. 2008.

[169] B. Fauqué, Y. Sidis, V. Hinkov, S. Pailhès, C. T. Lin, X. Chaud, and P. Bourges, "Magnetic order in the pseudogap phase of High-T_c superconductors," *Phys. Rev. Lett.*, vol. 96, p. 197001, May 2006.

List of publications

1. "Momentum and polarization dependence of single-magnon spectral weight for Cu L_3-edge resonant inelastic x-ray scattering from layered cuprates", L. Braicovich, M. Moretti Sala, L. J. P. Ament, V. Bisogni, M. Minola, G. Balestrino, D. Di Castro, G. M. De Luca, M. Salluzzo, G. Ghiringhelli, and J. van den Brink, *Phys. Rev. B* **81**, 174533 (2010).

2. "Energy and symmetry of dd excitations in undoped layered cuprates measured by Cu L_3 resonant inelastic x-ray scattering", M. Moretti Sala, V. Bisogni, L. Braicovich, C. Aruta, G. Balestrino, H. Berger, N. B. Brookes, G.M. De Luca, D. Di Castro, M. Grioni, M. Guarise, P. G. Medaglia, F. Miletto Granozio, M. Minola, M. Radovic, M. Salluzzo, T. Schmitt, K.-J. Zhou, and G. Ghiringhelli, *New Journal of Physics* **13**, 043026 (2011).

3. "Intense paramagnon excitations in a large family of high-temperature superconductors", M. Le Tacon, G. Ghiringhelli, J. Chaloupka, M. Moretti Sala, V. Hinkov, M. W. Haverkort1, M. Minola, M. Bakr, K. J. Zhou, S. Blanco-Canosa, C. Monney, Y. T. Song, G. L. Sun, C. T. Lin, G. M. De Luca, M. Salluzzo, G. Khaliullin, T. Schmitt, L. Braicovich, and B. Keimer, *Nature Physics* **7**, 725-730 (2011).

4. "Magnetic and ligand field properties of copper at the interfaces of $(CaCuO_2)_n/(SrTiO_3)_n$ superlattices studied with high resolution Resonant Inelastic X-ray Scattering", M. Minola, D. Di Castro, L. Braicovich, N. B. Brookes, D. Innocenti, M. Moretti Sala, A. Tebano, G. Balestrino, and G. Ghiringhelli, *Phys. Rev. B* **85**, 235138 (2012).

5. "Bimagnon studies in cuprates with resonant inelastic x-ray scattering at the O K edge. I - Assessment on La_2CuO_4 and comparison with the excitation at Cu L_3 and Cu K edges", V. Bisogni, L. Simonelli, L. J. P.

Ament, F. Forte, M. Moretti Sala, M. Minola, S. Huotari, J. van den Brink, G. Ghiringhelli, N.B. Brookes, and L. Braicovich, *Phys. Rev. B* **85**, 214527 (2012).

6. "Long-range incommensurate charge fluctuations in spin-gapped high-temperature superconductors", G. Ghiringhelli, M. Le Tacon, M. Minola, S. Blanco-Canosa, C. Mazzoli, N.B. Brookes, G.M. De Luca, A. Frano, D. G. Hawthorn, F. He, T. Loew, M. Moretti Sala, D.C. Peets, M. Salluzzo, E. Schierle, R. Sutarto, G. A. Sawatzky, E. Weschke, B. Keimer, and L. Braicovich, *Science* **337**, 821-825 (2012).

7. "Resonant Inelastic Scattering at the ESRF: hard and soft X-rays", L. Braicovich, N.B. Brookes, G. Ghiringhelli, M. Minola, G. Monaco, M. Moretti Sala, L. Simonelli, *Synchrotron Radiation News* **25**, 4 (2012).

8. "Off-stoichiometry effect on orbital order in A-site manganites probed by x-ray absorption spectroscopy", C. Aruta, M. Minola, A. Galdi, R. Ciancio, A. Yu. Petrov, N. B. Brookes, G. Ghiringhelli, L. Maritato, and P. Orgiani, *Phys. Rev. B* **86**, 115132 (2012).

9. "Distinct charge orders in the planes and chains of ortho-III ordered $YBa_2Cu_3O_{6+x}$ identified by resonant elastic x-ray scattering", A. J. Achkar, R. Sutarto, X. Mao, F. He, A. Frano, S. Blanco-Canosa, M. Le Tacon, G. Ghiringhelli, L. Braicovich, M. Minola, M. Moretti Sala, C. Mazzoli, Ruixing Liang, D. A. Bonn, W. N. Hardy, B. Keimer, G. A. Sawatzky, and D. G. Hawthorn, *Phys. Rev. Lett.* **109**, 167001 (2012).

10. "Occurrence of a high-temperature superconducting phase in cuprate/titanate $(CaCuO_2)_n/(SrTiO_3)_m$ superlattices", D. Di Castro, M. Salvato, A. Tebano, D. Innocenti, C. Aruta, W. Prellier, O. I. Lebedev, I. Ottaviani, N. B. Brookes, M. Minola, M. Moretti Sala, C. Mazzoli, P.G. Medaglia, G. Ghiringhelli, L. Braicovich, M. Cirillo, and G. Balestrino, *Phys. Rev. B* **86**, 134524 (2012).

11. "Charge localization at the interface between $La_{1-x}Sr_xMnO_3$ and the "infinite layer" cuprate $CaCuO_2$", Nan Yang, D. Di Castro, C. Aruta, C. Mazzoli, M. Minola, N. Brookes, M. Moretti Sala, W. Prellier, O. I. Lebedev, A. Tebano, and G. Balestrino, J. Appl. Phys. **112**, 123901 (2012).

12. "Measurement of the effect of lattice strain on magnetic interactions and orbital splitting in $CaCuO_2$ using resonant inelastic x-ray scattering", M. Minola, L. Hozoi, D. Di Castro, R. Felici, M. Moretti Sala, A.

Tebano, G. Balestrino, G. Ghiringhelli, Jeroen van den Brink, and L. Braicovich, submitted.

13. "Induced interface magnetism in n-type $SrTiO_3$ heterostructures", M. Salluzzo, S. Gariglio, D. Stornaiuolo, V. Sessi, S. Rusponi, C. Piamonteze, G. M. De Luca, A. Gadaleta, D. Marr, M. Minola, H. Brune, F. Nolting, N. B. Brookes, and G. Ghiringhelli, submitted.

14. "Three-phase competition in underdoped $YBa_2Cu_3O_{6+\delta}$", S. Blanco-Canosa, A. Frano, T. Loew, Y. Lu, G. Ghiringhelli, M. Minola, C. Mazzoli, L. Braicovich, E. Schierle, E. Weschke, M. Le Tacon and B. Keimer, submitted. Preprint as arXiv:1212.5580v1